Imprints of Ice Dynamics and Atmospheric Signals on the internal structure of Antarctic Ice as seen via Radar

Prägung der internen Struktur antarktischen Eises durch Eisdynamik und Atmosphäre aus Sicht des Radars

---

Cumulative Doctoral Thesis,
Kumulative Doktorarbeit

Reinhard Drews
Alfred-Wegener-Institut
für Polar- und Meeresforschung
Universität Bremen

Contents

Abstract

Different electromagnetic reflection methods can operate from satellites, airplanes or ground vehicles to illuminate the surface and the inside of ice sheets across varying spatial scales. The backscattered signal is formed by micro-physical ice properties, many of which in turn are influenced by mechanisms operating on a macro-scale: the alignment of crystal orientation fabric (COF) depends on the specific strain regime and the initial impurity loading; the pattern in internal layering is imprinted by accumulation and the surrounding flow regime; the brightness of the bottom reflection over ice-shelves depends on the melting or refreezing of platelet ice which is susceptible to changing ocean currents and grounding line positions.

The study is subdivided in five chapters which have been or will be published separately. All studies focus on the link between these small-scale features and their large-scale expressions. The synthesis of the different methods improves the capability of remote sensing to deliver variables from which the current state of the cryosphere can be determined. The study contributes to assimilating geophysical data into the coming generation of ice-dynamic models which improve the understanding of ice-sheet histories and prognose their future behaviour.

The starting point is the appearance of the radio-echo free zone (EFZ), which is a feature-less band observed above the ice–bed interface in many radargrams across Greenland and Antarctica. The comparison of the EFZ onset with optical ice-core images yields a connection between the mm-cm scale disturbances in the core's stratigraphy and the disappearance of radar reflection horizons. This is evidence that ice flow can disturb internal ice layering, which hampers the derivation of a coherent age–depth scale and indicates a changing flow behaviour with depth.

A polarimetric radar survey in the same study area shows that backscattered power varies with the horizontal orientation of the antennas (i.e. with the polarization plane).

0. ABSTRACT

Extrema in backscatter for a constant antenna angle change in direction at 900 m depth. By using different scattering models I differentiate between competing mechanisms for the observed anisotropy, namely a vertically varying COF or ellipsoidal air bubbles. The analysis suggests that the effect from a varying COF is superior. Radar polarimetry thus is capable to infer the principal components of COF, and with it the principal components of the corresponding stress–strain regime. Potentially, the different modes in COF variations are related to climate signals.

The detection of anisotropic COF is an important factor in terms of anisotropic ice flow, which in turn influences the shape in internal layering especially near ice divides. The third study combines satellite data and GPS measurements with airborne and ground-based radar surveys to characterize a potential drill site with respect to internal layering, accumulation, and the topography of surface and bedrock. Particular attention is given to the upwarping of internal layering beneath the divides, which is a consequence of a nonlinear and anisotropic rheology. All datasets are used as input for a two-dimensional, anisotropic flow model which estimates an age–depth distribution. Likely, ice from the last glacial is present at larger depths. Ice at intermediate depths seems suitable for studies targeting the last few thousand years. Based on the structure of internal layering, the ice divides and the surrounding flow regime were stable over the last 10 000 years. The investigated ice ridge is surrounded by ice shelves. Surface velocities as well as the transition of grounded and floating ice are mapped from satellite images.

This is used in the last two studies. In a collaborative project, the most landward freely floating line of ice shelves, and the most seaward line where ice flow is still influenced by the bedrock are mapped from optical satellite imagery around the Antarctic perimeter. The simultaneous derivation of coastal elevation as a basis for the derivation of flow velocities is a starting point for mass balance estimates, in which ice flow, but also sub-ice shelf melting are important parameters. The latter is treated in a case study. Using the continuity equation in a steady-state approximation, it is possible to spatially map the sub-ice shelf melt rates. A new approach is presented which circumnavigates the interpolation of ice-thickness data by applying the continuity equation only along profile lines.

Zusammenfassung

Verschiedene elektromagnetische Reflexionsverfahren können von Satelliten, Flugzeugen oder Fahrzeugen aus angewendet werden, um die Oberfläche und interne Strukturen der Eisschilde über verschiedene Skalen hinweg auszuleuchten. Das rückgestreute Signal wird von mikro-physikalischen Eiseigenschaften bestimmt, welche von auf der Makroskala wirkenden Mechanismen geprägt werden: Die Kristallstruktur hängt vom Spannungsregime und den enthaltenen Verunreinigungen ab; die interne Schichtung ist geprägt vom Fließregime und der Akkumulation; die Helligkeit der Bodenreflexion über Schelfeisen variiert zwischen marinem oder meteorischem Eis, welches wiederum von der Position der Gründungslinie und der Ozeanströmung beeinflusst wird.

Die Studie ist in fünf Teile unterteilt, die separat veröffentlich sind, oder sich zur Zeit im Prozess der Veröffentlichung befinden. Alle Studien befassen sich mit dem Zusammenhang von mikro-physikalischen Größen und deren makro-physikalischen Entsprechungen. Die Synthese verschiedener elektromagnetischer Verfahren der Fernerkundung liefert Parameter, die den momentanen Zustand der Kryosphäre beschreiben. Die Arbeit trägt dazu bei, geophysikalische Messgrößen in die nächste Generation eisdynamischer Modelle einzubauen, was das Verständnis für die Geschichte der Eisschilde verbessert, und es ermöglicht bessere Vorhersagen über deren zukünftige Entwicklung zu treffen.

In der ersten Studie wird die echofreien Zone (EFZ) untersucht. Als EFZ bezeichnet man einen strukturlosen Bereich über dem Felsbett, der in vielen Radargrammen von Grönland oder der Antarktis beobachtet wird. Für einen Beispieldatensatz wird das Verschwinden der Radar-Reflexionshorizonte mit beobachteten Störungen im mm-cm Bereich der optischen Stratigraphie eines Eiskerns korreliert. Dies liefert erste Anhaltspunkte, dass durch ein sich veränderndes Fließverhaltens die Schichtung in größeren Tiefen gestört werden kann. Dies erschwert die Ableitung einer Alters-Tiefen Skala.

Kurz überhalb der EFZ beobachtet man eine starke Änderung in der Eiskern - Kristallstruktur. Dies wird mit einem polarimetrischen Radardatensatz näher untersucht. Mit rotierenden Antennen (i.e. rotierende Polarisationsebenen) ändert sich die rückgestreute Energie. Die Rückstreuextrema für konstante Antennenwinkel ändern ihre Richtung in 900 m Tiefe. Anhand von Streumodellen wird zwischen konkurrierenden Mechanismen (variierende Kristalltextur und ellipsoide Luftblasen) für die beobachtet Anisotropie in der Rückstreuung differenziert. Die Analyse bestimmt die variierende Kristallstruktur als primären Faktor und zeigt, dass Messungen dieser Art in der Lage sind die Hauptkomponenten der Kristallstruktur zu bestimmen, die wiederum Aufschluß über das Spannungsregime geben. Möglicherweise erlaubt der Übergang der beiden anisotropen Reflexionszonen eine Kartierung des Übergangs vom holozänen zu glazialen Eis.

Die Erfassung der Kristalltextur spielt eine wichtige Rolle im Bezug auf die anisotrope Fließeigenschaft des Eises, die besonders nahe der Eisscheiden die Form der internen Schichtung prägt. Dies ist Thema der dritten Studie, die Satellitendaten und GPS-Messungen mit boden- und flugzeuggestützen Radardaten verbindet um eine mögliche Bohrlokation hinsichtlich der internen Schichtung, der Akkumulationsverteilung, und der Topographie von Oberfläche und Felsbett zu charakterisieren. Schwerpunkt ist die Aufwölbung der internen Schichten unter den Eisscheiden, welche als Konsequenz von nichtlinearem und anisotropem Fließen gedeutet wird. Die Ergebnisse dienen als Eingangsdatensatz für ein zweidimensionales, anisotropes Fließmodell. Die Ergebnisse deuten darauf hin, dass Eisalter und Schichtdicke in mittleren Tiefen besonders für Studien der letzten tausende von Jahren geeignet sind. In großen Tiefen wird glaziales Eis vermutet. Aus der internen Struktur wird die Stabilitt der Eisscheiden und des umgebenden Fließregimes über die letzten 10 000 Jahre abgeleitet. Der untersuchte Eisrücken ist von schwimmenden Schelfeisen umgeben. Der Übergang von gegründetem zur schwimmenden Eis sowie die Oberflächengeschwindigkeiten können aus Satellitendaten abgeleitet werden.

Dies ist die Grundlage für die beiden letzten Studien. In einem Kooperationsprojekt wurden zwei Linien für die gesamte Antarktis kartiert: Die landeinwärts gerichtete Grenze an der das Eis frei schwimmt, sowie die ozeanwärts gerichtete Linie auf der das Eis noch gegründet ist. Mit der ebenfalls abgeleiteten küstennahen Topographie sind wichtige Eingangsparameter für Massenbilanz-Studien gegeben. Für die Massenbilanz

ist die Eisgeschwindigkeit, aber auch Schmelzraten unter dem Schelfeis von Bedeutung. Letzteres wird in einer Fallstudie untersucht. Anhand der Kontinuitätsgleichung und unter der Annahme, dass sich das System im Gleichgewicht befindet, ist es möglich die variierenden Schmelzraten zu kartieren. Hierfür wird ein neuer Zugang präsentiert, der auf die Interpolation der Eisdicken verzichtet, indem die Kontinuitätsgleichung nur auf vorhandenen Profillinien angewendet wird.

Glossary

ASAID Antarctic Surface Accumulation and Ice Discharge; and IPY project initiated by R. Bindschadler, Goddard Space Flight Center, USA

AWI Alfred Wegener Institute; Institute for Polar and Marine Research in Bremerhaven

BP before present; references time-scale to years before1950 AD

COF Crystal Orientation Fabric; describes the alignment of crystal orientation for example via the distribution of the optical c-axes

DEM Digital Elevation Model;

DEP Dielectric Profiling; method to determine the electrical conductivity and permittivity of an ice core with curved electrodes

DML Dronning Maud Land; Coastal sector in Antartica facing the Weddel Sea and formally claimed by Norway

EDML EPICA Dronning Maud Land; name of ice core in Dronning Maud Land withing the EPICA program

EFZ Echo-Free Zone; depth interval in an ice-sheet with a sudden absence of internal reflections not related to the system sensitivity

EPICA European Project of Ice Coring in Antarctica; a joint European scientific program

GPR Ground-Penetrating Radar; often—but not exclusively—used for ground-based radar measurements

GPS Global Positioning System

GRACE Gravity Recovery and Climate Experiment; a satellite mission to map the earth's gravitational field and changes thereof.

InSAR Interferometric SAR; describes a method which combines different SAR images and evaluates the phas differences

IPCC International Panel on Climate Change; A scientific comittee, assessing, reviewing and summarizing the latest results for climate change in the IPCC reports. The latest assessment was done in 2007 (AR4), and preparations for the fith assesment report are on the way

IPY International Polar Year; An initiative in 2007-2008 to spur more collaborative research in polar regions and to increase public outreach. This is the fourth polar year.

RES Radio-Echo Sounding; often—but not exclusively—used for airborne radar measurements

SAR Synthetic Aperture Radar; Coherent radar system which allows to *synthetically* enlarge the aperture via a coherent post-processing

TWT Two-way traveltime

1. Introduction

1.1 The larger framework

This section incorporates the role of geophysical measurements and remote-sensing techniques on ice into the larger framework of global climate research. The double role of ice sheets in terms of archiving and forcing the state of the climate system is highlighted. Questions with respect to the interpretation of the ice-core records and the predictability of ice sheets in a changing climate are formulated. References are exemplary rather than exhaustive.

Studies on palaeoclimate proxies show that the earth's climate has changed on various time scales in the past. Temperature reconstructions from ice cores extent back to more than 800 ka before present (BP) and reveal at least eight glacial–interglacial cycles (Jouzel et al., 2007). The climate signal in that period is imprinted by 100 ka cyclicity whereas further back in time (prior to 1 Ma BP) marine records show a transition to variations with a 41 ka cyclicity (Lisiecki and Raymo, 2005). The different frequencies can be related to changes in the earth's orbital parameters due to gravitational effects from the solar system. The eccentricity, the obliquity (axial tilt), and the precession of the equinoxes (wobbling of poles) vary periodically and are referred to as the Milanković cycles (Milankovitch, 1941). The orbit's eccentricity changes in characteristic times of 100 and 400 ka and modulates the distance from Sun to Earth. The tilt of the earth's axis (obliquity) breaks the symmetry between North and South, leading to a reversed seasonality in the two hemispheres. The obliquity changes with a periodicity of 41 ka which alters, amongst others, the spatial boundary between the seasons. The precession modulates the latitudinal and seasonal distribution of solar radiation and imposes a 19 and 21 ka cycle onto the climate system. The variation in orbital parameters mostly redistributes the incoming solar radiation, and to a lesser extent it changes the overall radiation balance. The latter is more influenced by a changing solar activity

or feedback processes like a changing albedo[1] and changing atmospheric greenhouse gas concentrations reducing the long-wave radiation radiated back to space (International Panel on Climate Change (IPCC)-report AR4 Le Treut et al., 2007, chap. 1, p. 115f). While the solar activity and alterations in orbital parameters are relatively well understood, there is only a poor understanding for the nature of the feedbacks like a changing ice and vegetation cover (IPCC-report AR4, Jansen et al., 2007, chap. 6, pg. 435f). Simply speaking, the frequencies in which glacials and interglacials alternate can be linked to the Milanković cycles, but the amplitudes and the dominating frequency are determined by feedback processes. The extent and volume of the large ice sheets must play a pivotal role as they significantly determine the overall albedo, sea level and ocean currents. According to the Milanković theory, a glacial period can be triggered by a decreasing summer insolation in the northern latitudes leading to a build up of ice sheets on the northern land masses once the summer temperatures are not high enough to fully melt the snow accumulated in the winter seasons. Modeling studies (Bintanja and van de Wal, 2008) suggest that the transition from a 41 ka to a 100 ka cyclicity is related to critical sizes of ice sheets, and that oversized, wet-based ice sheets may collapse and thus also trigger the end of a glacial period.

Ice sheets play a double role in climate research, on the one hand by amplifying the effects of changing orbital parameters, and on the other hand by archiving the climate history through the incremental build-up of layers which record climate proxies and atmospheric composition. Ice cores provide direct access to atmospheric conditions in the past through the enclosure of gases, impurities and stable isotopes. To name a few applications: Trapped air bubbles are used to analyze the gas content of the greenhouse gases CO_2(Lüthi et al., 2008), CH_4(Loulergue et al., 2008, Bock et al., 2010) and N_2O (Schilt et al., 2010). Impurities like dust particles give insight into transport processes and/or changing conditions at the source (Fischer et al., 2007), and the ratio of stable isotopes enables temperature reconstructions (Dansgaard, 1964). However, the abundance of palaeoclimatic proxies in ice comes along with the burden of high logistic efforts and with a complex interpretation of the acquired climate record due to the dynamic nature of ice sheets. The retrieval of a deep ice core usually takes several seasons and requires an international collaboration. An overview in terms of pre-site surveys, logistics and major outcomes for the EPICA (European Project for Ice Coring in Antarctica) ice core in Dronning Maud Land (DML), Antarctica, is given by Oerter et al. (2009). Once the ice core is successfully retrieved, it is challenging to determine

[1] i.e. a changing ratio of incoming and reflected energy through changes in cloud cover, land cover or aerosol content in the atmosphere

the age–depth relationship. Accurate dating is needed in order to link ice-core data from both hemispheres (EPICA community members, 2006) and to connect the derived climate records to other climate archives (e.g. sediment cores). The individual age–depth scale of a single core is often established with a combination of layer counting and ice-flow modeling, both incorporating prominent time markers (e.g. known volcanic eruptions) if available. These methods rely on an undisturbed stratigraphy which is not always given (Bell et al., 2011). The derivation of an age–depth relationship for the deep core in DML is illustrated by Ruth et al. (2007). For a proper interpretation of the climate record the catchment area needs to be well defined, especially for ice cores drilled in a flank-flow setting in which ice parcels at a certain depth were originally deposited at some place further upstream along the flowline. Each ice core also faces the issue of how representative it is, meaning to which degree area-wide (and even global) conclusions can be drawn from a single point measurement. These difficulties and shortcomings in ice-core research can be eased with various remote-sensing techniques. The principles of these methods will be explained in the following sections, but in order to integrate them into a larger framework I mention some major outcomes already at this stage.

By now, satellites continuously monitor the ice-sheet surface with active and passive instruments in different frequency bands. Coherent, side-looking radar systems (referred to as synthetic aperture radar (SAR)) enable the derivation of surface velocities and topography (Drews et al., 2009, Bäßler, 2011) via a phase sensitive post-processing. The side-looking systems provide the only means for an area-wide derivation of flow fields, while the topography in gently sloped areas may also be interpolated from nadir-looking altimeters (Wesche et al., 2009, Bamber et al., 2009). The variation in backscattered intensity depends on many factors, among those the surface slope and the snow morphology. It is possible to link the intensity variations to spatially varying accumulation rates (Rotschky et al., 2006). Despite the persistent lack of sufficient ground control points—a major challenge for all satellite-based data products in polar regions—remote sensing from space adds significantly in defining the dynamics and extent of catchment areas around ice cores. However, no ground-penetrating radar has been successfully installed on a satellite orbiting Earth yet[1]. Therefore, airborne and ground-based ground-penetrating radar surveys are currently the only means to illuminate the interior of ice-sheets electromagnetically. The development of coherent ground-penetrating radars which allow a coherent post-processing to enhance the resolutoin is on the way (Paden et al., 2010), but so far most radar data is collected without

[1]Meanwhile two ground-penetrating radars systems (MARSIS and SHARAD) observe the ice-sheets and their interior structure on Mars.

applying such techniques.

The antennas emit successive electromagnetic pulses and receive reflections from within the ice in different time gates. The setup can be dragged (or flown) parallel to the surface with a constant antenna distance (common offset mode), or the antenna distance is varied around a fixed point between the two antennas (common midpoint mode). To differentiate between airborne and ground-based profiles in this thesis, I use the terms radio-echo sounding (RES) and ground-penetrating radar (GPR), respectively[1]. Ice thickness and internal layering (e.g. prominent volcanic ash horizons) are visualized in common offset mode by recording amplitude and two-way traveltime (TWT) of reflections from within the ice along a chosen profile. The applications for ice-core research are versatile: Ice thickness and bedrock topography is an important parameter for surveys prior to drilling (e.g. Steinhage et al., 2001), and from the geometry in internal layering it is possible to deduce accumulation estimates (Eisen et al., 2005) or link different ice cores (and thus synchronize the age–depth relationship) along prominent internal reflection horizons (e.g. Eisen et al., 2004). The extrapolation of reflection horizons linked to the ice core extends the point measurement spatially. Common midpoint measurements can be used to deduce the vertical profile of electromagnetic wave speed (Eisen et al., 2002). A synopsis of different remote-techniques is shown in Figure 1.1.

Apart from supporting and enhancing the results drawn from ice-core records with respect to paleo-climate, results from remote sensing give important insight into the status quo of the ice sheets and ultimately will contribute to ice-sheet modeling efforts to predict ice-sheet behavior under changing climatic boundary conditions. The big players in terms of fresh water input, ocean currents and sea level rise are the Greenland and the Antarctic ice sheets. It is important to accurately determine their mass (im)balance and to identify key components controlling changes thereof. Recent mass balance estimates for the two ice sheets are summarized in the IPCC-report (Lemke et al. (2007, chap. 4, pg. 361)). There is a tendency to believe that both ice sheets currently lose mass, but especially for Antarctica, the effect of increased accumulation versus increased discharge cannot be estimated with the accuracy needed (Alley et al., 2007). More recent studies (e.g. Rignot et al., 2011b) indicate a negative mass budget of Antarctica, and apply independent remote-sensing methods to monitor the ice sheets with respect to their mass balance. Repeat-pass laser- and radar-altimetry measure elevation changes. The elevation changes can be turned into changes of mass with a

[1]This distinction is not a universal standard in the glaciology community and may be handled differently in other studies

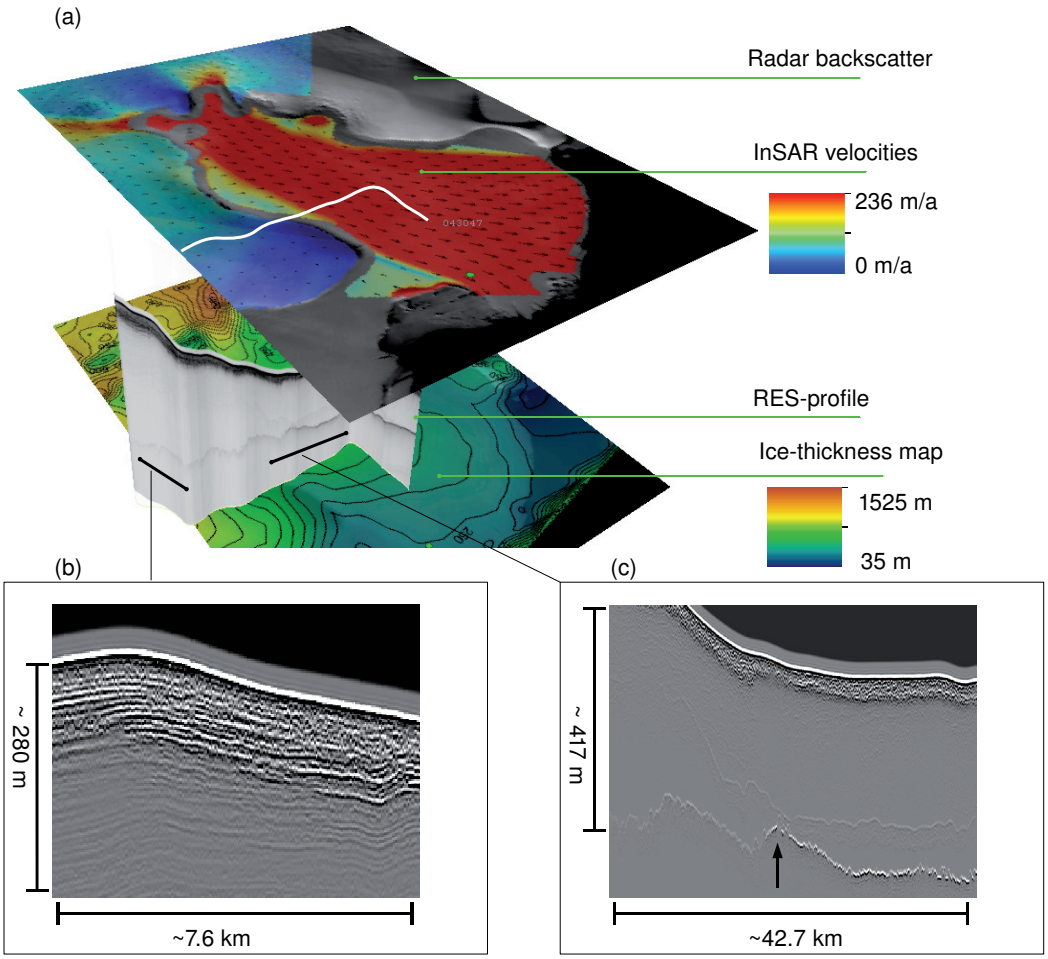

Figure 1.1: Illuminating ice sheets electromagnetically - **(a)** Three dimensional representation of ice flow, internal structure and ice thickness in the hinterland of the German permanent station Neumayer III, Dronning Maud Land, Antarctica. Scene diameter is approximately 150×100 km. At the top, the InSAR surface velocities (Neckel, 2011) are projected onto a (satellite-based) grayvalue radar backscatter image (Haran et al., 2005). Below the surface, the internal structure is visualized with an airborne RES profile crossing the grounding zone. The bottom image is an interpolated ice-thickness map based on various RES profiles; **(b)** Zoom of the upper third in the RES profile with evident internal layering; **(c)** Close-up of the grounding zone. The ice–ocean interface (right of arrow) exhibits a stronger amplitude compared to the ice–bedrock interface (left of arrow).

density–depth model that accounts for the lower density of unconsolidated firn and also includes seasonal densification processes. Prominent examples for this approach are the satellites CryoSat-2 and ICESat-1, as well as various airborne campaigns (ICEBridge and CryoVEX (Helm et al., 2007))[1]. Changes in the gravitational potential are determined via the varying distance of two specifically designed satellites in the Gravity Recovery and Climate Experiment (GRACE). This is the only method which directly infers changes in mass (Velicogna and Wahr, 2005, Velicogna and Wahr, 2006) with the main drawback of a low resolution and ambiguities as to where the changes of mass actually occur (in the mantle or at the surface). In a budgeting approach, the ice discharge at the margins is compared to the inland accumulation. Discharge estimates are obtained via the combination of surface velocities (predominately derived via satellite radar interferometry) and ice thickness estimates. Apart from evident uncertainties of the vertical velocity profile, the approach also heavily relies on in-situ ice-thickness and accumulation estimates from RES and GPR data. A natural gate for ice discharge estimates is given along the transition line where the grounded ice sheet first meets the ocean. This *grounding line* is the first contact point for direct ice–ocean interaction and changes in its horizontal position are a critical indicator for changes in the local mass balance of the corresponding discharge gate. At the freely floating parts, the flotation criterion can be applied to circumnavigate areas with insufficient ice thickness data coverage (Griggs and Bamber, 2011). However, this increases the uncertainty significantly. For the Greenlandic ice sheet, runoff of meltwater in the summer (in the lower elevated areas) and ice flow both contribute significantly to the overall mass balance. For the Antarctic ice sheet most of the discharge is governed by ice flow only. At both ice sheets, the sub-ice shelf melting and refreezing rates are not well quantified yet.

Basal sliding of ice depends strongly on the conditions at the ice–bedrock interface, and internal deformation is governed by a nonlinear and anisotropic rheology. This puts high demands on the modeling of ice flow. The conditions at the bed can be investigated with GPR surveys on the basis of a varying reflection amplitude from the bedrock return: reflections from a subglacial lake or a wet-based ice sheet are generally stronger compared to the ones from a dry bed. However, effects within the ice like birefringence and a spatially varying signal attenuation hamper the direct interpretation of the bed echo strength without prior assumptions about the overlying ice sheet (Matsuoka, 2011). The birefringent nature of polar ice is due to the dielectric anisotropy of the single

[1] CryoSat-2 has been launched in 2010. ICESat-1 started in 2003 and was decomissioned in 2009, ICESat-2 is scheduled for 2016. ICEBridge is an airborne mission to close the gap between ICESat-1 and ICESat-2. CryoVEX are validation campaigns for CryoSat-2.

ice crystals, which align macroscopically in different patters mostly determined by the corresponding stress–strain regimes within the ice. The anisotropy in crystal orientation fabric (COF) causes the anisotropic rheology of polar ice. Therefore, what at first appears as a hurdle for the determination of bed echo strength is advantageous in terms of determining anisotropic ice properties with polarimetric radar studies. In order to do so, it is important to enhance the understanding of the individual (anisotropic) reflection mechanisms via a successful link to ice-core data. This serves as a precursor for upcoming airborne polarimetric surveys (Dall, 2010).

Although instruments and techniques for polar remote sensing have significantly advanced in the past, the understanding of ice sheets in the climate system still remains incomplete. This became, for example, evident in the unexpected acceleration of some major outlet glaciers (e.g. Helheim Glacier (Nick et al., 2009) and Jakobshavn Isbræ (Motyka et al., 2010) in Greenland, or the Pine Island Glacier in Antarctica (Joughin et al., 2010a)), and the unforeseen disintegration of large ice-shelves (e.g. Larsen B in Antarctica (Rack and Rott, 2004)). These dynamic effects were not included in the latest projections of the IPCC-report and more work needs to be done in order to improve the predictability of ice sheet models in a changing climate. Lessons in that respect can also be learned from history, as ice not only stores valuable information about paleo-climate, but also about paleo ice-sheet dynamics. Ice-sheet elevation can be reconstructed from the isotopic signatures and total air content in ice-core records (Vinther et al., 2009). Specific patterns in internal layering give insight into the (in)stability of ice divides and their interconnected drainage systems. One major milestone for future ice-core research (proposed by the International Partnerships in Ice Core Science-panel) is to establish two dense networks of relatively shallow ice cores, focusing on the last ice age and its transition to the current Holocene (time frame around 40 000 a BP) as well as on the more recent history of anthropogenic impact (time frame around 2000 a BP) (Brook et al., 2006). Some of the envisaged drill sites are located in the previously mentioned areas where the seemingly independent priorities of ice as a paleo-climate archive and ice as an active player in the global climate system merge. Particularly, drill sites beneath pronounced ice divides or ice domes (typically in coastal areas) are subject to complex ice flow, which can only be fully understood when the three dimensional geometry as well as an anisotropic and non-linear rheology is taken into account. The task of remote sensing is to provide boundary conditions about surface and bedrock topography, the internal layering and—if possible—also about internal ice properties like the type of COF and its alignment. This narrows the broader view about the role of remote sensing of ice sheets in global climate research to the more specific points

dealt with in this thesis. The key questions and hypothesis will be presented after a brief introduction into the general methodology.

1.2 Methodology

This section introduces the basic principles of GPR and satellite-based radar interferometry. GPR serves as the main tool within this thesis to illuminate the interior of ice. To a lesser extent radar interferometry is used for the delineation of grounding zones and the derivation of surface velocity and topography. For both methods extensive literature already exists and the backgrounds presented here are by no means exhaustive, but merely aim to close the gap for readers that are not acquainted with GPR, RES or InSAR measurements on ice.

1.2.1 Ground-penetrating radar

Pulsed radar systems emit an electromagnetic pulse and record electromagnetic signals in predefined time intervals before the next pulse is emitted. Depending on the specific antenna arrangement, the receiving antenna either records reflections from the previously emitted pulse or the pulse is directly transmitted through a medium towards the receiving antenna. For standard surveys on ice, both antennas are generally placed on the surface, as other arrangements usually require a borehole (or something similar) which is often not available. In common midpoint mode, the distance of both antennas is varied during the survey, whereas in common offset mode the distance remains the same and the entire setup is moved along the surface. The polarization of emitted and received signals depends on the azimuth orientation of the (dipole) antennas. Two distinguished modes are the co-polarized mode in which both antennas have the same orientation, and the cross-polarized mode in which one antenna is shifted by 90° with respect to the other. A simple sketch for the different arrangements is given in Figure 1.2.

The recorded variables in all modes is the two-way traveltime (TWT) and the amplitude of the reflected (or transmitted) signal. Examples of common-offset (and co-polarized) radar profiles in a nadir-looking geometry[1] are displayed in Figure 1.1(b)-(c).

[1]The nadir-looking, common-offset and co-polarized mode will be considered as the standard mode from now on.

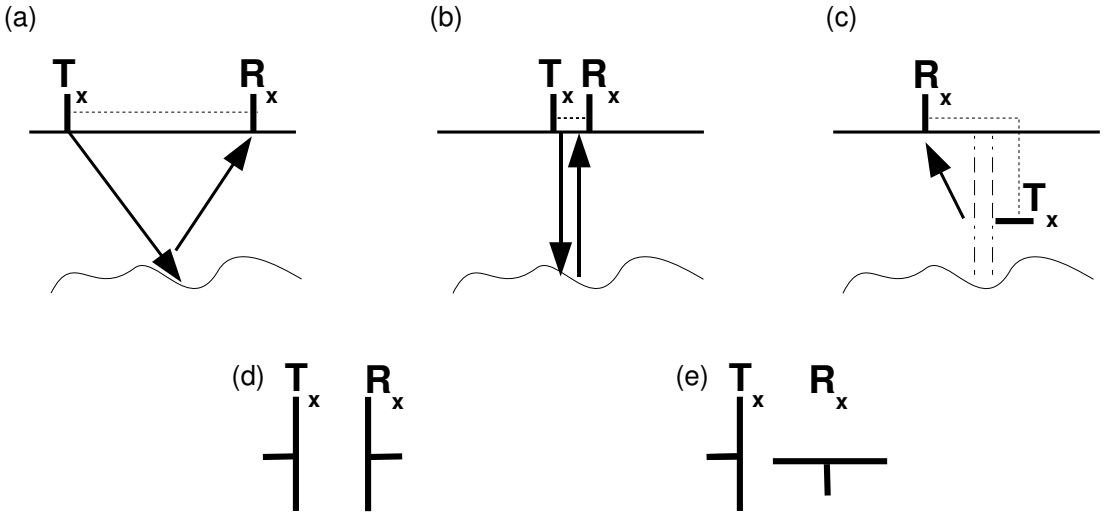

Figure 1.2: Different modes for radar surveys - The arrows indicate the propagation direction for the primary waves of interest; **(a)** Setup for a common midpoint survey; **(b)** Geometry for the common offset mode; **(c)** Simple sketch of a borehole tomography; **(d)-(e)** Plane view of antennas for co- and cross-polarized mode, respectively.

The TWT measurement can be turned into a distance (d) measurement if the propagation velocity (v) in the investigated medium is known ($d = \int_0^{TWT/2} v(t)dt$). In a nadir-looking geometry, the runtime measurement is always ambiguous as all signals originating from a sphere around the transmitter have the same TWT. Therefore, it is important to keep in mind, that the two-dimensional picture illustrated in Figure 1.2 is a strong simplification. The choice for the center frequency of the radar system always compromises penetration depth versus vertical resolution. In a back of the envelope calculation, the vertical resolution is half the spatial *pulse length* h in the medium (neglecting pulse compression techniques). If the *pulse duration* τ is known, h can be calculated as $h = v_m\tau$, with v_m as the propagation velocity in the medium. The system's bandwidth B and τ are inversely proportional ($\tau \sim 1/B$) and for most pulsed GPR systems, the bandwidth is tuned to be in the range of the center frequency. Therefore, the intuitive "the higher the frequency, the higher the (vertical) resolution" approach holds. The horizontal resolution in a common offset survey depends on the beam-opening angle and the distance of individual shots along the survey line. The penetration depth decreases with increasing frequency, and also depends on other antenna characteristics like the transmitted peak power or its directionality.

Whenever the emitted pulse encounters a boundary in dielectric properties, it is partly reflected and partly transmitted. The specific form of transmitted and reflected

fields depends on the shape of the dielectric disturbance. In a two-layer approximation both fields can be characterized with the Fresnel coefficients, which are based on the solutions of the corresponding Maxwell equations with plane waves (e.g. Paren and Robin, 1975, Paren, 1981). It premises that the interface is planar and describes specular reflection processes (incidence angle equals the reflection angle). The treatment of reflections from rough interfaces involves a diffuse component which is also observed at different angles than the incidence angle. The term *reflection* generally refers to the specular component, whereas *scattering* often also includes off-angle components. Whether an interface is planar or rough is a matter of ratio between wavelength and the unevenness of the interface. Analytically, this case is disproportionately more complicated and various approximations have to be used (a textbook introduction is given in Ulaby et al. (1986)). The theory of rough and planar interfaces assumes that the medium of interest is stratified, and links the acquired signals to the individual interfaces between the different layers. Volume scattering models, on the other hand, consider the diffuse response of spatially distributed targets which must not be ordered in strata. A typical example is the backscatter from rain in weather radar applications. Prominent mathematical methods for volume scattering either rely on approximations based on the Maxwell equations or use specific intensities and the radiative transfer theory. The main difference between the two methods is that using the Maxwell equations the full coherent nature of the electromagnetic fields is taken into account, whereas the radiative transfer theory deals with the field intensities. In both cases the inclusion of multiple scattering is the tricky part. Often this is done with self-consistent methods or via expanding the equations in a perturbation series with the different terms describing the different instances of multiple scattering. An introduction for both approaches is given by Tsang et al. (2000, 2001) and Tsang and Kong (2001).

Radar polarimetry exploits any dielectric anisotropy which leads to a polarization dependence of the backscattered (or reflected) signals. In this case, the corresponding vector-wave equations need to be solved, and the tensorial form of the dielectric properties must be taken into account. Planar reflections are sensitive to polarization for oblique incidence, or, for example, if the dielectric transition between the interfaces occurs mainly along one principal axis of the dielectric tensor. In terms of rough interfaces, different undulation types along the two directions perpendicular to the propagation direction introduce a polarization dependence (like a corrugated tin roof). In volume scattering, non-spherical and partly aligned particles in the illuminated volume scatter anisotropically. Although the treatment of the vector-wave equations is somewhat more challenging, it is a worthwhile endeavor since polarimetric measurements serve as

an additional tool to distinguish different reflection and scattering mechanisms. The preferable outcome of a radar survey, after all, is not only to visualize the distance (in time or space) between various layers or point targets, but—if possible—to infer the characteristics of the individual dielectric disturbances.

1.2.2 Internal reflections from within the ice

Airborne and ground-based radar measurements on ice are a routine and operational method by now, and have been used for over 50 years in glaciological research. A review about the initial efforts and advances since then is given by Bingham and Siegert (2007). Initial developments of radar systems aimed primarily at mapping the ice–bedrock interface. However, soon it became evident that the ice sheets appear stratified and that apart from the bedrock echo, internal reflection horizons could be tracked over hundreds of kilometers. Many conclusions about the nature of ice-sheets can be drawn without detailed knowledge of the specific mechanisms causing the dielectric inhomogeneities. Under the assumption that the dielectric properties of the individual layers are originally linked to depositional events on the former surface (e.g. large scale deposition of volcanic fallout), the internal layers can be considered to be isochrones. The shape of internal layers in this picture is determined by two factors, (a) the amount of snowfall that took place between the characteristic events forming the layers , and (b) the deformation of layers due to ice flow and densification. At shallow depths, ice-dynamical effects are mostly negligible and the variation in relative distance can be used to map accumulation rates spatially and also to infer timely changes (Eisen et al., 2008). At intermediate depths and below, the deformation through ice flow enables the deduction of ice-dynamic parameters. To name a few applications: Siegert et al. (2004) relate a fold structure in internal layering seen in RES profiles located in West Antarctica to a changing flow regime over time. They infer, that the ice sheet in that area potentially adapted its dynamics with the activation of different outlet glaciers at the margin. Raymond (1983) hypothesized that due to the nonlinear rheology of ice, layers should bend up characteristically beneath ice divides, below which deviatoric stresses are low causing a higher viscosity and thus a slower downward movement of ice parcels. This has been subsequently confirmed in numerous studies. From this pattern, it is possible, for example, to derive evidence for the (non)stability of the divide location, which in turn can be linked to the (non)stability of the surrounding flow system. This has been studied in great detail for an example at Siple Dome, Antarctica (Nereson and Waddington, 2002, and references therein). This is to say, that a lot of information can be drawn solely from the shape and characteristics of internal reflection horizons.

In order to identify individual reflection mechanisms, a comparison of radar data to snow pit or ice-core data is inevitable. Fujita et al. (2000) summarizes the dielectric properties of ice and discusses the respective link to radar measurements. Certainly not every individual layer in the in-situ measurements can be linked to an internal reflection horizon. The reflections are subject to interferences and several inhomogeneities in the ice (firn) core may contribute to a single reflector in the radar data. Eisen et al. (2006) used a numerical forward model in conjunction with measurement from ice-core dielectric profiling (DEP) to identify prominent reflection horizons caused by changes in conductivity. In a subsequent study (Eisen et al., 2007), a single reflector has been related to a strong change in COF as determined from fabric measurements on ice-core thin sections. At shallower depths, density variations are believed to be the primary mechanism. However, apart from prominent dust or ice-layers, the link of small-scale density variations from shallow firn cores to the radar data is difficult. Still, variations in density, electrical conductivity and COF are considered to be the most important mechanisms which determine the internal layering. Changes in COF are interrelated with both, the initial impurity loading when the layer was first deposited, and the stress-strain regime under which the layer migrated to larger depths. It is therefore not clear that COF-type layers also have isochronous character. Due to the single ice-crystal anisotropy, changes in macroscopically aligned COF are generally polarization dependent. The different reflection mechanisms can in theory be distinguished by using multiple polarizations, frequencies and pulse lengths (Fujita et al., 2003, 2006). More information about the ice fabric and its birefringent properties may also be obtained by using varying incidence angles (Matsuoka et al., 2009).

The large amount of information that is hidden in internal ice properties—and the burden that comes with it in determining the bedrock reflection amplitude—requires a good understanding of reflection mechanisms, signal attenuation and signal propagation in ice. Where possible, the picture must be complemented with other methods to overcome the limitations of RES and GPR surveys. One of them being (labor intensive) seismic surveys. Unlike electromagnetic waves, acoustic waves are able to penetrate water and the bedrock below the ice (Eisen et al., 2010). Within the ice, seismic reflectors are most likely due to a changing COF and thus not masked by other reflection mechanisms. At the surface, satellite remote sensing can provide elevation models and constrain the flow regime in the area. The basics of this methodology will be described in the next section.

1.2.3 Interferometric Synthetic Aperture Radar (InSAR)

The primary aim of InSAR analysis in glaciology is the large-scale derivation of ice flow and surface elevation from space. A secondary outcome is the delineation of the grounding zone, which marks the boundary of the grounded inland ice and the floating ice shelves at the margins of the large ice sheets. The technique is of importance, as especially in-situ flow measurements are mostly sporadic and require a high logistic effort for monitoring timely changes. The critical point in InSAR is the coherent treatment of the backscattered signal. This increases the spatial resolution of the satellite scenes, and enables the detection of surface displacement within fractions of the emitted signal frequency.

Without any post-processing, conventionally side-looking pulsed radar systems from space have a very limited resolution. In across-track (also referred to as *range*) direction, the backscattered signal can be range-gated and similar to GPR and RES systems the pulse duration defines the resolution in range. However, too short pulses result in a too low signal-to-noise ratio. Using pulse compression techniques it is possible to increase the resolution in range. If frequency content and shape of the emitted pulses are well known, the incoming signal is sharpened via a cross-correlation of emitted and received signal. Depending on the original frequency content, the intercorrelated signal shows compressed spikes in the time domain which can be linked to the individual targets. The signal compression improves with increasing bandwidth of the radar. In along-track (also referred to as *azimuth*) direction this is not possible off hand, as the pulse is only emitted along the range direction. The resolution in azimuth is thus traditionally determined by the width of the footprint in azimuth, which is quite large as the beam-widening from space is enormous. The major advantage of using a SAR is that the collected raw-data allows to increase the resolution in azimuth significantly, via a coherent post-processing which resembles the pulse compression in range. For that, a synthetic pulse along azimuth is generated by taking the multiple coverage of targets and their corresponding Doppler history into account. Counter-intuitively a larger footprint (i.e. more multiple coverage and a synthetically increased bandwidth due to larger Doppler shifts) now leads to a better azimuth resolution. The procedure is computationally intensive and requires a precise knowledge of the geometry (e.g. orbital parameters and the squint angle of the antenna). Details and pitfalls of this techniques are described by Cumming and Wong (2005).

The interferometric analysis of SAR data enables the deduction of surface topography and velocity. It exploits the phase information of two SAR scenes which illuminate a similar area from a slightly different imaging geometry at different times. Surface

slope and displacement induce a relative phase difference when the two scenes are subtracted. A precondition for this methodology is that the snow morphology between the acquisitions at two different points in time remains stable, so that the random scattering part cancels in the subtraction. Snow fall or melting limits the availability of adequate pairs of SAR scenes. The color-coded representation of the phase difference in an interferogramm already allows a rough characterization of the survey area: Smooth, contour-like lines of equal phase difference (i.e. *fringes*) represent the topography; distorted and elongated fringes mark areas of enhanced ice flow; densely spaced and confined fringes indicate the zone between grounded and floating ice through the vertical displacement of the floating ice by tides. In a differential approach (Drews et al., 2009) motion and topography can be separated by differencing two interferograms under the assumption of constant ice flow. Likewise the topographical part can be canceled by using an elevation model. The resulting displacement map is one-dimensional and marks the displacement along the satellite's look vector. In order to get a two-dimensional picture, different displacement maps need to be combined. Therefore at least four SAR scenes must be available. If this is not the case, other methods like speckle or feature tracking can be used to complement the flow fields (Joughin, 2002). The more detailed theory of the different InSAR processing steps is described in Rosen et al. (2000) or Hanssen (2001) and will not be repeated here.

Within the last two decades, InSAR analysis became a standard tool in glaciology. Flow velocities (and timely changes thereof) are by now available over large parts of the Antarctic and Greenlandic ice sheets (Rignot et al., 2008, Joughin et al., 2010b). However, the floating ice shelves require a separate treatment due to their tidal displacement (Rack and Rott, 2004), and also flow velocities on the grounded parts may be flawed through the inadequacy of large-scale elevation models in coastal areas[1] (Bäßler, 2011). A (re-)evaluation of SAR data is therefore useful in regions where good local elevation models exist and where ground control points are available, which can be used to refine individual steps in the InSAR processing chain.

[1] A pitfall that will be most likely be overcome once the TanDEM-X satellites finished their currently ongoing interferometric elevation mapping

2. Key questions, conclusions and implications of this thesis

The thesis is subdivided into five sections which will (and partly have been) published separately. The red thread that connects the individual sections is the application of electromagnetic methods (RES, GPR or InSAR) for the derivation of glaciological parameters across different spatial scales. Parameters of interest are stratigraphic integrity, alignment of COF, internal geometry in layering, delineation of the grounding zone, and spatial variation in surface accumulation and sub-ice shelf melt rates. The studies described in 2.1–2.3 focus more on the internal structure of ice, whereas the last two (2.4–2.5) work primarily with satellite data imaging the ice-sheet surface. The full reference and the current status of the individual publications, which are listed in the Appendix A–E, is as follows:

Drews R., Eisen O., Weikusat I., Kipfstuhl S., Lambrecht A., Steinhage D., Wilhelms F., Miller H., *Layer disturbances and the radio-echo free zone in ice sheets*, The Cryosphere **3**(2),195–203,2009

Drews R., Eisen O., Steinhage D., Weikusat I., Kipfstuhl S., *Anisotropy in radar data: Potential mechanisms and implications*, Journal of Glaciology, in revision.

Drews R., Steinhage D., Martín C., Eisen O., *Characterization of glaciological conditions at the Halvfarryggen ice dome, Dronning Maud Land, Antarctica*, Journal of Geophysical Research, submitted.

Bindschadler, R., Choi H., Wichlacz A, Bingham R., Bohlander J., Brunt K., Corr H., Drews R, Fricker H., Hall M., Hindmarsh R., Kohler J., Padman L., Rack W., Rotschky G., Urbini S., Vornberger P., Young N., *Getting around Antarctica: new high-resolution mappings of the grounded and freely-floating boundaries of the Antarctic ice sheet created for the International Polar Year*, The Cryosphere, 5, 569–588, 2011.

Neckel N., Drews R., Rack W., Steinhage D., *Basal melting ath the Ekström Ice Shelf mapped by SAR interferometry using the mass continuity assumption*, submitted to Annals of Glaciology.

For the quick reader, the major motivations, conclusions and implications of each study will be briefly described in the following sections. My own contribution (as opposed to the contributions of the various other authors) is highlighted at the beginning of each manuscript in the Appendix.

2.1 Origin of the radio-echo free zone in ice sheets

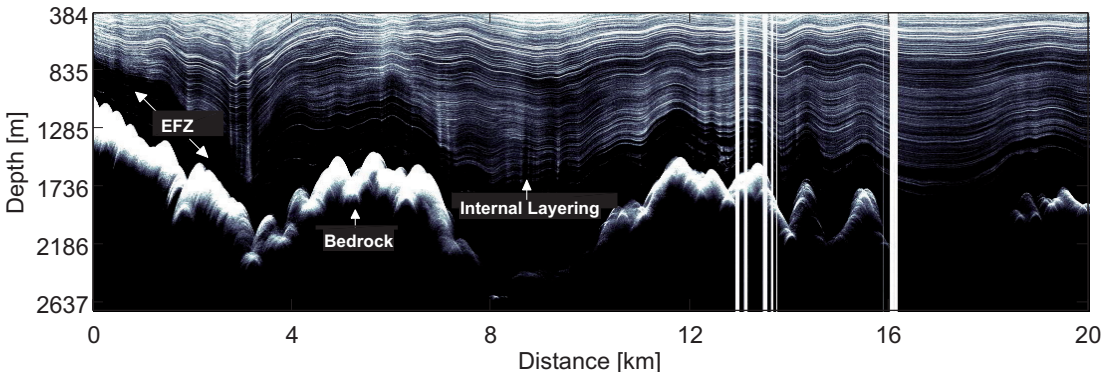

Figure 2.1: Image of the echo-free zone (EFZ) - along a transect in Dronning Maud Land, Antarctica. The EFZ stands out as a band above the bedrock with no continuous internal layering. The onset is variable in depth and follows the bedrock topography.

Motivation: Radar data collected over ice sheets sometimes shows lateral coherent internal layering which suddenly vanishes in the lower parts of the ice column (Figure 2.1). Apart from the bedrock return, the "echo-free" zone (EFZ) is characterized by very low, or not backscatter at all. Often the system sensitivity (or signal attenuation) can be excluded, but physical evidence as to what triggers the absence of reflections is rare. In a case study around the EDML deep drill site in Antarctica, it is investigated

whether or not ice-core data (line-scan images in particular) can provide the hitherto missing mechanism for the appearance of the EFZ. Line-scan images visualize optical high-scattering zones, also referred to as cloudy bands, in ice cores. They are linked to layers with high impurity content and serve as a proxy for the stratigraphic integrity of the ice core.

Conclusion: Rough and inclined cloudy bands (measured in the ice-core with a diameter of 12 cm) are an excerpt of larger scale (10–100 m) disturbances in the stratigraphy caused by ice flow which, at larger depths, is increasingly influenced by bed-parallel shear. The rough reflection surfaces of layers weaken the dielectric contrast and reduce the specular component in the radar data, which leads to the observed absence of internal reflection horizons in the radar data.

Implication: Since absolute dating of ice is currently not feasible, the derivation of an age–depth relationship for ice cores heavily relies on an undisturbed stratigraphy. Inclined (and potentially overturned) layers severely deteriorate the climate record. Pre-site surveys for future ice cores which show a pronounced EFZ should be considered as warning sign. Ice-sheet models currently assume that layers do not deform individually. If the EFZ onset indicates a changing rheology with depth, this needs to be accounted for.

2.2 Effect of anisotropic backscatter

Motivation: At the EDML drill site, the EFZ onset (at around 2100 m depth) is precluded by a strong change in COF which has been observed in the ice-core thin sections. The fabric changes from a girdle-type pattern to a single maximum distribution which remains (more or less) stable within the EFZ. This transition provided first direct evidence that a varying COF indeed causes reflection horizons in radar data (Eisen et al., 2007). However, it remains unclear on which scales the COF changes vertically in other depth ranges and whether or not it is the only mechanism which exhibits a polarization dependence. A polarimetric dataset at the same site (Figure 2.2) shows two anisotropic reflection zones at subsequent depths above the EFZ onset. These differ in their direction of maximum (and minimum) backscatter. The boundary of the two zones coincides with the transition from Holocene to glacial ice as well as with the bubble-clathrate transformation zone (air bubbles under increasing pressure are transformed to crystalline inclusions called clathrates). The primary mechanisms of anisotropic backscatter need to be determined so that the change in direction of backscatter extrema can be linked to physical properties within the ice.

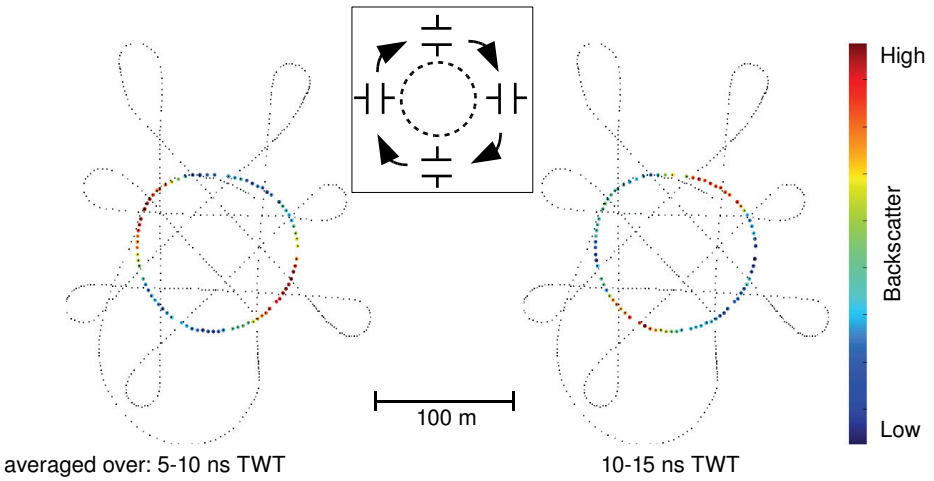

Figure 2.2: Plane view of shotpoint coordinates in circular profile for polarimetric measurements - with the color codes representing the depth-averaged backscattered power of the corresponding time windows (5–10 ns left, 10–15 right). The direction of extrema within those time intervals shift by 90°. The diameter of the circle is less than 100 m. The inset in the black box sketches the rotating (tangential) orientation of the co-polarized antennas.

Conclusion: Variations in COF are—also at intermediate depth—the primary mechanism for polarization dependent backscatter. Other effects like a directional layer roughness or ellipsoidal air bubbles are inferior. The two anisotropic reflection zones mark the transition into the last glacial, whereas a rotation of principal axes in COF can be neglected (for the characteristic setting at EDML). The direction of extrema in backscatter coincide with the principal axes of the stress–strain regime at the surface.

Implication: Polarimetric measurements are capable to determine the fabric alignment and variations thereof. An established link to ice-core data enables the mapping of COF away from ice cores and thus offers the capability to profile the stress–strain regime vertically. This is a crucial step towards the further development of an anisotropic flaw law, which is important to improve the understanding of near divide flow.

2.3 Glaciological conditions in the vicinity of triple junctions

Motivation: Ice flow beneath divides has a challenging theory, as higher-order models are required to include all components of the stress tensor. At triple junctions, where

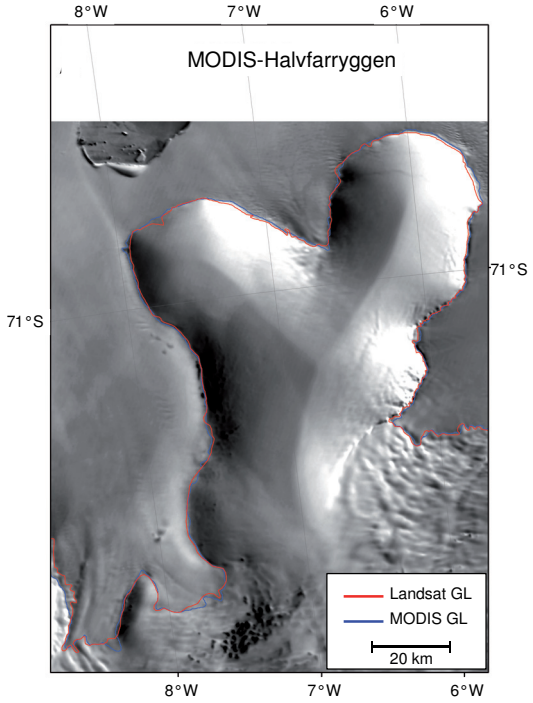

Figure 2.3: Modis backscatter image of Halvfarryggen - the ice divides are visible as three lines which merge at the triple junction near the dome of the ice ridge. The grounding line based on MODIS data is marked in blue and the grounding line from Landsat data is marked in red.

three divides merge, also the full three-dimensional structure needs to be considered (Figure 2.3). It has been known for a while that the nonlinearity of the flow law causes an upwarping of layers beneath the divides (a.k.a. isochrone arches or Raymond bumps). However, the role of along-ridge flow, tilted bedrock or anisotropic COF has not yet been fully understood. Therefore, it is difficult (to say the least) to replicate the bump-amplitude vs. depth distribution correctly. Only very recent studies are capable to explain the downward warping of the isochrone arches at larger depths (Martín et al., 2009a). As complicated as the internal structure may appear, it offers at the same time the possibility to draw conclusions about the surrounding flow regime and the temporal stability of the divide which is important information for pre-site surveys as well as for paleo-ice sheet dynamics. Needed parameters are the surface and bedrock topography, the spatial variation in accumulation and the three-dimensional upwards bending in internal layering. These datasets are used as input for an ice-flow model [1], in order to draw conclusions about the age–depth scale and the stability of the triple junction regime.

[1]The development of the ice-flow model was not part of this thesis, but resulted from a collaboration with C. Martín, British Antarctic Survey. For more details refer to C.

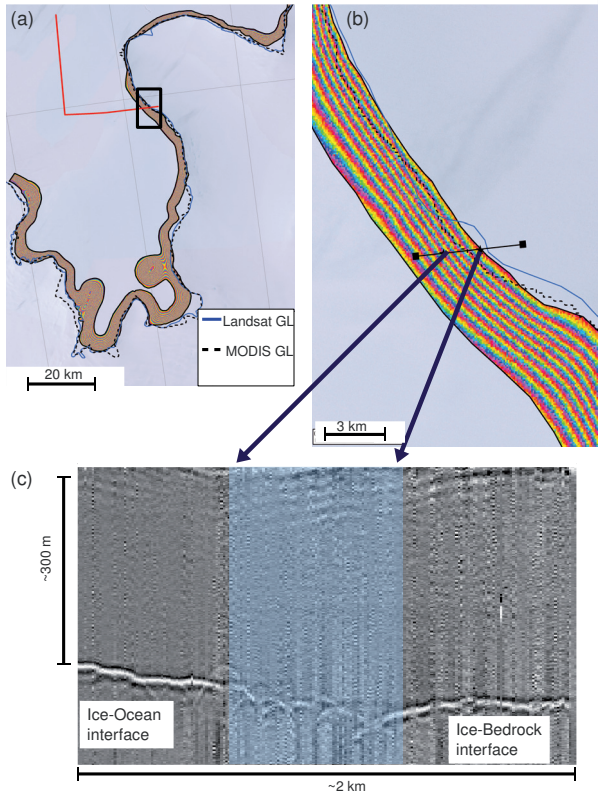

Figure 2.4: The InSAR derived grounding zone in the vicinity of the Neumayer III station, Antarctica. (a) displays cropped tidal fringes from an interferogramm (Neckel, 2011), with a Landsat image in the background (Bindschadler et al., 2008). The red line depicts a profile acquired with a low-frequency radar in the Antarctic field seasons 2009/2010; **(b)** is a close-up of the black box in (a) with an excerpt of the low-frequency radar profile shown in **(c)**; The ice–bedrock interface on the left and the ice–ocean interface on the right are separated by a crevassed area at the bottom of the ice shelf.

Conclusion: The triple junction near Halvfarryggen ice dome has been stable (at least) over the last 10 ka and is influenced by high and asymmetric accumulation rates. The large magnitude in accumulation results in an increased vertical resolution, especially in the time frame within the last 2 ka. The age–depth relationship beneath the divides differs significantly when compared to the flank-flow regime. The ice is frozen to the bed, and COF is most likely aligned and anisotropic.

Implication: A potential drill site at Halvfarryggen must be chosen carefully, as two deciding factors, namely the age of the ice (how far does it reach back in time) and the layer thickness (which resolution is to be expected) vary on relatively short spatial scales. Commonly used models to predict the age–depth relationship are inadequate and specifically tailored (preferably three dimensional) models are needed.

2.4 Coastal elevations and mapping of the grounding zone

Motivation: Two characteristic points mark the spatial extend of the grounding zone, the most seaward point of the grounded ice which is not influenced by tidal flexure, and the most landward point of the floating shelf ice which floats freely with the tides and is entirely disconnected from the tidal deformation regime in the transition zone to the grounded ice. Both points are important markers with respect to ice-sheet dynamics. An example of the grounding zone in the Ekströmisen area is shown in Figure 2.4. Mapping the most seaward grounded part of the ice sheet delineates the area in which ice flow is still influenced by the ice–bedrock interaction. The most landward freely floating point, enables the application of the flotation criterion to estimate the ice thickness (and thus to circumnavigate the lack of insufficient RES coverage). A migration of the grounding zone is a critical indicator for a changing mass flux and a thickening or thinning in the respective catchment area of the inland ice sheet. Coastal elevations are needed for mass flux calculations, and to determine points within the grounding zone via a prominent break in surface slope.

Conclusion: Landsat-7 (optical) imagery is suited for a high-resolution mapping of characteristic points in the grounding zone. A coastal elevation map can be generated from the optical data in combination with existing Antarctic-wide DEMs and the usage of ICESat Laser altimetry as ground control. The flotation criterion can be applied to estimate the ice thickness from the freely floating parts of the ice shelves.

Implication: The study provides a consistent dataset, derived with the same methodology and covering the entire Antarctic perimeter. It can be used for mass-flux estimates and as a benchmark dataset for monitoring changes in the grounding zone around Antarctica.

2.5 Quantifying sub-ice shelf melt rates at the Ekströmisen Ice Shelf

Motivation: Ice shelves are the main contact area for direct ice–ocean interaction in Antarctica. Melting and refreezing beneath the ice shelves redistributes mass and thus alters the overall mass balance. In order to map timely changes triggered by changing ocean temperatures, baseline datasets and techniques which allow continuous monitoring are needed. A feasible approach is the application of the continuity equation in steady state. This enables the mapping of melt-rates at the ice-shelf bottom by using datasets which can be measured from the surface. The Ekströmisen Ice shelf is a

well surveyed area where high-quality input data (accumulation, ice thickness, and ice velocity) can be derived. The study thus contributes to show limits and possibilities for the mapping of sub-ice shelf melt rates via the continuity equation.

Conclusion: The local imbalance in mass flux between different flux gates can be related to sub-ice shelf melting. Pitfalls are unknown atmospheric contributions in the InSAR velocities and a flawed RES ice thickness in profiles crossing crevasses. A spatially interpolated ice-thickness map deteriorates the results if the horizontal grid-spacing is smaller than the mean distance of RES lines. Preferably, the flux divergence should only be calculated in polygons given by the flight tracks of RES measurements.

Implication: The study delivers a map of sub-ice shelf melt rates of the Ekströmisen Ice Shelf which can be used as a baseline for the monitoring of changes over time. The requirements on the input data are highlighted and the new implementation of the continuity equation may also be of interest for other studies on the larger Antarctic ice shelves.

3. Synthesis and Perspectives

Application of GPR, RES and InSAR on the large ice sheets are relatively old techniques from a science perspective, but still yield a large amount of topics which require more work. Among those are:

(a) the incomplete RES and GPR coverage of the large ice sheets,

(b) the lack of understanding for the specific reflection mechanisms,

(c) the difficulties in interpreting the shape of internal layering with respect to a mixed effect of accumulation and different deformation regimes, and

(d) the ambiguities in determining the bedrock reflection power and the corresponding characterization of the ice–bed interface.

This thesis contributes, with varying amount, to all points mentioned above. The EFZ-manuscript presented in Appendix A offers the first direct comparison between the EFZ onset and ice-core data. The link of mm–cm scale disturbances seen in the linescan images to a (hypothesized) larger scale layer roughness indicates, that the deformational behavior of internal layers is likely more complicated than previously assumed. The layers may respond individually to the general stress–strain regime, depending for example on the varying impurity loading and the specific alignment in COF. Similarly, ice flow across an undulated bedrock may potentially result in left-over disturbances further downstream. After the publication of the paper referring to the EFZ in 2009, several profiles from more sophisticated radar systems in other areas became available. The newer systems enable a coherent post-processing, similar to the satellite-based SAR approach (see section 1.2.3). This results in increased horizontal resolution and penetration depth. A prominent example are the RES surveys over the Gamburtsev subglacial mountain ridges in Antarctica. In the latter, Bell et al. (2011) resolve clear features in what would earlier be called the EFZ. However, backscattered power is significantly reduced and large-scale disturbances with disrupted and disconnected internal layering

are clearly visible (Figure 4b in Bell et al., 2011). The specific mechanisms for the disturbances may differ from site to site (in case of the Gamburtsev mountains, subglacial melt rates and the extremely undulated topography are not comparable to the EDML drill site). However, the newer studies still show, that large-scale disturbances are indeed possible from a pure ice-dynamical point of view. Therefore, the term echo-free zone may be misleading and should rather be replaced by *low-backscatter zone*, but the conclusion with respect to pre-site surveys and ice-sheet modeling remain up to date and valid. For an improved understanding of these low-backscatter zones, it appears essential to map the zone's distribution spatially and relate it in more detail to the topographical setting, ice properties (crystal fabric and impurities) and ice age. Numerical flow modells are so far not designed to replicate this kind of 'turbulent' ice flow, and further constraints on the flow law from polarimetric radar surveys, but also from physical measurements on the grain-size scale are needed.

The case study near the EDML drill site presented in Appendix B improves the understanding for backscattering mechanisms in polarimetric surveys. The link to ice-core data solidifies varying COF as a dominant factor for radar backscatter, and illustrates the capability from radar polarimetry to infer principal components of the stress–strain regime. However, ambiguities remain and it is not understood whether or not COF appears stratified, and if so, which factors trigger the stratification. Once again, studies on a grain-size scale indicate that COF is imprinted by the impurity loading (which is stratified), but the exact mechanisms which cause a variation of the individual COF-Eigenvalues (or a rotation of the principal coordinate system) remain hidden. If the use of volume-scattering models is a promising path needs yet to be proven. So far, they are almost exclusively applied for the satellite-based case. With upcoming side-looking GPR systems, there is probably a need to model the full angular dependency of a biaxial media with random fluctuations induced by a varying COF. The volume-backscatter model for the randomly distributed, ellipsoidal air bubbles hereby helps to differentiate between different mechanisms, but can also be seen as a starting point for a type of modelling which has so far mostly been neglected in the community around GPR. The importance of a full understanding of COF induced amplitude variations is highlighted by Matsuoka (2011) in constructed examples in which variations in backscattered power caused by internal ice properties are wrongly attributed to changing conditions at the ice–bed interface. Dominating factors are a spatially varying attenuation, but also COF-induced birefringence. Polarimetric surveys combined with appropriate scattering models can identify the crystal texture and thus help to better visualize wet- or dry-based flow regimes. At the same time, a reliable detection of COF

patterns improves the understanding of anisotropic deformation of ice. Unfortunately, polarimetric measurements are somewhat labor-intensive and not all GPR-systems are sensitive enough to record the expected amplitude variations. Polarimetric airborne measurements (Dall, 2010) often only acquire two polarization modes (hh and vv) and since the same survey area is usually not crossed several times with varying headings, the measurements are heavily undersampled. Therefore, a combination with ice-flow modelling, which considers the principal directions of the ice-dynamical induced COF, seems essential. This closes the circle of unknowns, as it is unclear if the COF and especially changes thereof are purely related to ice-dynamics, or if they are also linked to a climate signal. In any case, more polarimetric measurements in different flow regimes are needed to get a more complete picture of polarization dependent backscatter. In terms of ice-core data, COF measurements should be available in a vertical spacing which is smaller than the applied radar wavelength.

The Halvfarryggen dome area is, for Antarctic conditions, covered with a dense net of GPR, RES, GPS and even seismic profiles. Unfortunately, polarimetric radar measurements are not available yet. Internal reflection horizons observed in the seismic data at intermediate depths can be linked to a changing COF. First analyses display multiple reflection horizons, and therefore it seems that the COF beneath Halvfarryggen's dome is aligned and changes with increasing depths. This justifies and necessitates the use of an ice-flow model with an anisotropic rheology for the prediction of the age–depth scale and corresponding layer thickness. The triple-junction geometry complicates the flow setting further, as virtually all radar intersections are imprinted by ice flow which crosses the intersection plane. This is the main reason for the observed mismatch between the two-dimensionally modelled isochrones and RES layering in the Halvfarryggen study. Although it is easy to call for a full three-dimensional model from an observer's point of view, one should keep in mind, that the three-dimensional visualization of internal layering is not an easy task. For the topographical correction, a good elevation model is required (the simultaneously acquired GPS profile with a two-dimensional GPR line is not enough). Although multiple elevation models are usually available, this is still a major pitfall, for example in terms of locating the ice divides. Different RES profiles can also easily be linked in theory via the connection of prominent reflection horizons. However, especially if isochrone arches are between the different RES lines, a small error in picking across the bump-onset can translate into a large misplacement of the internal reflection horizon on the other side of the isochrone arch. In spite of these difficulties, the Halvfarryggen pre-site surveys managed to illuminate the interior of the ice sufficiently so that conclusions about the asymmetry

in accumulation, the age–depth scale and the stability of the triple junction regime could be drawn. No final verdict about the suitability of Halvfarryggen as a potential drill site for the IPICS 2k and 40k networks has been spoken yet. In any case, the derived datasets are certainly capable to constrain the relatively fundamental problem of near-divide flow. This also includes the downward-warping of the isochrone arch at larger depths. Although the two-dimensional model from Martín et al. (2009b) predicts this as a direct consequence of anisotropic ice flow, it is still unclear how the three-dimensional structure looks like, especially in the vicinity of triple junctions. The recent studies from Hindmarsh et al. (2011) and Gillet-Chaulet and Hindmarsh (2011) emphasize that this topic is up-to-date and of current interest. The interplay of RES and GPR measurements with ice-flow modelling in the Halvfarryggen study is therefore part of the currently commencing pioneering work of the glaciological community, paving the way for operational applications in the future.

Nereson and Waddington (2002, and references therein) demonstrated the derivation of large-scale changes in the past flow behavior of ice streams which surround the inspected ice ridge (in this example Siple Dome). In coastal ice ridges surrounded by ice shelves, this leads inevitably to a closer examination of the transition zone between grounded and floating ice. The IPY Project "Antarctic Surface Accumulation and Ice Discharge (ASAID)" supplies the community with an Antarctic-wide, satellite-based dataset of coastal elevations in combination with two boundaries of freely floating and grounded ice. The datasets are mainly derived from Landsat-7 imagery. Rignot et al. (2011a) published the delineation of the Antarctic grounding zone based on differential SAR interferometry. The methods differ as they map different points in the transition zone, but to a certain extent also complement each other. The *ASAID grounding line* primarily maps the break in slope from the relatively steep inland ice to the smooth and plane ice shelves. The *interferometric grounding line* maps the landward side of the vertical displacement by tides. Particularly across ice streams (which may not exhibit a break in surface slope), this methodology is very powerful in characterizing the grounding zone. At the slower moving margins, the *ASAID grounding line* is spatially more highly resolved, less smoothed, and potentially closer to the *real grounding line* where the ice first meets the ocean. Both datasets are benchmarks for future studies focusing on grounding line migration. The freely floating boundary provides the ice thickness around the Antarctic perimeter, if the flotation criterion can be applied correctly. This requires the precise knowledge of the vertical density profile and the freeboard height (i.e. the height above sea level). For ice flux estimates, the ice thickness must be combined with InSAR flow velocities, which also require precise elevation

models. For both reasons, ASAID provides a new dataset for coastal elevation. The vertical density profile is mostly given by a model output. In that sense the table is set for an Antarctic-wide flux estimate. Caution is required when using the flotation-based ice thicknesses as a misplacement of the freely floating line towards the tidal-induced deformation zone can cause large errors. Griggs and Bamber (2011) published the ice thickness from Antarctic ice shelves based on the freeboard height from satellite radar and laser-altimetry. A comparison to the ASAID results has yet to be done, but it seems evident that all these datasets should be united in a way that combines the strengths and excludes the weaknesses of the individual approaches.

Accelerated or reduced ice flow are obvious indicators for a changing mass transport from the inland to the margins. Changing sub-ice shelf melt and refreezing rates are less obvious and harder to detect, but at the same time, changing ocean temperatures presumably directly affect this system. The case study for the Ekströmisen area addresses the quantification of melt rates in a budgeting approach. The use of mass conservation in combination with InSAR and RES measurements illustrates the requirements on the individual datasets for a successful evaluation. Since the availability of RES lines will always be restricted (especially in terms of determining timely changes), this study is of importance for the validation of other approaches which primarily rely on the adequate determination of elevation changes.

References

R. B. Alley, M. K. Spencer, and S. Anandakrishnan. **Ice-sheet mass balance: assessment, attribution and prognosis**. *Annals of Glaciology*, 46(1):1–7(7), October 2007. http://dx.doi.org/doi:10.3189/172756407782871738. 4

J. L. Bamber, J. L. Gomez-Dans, and J. A. Griggs. **A new 1 km digital elevation model of the Antarctic derived from combined satellite radar and laser data Part 1: Data and methods**. *The Cryosphere*, 3(1):101–111, 2009. http://dx.doi.org/10.5194/tc-3-101-2009. 3

M. Bäßler. **Untersuchungen zu Topographie und Bewegungsverhalten fr das Kstengebiet des Riiser-Larsen- und Brunt-Schelfeises mittels Radarfernerkundung**. *Dissertation, Fakultät Forst-, Geo- und Hydrowissenschaften,Technische Universitt Dresden*, 2011. 3, 14

R. E. Bell, F. Ferraccioli, T. T. Creyts, D. Braaten, H. Corr, I. Das, D. Damaske, N. Fr earson, T. Jordan, K. Rose, M. Studinger, and M. Wolovick. **Widespread Persistent Thickening of the East Antarctic Ice Sheet by Freezing from the Base**. *Science*, 331(6024):1592–1595, 2011. http://dx.doi.org/10.1126/science.1200109. 3, 23, 24

R. Bindschadler, P. Vornberger, A. Fleming, A. Fox, J. Mullins, D. Binnie, S. J. P. sen, B. Granneman, and D. Gorodetzky. **The Landsat Image Mosaic of Antarctica**. *Remote Sensing of Environment*, 112(12):4214 – 4226, 2008. ISSN 0034-4257. http://dx.doi.org/10.1016/j.rse.2008.07.006. 20

R. G. Bingham and M. J. Siegert. **Radio-Echo Sounding Over Polar Ice Masses**. *Journal of Environmental and Engineering Geophysics*, 12(1):47–62, 2007. http://dx.doi.org/10.2113/JEEG12.1.47. 11

R. Bintanja and R. S. W. van de Wal. **North American ice-sheet dynamics and the onset of 100,000-year glacial cycles**. *Nature*, 454:869–872, 2008. http://dx.doi.org/10.1038/nature07158. 2

M. Bock, J. Schmitt, L. Möller, R. Spahni, T. Blunier, and H. Fischer. **Hydrogen Isotopes Preclude Marine Hydrate CH4 Emissions at the Onset of Dansgaard-Oeschger Events**. *Science*, 328(5986):1686–1689, 2010. http://dx.doi.org/10.1126/science.1187651. 2

E. Brook, E. W. Wolff, D. Dahl-Jensen, H. Fischer, and E. Steig. **The future of ice coring: International Partnerships in Ice Core Sciences (IPICS)**. *PAGES News*, 14(1):6–10, 2006. 7

I. Cumming and F. Wong. *Digital processing of Synthetic Aperture Radar data*. Artech House, 2005. 13

J. Dall. **Ice sheet anisotropy measured with polarimetric ice sounding radar**. *Geoscience and Remote Sensing Symposium (IGARSS), 2010 IEEE International*, pages 2507–2510, 2010. http://dx.doi.org/10.1109/IGARSS.2010.5653528. 7, 25

W. Dansgaard. **Stable isotopes in precipitation**. *Tellus*, 16(4):436–468, 1964. 2

R. Drews, W. Rack, C. Wesche, and V. Helm. **A Spatially Adjusted Elevation Model in Dronning Maud Land, Antarctica, Based on Differential SAR Interferometry**. *IEEE Transactions on Geoscience and Remote Sensing*, 47(8):2501–2509, 2009. http://dx.doi.org/10.1109/TGRS.2009.2016081. 3, 14

O. Eisen, U. Nixdorf, F. Wilhelms, and H. Miller. **Electromagnetic wave speed in polar ice: validation of the common-midpoint technique with high-resolution dielectric-profiling and -density measurements**. *Annals of Glaciology*, 34:150–156(7), 2002. http://dx.doi.org/10.3189/172756402781817509. 4

O. Eisen, U. Nixdorf, F. Wilhelms, and H. Miller. **Age estimates of isochronous reflection horizons by combining ice core, survey, and synthetic radar data**. *Journal of Geophysical Research - Solid Earth*, 109(B04 106), 2004. http://dx.doi.org/10.1029/2003JB002858. 4

O. Eisen, W. Rack, U. Nixdorf, and F. Wilhelms. **Characteristics of accumulation rate in the vicinity of the EPICA deep-drilling site in Dronning Maud Land, Antarctica**. *Annals of Glaciology*, 41:41–46(6), 2005. http://dx.doi.org/10.3189/172756405781813276. 4

O. Eisen, F. Wilhelms, D. Steinhage, and J. Schwander. **Improved method to determine radio-echo sounding reflector depths from ice-core profiles of permittivity and conductivity**. *Journal of Glaciology*, 52(177):299–310(12), 2006. http://dx.doi.org/10.3189/172756506781828674. 12

O. Eisen, I. Hamann, S. Kipfstuhl, D. Steinhage, and F. Wilhelms. **Direct evidence for continuous radar reflector originating from changes in crystal-orientation fabric**. *The Cryosphere*, 1(1):1–10, 2007. 12, 17

O. Eisen, M. Frezzotti, C. Genthon, E. Isaksson, O. Magand, M. R. van den Broeke, D. A. Dixon, A. Ekaykin, P. Holmlund, T. Kameda, L. Karlöf, S. Kaspari, V. Y. Lipenkov, H. Oerter, S. Takahashi, and D. G. Vaughan. **Ground-based measurements of spatial and temporal variability of snow accumulation in East Antarctica**. *Reviews of Geophysics*, 46:2001-+, Apr. 2008. http://dx.doi.org/10.1029/2006RG000218. 11

O. Eisen, C. Hofstede, H. Miller, Y. Kristoffersen, R. Blenkner, A. Lambrecht, and C. Mayer. **A New Approach for Exploring Ice Sheets and Sub-Ice Geology**. *EOS Transactions*, 91(46):429–430, Nov. 2010. http://dx.doi.org/10.1029/2010EO460001. 12

EPICA community members. **One-to-one coupling of glacial climate variability in Greenland and Antarctica.** *Nature*, 444:195–198, 2006. http://dx.doi.org/10.1038/nature05301. contrib. authors: C. Barbante, J.-M.

Barnola, S. Becagli, J. Beer, M. Bigler, C. Boutron, T. Blunier, E.Castellano, O. Cattani, J. Chappellaz, D. Dahl-Jensen, M. Debret, B. Delmonte, D. Dick, S. Falourd, S. Faria, U. Federer, H. Fischer, J. Freitag, A. Frenzel, D. Fritzsche, F. Fundel, P. Gabrielli, V. Gaspari, R. Gersonde, W. Graf, D. Grigoriev, I. Hamann, M. Hansson, J. Jouzel, M. Kaczmarska, T. Karlin, P. Kaufmann, S. Kipfstuhl, M. Kohno, F. Lambert, Anja Lambrecht, Astrid Lambrecht, A. Landais, G. Lawer, M. Leuenberger, G. Littot, L. Loulergue, D. Luthi, V. Maggi, F. Marino, V. Masson-Delmotte, H. Meyer, H. Miller, R. Mulvaney, B. Narcisi, J. Oerlemans, H. Oerter, F. Parrenin, J.-R. Petit, G. Raisbeck, D. Raynaud, R. Röthlisberger, U. Ruth, O. Rybak, M. Severi, J. Schmitt, J. Schwander, U. Siegenthaler, M.-L. Siggaardandersen, R. Spahni, J. P. Steffensen, B. Stenni, T. F. Stocker, J.-L. Tison, R. Traversi, R. Udisti, F. Valero-Delgado, M. R. van den Broeke, R. S. W. van de Wal, D. Wagenbach, A. Wegner, K. Weiler, F. Wilhelms, J.-G. Winther, E. Wolff. 3

H. Fischer, F. Fundel, U. Ruth, B. Twarloh, A. Wegner, R. Udisti, S. Becagli, E. Castellano, A. Morganti, M. Severi, E. Wolff, G. Littot, R. Röthlisberger, R. Mulvaney, M. A. Hutterli, P. Kaufmann, U. Federer, F. Lambert, M. Bigler, M. Hansson, U. Jonsell, M. de Angelis, C. Boutron, M.-L. Siggaard-Andersen, J. P. Steffensen, C. Barbante, V. Gaspari, P. Gabrielli, and D. Wagenbach. **Reconstruction of millennial changes in dust emission, transport and regional sea ice coverage using the deep EPICA ice cores from the Atlantic and Indian Ocean sector of Antarctica**. *Earth and Planetary Science Letters*, 260(1-2):340 – 354, 2007. ISSN 0012-821X. http://dx.doi.org/10.1016/j.epsl.2007.06.014. 2

S. Fujita, T. Matsuoka, T. Ishida, K. Matsuoka, and S. Mae. **A summary of the complex dielectric permittivity of ice in the megahertz range and its applications for radar sounding of polar ice sheets**. *Physics of Ice Core Records*, pages 185–212, 2000. International Symposium on Physics of Ice Core Records. Shikotsukohan Hokkaido, Japan, September 14-17, 1998. 12

S. Fujita, K. Matsuoka, H. Maeno, and T. Furukawa. **Scattering of VHF radio waves from within an ice sheet containing the vertical-girdle-type ice fabric and anisotropic reflection boundaries**. *Annals of Glaciology*, 37:305–316(12), 2003. http://dx.doi.org/10.3189/172756403781815979. 12

S. Fujita, H. Maeno, and K. Matsuoka. **Radio-wave depolarization and scattering within ice sheets: a matrix-based model to link radar and ice-core measurements and its application**. *Journal of Glaciology*, 52(178):407–424(18), 2006. http://dx.doi.org/10.3189/172756506781828548. 12

F. Gillet-Chaulet and R. C. A. Hindmarsh. **Flow at ice-divide triple junctions I: three-dimensional full-Stokes modelling**. *Journal of Geophysical Research*, 116(F2):F02023, 2011. http://dx.doi.org/10.1029/2009JF001611. 26

J. Griggs and J. Bamber. **Antarctic ice-shelf thickness from satellite radar altimetry**. *Journal of Glaciology*, 57(203):485–498, 2011. http://dx.doi.org/doi:10.3189/002214311796905659. 6, 27

R. Hanssen. *Radar Interferometry, Data Interpretation and Error Analysis*. Kluwer Academic Publishers, 2001. 14

T. Haran, J. Bohlander, T. Scambos, and M. c. Fahnestock. **MODIS mosaic of Antarctica (MOA) image map.** *Boulder, CO, USA: National Snow and Ice Data Center. Digital media.*, 2005. 5

V. Helm, W. Rack, R. Cullen, P. Nienow, D. Mair, V. Parry, and D. J. Wingham. **Winter accumulation in the percolation zone of Greenland measured by airborne radar altimeter**. *Geophysical Research Letters*, 34: L06501, 2007. http://dx.doi.org/10.1029/2006GL029185. 6

R. C. A. Hindmarsh, E. C. King, R. Mulvaney, H. F. J. Corr, G. Hiess, and F. Gillet-Chaulet. **Flow at ice-divide triple junctions II: three-dimensional views of isochrone architecture from ice-penetrating radar surveys**. *Journal of Geophysical Research*, 161(F2): F02024, 2011. http://dx.doi.org/10.1029/2009JF001622. 26

E. Jansen, J. Overpeck, K. Briffa, J.-C. Duplessy, F. Joos, V. Masson-Delmotte, D. Olago, B. Otto-Bliesner, W. Peltier, S. Rahmstorf, R. Ramesh, D. Raynaud, D. Rind, O. Solomina, R. Villalba, and D. Zhang. **Palaeoclimate. In: Climate Change 2007: The Physical Science Basis. Contribution of Working Group I to the Fourth Assessment Report of the Intergovernmental Panel on Climate Change**. *[Solomon, S., D. Qin, M. Manning, Z. Chen, M. Marquis, K.B. Averyt, M. Tignor and H.L. Miller (eds.)] Cambridge University Press, Cambridge, United Kingdom and New York, NY, USA.*, 2007. 2

I. Joughin. **Ice-sheet velocity mapping: a combined interferometric and speckle-tracking approach**. *Annals of Glaciology*, 34:195–201(7), January 2002. http://dx.doi.org/10.3189/172756402781817978. 14

I. Joughin, B. E. Smith, and D. M. Holland. **Sensitivity of 21st century sea level to ocean-induced thinning of Pine Island Glacier, Antarctica**. *Geophysical Research Letters*, 37:L20502, 2010a. http://dx.doi.org/10.1029/2010GL044819. 7

I. Joughin, B. E. Smith, I. M. Howat, T. Scambos, and T. Moon. **Greenland flow variability from ice-sheet-wide velocity mapping**. *Journal of Glaciology*, 56(197): 415–430(16), August 2010b. http://dx.doi.org/10.3189/002214310792447734. 14

J. Jouzel, V. Masson-Delmotte, O. Cattani, G. Dreyfus, S. Falourd, G. Hoffmann, B. Minster, J. Nouet, J. M. Barnola, J. Chappellaz, H. Fischer, J. C. Gallet, S. Johnsen, M. Leuenberger, L. Loulergue, D. Luethi, H. Oerter, F. Parrenin, G. Raisbeck, D. Raynaud, A. Schilt, J. Schwander, E. Selmo, R. Souchez, R. Spahni, B. Stauffer, J. P. Steffensen, B. Stenni, T. F. Stocker, J. L. Tison, M. Werner, and E. W. Wolff. **Orbital and millennial Antarctic climate variability over the last 800 000 years**. *Science*, 317:793–796, 2007. http://dx.doi.org/10.1126/science.1141038. 1

H. Le Treut, R. Somerville, U. Cubasch, Y. Ding, C. Mauritzen, A. Mokssit, T. Peterson, and M. Prather. **Historical overview of climate change**. *In: Climate Change 2007: The Physical Science Basis. Contribution of Working Group I to the Fourth Assessment Report of the Intergovernmental Panel on Climate Change [Solomon, S., D. Qin, M. Manning, Z. Chen, M. Marquis, K.B. Averyt, M. Tignor and H.L. Miller (eds.)]. Cambridge University Press, Cambridge, United Kingdom and New York, NY, USA.*, 2007. 2

P. Lemke, J. Ren, R. Alley, I. Allison, J. Carrasco, G. Flato, Y. Fujii, G. Kaser, P. Mote, R. Thomas, and T. Zhang. **Observations: Changes in Snow, Ice and Frozen Ground. In: Climate Change 2007: The Physical Science Basis. Contribution of Working Group I to the Fourth Assessment Report of the Intergovernmental Panel on Climate Change**. *[Solomon, S., D. Qin, M. Manning, Z. Chen, M. Marquis, K.B. Averyt, M. Tignor and H.L. Miller (eds.)]. Cambridge University Press, Cambridge, United Kingdom and New York, NY, USA.*, 2007. 4

L. E. Lisiecki and M. E. Raymo. **A Pliocene-Pleistocene stack of 57 globally distributed benthic δ^{18}O records**. *Paleoceanography*, 20:PA1003, 2005. http://dx.doi.org/10.1029/2004PA001071. 1

L. Loulergue, A. Schilt, R. Spahni, V. Masson-Delmotte, T. Blunier, B. Lemieux, J.-M. Barnola, D. Raynaud, T. F. Stocker, and J. Chappellaz. **Orbital and millennial-scale features of atmospheric CH_4 over the past 800,000 years**. *Nature*, 453:383–386, 2008. http://dx.doi.org/10.1038/nature06950. 2

D. Lüthi, M. L. Floch, B. Bereiter, T. Blunier, J.-M. Barnola, U. Siegenthaler, D. Raynaud, J. Jouzel, H. Fischer, K. Kawamura, and T. F. Stocker. **High-resolution CO_2 concentration record 650,000−800,000 years before present**. *Nature*, 453:379–382, 2008. http://dx.doi.org/10.1038/nature06949. 2

C. Martín, G. H. Gudmundsson, H. D. Pritchard, and O. Gagliardini. **On the effects of divide migration, alongridge flow, and basal sliding on isochrones near an ice divide** . *Journal of Geophysical Research*, 114(F4), October 2009a. ISSN 0148-0227. http://dx.doi.org/10.1029/2008JF001204. 19

C. Martín, G. H. Gudmundsson, H. D. Pritchard, and O. Gagliardini. **On the effects of anisotropic rheology on ice flow, internal structure, and the age-depth relationship at ice divides**. *Journal of Geophysical Research*, 114(F4):F04001, Oct. 2009b. ISSN 0148-0227. 26

K. Matsuoka. **Pitfalls in radar diagnosis of ice-sheet bed conditions: Lessons from englacial attenuation models**. *Geophysical Research Letters*, 38:L05505, 2011. http://dx.doi.org/10.1029/2010GL046205. 6, 24

K. Matsuoka, L. Wilen, S. P. Hurley, and C. F. Raymond. **Effects of Birefringence Within Ice Sheets on Obliquely Propagating Radio Waves**. *IEEE Transactions on Geoscience and Remote Sensing*, 47:1429–1443, May 2009. http://dx.doi.org/10.1109/TGRS.2008.2005201. 12

M. Milankovitch. *Kanon der Erdbestrahlung und seine Anwendung auf das Eiszeitenproblem, Special Publications Vol. 132*, volume 33 of *Section Mathematics and Natural Sciences*. Royal Serbian Acadademy, Belgrad, 1941. 1

R. J. Motyka, M. Fahnestock, and M. Truffer. **Volume change of Jakobshavn Isbrae, West Greenland:: 1985-1997-2007**. *Journal of Glaciology*, 56(198):635–646(12), 2010. http://dx.doi.org/10.3189/002214310793146304. 7

N. Neckel. **Surface velocities in the hinterland of the Neumayer III station (Antarctica) derived from SAR-Interferometry**. Master's thesis, Universität Heidelberg, Fachbereich Geographie, 2011. 5, 20, 91

N. A. Nereson and E. D. Waddington. **Isochrones and isotherms beneath migrating ice divides**. *Journal of Glaciology*, 48(160):95–108(14), January 2002. http://dx.doi.org/10.3189/172756502781831647. 11, 26

F. M. Nick, A. Vieli, I. M. Howat, and I. Joughin. **Large-scale changes in Greenland outlet glacier dynamics triggered at the terminus.** *Nature Geoscience*, 2(2):110–114, February 2009. http://dx.doi.org/10.1038/ngeo394. 7

H. Oerter, C. Drücker, S. Kipfstuhl, and F. Wilhelms. **Kohnen station - the drilling camp for the EPICA deep ice core in Dronning Maud Land**. *Polarforschung*, 78 (1-2):1–23, 2009. 2

J. Paden, T. Akins, D. Dunson, C. Allen, and P. Gogineni. **Ice-sheet bed 3-D tomography**. *Journal of Glaciology*, 56(195):3–11(9), April 2010. http://dx.doi.org/10.3189/002214310791190811. 3

J. Paren. **Correspondence**. *Journal of Glaciology*, 27(95): 203–204, 1981. 10

J. Paren and G. Q. Robin. **Internal reflections in Polar Ice Sheets**. *Journal of Glaciology*, 14:251–259, 1975. 10

W. Rack and H. Rott. **Pattern of retreat and disintegration of the Larsen B ice shelf, Antarctic Peninsula**. *Annals of Glaciology*, 39:505–510(6), June 2004. http://dx.doi.org/10.3189/172756404781814005. 7, 14

C. F. Raymond. **Deformation in the vicinity of ice divides**. *Journal of Glaciology*, 29(103):357–373, 1983. 11

E. Rignot, J. L. Bamber, M. R. van den Broeke, C. Davis, Y. Li, W. J. van de Berg, and E. van Meigaard. **Recent Antarctic ice mass loss from radar interferometry and regional climate modelling**. *Nature Geoscience*, 1: 106–110, 2008. http://dx.doi.org/10.1038/ngeo102. 14

E. Rignot, J. Mouginot, and B. Scheuchl. **Antarctic grounding line mapping from differential satellite radar interferometry**. *Geophysical Research Letters*, 38:L10504, 2011a. http://dx.doi.org/10.1029/2011GL047109. 26

E. Rignot, I. Velicogna, M. R. van den Broeke, A. Monaghan, and J. Lenaerts. **Acceleration of the contribution of the Greenland and Antarctic ice sheets to sea level rise**. *Geophysical Research Letters*, 38:L05503, 2011b. http://dx.doi.org/10.1029/2011GL046583. 4

R. Rosen, S. Hensley, I. Joughin, S. F. Li, E. Rodríguez, and R. Goldstein. **Synthetic Aperture Radar Interferometry**. *Proceedings of the IEEE*, 88 No. 3, march 2000. 14

G. Rotschky, W. Rack, W. Dierking, and H. Oerter. **Retrieving Snowpack properties and Accumulation Estimates from Combination of SAR and Scatterometer Measurements**. *IEEE Transactions on Geoscience and Remote Sensing*, 44(4):943–956, April 2006. http://dx.doi.org/10.1109/TGRS.2005.862524. 3

U. Ruth, J. M. Barnola, J. Beer, M. Bigler, T. Blunier, E. Castellano, H. Fischer, F. Fundel, P. Huybrechts, P. Kaufmann, S. Kipfstuhl, A. Lambrecht, A. Morganti, H. Oerter, F. Parrenin, O. Rybak, M. Severi, R. Udisti, F. Wilhelms, and E. Wolff. **EDML1: A chronology for the EPICA deep ice core from Dronning Maud Land, Antarctica, over the last 150 000 years**. *Climate of the Past*, 3:475–484, 2007. http://dx.doi.org/10.1594/PANGAEA.602127. 3

A. Schilt, M. Baumgartner, T. Blunier, J. Schwander, R. Spahni, H. Fischer, and T. F. Stocker. **Glacial-interglacial and millennial-scale variations in the atmospheric nitrous oxide concentration during the last 800 000 years**. *Quaternary Science Reviews*, 29:182–192, 2010. http://dx.doi.org/10.1016/j.quascirev.2009.03.011. 2

M. J. Siegert, B. Welch, D. Morse, A. Vieli, D. D. Blankenship, I. Joughin, E. C. King, G. J.-M. C. L. y. Vieli, A. J. Payne, and R. Jacobel. **Ice Flow Direction Change in Interior West Antarctica**. *Science*, 305(5692):1948–1951, 2004. http://dx.doi.org/10.1126/science.1101072. 11

D. Steinhage, U. Nixdorf, U. Meyer, and H. Miller. **Subglacial topography and internal structure of central and western Dronning Maud Land, Antarctica, determined from airborne radio echo sounding**. *Journal of Applied Geophysics*, 47(3-4):183 – 189, 2001. ISSN 0926-9851. http://dx.doi.org/10.1016/S0926-9851(01)00063-5. 4

L. Tsang and J. A. Kong. *Scattering of Electomagnetic Waves: Advanced Topics*. John Wiley and Sons, Inc, New York, NY, 2001. 10

L. Tsang, J. A. Kong, and K. H. Ding. *Scattering of Electomagnetic Waves: Theories and Applications*. John Wiley and Sons, Inc, New York, NY, 2000. 10

L. Tsang, J. A. Kong, K. H. Ding, and C. O. Ao. *Scattering of Electomagnetic Waves: Numerical Simulations*. John Wiley and Sons, Inc, New York, NY, 2001. 10

F. T. Ulaby, R. K. Moore, and A. K. Fung. *Microwave Remote Sensing: Active and Passive*, volume 2. Artech House, 1986. 10

I. Velicogna and J. Wahr. **Greenland mass balance from GRACE**. *Geophysical Research Letters*, 32:L18505, Sept. 2005. http://dx.doi.org/10.1029/2005GL023955. 6

I. Velicogna and J. Wahr. **Measurements of Time-Variable Gravity Show Mass Loss in Antarctica**. *Science*, 311(5768):1754–1756, 2006. http://dx.doi.org/10.1126/science.1123785. 6

B. M. Vinther, S. L. Buchardt, H. B. Clausen, D. Dahl-Jensen, S. J. Johnen, D. A. Fisher, R. M. Koerner, D. Raynaud, V. Lipenkov, K. K. Andersen, T. Blunier, S. O. Rasmussen, J. P. Steffensen, and A. M. Svensson. **Holocene thinning of the Greenland ice sheet**. *Nature*, 461, 2009. http://dx.doi.org/10.1038/nature08355. 7

C. Wesche, S. Riedel, and D. Steinhage. **Precise surface topography of the grounded ice ridges at the Ekstrmisen, Antarctica, based on several geophysical data sets**. *ISPRS Journal of Photogrammetry and Remote Sensing*, 64(4):381 – 386, 2009. ISSN 0924-2716. http://dx.doi.org/10.1016/j.isprsjprs.2009.01.005. 3

A. Layer disturbances and the radio-echo free zone in ice sheets

Own contribution: Differentiation of EFZ onset and loss of RES sensitivity; Automated image analysis to quantify the dip angle of cloudy bands in line-scan data; Comparison of RES with DEP measurements; Literature review; Creation of all Figures; Writing of publication.
Current status: published.

The Cryosphere, 3, 195–203, 2009
www.the-cryosphere.net/3/195/2009/

The Cryosphere

Layer disturbances and the radio-echo free zone in ice sheets

R. Drews[1], **O. Eisen**[1,2], **I. Weikusat**[1], **S. Kipfstuhl**[1], **A. Lambrecht**[1,*], **D. Steinhage**[1], **F. Wilhelms**[1], **and H. Miller**[1]

[1]Alfred-Wegener-Institut für Polar- und Meeresforschung, Bremerhaven, Germany
[2]Institut für Umweltphysik, Heidelberg, Germany
[*]now at: DMT GmbH & Co. KG, Am Technologiepark 1, 45307 Essen, Germany

Received: 20 March 2009 – Published in The Cryosphere Discuss.: 28 April 2009
Revised: 22 July 2009 – Accepted: 28 July 2009 – Published: 25 August 2009

Abstract. Radio-echo sounding of the Antarctic and Greenlandic ice sheets often reveals a layer in the lowest hundreds of meters above bedrock more or less free of radio echoes, known as the echo-free zone (EFZ). The cause of this feature is unclear, so far lacking direct evidence for its origin. We compare echoes around the EPICA drill site in Dronning Maud Land, Antarctica, with the dielectric properties, crystal orientation fabrics and optical stratigraphy of the EPICA-DML ice core. We find that echoes disappear in the depth range where the dielectric contrast is blurred, and where the coherency of the layers in the ice core is lost due to disturbances caused by the ice flow. At the drill site, the EFZ onset at ∼2100 m marks a boundary, below which the ice core may have experienced flow induced disturbances on various scales. The onset may indicate changing rheology which needs to be accounted for in the modeling of ice sheet dynamics.

1 Introduction

For over 40 years radio-echo sounding (RES) has been successfully applied to determine ice thickness and internal structure of large ice bodies. Internal echoes (horizons) are caused by layers contrasting significantly in the dielectric properties of the surrounding ice. The three causes for such changes are: density variations in shallow ice, acid layers and changing crystal orientation fabric (COF) in deeper ice (Fujita et al., 1999). Changes in density and conductivity have isochronous character (Vaughan et al., 2004; Eisen et al., 2004). Changing COF might have isochronous character, but is also influenced by the ice flow (Eisen et al., 2007).

A commonly observed but hitherto unexplained phenomenon is the basal echo free zone (EFZ), a hundreds of meters thick band above the ice bed interface more or less free of radio echoes. The absence of layering was first discussed by Robin et al. (1977) and eventually named as EFZ by Drewry and Meldrum (1978). It is often characterized by an abrupt transition, and an upper onset that varies with depth. It is usually not attributed to the loss of RES sensitivity. Typically it follows the bedrock topography and increases in thickness away from ice domes (Matsuoka et al., 2003). Because direct evidence has been unavailable, it is unclear what triggers the absence of internal reflections within the EFZ, although the EFZ is observed in extensive parts of the Antarctic ice sheet (e.g. Drewry and Meldrum, 1978; Robin and Millar, 1982; Fujita et al., 1999; Siegert and Kwok, 2000; Matsuoka et al., 2003; Wang et al., 2008). Russell-Head and Budd (1979) connected the EFZ observed by Robin et al. (1977) to a layer with low shear stress in the lower third of the ice sheet by Law Dome. Robin and Millar (1982) suggested that the EFZ, observed North of Lake Vostok, is due to a buckling of layers which become increasingly deformed as the bedrock relief starts to influence stress and strain rates towards the bottom. Maccagnan and Duval (1982) proposed that the EFZ onset near the Dome C area represents an isotherm in ice. Fujita et al. (1999) argued for examples at Dome F that variable shear over an irregular surface causes folding, mixing, and faulting of layers and thus inhibits the return of coherent reflections. Siegert and Kwok (2000) discussed the EFZ observed in subglacial valleys West of Lake Vostok. They described the ice as being potentially stagnant and suggest that recrystallization and recirculation of ice may also play a role.

Correspondence to: R. Drews
(reinhard.drews@awi.de)

Published by Copernicus Publications on behalf of the European Geosciences Union.

If the EFZ is not due to the system sensitivity, Bogorodsky et al. (1985) consider it as a proxy for the reliability of ice-core records in paleoclimate resarch which relies on parallel layering for the age-depth conversion. As the EFZ likely indicates a change in flow behavior, the mechanisms are also important for the modeling of ice sheet dynamics and stability (Dowdeswell and Evans, 2004).

In order to check the existing hypotheses we compare airborne RES data around the EPICA drill site at Kohnen station in Dronning Maud Land (DML), Antarctica, with the crystal fabric, optical stratigraphy and dielectrical properties of the 2774 m long EPICA-DML (EDML) ice core. The geographical setting (Fig. 1) indicates the locations of the RES profiles used in this study (Fig. 2) . The ice core is situated on an ice divide in a flank-flow regime. Ice flows towards the Kirwanveggen mountain range, which potentially acts as a barrier for ice flow.

Along with data from dielectric profiling (DEP) and the distribution of COF, we use line-scan images to visualize the integrity of layering. Line-scan images (see Fig. 3) display the stratigraphy of high-scattering zones for light, called cloudy bands (CBs). They correlate with the impurity content of ice (Svensson et al., 2005) and we take them as a proxy for the layering of RES horizons.

So far the comparison of CB layering with RES has not been achieved, because no continuous CB stratigraphy is available for other ice cores from Antarctica. Moreover, only few CBs are seen in the deep ice cores from Byrd, Vostok, and Dome Concordia. The EDML core is the only core from Antarctica with continuous visual stratigraphy and cloudy bands enable a direct comparison with RES data. We find that radio echoes disappear below ∼2100 m at the drill site and that this transition coincides with progressive disturbances in CB-stratigraphy. We discuss possible reasons for the absence of echoes in that zone and implications for the suitability of ice for paleoclimate research and ice-sheet modeling.

2 Methods and findings

2.1 Dielectric profiling and fabric analyzer

For DEP the ice core is placed between cylindrical electrodes to measure the complex dielectric permittivity from which bulk density and conductivity can be inferred (Wilhelms et al., 1998). The 1-cm electrodes were driven with a 250 kHz signal and shifted along-core with a 0.5 cm increment. DEP records are corrected for variations in temperature, core diameter, and breaks. The data are scaled (Eisen et al., 2006) to the center frequency of the RES system (150 MHz). In the conductivity profile in Fig. 5a the number and height of peaks decreases towards greater depths. The last dominant peaks rising three times above the background

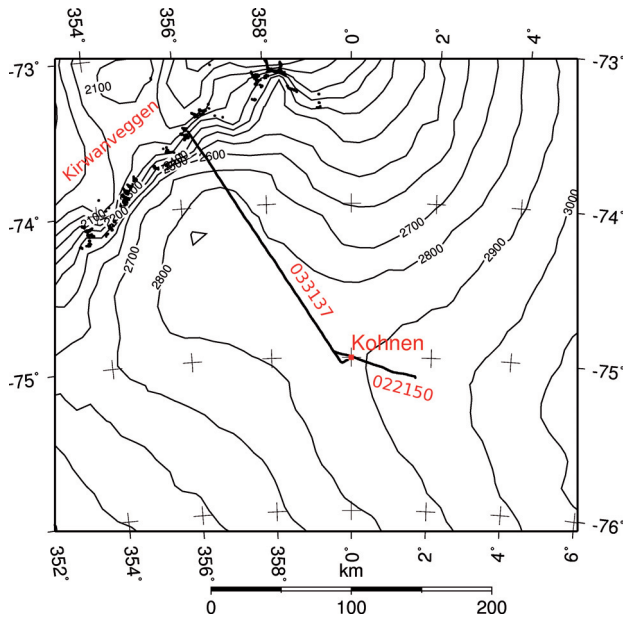

Fig. 1. Location of radar profiles 022150 and 033137 (long black lines) in the vicinity of Kohnen (red dot). Profile 033137 intersects the Kirwanveggen mountain range, which acts as barrier for ice flow. Outcrops of the mountain range are indicated with black dots.

noise occur at 2180 m. Below 2400 m the typical conductivity peaks are missing.

The fabric data in Fig. 5b are collected from thin sections between crossed polarizers (Wilson et al., 2003). The data are usually displayed in Schmidt diagrams or in terms of three Eigenvalues characterizing an ellipsoid which best approximates the c-axes distribution. Between 2025–2045 m the distribution in COF changes from a vertical girdle type to a single maximum distribution continuing to the bottom. At ∼2375 m the fabric resembles a vertical girdle distribution, but COF data in this depth interval are sparse.

2.2 Line-scans and ice-core characteristics

The line-scan camera images 1-m segments of the ice core at a resolution of 0.1 mm with light (Svensson et al., 2005). While being moved along the core, the camera records light which is scattered by grain boundaries, air-bubbles and microparticles. Transparent zones appear black, and zones with inclusions appear milky (see Fig. 3).

We see progressive disturbances in CB-stratigraphy with depth which correspond to other ice-core characteristics: above 1700 m the CBs appear straight, smooth, and parallel. They dip slightly due to the inclination of the borehole. Between ∼1700–2050 m the CBs develop mm-scale undulations. From approximately 2050 m downwards the dip of CBs increases to 10–15°. Most CBs are still parallel, but mm-scaled z-folds start to develop.

Crystals with diameters larger than 10 cm are present in the last interglacial (MIS5, ∼2300–2375 m, age-depth values are based on Ruth et al., 2007) and below ∼2600 m. A plot of mean crystal size is published by Weikusat et al. (2009) in Fig. 2a. At the transition from MIS5 to glacial MIS6 (below about 2400 m), we see a mixture of dipping and undulating CBs on various scales. In the fine-grained ice of MIS6, the CBs appear parallel, horizontal or inclined up to 30° alternated with isoclinal z-folds on the cm- to dm-scale. Below a depth of about 2400 m, CBs increasingly occur with opposite sign of dip within a single core segment of 1 m length.

We quantified the dip angle of CBs along depth via an automated image analysis. After contrast enhancement and edge detection, the line-scan image of a 1-m segment was binarized. Remaining straight lines with a maximal dip angle of ±45° from the horizontal (namely CBs) were detected by using a Hough transformation (Hough and Arbor, 1960). In this approach every line connecting two or more pixels is represented as a point in a parameter space (offset and slope), and the strongest lines are identified with a voting procedure (see for example: Burger and Burge, 2008). Between 1500 m–2100 m, CBs are clearly visbile and approximately 8–15 CBs are detected per image. From 2100 m–2370 m, stronger contrast enhancement is necessary and the stratigraphy appears more blurred. In average only 3–7 CBs are detected. Between 2370 m down to 2500 m, the stratigraphy is more pronounced again. In Fig. 3 the so detected CBs are marked with green lines. It is evident that the procedure does not capture the CBs in their full complexity, but is biased towards thick and non-undulated CBs with a strong contrast. It neglects weaker and undulated CBs. Thus the results should only be regarded as a general trend (for example the mean value of dip angles may vary, depending on the thresholds chosen for the contrast enhancement).

Figure 5d displays the absolute mean dip in a 1-m segment along depth. The mean dip angle varies gradually from 1400–2000 m depth and then exhibits larger variations. Segments with strong mean dip are intersected with segments of smaller mean dip. Below 2100 m the most of the CBs appear perturbed, but also undisturbed CBs can be found.

2.3 RES internal structure

The airborne RES system operates at a frequency of 150 MHz in a toggle mode alternately transmitting a pulse with length of 60 and 600 ns. The theoretical vertical resolution is 5 and 50 m in ice respectively. Specifics about the radar system are summarized in Table 1, and also discussed by Nixdorf et al. (1999).

Figure 2 displays two profiles in the vicinity of the drill site at Kohnen station. Conversion of two-way traveltime (TWT) to depth is based on synthetic traces (Eisen et al., 2006). Profile 022150 was recorded in 2002 and runs parallel to the ice divide. Profile 033137 was recorded in 2003 and connects Kohnen with the German overwintering station Neumayer.

Table 1. Radar system specification; for wavelength λ a permittivity of 3.15 was assumed, Δz corresponds to half the pulse length, two antennas with equal transmitting and receiving gain G are used, P_t is damped for the short pulse data to maintain a rectangular shape of the ougoing pulse.

Parameter	Variable	60 ns pulse	600 ns pulse
transm. peak power [dBm]	τ	47	62
vert. resolution in ice [m]	Δz	5	50
wave length in ice [m]	λ	2	2
center frequency [MHz]	–	150	150
antenna type (trans.& receiv.)	–	short backfire	short backfire
antenna gain [dB]	G	14.2	14.2

Detailed internal layering is evident at both pulse lengths in the upper two thirds of the ice column and prominent layers can be traced from one profile to the other. At EDML, the majority of internal reflectors below ∼900 m originate from individual conductivity peaks, with some being an interference signal of closely spaced peaks (Eisen et al., 2006). The last two detected signals in the 60 ns RES data at EDML correspond to a reflector from changes in COF at 2040 m (Eisen et al., 2007) and a conductivity peak at 2080 m. The EFZ is observed in both profiles. Figure 4a and b display an example from profile 033137 (trace 6297), where the last continuous reflector is found at 1654 m depth, 690 m above the ice-bed interface. The backscattered intensity in the long pulse data drops by 8 dB. At EDML, the EFZ is less pronounced but still evident (see Fig. 4c and d). Below about 2100 m no continuous internal layering can be found, short and long pulse data fade at similar depth. The last reflector in the long pulse data is about 2 dB above the noise level. Small signals sometimes appear within the EFZ but these are usually not continuous laterally. An example is visible in Fig. 5e between 2300 and 2400 m depth. The usually invisible signal becomes only apparent in the differentiated data of the long pulse. The backscattered power is just a few tenths of dB above the noise level. It coincides with the previously mentioned change in COF at 2375 m, and a section of undisturbed CBs below about 2385 m depth. Similar reflectors within the EFZ are also observed at other locations (Robin and Millar, 1982).

2.4 Definition of EFZ-onset and system performance

The EFZ has been characterized so far by the absence of continuous internal layering above the bedrock, which starts with a sudden drop in backscattered power. The abruptness often negates insufficient radar performance as a primary reason for the EFZ. There is no consensus how strong the drop in backscattered power should be, and since the power drop must be a function of depth, it seems inadequate to tie it to a fixed number.

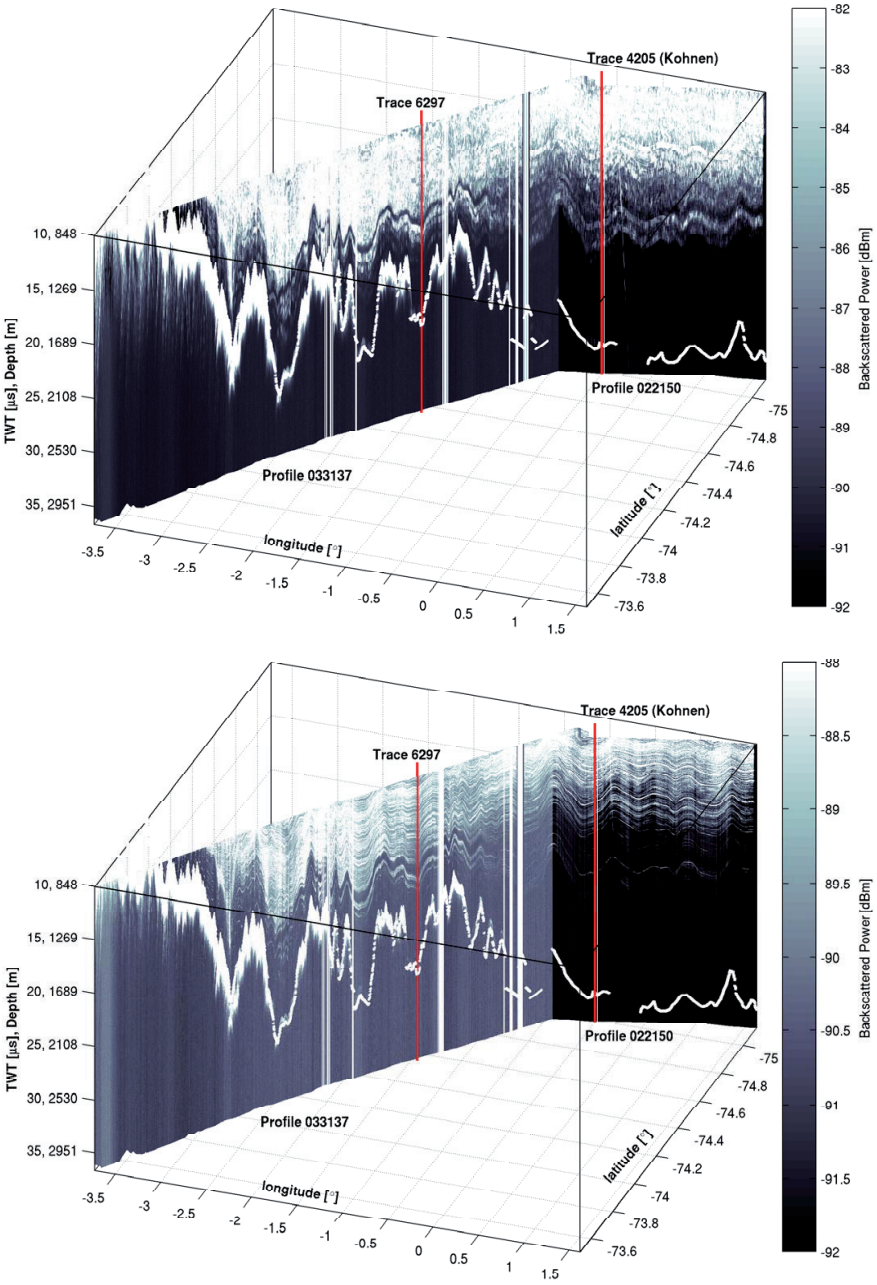

Fig. 2. Radar profiles in the vicinity of Kohnen station recorded with the 60 ns (bottom) and 600 ns (top) pulse. Bedrock was picked from differentiated data. The TWT is corrected to the first break of the surface reflection. Units of backscattered power are referenced to 1 mW (dBm). For better visibility of deeper layers the upper layers have been excluded. Profile 022150 has a length of 40 km and runs parallel to the ice divide. Ice flow is approximately 1 m/a. Profile 033137 has a length of 200 km and intersects the Kirwanveggen mountain range. Although the upper boundary of the EFZ cannot be mapped everywhere, it is clearly visible that it is variable in height and follows the bedrock topography. Traces shown in Fig. 4 are labeled at the top.

We propose two ways how to keep RES sensitivity and other physical mechanisms for the EFZ apart: firstly a comparison of calculated power reflection coefficients (PRCs) from ice-core data with the estimated detection limit of the system, and secondly an in-situ comparison of long and short pulse data.

The PRCs ($|R|^2$) approximate the scattering cross section in case of an ideal interface. We calculate them from DEP and COF data with the two-layer approximation from Paren (1981). Following Nixdorf et al. (1999), an estimate for the signal to noise ratio S/N can be parameterized with

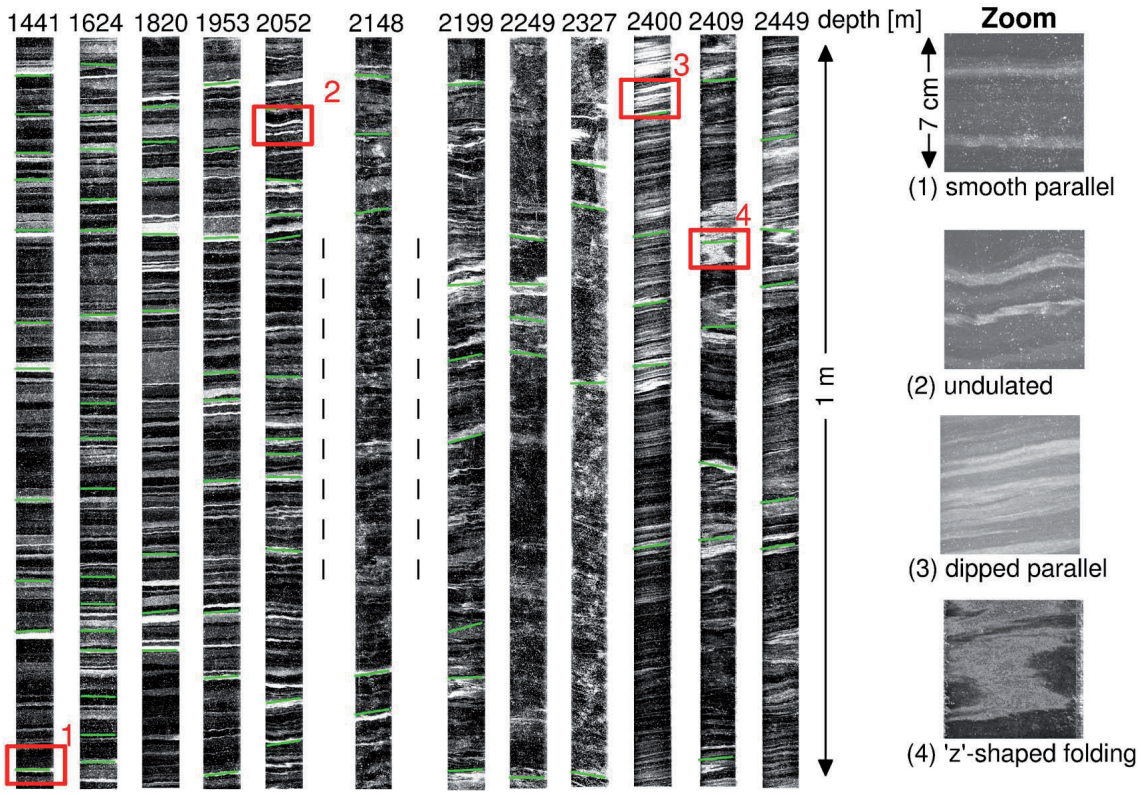

Fig. 3. Line-scan images of the EDML ice core (left) after contrast enhancement. Close-ups of the originial images are visible on the right. Cloudy bands that have been detected with the image analysis are marked in green. The EFZ onset at approximately 2100 m depth is indicated with dashed lines. Cloudy band stratigraphy appears undisturbed (zoom 1) above EFZ with small-scale undulations (zoom 2) slowly developing. Within the EFZ, layers appear partly dipped parallel (zoom 3) and partly rough as dips point into opposite directions. Dips can be intersected with z-shaped folds (zoom 4).

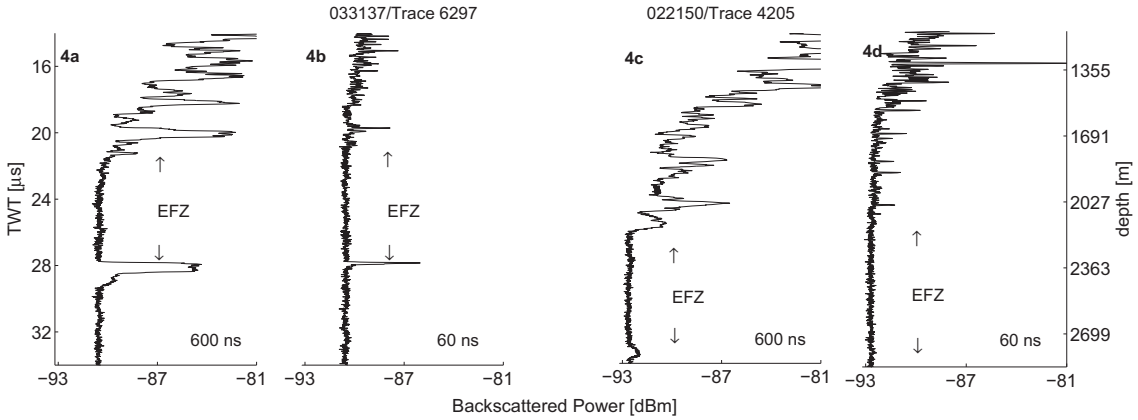

Fig. 4. The EFZ is identified by the simultaneous disappearance of continuous layers in the 60 and 600 ns data, whereby backscattered power in the 600 ns data drops by several dB. In **(a)** and **(b)** trace 6297 (profile 033137) of 600 and 60 ns data is a typical example for the EFZ. The last continuous signal is visbile at 20.1 μs in the 600 ns and at 19.7 μs (∼1654 m depth) in the 60 ns pulse. Bedrock is clearly visible in both traces at 27.9 μs (∼2344 m depth). **(c)** and **(d)** display trace 4205 (profile 022150) for both pulses at the EPICA drill site. Bedrock is visible in both traces at about 2790 m depth. Last continuous signals above the bedrock are detected at 25.4 and 25 μs TWT (∼2100 m depth). Because of the larger depth, the signal drop in the 600 ns data is smaller than in (a).

$$\frac{S}{N} = \frac{P_t \tau G^2 q g_{st} \lambda^2 |R|^2}{(4\pi)^2 [2(H+h)]^2 LkT} \quad (1)$$

where q is the refraction gain, g_{st}=200 is the stacking gain, H=500 m is the flight level above surface, k is the Boltzmann constant, T=400 K is the noise temperature and L is the attenuation at depth h. All other parameters are summarized in Table 1. The loss factor $L=L_K^2 (L_T)^2 L_A$ includes the transmission loss through the surface (L_T=1.11), the cable loss (L_K=1.99), and the two-way dielectric loss L_A. In analogy to other approaches (MacGregor et al., 2007), we neglect power loss through multiple internal reflections and calculate the total two-way dielectric loss L_A as the product of incremental attenuation rates for each measured value of the conductivity. Conductivity has been corrected for temperature with an Arrhenius relation (e.g. MacGregor et al. (2007), Eq. 2). Rearranging Eq. (1) for $|R|^2$ with an empirical signal to noise ratio of 1.02 and plotting it along depth results in the two lines displayed in Fig. 5c. These lines mark the estimated detection limit for PRCs for the two different pulses. Compared to the calculated (ideal) PRCs from ice-core data, we would expect to detect at least three more layers within the EFZ. However, the estimation of the detection limit does not take into account interference effects and the temperature dependence of the attenuation rates is not fully known. Thus this approach is only a rough estimation.

The radar is usually flown in toggle mode, so that the short pulse can be used to detect internal layering at high vertical resolution and the long pulse for the sounding of bedrock topography. Equation (1) somewhat quantifies this behaviour with the dependency on pulse length (τ) and emitted peak power (P_t). Pulse length and peak power do not always translate linearly into the signal to noise ratio, as for example R is also dependent on the pulse length (the short pulse layering results from interferences within a smaller vertical interval leading to some differences). However, there is often a direct correspondence between peaks in long and short pulse data – with a better signal to noise ratio in the long pulse data. Therefore we use the deepest layering in the short pulse data as an upper boundary for the detection limit of the long pulse. If layering in long and short pulse data vanish at similar depth, we suspect that at least the absence of layering in long pulse data in a certain interval below that depth is not caused by the system sensitivity. The vertical extent of that interval depends on the drop in backscattered power of the long pulse data. A definition of the EFZ onset in that way is inherently radar dependent, but it bypasses the uncertainties in estimating the detection limit based on the radar equation.

The single traces in Fig. 4a, b demonstrate clearly a correspondence between long and short pulse, together with an 8 dB drop in backscattered power in the long pulse data. Since it is unlikely that the long pulse is attenuated by 8 dB within 100 m below the last reflector, we assume that other mechanisms than mere running out of signal strength must be responsible for the absence of echoes. Single traces at the drill site (Fig. 4c, d) correspond well in long and short pulse data, but the drop in backscattered power in the long pulse data is smaller (≈2 dB). From this example alone, the separation between system performance and other physical mechanisms is not so clear-cut, because the long pulse could be attenuated shortly beneath the disappearance of the short pulse by a slight increase in temperature. However, since the drop in backscattered power must be a function of depth, and because we can trace the EFZ from the previous example (Fig. 4a, b) to the drill site (see also Fig. 2), we conclude that the EFZ is also evident at the drill site. The correspondence of long and short pulse data, and the lateral variation of the EFZ onset around the drill site are indicated in Fig. 5e.

3 Potential physical mechanisms of the EFZ

Using the dual-pulse technique described in Sect. 2.4 we identify the EFZ in many places of Fig. 2. An example is shown in Fig. 5e. It is evident that the EFZ's upper onset is variable in height and largely follows the bedrock topography. The onset in Fig. 2 ranges from 1600–2100 m depth, with a 600–700 m thick gap to the bedrock. Here we discuss potential mechanisms – other than the RES sensitivity – for the absence of internal layering around the EPICA-DML drill site. In particular we consider (1) a lack of dielectric contrast, (2) the role of temperature with respect to signal attenuation and the mechanical properties of ice, and (3) the lack of suitable reflecting surfaces due to layer roughness.

The DEP record changes its characteristic below about 2200 m. Conductivity peaks are broader, less distinct and not as frequent. Thus a one dimensional forward model of electromagnetic wave propagation (Eisen et al., 2006) does not predict reflections within the EFZ. The lack of strong conductivity signals can be related to the dipping of layers in the CB stratigraphy. Non-horizontal conductivity signals cause broader and less pronounced peaks, since the DEP device integrates over the entire core diameter D along the horizontal. The magnitude of this effect can be estimated by assuming the conductivity signal $\sigma(z,x)$ to be Gaussian along the vertical z and dipped with slope m along the horizontal x. This means $\sigma(z,x)=A\exp\left(-\frac{(z-mx)^2}{d^2}\right)$, with A determining the peak amplitude and d the peak width. The integration over the core diameter D yields $\sigma(z)=\int_0^D \sigma(z,x)dx = A\frac{\sqrt{\pi d}}{2m}\left[\mathrm{ERF}\left(\frac{m}{d}x-\frac{z}{\sqrt{d}}\right)\right]_0^D$, where ERF stands for the error function. The magnitude of peak broadening is mainly determined by the initial peak width and the dip angle. With an exemplary peak width of d=2.5 cm and a dip angle of 15°, the initial peak height decreases by ∼15%. However, whether ice dynamics or simple diffusion is the main reasons for the absence of strong conductivity peaks has yet to be determined. As a physical mechanism for the EFZ, a simple lack of dielectric contrast cannot be excluded.

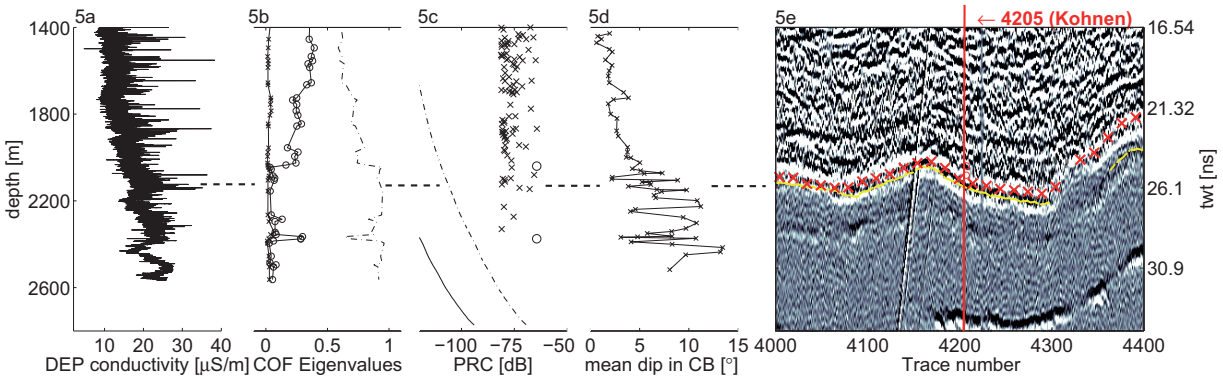

Fig. 5. DEP conductivity profile **(a)** and COF Eigenvalues **(b)** from measurements on the EPICA-DML ice core at Kohnen. Power reflection coefficients in **(c)** are calculated from peaks in DEP-data (x) and change in COF (o) based on the two-layer interface approximation after Paren (1981). The lines indicate the estimated limit of detectable power reflections coefficients for the 60 and 600 ns pulse dashed and solid, respectively (adapted from Nixdorf et al., 1999). The stratigraphic disturbances observed in the line-scan images are illustrated in **(d)** as the mean absolute dip of CBs averaged over a 1-m interval along depth. **(e)** displays differentiated radar data (600 ns) of profile 022150 centered around Kohnen. The last continuous reflector in the 600 ns data is indicated with the yellow line. The same reflector can be picked in the 60 ns data (overlaid on the 600 ns data with red crosses) between traces 4000 and 4300.

The connection of EFZ onset with an isotherm in ice was previously suggested by Maccagnan and Duval (1982). The temperature distribution in the lower third of an ice sheet is dominated by the geothermal heat flux, but it is also affected by the overburden ice column. If the EFZ onset represents an isotherm, two effects need to be considered: The effect of temperature with respect to attenuation, and the effect of temperature with respect to the mechanical properties of ice. Attenuation usually does not suggest a threshold behaviour. Whereas temperature might play a role in the example of Fig. 4c–d, it seems unlikely to be the case for Fig. 4a–b where the dielectric loss would need to be 8 dB/100 m. A change in the mechanical properties of ice around the EFZ onset is supported by the disturbances observed in the line-scan data. However, so far there is no evidence that ice develops a threshold behaviour at a certain temperature. We therefore exclude temperature for a driving mechanism for the EFZ onset at EDML.

The correspondence of progressive CB disturbances and the EFZ onset (see Fig. 5d, e) suggests a physical connection. If the CB stratigraphy is taken as a proxy for the large scale layering of RES reflectors, it seems that above the EFZ the layering is quasi-parallel, whereas below the EFZ onset the layering is disturbed. A roughening of layer surfaces within the first few Fresnel zones increases the diffuse scattering and reduces the coherent component. A dipping of layers reflects the signal away from the receiver. Studies about scattering on rough interfaces are often based on the Kirchhoff approximation (see for example Ogilvy, 1991), where random and isotropic Gaussian surfaces with a specified rms-roughness and correlation length are used. In our case, we estimate that a rms-roughness of ∼0.2 m results in ∼10 dB loss in the specular component (Peters et al., 2005). In case layers are dipped, it is possible that the main lobe of the signal is lost, and only sidelobe reflections are received. Both effects cannot be evaluated quantitvely because it is impossible to extrapolate the disturbances seen in the ice core (diameter 10 cm) to the entire Fresnel zone (≈60 m at 2100 m depth). If we assume that CB-layers do not intersect (as they are isochrones) we can linearely extrapolate dipped cloudy bands in a single core segment and estimate the layer roughness and correlation length from anticipated intersection points. However, this strongly depends on which CBs are used for extrapolation and also does not boarder the parameters with an upper or lower boundary.

We favour large-scale disturbances in the layering of RES reflectors caused by ice flow as the primary reason for the EFZ at EDML. Deformations on a larger scale are suggested by changing COF at the EFZ onset (see Fig. 5c), and by a change in borehole geometry at 2385 m depth, when drilling was interrupted for two years during 2004 and 2006 (Faria et al., 2006). The measured borehole closure of 2 mm/a indicates an increase in differential flow by an order of magnitude compared to the upper ice column. The climate record is dated to 2417 m depth. However, Ruth et al. (2007) report increasing difficulties in matching volcanic events with the Dome Concordia record below 1900 m depth. It is hypothesized that starting at 2050 m depth, complex flow history and increasing shear stress makes the climate record less reliable until dating is impossible below 2400 m (S. Faria, personal communication, 2009).

In the vicinity around Dome F an EFZ is also observed. Directly at the dome position the radar signal decreases gradually, but away from the dome in the flank-flow regions the EFZ is evident (S. Fujita, personal communication, 2003, 2008), indicating an ice-dynamical link. The EDML ice

core is situated in such a flank-flow regime likewise as the GISP2 (Greenland Ice Sheet Project) ice core in Greenland. For GISP2, Jacobel and Hodge (1995) describe the coincident loss of internal layering in analog radar data, at equal depth with dipped stratigraphy in the ice core. Therefore we suggest that for EDML layer roughness (or dip) is the main reason for the loss of internal layering. Not enough data are currently at hand to generalize our results for other places in Greenland and Antarctica.

4 Conclusions

It is not finally established whether the primary reason for the EFZ at EDML is related to the dielectric contrast, the temperature, or a larger scale layer roughness. We favour the latter: rough or dipped layers reduce the level of backscatterd power. Possibly other radar systems find the EFZ onset at EDML at a different depth, but a change in backscattered power would still be expected. It is likely that the EFZ is enhanced in flank-flow regimes. The small-scale CB features we describe may belong to disturbances on a larger scale, with overturning and thus age reversal of layers as modeled by Jacobson and Waddington (2005). If this holds true, the onset of the EFZ indicates the beginning of differential flow, with mixing and folding of layers towards greater depth. The interrelation of reflections from changing COF and the EFZ onset, which has also been observed by Matsuoka et al. (2003) and Fujita et al. (1999), has yet to be determined. It is likely that the changing rheology needs to be accounted for in ice-sheet modeling. The EFZ marks the depth within the ice, below which paleoclimate ice-core records may have been influenced by ice flow and need to be interpreted with care.

As the EFZ is detected from above the ice sheet, it is an excellent indicator of disturbances in internal stratigraphy. This is important for future surveys of ice-core sites, particularly for the upcoming search for the oldest ice within the framework of the International Partnerships in Ice Core Sciences (IPICS).

Acknowledgements. This work is a contribution to the European Project for Ice Coring in Antarctica (EPICA), a joint European Science Foundation/European Commission scientific programme, funded by the EU and by national contributions from Belgium, Denmark, France, Germany, Italy, The Netherlands, Norway, Sweden, Switzerland and the United Kingdom. The main logistic support was provided by IPEV and PNRA (at Dome C) and AWI (at Dronning Maud Land). This is EPICA Publication Number 232.

Preparation of this work was supported by the Emmy Noether-programme of the Deutsche Forschungsgemeinschaft grant EI 672/5 to O. Eisen and a scholarship of the "Evangelisches Studienwerk e.V. Villigst" to R. Drews.

Edited by: J. L. Bamber

References

Bogorodsky, V., Bentley, C., and Gudmandsen, P.: Radioglaciology, D. Reidel Publishing Co., 1985.

Burger, W. and Burge, M. J.: Digital Image Processing – An Algorithmic Introduction using Java, Springer, 2008.

Dowdeswell, J. A. and Evans, S.: Investigations of the form and flow of ice sheets and glaciers using radio-echo sounding, Reports on Progress in Physics, 67, 1821–1861, 2004.

Drewry, D. J. and Meldrum, D. T.: Antarctic Airborne Radio Echo Sounding, 1977–78, Polar Record, 19, 267–273, 1978.

Eisen, O., Nixdorf, U., Wilhelms, F., and Miller, H.: Age estimates of isochronous reflection horizons by combining ice core, survey, and synthetic radar data, J. Geophys. Res. – solid earth, 109, B04106, doi:10.1029/2003JB002858, 2004.

Eisen, O., Wilhelms, F., Steinhage, D., and Schwander, J.: Improved method to determine radio-echo sounding reflector depths from ice-core profiles of permittivity and conductivity, J. Glaciol., 52(12), 299–310, doi:10.3189/172756506781828674, 2006.

Eisen, O., Hamann, I., Kipfstuhl, S., Steinhage, D., and Wilhelms, F.: Direct evidence for continuous radar reflector originating from changes in crystal-orientation fabric, The Cryosphere, 1, 1–10, http://www.the-cryosphere.net/1/1/2007/, 2007.

Faria, S. H., Hamann, I., Kipfstuhl, S., and Miller, H.: Is Antarctica like a birthday cake?, www.mis.mpg.de/preprints/2006/preprint2006_33.pdf, mPI für Mathematik in den Naturwissenschaften. Leipzig, Communication Preprint No. 33/06, 2006.

Fujita, S., Maeno, H., Uratsuka, S., Furukawa, T., Mae, S., Fujii, Y., and Watanabe, O.: Nature of radio echo layering in the Antarctic ice sheet detected by a two frequency experiment, J. Geophys. Res., 104, 13013–13024, 1999.

Hough, P. V. C. and Arbor, A.: Method and Means for Recognizing Complex Patterns, US Patent 3069654, 1960.

Jacobel, R. W. and Hodge, S. M.: Radar internal layers from the Greenland summit, Geophys. Res. Lett., 22, 587–590, 1995.

Jacobson, H. P. and Waddington, E. D.: Recumbent folding of divide arches in response to unsteady ice-divide migration, J. Glaciol., 51, 201–209, 2005.

Maccagnan, M. and Duval, P.: Electrical behaviour of Antarctic ice and radio echo layers in ice sheets, Ann. Glaciol., 3, 195–198, 1982.

MacGregor, J. A., Winebrenner, D. P., Conway, H., Matsuoka, K., Mayewski, P. A., and Clow, G. D.: Modeling englacial radar attenuation at Siple Dome, West Antarctica, using ice chemistry and temperature data, J. Geophys. Res., 112, F03008, doi:10.1029/2006JF000717, 2007.

Matsuoka, K., Furukawa, T., Fujita, S., Maeno, H., Uratsuka, S., Naruse, R., and Watanabe, O.: Crystal orientation fabrics within the Antarctic ice sheet revealed by a multipolarization plane and dual-frequency radar survey, Geophys. Res. Solid Earth, 108(B10), 2499, doi:10.1029/2003JB002425, 2003.

Nixdorf, U., Steinhage, D., Meyer, U., Hempel, L., Jenett, M., Wachs, P., and Miller, H.: The newly developed airborne radio-echo sounding system of the AWI as a glaciological tool, Ann. Glaciol., 29, 231–238, doi:10.3189/172756499781821346, 1999.

Ogilvy, J. A.: Theory of Wave Scattering from Random Rough Surfaces, Taylor & Francis, 1991.

Paren, J.: Correspondence, J. Glaciol., 27, 203–204, 1981.

Peters, M. E., Blankenship, D. D., and Morse, D. L.: Analysis techniques for coherent airborne radar sounding: Application to West Antarctic ice streams, J. Geophys. Res., 110, B06303, doi: 10.1029/2004JB003222, 2005.

Robin, G. Q. and Millar, D. M.: Flow of ice sheets in the vicinity of subglacial peaks, Ann. Glaciol., 3, 290–294, 1982.

Robin, G. Q., Drewry, D., and Meldrum, D.: International studies of ice sheet and bedrock, Philos. T. Roy. Soc. London, 279, 185–196, 1977.

Russell-Head, D. and Budd, W.: Ice-sheet flow properties derived from bore-hole shear measurements combined with ice-core studies, J. Glaciol., 27, 117–130, 1979.

Ruth, U., Barnola, J.-M., Beer, J., Bigler, M., Blunier, T., Castellano, E., Fischer, H., Fundel, F., Huybrechts, P., Kaufmann, P., Kipfstuhl, S., Lambrecht, A., Morganti, A., Oerter, H., Parrenin, F., Rybak, O., Severi, M., Udisti, R., Wilhelms, F., and Wolff, E.: "EDML1": a chronology for the EPICA deep ice core from Dronning Maud Land, Antarctica, over the last 150000 years, Clim. Past, 3, 475–484, 2007, http://www.clim-past.net/3/475/2007/.

Siegert, M. and Kwok, R.: Ice-sheet radar layering and the development of preferred crystal orientation fabrics between Lake Vostok and Ridge B, central East Antarctica, Earth Planet. Sci. Lett., 179, 227–235, 2000.

Svensson, A., Nielsen, S. W., Kipfstuhl, S., Johnsen, S. J., Steffensen, J. P., Bigler, M., Ruth, U., and Rüthlisberger, R.: Visual stratigraphy of the North Greenland Ice Core Project (NorthGRIP) ice core during the last glacial period, J. Geophys. Res., 110, D02108, doi:10.1029/2004JD005134, 2005.

Vaughan, D. G., Anderson, P. S., King, J. C., Mann, G. W., Mobbs, S. D., and Ladkin, R. S.: Imaging of firn isochrones across an Antarctic ice rise and implications for patterns of snow accumulation rate, J. Glaciol., 50(6), 413–418, doi:10.3189/172756504781829882, 2004.

Wang., B, Tian, G., Cui, X., and Zhang, X.: The internal COF features in Dome A of Antarctica revealed by multi-polarization-plane RES, Appl. Geophys., 5, 230–237, doi:10.1007/s11770-008-0029-z, 2008.

Weikusat, I., Kipfstuhl, S., Faria, S., Azuma, N., and Miyamot, A.: Subgrain boundaries and related microstructural features in EDML (Antarctica) deep ice core, J. Glaciol., 55, 461–472, 2009.

Wilhelms, F., Kipfstuhl, S., Miller, H., Heinloth, K., and Firestone, J.: Precise dielectric profiling of ice cores: A new device with improved guarding and its theory, J. Glaciol., 44, 171–174, 1998.

Wilson, C. J. L., Russell-Head, D., and Sim, H. M.: The application of an automated fabric analyzer system to the textural evolution of folded ice layers in shear zones, Ann. Glaciol., 37(11), 7–17, doi:10.3189/172756403781815401, 2003.

B. Anisotropy in radar data: Potential mechanisms and implications

Own contribution: Alignment of RES profile with strain net at the surface; Differentiation of birefringence and anisotropic reflections; Solution of the radiative transfer equation and corresponding numerical implementation; Comparison of RES and COF data; Literature review; Creation of all Figures; Writing of publication.
Current status: Submitted to Journal of Glaciology, suggested for publication subject to revisions.

Anisotropy in radar data: Potential mechanisms and implications

R. Drews, O. Eisen, D. Steinhage, I. Weikusat, S. Kipfstuhl

Alfred Wegener Institute for Polar and Marine Research, Postfach 12 01 61, 27515 Bremerhaven,Germany
E-mail: reinhard.drews@awi.de

ABSTRACT. Radar data collected at the Antarctic Plateau near the EPICA deep-drilling site in Dronning Maud Land varies systematically in backscattered power depending on the azimuth antenna orientation. Backscatter extrema are aligned with the principal directions of surface strain and change with depth: In the upper 900 m backscatter is strongest when the antennas are aligned in the direction of along-flow compression, below 900 m the maxima shift by 90° pointing towards the lateral flow dilatation. Backscatter mechanisms of elongated air bubbles and a vertically varying crystal orientation fabric (COF) are investigated using different scattering models in combination with ice-core data. We hypothesize that short-scale variations in COF are likely the primary mechanism for the observed anisotropy and the 900 m boundary between the two regimes is caused by ice with varying impurity content. Observations of this kind allow to deduce the COF along the vertical and are potentially also suited to map the transition between Holocene and glacial ice.

INTRODUCTION

In the light of upcoming airborne and potentially spaceborne polarimetric surveys with a p-band sounder (Dall, 2010), it is important to understand the polarization dependence of the backscattered signal and to successfully link it to physical properties within the ice. This delivers important input for ice-sheet modeling which enhances both, the correct interpretation of paleo ice-core records and the predictability of the ice sheets. We consider polarimetric radio-echo sounding (RES) data from the Antarctic Plateau, collected near the German summer station Kohnen in eastern Dronning Maud Land (DML), Antarctica. The data have been acquired with an airplane on the ground, measuring the effect of varying polarization with a circular profile and several cross profiles with different headings. The backscattered power is strongly related to the antenna orientation (i.e. incident polarisation) and backscatter patterns change with depth. We use physical properties gained from a nearby deep ice core to discuss mechanisms for anisotropic scattering. Particularly, we focus on ellipsoidal air bubbles and preferred crystal orientation fabric (COF). The ice core was drilled within the European Project for Ice Coring in Antarctica (EPICA) and is referred to as EDML. An overview of the scientific program at Kohnen station and major results from the EDML ice core is given by Oerter and others (2009).

In the upper 900 m the radar backscatter is strongest in the direction roughly perpendicular to a nearby ice divide situated in a flank-flow regime. The orientation of maximum backscatter changes by 90° in direction at approximately 900 m depth, coinciding with the bubble-air hydrate clathrate transition (under increasing pressure the air bubbles turn into a second solid phase of crystalline air hydrates, also called clathrates) and the transition from the Holocene to the last glacial period. The polarization dependence exhibits primarily a 180° symmetry. The aim of this study is to pinpoint a mechanism causing the anisotropy observed in the RES data, and to elucidate the capability of polarimetric RES surveys for the profiling of stress–strain regimes along the vertical.

RES measurements over ice sheets record reflections from dielectric non-uniformities. Density variations are dominant at shallow depths and alter the real and imaginary part of the complex dielectric constant ($\varepsilon = \varepsilon' - i\varepsilon''$). Changes in electrical conductivity influence the imaginary part and become unmasked from density changes at intermediate depths and below. Both effects often appear as lateral coherent internal reflection horizons in the radar data. The dependence of the backscattered signal on the polarization of the incoming wave has been noted already in the early days of radio-glaciology (for an overview see e.g. Doake (1981)). The backscattered signal appeared elliptically polarized, and showed a varying amplitude, depending on the relative azimuth orientation of receiving and transmitting antenna. Using solutions of the Maxwell equations in layered media with a tensorial form for the dielectric properties (Hargreaves, 1977, 1978; Doake, 1981), this could be explained in terms of birefringence and anisotropic reflection coefficients. Hargreaves (1978) proposed as a mechanism for the birefringence the dielectric anisotropy of the single ice crystal in combination with preferred COF. The dielectric anisotropy has been confirmed in subsequent studies (Fujita and others, 1993; Matsuoka and others, 1997; Fujita and others, 2000), which found a difference in the real part of the dielectric constant of $\varepsilon'_{\parallel} - \varepsilon'_{\perp} \approx 0.035$ for the components parallel and perpendicular to the crystal's c-axis. The temperature and frequency dependence is considered to be small.

Numerous multi-frequency and multi-polarization measurements have been performed since then to infer various COF-types from RES measurements (Fujita and Mae, 1993; Liu and others, 1994; Fujita and others, 1999; Siegert and Kwok,

2000; Doake and others, 2002; Fujita and others, 2003; Matsuoka and others, 2003, 2004; Fujita and others, 2006; Eisen and others, 2007; Wang, 2008; Dall, 2010; Kravchenko and others, 2011). Variations in density, electrical conductivity, and changing COF are by now accepted to be the major mechanisms for RES horizons. Nevertheless, predominantly due to a lack of ice-core data, uncertainties about the nature of the anisotropic reflection mechanisms still remain. Particularly effects from volume scattering have so far mostly been neglected. Independent of the specific mechanism for the polarization dependence, the theory of birefringence and anisotropic reflections is well understood.

In birefringent media, the refractive indices depend on the incoming polarization. The solution of the corresponding wave equation results in two characteristic waves with different polarization and wave speed. In uniaxial media (i.e. two out of three principal components of the dielectric tensor are equal) an ordinary wave—with the Poynting vector parallel to the wave vector—and an extraordinary wave—with the Poynting vector non-parallel to the wave vector—superimpose. In biaxial media (i.e. all three principal components of the dielectric tensor differ) two extraordinary waves are generated. Typical polarimetric experiments on ice emit an electromagnetic pulse and record amplitude variations of the reflected signal as a function of the azimuth antenna orientation. In this study we only discuss the co-polarized case, which means that the emitting and receiving antenna remain parallel. The azimuth dependency of the backscattered power is a function of both, anisotropic scattering and birefringence. Both effects have different symmetries. In birefringence the amplitude variation is caused by the superposition of the two characteristic waves with a phase shift at the surface. The phase shift depends, amongst others, on the two-way penetration length and the integrated difference in dielectric components perpendicular to the propagation direction. The latter causes a 90° periodicity since this difference remains the same for a 90° rotation of the coordinate system. Anisotropic scattering, on the other hand, only has the smallest possible periodicity of 180°, where the corresponding antenna orientations are indistinguishable. Apart from some special cases (e.g. a fully random COF or a perfect single maximum COF aligned with the direction of propagation), polar ice is generally always birefringent. Anisotropic scattering requires anisotropic changes in the dielectric properties for example due to a vertically varying COF, aligned and non-spherical inclusions or a preferred roughness at the interfaces of internal layers. Birefringence and anisotropic scattering are interrelated, and when combined lead to a complex amplitude variation with changing antenna orientation. This can be simulated for the different cases with matrix-based models (Doake, 1981; Fujita and others, 2006; Matsuoka and others, 2009). However, sometimes either a 90° or a 180° periodicity in backscattered power is dominant, which allows to solely focus either on birefringence or anisotropic scattering, respectively.

Site characteristics and previous studies

The location of the circular RES profile (Figure 1) is in eastern Dronning Maud Land on the Antarctic Plateau, approximately 500 m downstream of the deep-drilling site for the EDML ice core. The topography is smooth, with gradients

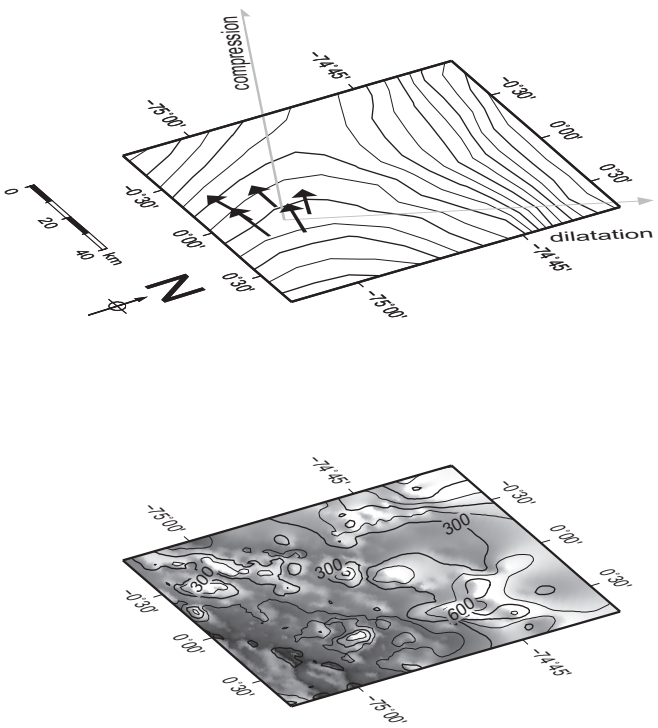

Fig. 1. Map of surface elevation, ice flow (Wesche and others, 2007), and bedrock topography (Steinhage and others, 1999).

of a few meters per kilometer. Ice thickness at the drill site is 2774 m and local surface velocities average to less than 1 m/a. The drill site is located near a triple junction, close to one arm of the forking ice-divide. The entire setting is in a flank-flow regime.

During pre-site surveys the bedrock topography was mapped with a dense grid of RES profiles (Steinhage and others, 2001). After the ice core was drilled, Eisen and others (2006) used data from dielectric profiling and a forward model to link several internal reflectors in the RES data to prominent changes in electrical conductivity. Using the same circular profile as presented here, a subsequent study (Eisen and others, 2007) showed that another localized reflector at 2035 m depth is caused by a drastic change in COF which is observed in ice-core data. Linescan images from the ice core visualize the stratigraphy (on a sub-cm scale), which appears increasingly disturbed with larger depths. This suggests that the disappearance of internal reflection horizons below about 2100 m depth may be caused by stratigraphic disturbances on a larger scale (Drews and others, 2009).

Wesche and others (2007) derived an elevation model as well as surface velocities with corresponding stress–strain rates, based on a pentagon-shaped stake network. The flow regime is characterized by along-flow compression and lateral dilatation. The maximal (minimal) principal strain-rate component has a magnitude of $-1.85 \cdot 10^{-4}\mathrm{a}^{-1}$ ($2.32 \cdot 10^{-5}\mathrm{a}^{-1}$) pointing towards 24°N (114°N).

Ueltzhöffer and others (2010) investigated size, number and shape of the air bubbles in vertical cuts from the ice core. The transition of air bubbles into clathrates starts at about 700 m and progresses rapidly below 800 m. Typical effective bubble

radii cluster around 0.1 mm decreasing with depth, similar to the volume fraction which ranges from ∼0.004 (200 m depth) to ∼ 0.001 (900 m depth). In vertical cuts, it was found that the bubbles are elongated with eccentricities varying from 0.3–0.8. Due to the lack of continuous azimuth control of the ice core, no correlation with ice flow is possible. Bendel (2009) did some further analysis on vertical cuts and found that number density and aspect ratio vary on cm-scales, in particular for glacial ice, but also at shallower depths.

COF studies on horizontal and vertical thin sections exploit the birefringent nature of the single crystals by using crossed polarizes to determine the c-axes orientation. The orientation distribution is often visualized using Schmidt diagrams which project the piercing point of the c-axes through a hemisphere onto a plane. Fitting an ellipsoid results in three Eigenvalues (λ_1,λ_2,λ_3) for the principal axes which describe the orientation distribution. More details of the fabric measurements and the results will be presented later.

DATA ACQUISITION AND OBSERVATION

The radar data was acquired in 2003 with a RES system designed for the airborne sounding of ice sheets (Nixdorf and others, 1999). The short backfire antennas emit bursts with a pulse length of 60 or 600 ns at a center frequency of 150 MHz. The polarization of the electric field is in the vertical plane, parallel to the airplane's heading. For this study the short pulse was used which increases the vertical resolution, at the cost of total penetration depth. Since the antennas are fixed on the wings, the azimuth orientation cannot be changed. To investigate the response with varying incoming polarization, the airplane (a Dornier 228) slid on the ground in a circular profile. In this co-polarized mode, the emitted and recorded polarization planes are always parallel and rotate continuously around the vertical while the airplane slides along the circle. Traveltime-to-depth conversion was done with the interpolation of tie-points from ice-core dielectric profiling data with RES horizons (Eisen and others, 2006). The angle *heading* is defined as the heading angle of the aircraft in respect to true North. It depicts the angle of the polarization plane.

The backscattered power along the circular profile is displayed for the depth interval of 200–1400 m in Figure 2(a). The diameter of the circle is about 100 m and the profile consists of 170 traces with an average trace spacing of 1.8 m. The stacking of each shot is ten-fold and no further processing has been applied. The dominant feature is the overlying sinusoidal variation with changing azimuth orientation of the two antennas. The signal has a clear 180° periodicity and splits in two parts along the vertical: Starting at about 300–400 m and reaching down to 900 m depth the maxima develop at a heading angle of $\sim 206^\circ N/26^\circ N$ (note that he heading is tangential to the circle). Below 900 m the maxima shift by 90°, and occur at a heading of ∼116°N/296°N. We refer to the two depth intervals as anisotropic reflections zones (ARZ) 1 and 2, respectively. The different directions are exemplified in Figure 2(b). The strain-ellipsoid marks the directions of compression and dilatation as given by Wesche and others (2007). The directions of minimal and maximal backscatter correspond well with the principal axes of the strain ellipsoid.

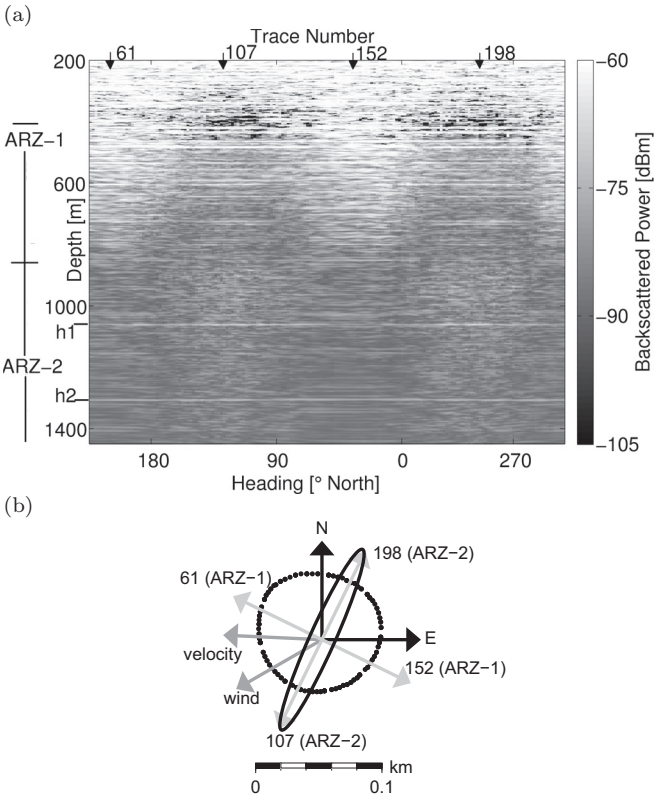

Fig. 2. (a) The backscattered power of the circular profile varies sinusoidally. The two horizontal lines marked with h1 and h2 are internal reflection horizons linked to prominent peaks in dielectric profiling data by Eisen and others (2006). **(b)** Top view of (a) marking the main flow direction of ice together with main wind direction as well as the extrema in backscatter on the circle for the different zones. The strain ellipsoid gives the directions for the principal components of compression and dilatation which correspond well with the characteristics of the RES profile.

MECHANISMS FOR POLARIZATION DEPENDENT BACKSCATTER

As described above, the polarization dependence of the backscattered radar signal can principally be induced by birefringence and by anisotropic scattering. Birefringence is a direct consequence of the ice crystal's dielectric anisotropy. Anisotropic scattering requires anisotropic changes in the dielectric properties. The two effects can be distinguished on the basis of symmetry.

To visualize the symmetry better, vertically averaged intervals of 200 m are displayed in Figure 3. Due to absorption and spherical spreading, the averages within the individual intervals are biased towards shallower values, but this does not affect the symmetry. The 180° periodicity in backscattered power appears overlaid by a 90° pattern resulting in two small local maxima between the main maxima mentioned above. From these two symmetries we deduce that both, birefringence and anisotropic scattering influence the azimuth dependency of the backscattered power. However, anisotropic

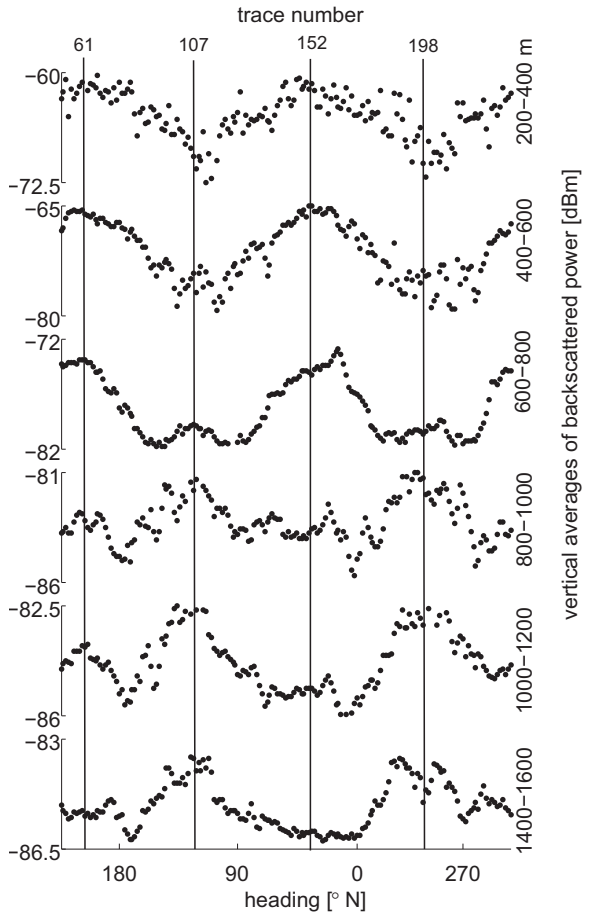

Fig. 3. Vertical averages of backscattered power in 200 m intervals from 200 m to 1400 m depth plotted along heading (bottom-axis) and trace number (top-axis). The main maxima with the 180° periodicity are partly interweaved with small maxima with a 90° offset.

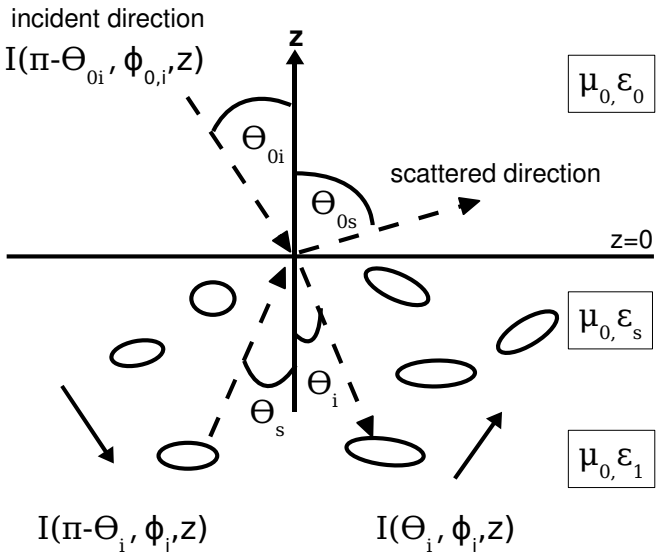

Fig. 4. Sketch for the model of discreet ellipsoidal scatterer, modified after Figure 1 in Tsang and others (1981).

scattering is the dominant effect due to the larger amplitudes of the 180° cycle. The interweaved smaller maxima have a 90° offset, so both effects appear to have similar principal axes which do not change noticeably with increasing depth. Due to the dominance of the 180° periodicity, we focus on potential anisotropic scattering mechanisms. The 900 m boundary, where the maxima in backscatter shift, is hereby particularly intriguing, and has also been observed in other studies: Fujita and Mae (1993) compared data from a 179 MHz ground-based radar to fabric measurements from the ice core at Mizuho Station, Antarctica. They observed high amplitudes in the upper part of the ice column with the antennas being parallel to the flow-line and lower amplitudes for the perpendicular arrangement. Changing at 800 m depths the effect appears in the reversed order. The Mizuho ice-core does not reach the bedrock and ends at around 700 m. This depth is above both, the bubble-clathrate transition (Wataru and Takeo, 2004) and the transition from the Holocence into the last glacial period (Nakawo and others, 1989) at this site. Using different frequencies, pulse lengths and antenna orientations in the same study area, Fujita and others (2003) confirmed the previous findings of changing anisotropy with depth. They proposed as mechanisms for the upper anisotropy a varying cluster strength for the girdle-type fabric, and for the lower anisotropy a layered strata composed of girdle- and single-pole transitions. Using similar techniques Matsuoka and others (2003) also observed the two different zones along a ground-based traverse from Dome Fuji, Antarctica, towards the Shirase glacier drainage basin. For the lower anisotropy they support the idea of transitions from girdle to single-pole COF as the primary mechanism. An airborne survey (Matsuoka and others, 2004) identified high scattering in the deeper layers of convergent and compressional ice-flow regimes when the polarization was perpendicular to the flow direction. Using a matrix model, Fujita and others (2006) discriminate between birefringence and anisotropic scattering at Mizuho and Dome Fuji. In both cases aligned COF and changes thereof were assumed as the main mechanism for the observed polarization dependence. Based on the previous studies the scenario for the two ARZs near Mizuho station is:

(1) One axis of the dielectric tensor's principal component system is close to the vertical. A varying cluster strength of a girdle-type COF translates into a variation of the first Eigenvalue in the horizontal plane. This increases the backscatter for an incoming polarization parallel to the corresponding principal axes. The second Eigenvalue in the horizontal remains stable.

(2) At larger depths, girdle to single-pole transitions change the vertical, and the second horizontal principal component. The latter increases backscatter perpendicular to the direction observed in the upper interval.

If only one Eigenvalue varies in the horizontal, a rotation of the principal axis with increasing depth may result in a similar pattern. The problem with the hypotheses is, that only a single study (Eisen and others, 2007) directly linked (an exceptional large) short-scale variation in COF from ice-core data to a reflector in RES data in the lower part of the ice sheet. For the middle to upper depths, vertically higher re-

solved COF data in conjunction with polarimetric RES measurements are needed to confirm this idea. Therefore, before discussing the effect of variable COF at the EDML drill site, we also consider other possibilities like anisotropic inclusions (ellipsoidal air bubbles) or layer boundaries with a directional roughness.

It can be speculated, that patterns which arise on the surface from preferred wind directions are advected to larger depths while preserving their directionality thus causing anisotropic interfaces between different layers. However, deep ice seems to have no memory to structures caused by the deposition at the surface. First analyses of the density and microstructure of firn indicate that impurities significantly influence, or maybe even control the pore-space structure in deeper firn. Characteristic surface features like sastrugis or snow dunes seem not to be imprinted in deep ice as at the firn–ice transition the pore-space structure is correlated with the concentration of impurities. In any case, it seems reasonable to assume that in the depth interval of interest, a preferred roughness will decrease with increasing depths. The sinusoidal pattern observed in Figure 2 starts at about 300–400 m and sharpens its directional dependence with increasing depth. Although we cannot fully exclude that wind-induced anisotropy is also presented in the upper 0–300 m, we argue on the basis of the vertical gradient that it does not play a major role for the anisotropy observed in the depth interval of 300–2200 m (2200 m being the detection limit of the short pulse). Moreover, the mean wind-direction originates from 60° North (Reijmer, 2001) which does not coincide with any extrema in backscatter (Figure 2(b)).

The effect of enclosed—and possibly distorted—air bubbles on the radar backscatter has been discussed in several studies. Using a spherical shape, a frequency of 35 MHz, the dipole approximation and a volume-type radar equation, Robin and others (1969) suggest that air bubbles may have a small, but noticeable effect on the backscattered power. Discussing birefringence, Hargreaves (1978) estimates the effect from elongated air bubbles as too small to explain experimental results. Ackley and Keliher (1979) used data from the Cape Folger ice core near the coast of East Antarctica, and estimated the effect from the elongated air bubbles to be larger than the one from COF variations. They observed a layered strata where the bubble elongation corresponded to density fluctuations suggesting a link to deformation. Alley and Fitzpatrick (1999) analytically described the bubble elongation as an interplay between strain induced deformation and diffusive restoration. Very elongated bubbles with the long half axis being several times the short half axis are seen mostly in ice cores near the coast within high-shear regimes. The observed eccentricities in the EDML ice core are much smaller. Fujita and others (2000) use new COF data and place the effect from air bubbles on the backscatter lower than the dominating density, electrical conductivity and COF mechanisms.

Three indications motivate us to investigate the effect of air bubbles on the backscatter more closely: (1) Ueltzhöffer and others (2010) showed in vertical cuts that air bubbles at the EDML drill site are partly complanate. This means that bubbles can maintain an ellipsoidal shape within the ice matrix, and there is reason to believe that they might be deformed in the horizontal plane as well, (2) the coincidence of the clathrate transition zone with the transition between the ARZ 1 and the ARZ 2 and (3) the strain ellipsoid in Figure 2(b) indicates the orientation of deformed bubbles (if surface strain is considered as the exclusive mechanism for bubble deformation). The direction of the long half-axis coincides with the direction of maximum backscatter. In the following section we apply an analytical volume scattering model to estimate the effect of discrete ellipsoidal scatterers in the ice matrix. In the subsequent section, COF data from the EDML ice core and the corresponding effect on scattering will be discussed.

Volume scattering model for a half space with discrete ellipsoids

Model setup

The analysis presented here is based on the publication of Tsang and others (1981). Volume scattering models of this kind have primarily been developed for satellite applications. We adapt the model for our purpose by changing the boundary conditions and focusing on a nadir looking case. The geometry is shown in Figure 4. It includes two half spaces 0 and 1, with permittivity ε_0 for air and ε_1 for ice, separated at the boundary z=0. The lower half space is filled with ellipsoids with permittivity ε_s. The approach is based on the radiative transfer theory, which deals with intensities rather than the electromagnetic fields (for a textbook introduction see for example Tsang and others (2000)). The governing equation is:

$$\cos(\theta)\frac{d\mathbf{I}}{dz} = -\underline{\mathbf{k}}_e\mathbf{I}(\theta,\phi,z) + \int d\Omega'\underline{\mathbf{P}}(\theta,\phi,\theta',\phi')\mathbf{I}(\theta,\phi,z) \tag{1}$$

where 4×1 vectors are bold and 4×4 matrices are bold and underlined. The modified Stokes vectors

$$\mathbf{I} = [\mathrm{I}_h, \mathrm{I}_v, 2\mathrm{Re}(E_v E_h^*), 2\mathrm{Im}(E_v E_h^*)]$$

depict the specific intensities of the electromagnetic field E where [1,0,0,0] corresponds to fully vertically polarized (v) and [0,1,0,0] to fully horizontally polarized (h) case. Although for nadir incidence the distinction of vertical and horizontal becomes obsolete (see discussion by Doake and others (2002)), we keep the notation to remain consistent with other models. The indices v and h thus represent polarization types corresponding to orthogonal antenna orientations in the horizontal plane. The changes of the incoming intensity along depth are caused by extinction and scattering. The extinction is described with the extinction matrix $\underline{\mathbf{k}}_e = \underline{\mathbf{k}}_a + \underline{\mathbf{k}}_s$ as a sum of absorption and scattering away from the receiver. We consider absorption to be isotropic. The phase matrix $\underline{\mathbf{P}}$ operates for scattering from direction θ', ϕ' into the direction θ, ϕ. The integration is over the solid angle $d\Omega' = \sin(\theta')d\theta' d\phi'$. The angles are displayed in Figure 4, with ϕ being the azimuthal angle in the horizontal plane.

We first treat the general case of oblique incidence and consider the backscattering for a nadir looking geometry as a special case. The individual elements of $\underline{\mathbf{P}}$ are calculated in the Rayleigh approximation using scattering dyads. The ellipsoids have the three half axes a,b,and c. The special case of spherical inclusions results in a diagonal phase matrix, ellipsoidal inclusions lead to off-diagonal elements which cause

mixing of vertical and horizontal components. Each element is averaged over a common orientation density distribution $\psi(\alpha, \beta, \gamma, \Delta\alpha, \Delta\beta, \Delta\gamma)$ which quantifies the degree of alignment for the inclusions. The position of the individual bubbles within the ice matrix is assumed to be random. The Euler angles α, β, γ define the orientation of the bubbles. The rotation around the z-axis corresponds to the angle α, for a definition of all angles see Figure 2 in Tsang and others (1981). The half axes a and b are in the horizontal plane when $\alpha = \beta = \gamma = 0$. For simplicity, ψ is assumed to be box-like in all three angles. The box width is defined with the corresponding Δ-values. The fully aligned and the fully random case for α correspond to $\Delta\alpha = 0^\circ$ and $\Delta\alpha = 90^\circ$, respectively.

The integro-differential equation (1) can be solved using perturbation theory. The different terms of the perturbation series correspond to the different instances of multiple scattering. For backscattering, the incoming direction (index i) equals the scattered direction (index s). In terms of the normalized wave vectors this means $\hat{\mathbf{k}}_i = -\hat{\mathbf{k}}_s$ with $k = 2\pi f\sqrt{\mu_0\varepsilon}$ and f being the frequency. The backscattering coefficient is defined as:

$$\sigma_{\gamma\delta}(\hat{k}_i, -\hat{k}_i) = 4\pi\cos(\theta_{oi})\frac{I_{\gamma s}}{I_{\delta i}} \qquad (2)$$

where the indices γ, δ are place holders for vertical and horizontal polarizations. The solution is outlined in the Appendix. The first-order approximation, marked with superscript (1), corresponds to independent scattering. For the nadir looking geometry ($\theta_{oi} = \theta_i = 0; \quad \pi + \phi_i = \phi_{oi} = 0$) we get:

$$\begin{aligned}
\sigma_{vv}^{(1)} &= 2\pi t_{v10}^2(\theta_i = 0)\frac{\varepsilon_0}{\varepsilon_1}\frac{P_{11}(0,\pi,\pi,0)}{k_v},\\
\sigma_{hh}^{(1)} &= 2\pi t_{h10}^2(\theta_i = 0)\frac{\varepsilon_0}{\varepsilon_1}\frac{P_{22}(0,\pi,\pi,0)}{k_h},\\
\sigma_{hv}^{(1)} &= 2\pi t_{v10}(\theta_i = 0)t_{h01}(\theta_i = 0)\frac{\varepsilon_0}{\varepsilon_1}\frac{P_{12}(0,\pi,\pi,0)}{k_h},\\
\sigma_{vh}^{(1)} &= 2\pi t_{h10}(\theta_i = 0)t_{v01}(\theta_i = 0)\frac{\varepsilon_0}{\varepsilon_1}\frac{P_{21}(0,\pi,\pi,0)}{k_v}.
\end{aligned}$$

Via the calculations of the phase matrix elements, the scattering coefficient is a function of several parameters (e.g. frequency, volume fraction, incidence angles, eccentricities, alignment of bubbles). The transmission between air (index 0) and ice (index 1) for the different polarizations is labeled with the power transmission coefficients t_{vij} and t_{hij} with i, j=0,1. Since the air–ice interface is assumed to be isotropic they play a minor role. The variables k_v and k_h are the first two diagonal elements of the extinction matrix $\underline{\mathbf{k}}_e$. Extinction includes off-angle scattering and absorption in ice. The latter is considered with the complex part of the permittivity: $\varepsilon_1'' = \sigma/(2\pi f\varepsilon_0)$.

We also calculated a second order solution (see Appendix), but apart from depolarization effects this is of minor importance for the parameters used here. The analytical solution for higher-order terms is tedious and a fully numerical approach or other approximations are needed if higher order terms are desired.

Model Outcomes

The polarization dependence of the backscatter coefficient is simulated with keeping the incoming Stokes vector fixed, and rotating the bubbles in the horizontal by changing the values for the Euler angle α. The sinusoidal variation is shown in Figure 5(a) for the case of fully aligned ellipsoids ($\Delta\alpha = \Delta\beta = \Delta\gamma = 0$). The absolute value of the phase matrix elements is mainly dependent on the ratio of bubble volume to wavelength. The magnitude of the backscatter coefficient is additionally influenced by absorption. For the examples presented here, we assume an average conductivity of 15μ S/m, as determined via dielectric profiling measurements (Wilhelms and others, 1998; Wilhelms, 2000) from the EDML ice core, and scale it to the center frequency of the radar system. The difference of vertical and horizontal backscatter coefficients depends on the bubble eccentricity and the degree of alignment determined by the orientation density function.

The effect of order and disorder in bubble alignment is shown in Figure 5(b). The Euler angles β and γ are kept fully aligned whereas the disorder in α increases with increasing $\Delta\alpha$. For the fully random case ($\Delta\alpha = 90^\circ$) the polarization dependence ceases.

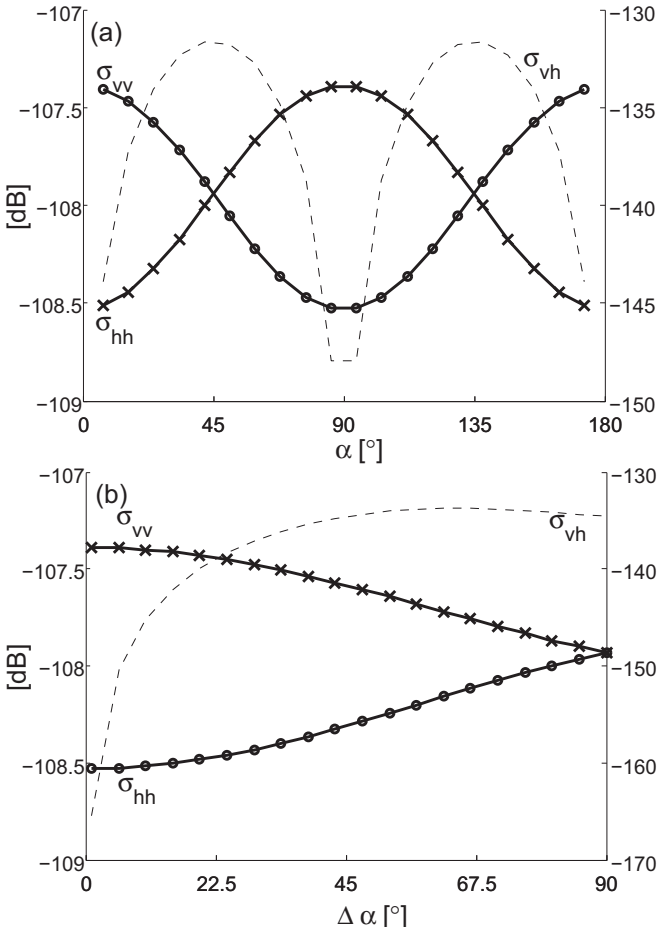

Fig. 5. Model outcomes for the backscatter coefficients (hh, vv with solid lines, hv with dashed lines). **(a)** α rotates in the horizontal plane while β and γ remain fixed. No orientation density distribution is applied which corresponds to the fully aligned case ($\Delta\alpha = \Delta\beta = \Delta\gamma = 0$). **(b)** Increasing disorder is simulated for $\alpha = \beta = \gamma = 0$ and increasing $\Delta\alpha$. Parameters are for (a) and (b) are $\varepsilon_1 = (3.2 + 0.0018i)\varepsilon_0$, $\varepsilon_s = \varepsilon_0$, $\Theta_{oi} = \phi_{oi} = 0$, v=0.0001 (volume fraction), a=0.15 mm, b=c=0.1 mm.

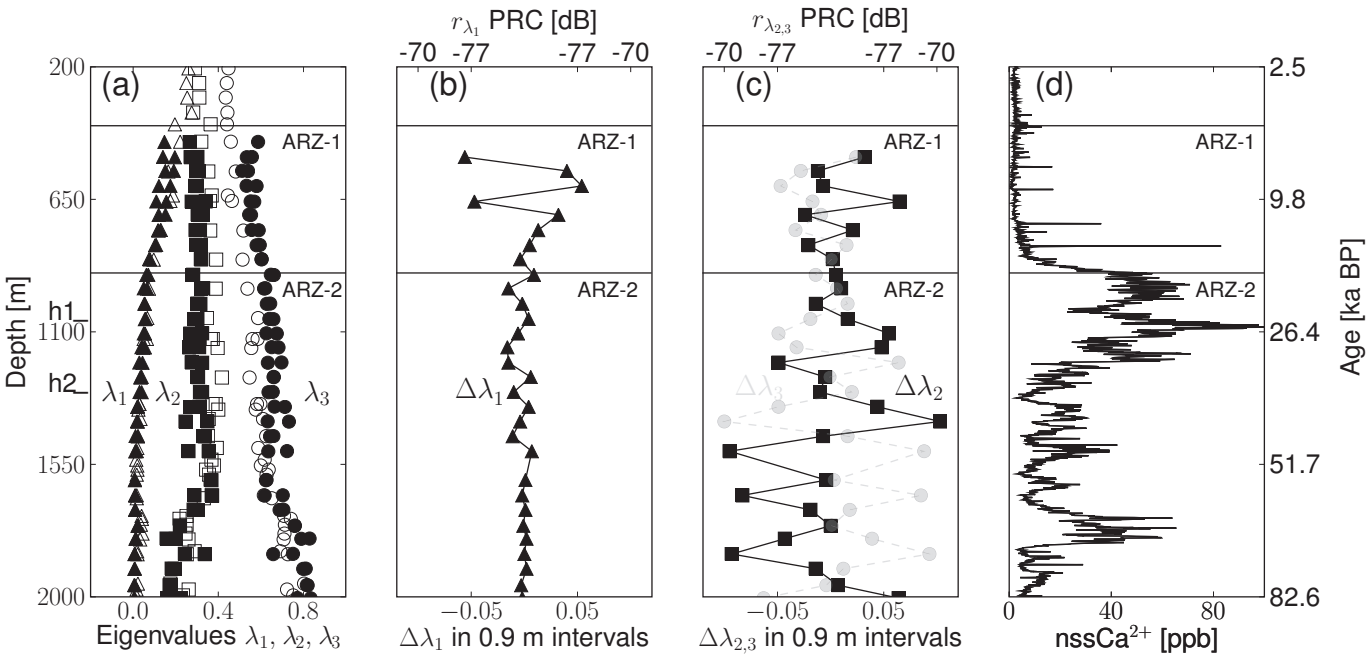

Fig. 6. (a) Crystal orientation fabric data from the EDML ice core in terms of Eigenvalues (λ_1=triangle, λ_2=square, λ_3=circle; filled symbols for horizontal cuts, open symbols for vertical cuts). The depths of two prominent internal reflections horizons in the radar data are marked with h1 and h1. The difference $\Delta\lambda_i$ for horizontal cuts measured in 0.9 m intervals is displayed in **(b)** and **(c)**. The top axis mark the corresponding power reflection coefficients (PRCs) as calculated from a two-layer approximation given in equation (3). Changes parallel to the propagation direction (i.e. changes in λ_3) do not influence the backscatter; **(d)** Non sea salt (nss) Ca^{2+}concentration as published by Fischer and others (2007) serves as a proxy for impurities within the ice which decrease in concentration during the transition from the last glacial into the Holocene (700–900 m depth).

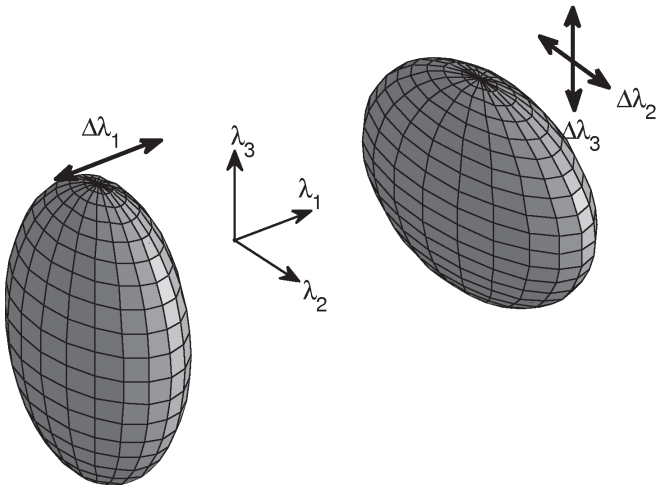

Fig. 7. Illustration of changes in principal components for the dielectric tensor for ARZ 1 (left) and ARZ 2 (right).

Changing crystal orientation fabric

COF data of the EDML ice core have been measured in 2005 in a –20°C cold room using an automatic fabric analyzer system (Wilson and others, 2003). The EDML core has been drilled between 2001 and 2004 and was stored at –30°C after transportation to the storage facilities in Bremerhaven. Thin sections have been prepared according to standard procedures using a microtome from samples cut horizontally (ca. $0.5 \cdot 50 \cdot 50$ mm^3) and vertically (ca. $0.5 \cdot 50 \cdot 100$ mm^3) to the core axis. The automatic fabric analyzer enables complete measurements of these samples within 30 minutes. This is possible due to the fully automatization of a polarization microscope principle (Wilen and others, 2003) with a CCD camera acquiring images of the thin section between rotating crossed polarizers from nine different viewing angles. Eigenvalues obtained from vertical and horizontal sections should in theory be alike, but in the data they vary systematically in λ_2 and λ_3. This observation is most probably due to filtering of the data with respect to their quality given by the accuracy of c-axis determination from the necessary nine different viewing angles through the polarizers. This quality filtering introduces an artifact of our instrument, caused by difficulties of accurate c-axis determination in special orientations (e.g. the c-axes being parallel to the section plane). As with a non-random, but preferred COF such special orientations occur in different frequencies when the cutting direction of samples is changed. The quality filtering produces slightly different distributions reflected in different, systematically changing Eigenvalues for vertical and horizontal cuts. This is displayed in Figure 6(a). However, the impact of these local effects on the statistics (typically 60–600 grains per thin section) has been checked by repeated measurements with changing sample orientations and was shown to be negligible. Less than 10% of the grains showed these effects. The estimated uncertainty for the magnitude of the individual Eigenvalues is 0.1, but relative changes of Eigenvalues determined with the same methodology can be treated with higher confidence.

The evolution of COF in EDML shows a gradual transition from randomly oriented c-axes in shallower depths (down to ca. 450 m) to a broad girdle fabric (ca. 450–1700 m depth). The Eigenvalues in Figure 6(a) reflect this transition by evolving from three similar values into three separated value levels ($\lambda_1 < \lambda_2 < \lambda_3$) due to evolving influence of uni-axial extension deformation caused by the lateral flow dilatation. A narrowing of the girdle fabric follows (1700 m down to ca. 2000 m depth) indicated by converging λ_2 towards λ_1 which is possibly caused by a destabilization of the horizontal uni-axial extension and a transition to the next deformation geometry (bed-parallel simple shear).

Fabric data is measured at the coarsest in 50 m intervals using vertical cuts. Starting at 450 m depth, the measurements are complemented with two horizontal cuts within 0.9 m distance every 50 m. We use this dataset here as a proxy for short-scale variations in COF. The difference $\Delta\lambda_i$ (i=1,2,3) within the 0.9 m interval for the three Eigenvalues is plotted for increasing depth in Figure 6(b) and (c). In the range of ARZ 1 the variation of the smallest Eigenvalue λ_1 is noticeable and fades towards larger depths. This corresponds to the previously discussed variation in girdle strength for the ARZ 1. The opposite behavior becomes apparent for the two other Eigenvalues λ_2 and λ_3, which eventually swing in anti-phase parallel to ARZ 2's appearance in the radar data. This implies the tendency of girdle to single-pole transitions in the ARZ 2. An illustration of the corresponding ellipsoid variation is illustrated in Figure 7. The relative changes of the Eigenvalues considered here are close to the detection limit of the fabric measurements. However, at least at larger depths the general tendency appears systematic and seems to fit to the effects seen in the radar data as discussed in the next section. We therefore carry on, but bear in mind that more accurate (and preferably vertically higher resolved) COF data is needed to solidify the later conclusions drawn from this dataset with respect to the interaction with radar waves.

We use a layer approximation to estimate the effect on the backscatter. A premise is that the changes in COF as observed in the ice core are laterally coherent on the scale of the first few Fresnel zones. For larger depths, this has been shown by Eisen and others (2007), who linked a single RES reflector to changes in COF and traced it laterally for a few kilometers. For the intermediate depths this cannot easily be done as changes in COF are less distinct and vertically lower resolved. However, the evolution of COF is related to strain rates, and there are also indications that a varying impurity content influences the crystal size and thus the formation of COF (Thorsteinsson, 1996). Both effects act on a larger scale, favouring a laterally coherent stratification of COF. Two prominent internal reflections horizons (h1 and h2) are visible at 1068 m and 1312 m depth in Figure 2 (a). Eisen and others (2006) linked both of them to isotropic reflectors caused by changes in electrical conductivity and we would expect—if at all—brightness variation in the polarimetric data with the symmetry of birefringence. The internal horizon h2 appears independent on the incoming polarization whereas h1 shows some brightness variations with minima and maxima coinciding with the characteristics of the ARZ 2. Not enough data is at hand to fully explain this, but it may be an example that a varying impurity content in ice imprints the formation of crystal texture: Changes in electrical conductivity may be accompanied by laterally coherent changes in COF, leading to a polarization dependence of the corresponding reflection horizon. It seems that the layer approximation is certainly simplified but not unrealistic.

In order to characterize the dielectric properties of the individual layers we need to know the principal directions of the individual Eigenvalues. This is partly impossible, since no continuous azimuth control in the horizontal plane is available for the fabric data. However, the third Eigenvector seems to be in the vertical, which becomes apparent in some Schmidt diagrams by an accumulation of points in the center of the girdle. We therefore tentatively assume that λ_3 is pointing along the z-direction (see also the discussion in Eisen and others (2007)). The directions of λ_1 and λ_2 remain undefined in the horizontal plane, but based on the vertical alignment of minima and maxima in Figure 3 we assume that they do not change with increasing depth.

Fujita and others (2006) give a method on how to incorporate the Eigenvalues into the dielectric tensor. Power reflection coefficients (PRCs) determine the ratio of incoming and scattered fields. They can be calculated in a planar two-layer approximation for changes in the permittivity ε' as illustrated by Paren (1981). Along the principal axes of λ_i, (i=1,2,3), the PRC is given by:

$$r_{\lambda_i, z1-z2} = \left(\frac{(\lambda_{i,z1} - \lambda_{i,z2})(\varepsilon'_{\parallel} - \varepsilon'_{\perp})}{4\varepsilon'} \right)^2 . \qquad (3)$$

The values of r resulting from changes in Eigenvalues in the 0.9 m intervals are displayed in the top-axis of the Figures 6(b) and (c).

For nadir incidence the polarization of the electromagnetic wave is in the vertical plane. Therefore changes in the third Eigenvector do not contribute to the scattering process in this approximation. The stronger variation of λ_1 in the ARZ 1 fades in the ARZ 2 and simultaneously the variation of λ_2 increases. This directly translates into the polarization dependence of the PRCs. In the ARZ 1, backscatter is largest when the polarization is parallel to the principal direction of λ_1, vice versa in the ARZ 2 the maxima in backscatter is shifted by 90° and aligns with the principal direction of λ_2. The differences in the corresponding PRCs reach up to 10 dB.

Discussing the effects of ellipsoidal air bubbles and changing COF

We estimated the effect of ellipsoidal air bubbles with a volume scattering model, and the effect of changing COF with reflections from a stratified medium. For the ARZ 1, it is not straightforward to distinguish the effect of elongated bubbles and varying cluster strength in COF in terms of their orientation since they most likely operate in similar directions. The deformation of air bubbles in the horizontal plane, as expected from strain measurements on the surface, is indicated with the strain ellipsoid in Figure 2(b). The direction of the long half-axis is almost parallel to the polarization plane with maximum backscatter in the ARZ 1. The azimuth angle of the COF measurements is not constraint, however, the study of Eisen and others (2007) identified the girdle at around 2025 m depth to be in the vertical plane parallel to the nearby ice

divide. A recent modelling study for COF evolution at this site by Bargmann and others (in press) confirms this result in a sense that the girdle is aligned with the principal axes of the strain ellipsoid. One of the axis is near-parallel to the ice divide. It is therefore reasonable to assume that both effects of elongated air bubbles and a varying cluster strength in COF superimpose and are aligned with the strain regime on the surface.

Both, the estimation of scattering coefficients and PRCs have their shortcomings due to the applied simplifications. The volume scattering model neglects characteristics of the finite radar pulse, as only the center frequency and scattering contributions from incoming nadir incidence are taken into account. The system's bandwidth is about 20 MHz and an interplay with higher frequency components already translates into a few decibels since the frequency enters the equations with a power of four. The beam widening with increasing traveltime may also give rise to scattering components with non-nadir incidence. This generally increases the polarization dependence. The absolute value for the scattering coefficient also heavily depends on the absorption which dominates the extinction since the phase matrix elements are small. Potential effects of anisotropic absorption, or a non-diagonal extinction matrix have been neglected. The bubbles were assumed to be randomly distributed. However, it is known that bubbles cluster in so called cloudy bands which leads to a non-uniform bubble distribution within the ice (Svensson and others, 2005). Ackley and Keliher (1979) took this thought further and estimated the effect of air bubbles in a similar way we did in this study for the varying COF. The bubble stratification was modelled with a scalar mixing formula for air and ice with a different depolarization factor for each layer due to varying bubble eccentricities. The corresponding anisotropy and backscattered power with the approach for stratified media is larger than what is estimated with the volume scattering model using similar parameters. More data for air bubble statistics in ice are needed—especially in the horizontal plane—in order to decide whether surface or volume scattering is a more suitable description. In any case, the absolute values of the scattering coefficients are inflicted with a high uncertainty. This is also the case for the PRCs derived for the variations in COF: Reflections from within the ice are subject to interferences, and the sample interval of the COF data is not dense enough to identify potential reflection layers in the range of the wavelength. The actual changes in COF may be larger than the ones portrayed in Figure 6. The interfaces, however, must not be planar, but could be slanted or rough. This substantially decreases the magnitude of the PRCs. This is to say that the absolute values of scattering coefficients and PRCs should be handled with care. Hence, we relinquish to identify the dominant effect via the radar equation which encompasses to resolve the different normalizations (the scattering coefficient is normalized per unit volume, the PRCs are normalized per unit area).

We rather focus on the relative polarization dependence. The example for volume scattering in Figure 5(a) yields a $\sim$1 dB difference in a somewhat favourable case of fully aligned air bubbles with typical size parameters for intermediate depths. In the upper half of the ARZ 1, the PRCs due to changes in Eigenvalue λ_1 appear several dBs stronger than the ones caused by the changes in Eigenvalue λ_2 (Figure 6(b) and (c)) whereas in the lower half of the ARZ 1 they appear almost equal. For the ARZ 2, the PRCs due to changes in λ_2 outweigh the PRCs due to changes in λ_1 by more than 10 dBs. Based on the relative polarization dependence, we estimate that in the ARZ 2 and likely also in the ARZ 1 changes in COF are the dominant mechanisms for the observed anisotropy.

We briefly discuss the shading of the ARZ 2 by the ARZ 1: The increased backscatter parallel to the along-flow compression diminishes the transmitted power with the corresponding polarization in that direction. Therefore, polarization-dependent variations in backscattered power from the ARZ 2 are to be expected, even without a specific anisotropic backscatter mechanism in that zone. To estimate this effect, we consider a lossless, stratified medium containing n equidistant layers with thickness Δz and anisotropic PRCs r_x and $r_y = r_x \cdot \delta a$. The ratio $|E_{t,x}|^2/|E_{t,y}|^2$ of the transmitted power after two-way penetration for the two polarization types is

$$\frac{|E_{t,x}|^2}{|E_{t,y}|^2} = \left(\frac{1 - r_x}{1 - r_x \cdot \delta a}\right)^{2n\Delta z} \tag{4}$$

which ignores multiple reflections as they are small. To estimate an upper boundary we assume n=900 layers with strongly anisotropic PRCs of $R_x = -40$ dB and $R_y = -50$ dB with a layer thickness $\Delta z = 1$ m. This rather extreme case results in a ratio of -0.7 dBs, which is smaller than what is observed in the ARZ 2.

CONCLUSION

In this study we observe a variation in signal strength depending on the antenna orientation. The dominant symmetry has a 180° periodicity which we assign to anisotropic scattering from within the ice. To a lesser extent we also observe a 90° periodicity due to birefringence caused by the macroscopic alignment of COF. The polarization-dependent backscatter changes its direction with depth at about 900 m, coinciding with the clathrate transition and the transition from the Holocene to the last glacial (700–900 m depth). On the basis of mean-wind direction and the start of the polarization dependence at around 300–400 m depths, we excluded a directional layer roughness as a primary mechanism for the observed anisotropy. The investigation of backscatter mechanisms above (ARZ 1) and below (ARZ 2) 900 m depth included elongated air bubbles and changes in COF. For the ARZ 1, we propose that both effects superimpose and operate in similar directions predetermined by the principal axes of the stress regime at the surface. We assume that bubbles are complanate parallel to the axis of along-flow compression and elongated along the axis of lateral extension, causing minimum and maximum in backscatter in these directions respectively. Similarly we hypothesize that the girdle in COF is aligned along the same axes which is supported by recent modelling results in this area (Bargmann and others, in press). The Eigenvalues in the ARZ 1 indicate weakly that the cluster strengths varies with depth, increasing the backscatter perpendicular to the along-flow compression. Most likely the variations in COF dominate the observed anisotropy, since

the induced polarization dependence through elongated bubbles is small. However, higher-resolved COF measurements and the orientation distribution with eccentricities of air bubbles in the horizontal plane are needed to quantify the effects reliably. The volume scattering for anisotropic inclusions becomes more important at shallower depths when higher frequencies are used and the volume fraction of air is larger.

In the ARZ 2, we propose that changes in the Eigenvalue λ_2 and a stable Eigenvalue λ_1 increase the backscatter in the opposite directions than observed in the ARZ 1. This corresponds to the earlier suggested girdle to single-pole transitions (Fujita and others, 2003; Matsuoka and others, 2003). In contrast to the ARZ 1, the variations in COF appear more clearly in the ice-core data.

So far, it is mostly unclear how the Eigenvalues of COF change vertically in meter and sub-meter intervals and how the evolution is influenced by the impurity content of the ice. Given the available evidence we find it possible that the transition in anisotropic backscatter patterns caused by changing modes of COF variation indicates the climate transitions at the end of the last glacial. The relationship with the clathrate transition in similar depths appears merely coincidental. To visualize the relationship of increasing dust concentration with changing modes of COF, Figure 6(d) displays the non-seasalt Ca^{2+} concentration (Fischer and others, 2007) as an impurity proxy along-side the COF measurements. For the ARZ 1, the concentrations are low compared to all other depths. The exact mechanism on a grain-size scale still have to be investigated and it seems that the flank-flow setting is important as Fujita and others (2006) identified anisotropic scattering near Mizuho station (converging ice-flow region), but not near Dome-Fuji (located near a dome summit). More data is needed to find out whether the appearance of the ARZs is a universal feature in flank-flow regimes.

ACKNOWLEDGEMENTS

This work is a contribution to the European Project for Ice Coring in Antarctica (EPICA), a joint European Science Foundation/European Commission scientific programme, funded by the EU and by national contributions from Belgium, Denmark, France, Germany, Italy, The Netherlands, Norway, Sweden, Switzerland and the United Kingdom. The main logistic support was provided by IPEV and PNRA (at Dome C) and AWI (at Dronning Maud Land). This is EPICA Publication Number XXX.

Preparation of this work was supported by the Emmy Noether program of the Deutsche Forschungsgemeinschaft grant EI 672/5 to O. Eisen and a scholarship of the Evangelisches Studienwerk e.V. Villigst to R. Drews. We appreciate helpful discussions with Wolfgang Rack.

APPENDIX

The calculation of phase and extinction matrix for ellipsoidal scatterers has been demonstrated by Tsang and others (1981) and was modified by Karam and Fung (1983). We adapt the geometry so that it contains two half spaces (labeled 0 and 1) representing air and ice respectively. The change of geometry involves changing boundary conditions which alter the final results slightly. The boundary conditions used here were also used by Tsang and Kong (1978). We outline the calculations briefly.

Equation 1 can be split into two equations (upward/downward radiation):

$$\frac{d\mathbf{I}(\theta,\phi,\mathbf{z})}{\sec(\theta)dz} = -\underline{\mathbf{k_e}}(\theta,\phi)\mathbf{I}(\theta,\phi,z) + \mathbf{S_u} \quad \text{(A1)}$$

$$\frac{d\mathbf{I}(\pi-\theta,\phi,\mathbf{z})}{\sec(\theta)dz} = \underline{\mathbf{k_e}}(\pi-\theta,\phi)\mathbf{I}(\pi-\theta,\phi,z) - \mathbf{S_d} \quad \text{(A2)}$$

where $\pi-\theta$ stands for the downward direction. In this approximation the extinction matrix is assumed to be diagonal. The source terms $\mathbf{S_u}$ and $\mathbf{S_d}$ mark the amount of radiation scattered in the upward ($\mathbf{u}$) and downward ($\mathbf{d}$) direction, respectively. They are mainly determined by the phase matrix

$$\begin{aligned}\mathbf{S_u} &= \int d\Omega' \ \underline{\mathbf{P}}(\theta,\phi,\theta',\phi')\mathbf{I}(\theta',\phi') \\ &+ \quad \underline{\mathbf{P}}(\theta,\phi,\pi-\theta',\phi')\mathbf{I}(\pi-\theta',\phi'), \quad \text{(A3)}\\ \mathbf{S_d} &= \int d\Omega' \ \underline{\mathbf{P}}(\pi-\theta,\phi,\theta',\phi')\mathbf{I}(\theta',\phi') \\ &+ \quad \underline{\mathbf{P}}(\pi-\theta,\phi,\pi-\theta',\phi')\mathbf{I}(\pi-\theta',\phi'). \quad \text{(A4)}\end{aligned}$$

The phase matrix elements are calculated using scattering dyads which include the half axes describing the ellipsoid. The dashed angles mark the incoming, the non-dashed angles the scattered directions. The degree of alignment of the inclusions is considered with averaging the matrix elements over an orientation density distribution $\psi(\alpha,\beta,\gamma)$ for the Euler angles α,β,γ. This distribution is not known from ice-core data yet. To simplify the (numerical) integration we use a box-like shape of

$$\psi(\alpha,\beta,\gamma,\Delta\alpha,\Delta\beta,\Delta\gamma) = \begin{cases} & \alpha\in[\alpha-\Delta\alpha,\alpha+\Delta\alpha] \\ \frac{1}{8\Delta\alpha\Delta\beta\Delta\gamma} & \beta\in[\beta-\Delta\beta,\beta+\Delta\beta] \\ & \gamma\in[\gamma-\Delta\gamma,\gamma+\Delta\gamma] \\ 0 & \text{otherwise,}\end{cases}$$

which results in a mere change of integration boundaries during the integration:

$$P_{mn}(\theta,\phi) = \int d\alpha d\beta d\gamma \psi(\alpha,\beta,\gamma) P_{mn}(\alpha,\beta,\gamma,\theta,\phi)$$

with m,n=1..4 depicting the different matrix components (m=1..4 is also used later on to mark components of vectors). At this step, averaging over a size or eccentricity distribution is also possible. The first two diagonal elements of the extinction matrix are given by

$$\begin{aligned}k_v &= k_{ab} + k_{sv}(\Omega') \\ &= 2(1-v)\mathrm{Im}(k_1) + \int d\Omega P_{11}(\Omega,\Omega') + P_{21}(\Omega,\Omega') \quad \text{(A5)}\\ k_h &= k_{ab} + k_{sh}(\Omega') \\ &= 2(1-v)\mathrm{Im}(k_1) + \int d\Omega P_{12}(\Omega,\Omega') + P_{22}(\Omega,\Omega') \quad \text{(A6)}\end{aligned}$$

which assumes that there is no anisotropy in absorption. The inclusion of absorption influences the magnitude of the scattering coefficient and introduces the dependency on the volume fraction which cancels otherwise (see also Karam and Fung (1983)). The system of equations in (A1)–(A2) with the transmissivity ($\underline{\mathbf{T}}_{01}$) and reflectivity ($\underline{\mathbf{R}}_{11}$) matrices and the boundary condition

$$\mathbf{I_d}(z=0) = \underline{\mathbf{T}}_{01}\mathbf{I_0}(z=0) + \underline{\mathbf{R}}_{11}\mathbf{I_u}(z=0) \quad \text{(A7)}$$

can be turned into a system of integral equations (using an integrating factor):

$$I_{u,m}(z) = \int_{-\infty}^{z} dz' e^{-\frac{k_{e,mm}}{\cos(\theta)}(z-z')} \frac{S_{u,m}(\theta,\phi)}{\cos(\theta)} \quad \text{(A8)}$$

$$I_{d,m}(z) = \int_{z}^{0} dz' \frac{S_{d,m}}{\cos(\theta)} e^{\frac{k_{e,mm}}{\cos(\theta)}(z-z')} + \underline{\mathbf{T_{01}}}\mathbf{I_0}(z=0))_m e^{\frac{k_{e,mm}}{\cos(\theta)}z} + (\underline{\mathbf{R_{11}}} \int_{-\infty}^{0} dz' e^{\frac{k_{e,mm}}{\cos(\theta)}(z-z')} \frac{\mathbf{S_u}(\theta,\phi)}{\cos(\theta)})_m. \quad \text{(A9)}$$

The incoming intensity originates from a single direction only:

$$\mathbf{I_0}(\pi-\theta,\phi) = \mathbf{I_{inc}}\delta(\cos(\theta_0)-\cos(\theta_{0i}))\delta(\phi_0-\phi_{0i}) \quad \text{(A10)}$$

with δ representing the delta function. Once the upward intensity at z=0 is determined, the outgoing intensity is:

$$\mathbf{I_0}(\theta_{os},\phi_{os}) = \underline{\mathbf{T}}_{\mathbf{10}}\mathbf{I}(\theta_s,\phi_s,z=0). \quad \text{(A11)}$$

Equations (A8)–(A9) can be solved iteratively by assuming the scattering part $(\mathbf{S_d}, \mathbf{S_u})$ to be small. We mark the individual terms of the perturbation series with superscripts according to the order. In zeroth order scattering is entirely neglected, therefore:

$$I^{(0)}_{u,m}(z) = 0 \quad \text{(A12)}$$

$$I^{(0)}_{d,m}(z) = (\underline{\mathbf{T_{01}}}\mathbf{I_0}(z=0))_m e^{\frac{k_{e,mm}}{\cos(\theta)}z}. \quad \text{(A13)}$$

That means the incoming wave dominates, there is no volume scattering and the downwards radiation is simply attenuated. For the first-order approximation we use the zeroth order solution in the scattering term of (A8) and (A9):

$$\frac{I^{(1)}_{u,m}(z)}{\sec(\theta)} = \quad \text{(A14)}$$

$$\int_{-\infty}^{z} dz' e^{-\frac{k_{e,mm}}{\cos(\theta)}(z-z')} \int d\Omega' (\underline{\mathbf{P}}(\theta,\phi,\pi-\theta',\phi')\underline{\mathbf{T_{01}}}\mathbf{I_0})_m e^{\frac{k_{e,mm}}{\cos(\theta)}z'}$$

$$= \int d\Omega' (\underline{\mathbf{P}}(\theta,\phi,\pi-\theta',\phi')\underline{\mathbf{T_{01}}}\mathbf{I_0})_m \frac{e^{k_{e,mm}\sec(\theta')z}}{k_{e,mm}(\sec(\theta)+\sec(\theta'))}$$

$$\frac{I^{(1)}_{u,m,z=0}}{\sec(\theta)} = \quad \text{(A15)}$$

$$\int d\Omega' (\underline{\mathbf{P}}(\theta,\phi,\pi-\theta',\phi')\underline{\mathbf{T_{01}}}\mathbf{I_{inc}})_m \frac{\delta(\cos(\theta_0)-\cos(\theta_{0i}))\delta(\phi_0-\phi_{0i})}{k_{e,mm}(\sec(\theta)+\sec(\theta'))}$$

In order to make use of the delta functions substitute $d\theta'$ with $d\cos(\theta')$ and relate the incoming angles θ_0 and ϕ_0 in medium 0 via Snell's law to the angles in medium 1 ($d\theta'\sin(\theta') = d\theta'_0\sin(\theta'_0)\frac{\varepsilon_0\cos(\theta'_0)}{\varepsilon_1\cos(\theta')}$):

$$I^{(1)}_{u,m,z=0} = \sec(\theta)\frac{\varepsilon_0}{\varepsilon_1}\int_0^{2\pi} d\phi' \int_1^0 d\cos(\theta'_0)\sec(\theta')\cos(\theta'_0) \quad \text{(A16)}$$

$$(\underline{\mathbf{P}}(\theta,\phi,\pi-\theta',\phi')\underline{\mathbf{T_{01}}}\mathbf{I_{inc}})_m \frac{\delta(\cos(\theta')-\cos(\theta_{i'}))\delta(\phi'-\phi_{i'})}{k_{e,mm}(\sec(\theta)+\sec(\theta'))}$$

$$= \frac{\varepsilon_0}{\varepsilon_1}(\underline{\mathbf{P}}(\theta,\phi,\pi-\theta',\phi')\underline{\mathbf{T_{01}}}\mathbf{I_{inc}})_m \frac{\sec(\theta)\cos(\theta_{0i})}{k_{e,mm}(\sec(\theta)+\sec(\theta_i)\cos(\theta_i))}.$$

Using the boundary condition (A11) the first-order approximation is:

$$I(\theta_s,\phi_s)^{(1)}_{u,m,z=0} = \frac{\varepsilon_0}{\varepsilon_1}\frac{\sec(\theta_s)\cos(\theta_{oi})}{k_{e,mm}(\sec(\theta_s)+\sec(\theta_i))\cos(\theta_i)} (\underline{\mathbf{T_{10}}}\underline{\mathbf{P}}(\theta_s,\phi_s,\pi-\theta_i,\phi_i)\underline{\mathbf{T_{01}}}\mathbf{I_{inc}})_m. \quad \text{(A17)}$$

The bistatic scattering coefficient becomes the backscattering coefficient for $\theta_{os} = \theta_{oi}, \phi_{os} = \pi+\phi_{oi}$. Therefore by using equation (2):

$$\sigma^{(1)}_{vv} = 2\pi t^2_{v10}(\theta_i)\frac{\cos(\theta_{oi})^2\varepsilon_0}{\cos(\theta_i)\varepsilon_1}\frac{P_{11}(\theta_i,\pi+\phi_i,\pi-\theta_i,\phi_i)}{k_v},$$

$$\sigma^{(1)}_{hh} = 2\pi t^2_{h10}(\theta_i)\frac{\cos(\theta_{oi})^2\varepsilon_0}{\cos(\theta_i)\varepsilon_1}\frac{P_{22}(\theta_i,\pi+\phi_i,\pi-\theta_i,\phi_i)}{k_h},$$

$$\sigma^{(1)}_{hv} = 2\pi t_{v10}(\theta_i)t_{h01}(\theta_i)\frac{\cos(\theta_{oi})^2\varepsilon_0}{\cos(\theta_i)\varepsilon_1}\frac{P_{12}(\theta_i,\pi+\phi_i,\pi-\theta_i,\phi_i)}{k_h},$$

$$\sigma^{(1)}_{vh} = 2\pi t_{h10}(\theta_i)t_{v01}(\theta_i)\frac{\cos(\theta_{oi})^2\varepsilon_0}{\cos(\theta_i)\varepsilon_1}\frac{P_{21}(\theta_i,\pi+\phi_i,\pi-\theta_i,\phi_i)}{k_v}.$$

Integrating the phase matrix elements over the Euler angles and the solid angle $d\Omega$ results in a five-fold integral. Analytically, this case is only feasible for the case of fully aligned spheroids. This serves as a cross check for the numerical solution. The numerical integration is implemented with a Monte Carlo integration scheme. We also calculated the second order solution, using the first order solution as input for the equations (A8)–(A9). The integrals become more tedious, and to simplify the result we neglect small terms resulting from a second order reflections from the air–ice interface ($\mathbf{R_{11}}$ is small). Only internal multiple scattering is considered. For the outgoing intensity in region 0 the result is:

$$\mathbf{I}^{(2)}_0(\theta=\theta_i,\phi=\pi+\phi_i,z=0)_m = \quad \text{(A18)}$$

$$A\int d\Omega \frac{\sec(\theta')\sec(\theta_i)}{2k^2_{e,mm}(\sec(\theta')+\sec(\theta_i))}\left(\underline{\mathbf{T}}_{\mathbf{1},\mathbf{0}}\underline{\mathbf{P}}_{\mathbf{u_i},\mathbf{u}}\underline{\mathbf{P}}_{\mathbf{u},\mathbf{d_i}}\underline{\mathbf{T}}_{\mathbf{0},\mathbf{1}}\mathbf{I_{0i}}\right)_m +$$

$$A\int d\Omega \frac{\sec(\theta_i)\sec(\theta')}{k^2_{e,mm}(\sec(\theta_i)-\sec(\theta'))}\left(\frac{1}{\sec(\theta_i)+\sec(\theta')}-\frac{1}{2\sec(\theta_i)}\right)$$

$$\left(\underline{\mathbf{T}}_{1,0}\underline{\mathbf{P}}_{\mathbf{u_i},\mathbf{d}}\underline{\mathbf{P}}_{\mathbf{d},\mathbf{d_i}}\underline{\mathbf{T}}_{\mathbf{0},\mathbf{1}}\mathbf{I_{0i}}\right)_m$$

$$+ A\frac{\sec(\theta_s)}{k_{e,mm}(\sec(\theta_s)+\sec(\theta_i))}\left(\underline{\mathbf{T}}_{1,0}\underline{\mathbf{P}}_{\mathbf{u_i},\mathbf{d_i}}\underline{\mathbf{T}}_{\mathbf{0},\mathbf{1}}\mathbf{I_{0i}}\right)_m$$

where the indices $\mathbf{u}$ and $\mathbf{d}$ mark the direction up and down, $A = \frac{\varepsilon_0\cos(\theta_{0i})}{\varepsilon_1\cos(\theta_i)}$, and the subscript i marks the direction of incidence. The multiple scattering terms are represented via the multiplication of phase matrices for the different directions. The corresponding backscattering coefficients can be calculated by expanding equation (A18) and substituting into equation (2) with the same boundary conditions as above.

REFERENCES

Ackley, S. and T. Keliher, 1979. Ice Sheet Internal Radio-Echo Reflections and Associated Physical Property Changes With Depth, *Journal of Geophysical Research*, **84(B10)**, 5675–5680.

Alley, R. B. and J. J. Fitzpatrick, 1999. Conditions for bubble elongation in cold ice-sheet ice, *Journal of Glaciology*, **45**, 147–153.

Bargmann, S., H. Seddik and R.. Greve, in press. Computational modeling of flow-induced anisotropy of polar ice for the EDML deep drilling site, Antarctica: the effect of rotation recrystallization and grain boundary migration, *International Journal for Numerical and Analytical Methods in Geomechanics*.

Bendel, V., 2009. Untersuchung an Luftblasen im EDML-Eisbohrkern mit Bildanalyse und Ramanspektroskopie, (Master's thesis), Universität Göttingen, Fachbereich Geowissenschaften.

Dall, J., 2010. Ice sheet anisotropy measured with polarimetric ice sounding radar, *Geoscience and Remote Sensing Symposium (IGARSS), 2010 IEEE International*, 2507–2510.

Doake, C. S. M., 1981. Polarization of radio waves in ice sheets, *Geophysical Journal of the Royal Astronomical Society*, **64**, 539–558.

Doake, C. S. M., H. F. J. Corr and A. Jenkins, 2002. Polarization of radio waves transmitted through Antarctic ice shelves, *Annals of Glaciology*, **34**(1), 165–170.

Drews, R., O. Eisen, I. Weikusat, S. Kipfstuhl, A. Lambrecht, D. Steinhage, F. Wilhelms and H. Miller, 2009. Layer disturbances and the radio-echo free zone in ice sheets, *The Cryosphere*, **3**(2), 195–203.

Eisen, O., I. Hamann, S. Kipfstuhl, D. Steinhage and F. Wilhelms, 2007. Direct evidence for continuous radar reflector originating from changes in crystal-orientation fabric, *The Cryosphere*, **1**(1), 1–10.

Eisen, O., F. Wilhelms, D. Steinhage and J. Schwander, 2006. Improved method to determine radio-echo sounding reflector depths from ice-core profiles of permittivity and conductivity, *Journal of Glaciology*, **52**(177), 299–310(12).

Fischer, H., F. Fundel, U. Ruth, B. Twarloh, A. Wegner, R. Udisti, S. Becagli, E. Castellano, A. Morganti, M. Severi, E. Wolff, G. Littot, R. Röthlisberger, R. Mulvaney, M. A. Hutterli, P. Kaufmann, U. Federer, F. Lambert, M. Bigler, M. Hansson, U. Jonsell, M. de Angelis, C. Boutron, M.-L. Siggaard-Andersen, J. P. Steffensen, C. Barbante, V. Gaspari, P. Gabrielli and D. Wagenbach, 2007. Reconstruction of millennial changes in dust emission, transport and regional sea ice coverage using the deep EPICA ice cores from the Atlantic and Indian Ocean sector of Antarctica, *Earth and Planetary Science Letters*, **260**(1-2), 340 – 354.

Fujita, S. and S. Mae, 1993. Relation between ice sheet internal radio-echo reflections and ice fabric at Mizuho Station, Antarctica, *Annals of Glaciology*, **17**, 269–275.

Fujita, S., S. Mae and T. Matsuoka, 1993. Dielectric anisotropy in ice Ih at 9.7 GHz, *Annals of Glaciology*, **17**, 276–280.

Fujita, S., H. Maeno and K. Matsuoka, 2006. Radio-wave depolarization and scattering within ice sheets: a matrix-based model to link radar and ice-core measurements and its application, *Journal of Glaciology*, **52**(178), 407–424(18).

Fujita, S., H. Maeno, S. Uratsuka, T. Furukawa, S. Mae, Y. Fujii and O. Watanabe, 1999. Nature of radio echo layering in the Antarctic ice sheet detected by a two frequency experiment, *Journal of Geophysical Research*, **104**(B6), 13013–13024.

Fujita, S., K. Matsuoka, H. Maeno and T. Furukawa, 2003. Scattering of VHF radio waves from within an ice sheet containing the vertical-girdle-type ice fabric and anisotropic reflection boundaries, *Annals of Glaciology*, **37**, 305–316(12).

Fujita, S., T. Matsuoka, T. Ishida, K. Matsuoka and S. Mae, 2000. A summary of the complex dielectric permittivity of ice in the megahertz range and its applications for radar sounding of polar ice sheets, *Physics of Ice Core Records*, 185–212, international Symposium on Physics of Ice Core Records. Shikotsukohan Hokkaido, Japan, September 14-17, 1998.

Hargreaves, N. D., 1977. The polarization of radio signals in the radio echo sounding of ice sheets, *Journal of Physics D: Applied Physics*, **10**, 1285–1304.

Hargreaves, N. D., 1978. The radio-frequency birefringence of polar ice, *Journal of Glaciology*, **21**(85), 301–313.

Karam, M. A. and A. K. Fung, 1983. Scattering from randomly oriented circular discs with application to vegetation, *Radio Science*, **18**, 557–565.

Kravchenko, I., D. Besson, A. Ramos and J. Remmers, 2011. Radio frequency birefringence in south polar ice and implications for neutrino reconstruction, *Astroparticle Physics*, **34**(10), 755 – 768.

Liu, C., C. R. Bentley and N. E. Lord, 1994. c axes from radar depolarization experiments at Upstream B Camp, Antarctica, in 1991-92, *Annals of Glaciology*, **20**, 169–176(8).

Matsuoka, K., T. Furukawa, S. Fujita, H. Maeno, S. Uratsuka, R. Naruse and O. Watanabe, 2003. Crystal orientation fabrics within the Antarctic ice sheet revealed by a multipolarization plane and dual-frequency radar survey, *Geophysical Research solid earth*, **108**(B19), EPM10.1–EPM10.17.

Matsuoka, K., S. Uratsuka, Fujita S. and F. Nishio, 2004. Ice-flow-induced scattering zone within the Antarctic ice sheet revealed by high-frequency airborne radar, *Journal of Glaciology*, **50**(170), 382–388.

Matsuoka, K., L. Wilen, S. P. Hurley and C. F. Raymond, 2009. Effects of Birefringence Within Ice Sheets on Obliquely Propagating Radio Waves, *IEEE Transactions on Geoscience and Remote Sensing*, **47**, 1429–1443.

Matsuoka, T., S. Fujita, S. Morishima and S. Mae, 1997. Precise measurement of dielectric anisotropy in ice Ih at 39 GHz, *Journal of Applied Physics*, **81**, 2344–2348.

Nakawo, M., H. Ohmae, F. Nishio and T. Kameda, 1989. Dating the Mizuho 700 m Core from Core Ice Fabric Data, *Proc. NIPR Symp. Polar Meteorol. Glaciol.*, **2**, 105–110.

Nixdorf, U., D. Steinhage, U. Meyer, L. Hempel, M. Jenett, P. Wachs and H. Miller, 1999. The newly developed airborne radio-echo sounding system of the AWI as a glaciological tool, *Annals of Glaciology*, **29**, 231–238(8).

Oerter, H., C. Drücker, S. Kipfstuhl and F. Wilhelms, 2009. Kohnen station - the drilling camp for the EPICA deep ice core in Dronning Maud Land, *Polarforschung*, **78 (1-2)**, 1–23.

Paren, J.G., 1981. Correspondence, *Journal of Glaciology*, **27**(95), 203–204.

Reijmer, C. H., 2001. Antarctic meteorology: a study with automatic weather stations, *PhD thesis, University of Utrecht*.

Robin, G. Q., S. Evans and J. T. Bailey, 1969. Interpretation of Radio Echo Sounding in Polar Ice Sheets, *Philosophical Transactions of the Royal Society of London. Series A, Mathematical and Physical Sciences*, **265**(1166), 437–505.

Siegert, M.J. and R. Kwok, 2000. Ice-sheet radar layering and the development of preferred crystal orientation fabrics between Lake Vostok and Ridge B, central East Antarctica, *Earth and Planetry Science Letters*, **179**, 227–235.

Steinhage, D., U. Nixdorf, U. Meyer and H. Miller, 1999. New maps of the ice thickness and subglacial topography in Dronning Maud Land, Antarctica, determined by means of airborne radio-echo sounding, *Annals of Glaciology*, **29**, 267–272(6).

Steinhage, D., U. Nixdorf, U. Meyer and H. Miller, 2001. Subglacial topography and internal structure of central and western Dronning Maud Land, Antarctica, determined from airborne radio echo sounding, *Journal of Applied Geophysics*, **47**(3-4), 183 – 189.

B.1 Second order solution of the radiatvie transfer equations

In the process of deriving the volume scattering coefficients for the radiative transfer equations mentioned in the previous manuscript, a second order solution was derived, but not explained in full detail in the corresponding publication. It will be presented here, as it may be of interest for other studies in the future.

First calculate the first order solution for $I_d(z)$ making use of the zeroth order solution. This is a somewhat longer expression.

$$\begin{aligned}
\frac{I^{(1)}_{d,m}(\Theta,\phi,z)}{\sec(\theta)} &= \int_z^0 dz' e^{\frac{k_{e,ii}}{\cos(\theta)}(z-z')} \int d\Omega' (\underline{\mathbf{P}}(\pi-\theta,\phi,\pi-\theta',\phi')\underline{\mathbf{T}}_{\mathbf{01}}\mathbf{I_0})_m e^{\frac{k_{e,mm}}{\cos(\theta')}z'} \\
&+ (\underline{\mathbf{T}}_{\mathbf{01}}\mathbf{I_0}(z=0))_m e^{\frac{k_{e,mm}}{\cos(\theta)}z} \\
&+ \underline{\mathbf{R}}_{\mathbf{11}} \int_{-\infty}^0 dz' e^{\frac{-k_{e,mm}}{\cos(\theta)}(z-z')} \sec(\theta) \int d\Omega' (\underline{\mathbf{P}}(\theta,\phi,\pi-\theta',\phi')(\underline{\mathbf{T}}_{\mathbf{01}}\mathbf{I_0}(z=0))_m e^{\frac{k_{e,mm}}{\cos(\theta)}z'})_m \\
&\approx \int d\Omega' (\underline{\mathbf{P}}(\pi-\theta,\phi,\pi-\theta',\phi')(\underline{\mathbf{T}}_{\mathbf{01}}\mathbf{I_0}(z=0))_m \frac{e^{k_{e,mm}z\sec(\theta)} - e^{k_{e,mm}z\sec(\theta')}}{k_{e,mm}(\sec(\theta')-\sec(\theta))} \\
&+ (\underline{\mathbf{T}}_{\mathbf{01}}\mathbf{I_0}(z=0))_m e^{\frac{k_{e,mm}}{\cos(\theta)}z} \\
&= \frac{\varepsilon_0\cos(\theta_{0i})}{\varepsilon_1\cos(\theta_i)} (\underline{\mathbf{P}}(\pi-\theta,\phi,\pi-\theta_i,\phi_i)\underline{\mathbf{T}}_{\mathbf{01}}\mathbf{I_{0i}})_m \frac{e^{k_{e,mm}z\sec(\theta)} - e^{k_{e,mm}z\sec(\theta_i)}}{k_{e,mm}(\sec(\theta_i)-\sec(\theta))} \\
&+ (\underline{\mathbf{T}}_{\mathbf{01}}\mathbf{I_0}(z=0))_m e^{\frac{k_{e,mm}}{\cos(\theta)}z}
\end{aligned}$$

This approximation neglects all terms originating from R_{11} as for this case it is small compared to all terms preceded with the transmission matrix coefficients. In a next step we insert $I^{(1)}_{d,m}$ and $I^{(1)}_{u,m}$ in equations A(8)–A(9) with $A = \frac{\varepsilon_0\cos(\theta_{0i})}{\varepsilon_1\cos(\theta_i)}$:

$$\begin{aligned}
\frac{I^{(1)}_{d,m}}{\sec(\theta)} &= A(\underline{\mathbf{P}}(\pi-\theta,\phi,\pi-\theta_i,\phi_i)\underline{\mathbf{T}}_{\mathbf{01}}\mathbf{I_{0i}})_m \frac{e^{k_{e,mm}z\sec(\theta)} - e^{k_{e,mm}z\sec(\theta_i)}}{k_{e,mm}(\sec(\theta_i)-\sec(\theta))} + (\underline{\mathbf{T}}_{\mathbf{01}}\mathbf{I_0}(z=0))_m e^{\frac{k_{e,mm}}{\cos(\theta)}z} \\
\frac{I^{(1)}_{u,i}}{\sec(\theta)} &= A(\underline{\mathbf{P}}(\theta,\phi,\pi-\theta_i,\phi_i)\underline{\mathbf{T}}_{\mathbf{01}}\mathbf{I_{0i}})_m \frac{e^{k_{e,mm}\sec(\theta_i)z}}{k_{e,mm}(\sec(\theta)+\sec(\theta_i))}
\end{aligned}$$

and:

$$\begin{aligned}
\mathbf{I^{(2)}}_u|_{z=0} &= \sec(\theta) \int_{-\infty}^0 dz' e^{-\frac{k_{e,mm}}{\cos(\theta)}(-z')} \\
&\cdot \int d\Omega \underline{\mathbf{P}}(\theta,\phi,\theta',\phi')\mathbf{I^{(1)}}_u(\theta',\phi',z')|_{z=0} + \int d\Omega \underline{\mathbf{P}}(\theta,\phi,\pi-\theta',\phi')\mathbf{I^{(1)}}_d(\theta',\phi',z')|_{z=0})
\end{aligned}$$

the second order intensity results in (after the z-integration):

$$\begin{aligned}
\mathbf{I^{(2)}}_u \quad |_{z=0} &= \int d\Omega \frac{A\sec(\theta)\sec(\theta')}{k^2_{e,mm}(\sec(\theta')+\sec(\theta_i)(\sec(\theta)+\sec(\theta_i))} \underline{\mathbf{P}}_{\mathbf{u,u}} \underline{\mathbf{P}}_{\mathbf{u,d_i}} \underline{\mathbf{T}}_{\mathbf{0,1}} \mathbf{I_{0i}} \\
+ \quad & \int d\Omega \frac{A\sec(\theta)\sec(\theta')}{k^2_{e,mm}(\sec(\theta_i)-\sec(\theta'))} \left(\frac{1}{(\sec(\theta)+\sec(\theta'))} - \frac{1}{(\sec(\theta)+\sec(\theta_i))} \right) \underline{\mathbf{P}}_{\mathbf{u,d}} \underline{\mathbf{P}}_{\mathbf{d,d_i}} \underline{\mathbf{T}}_{\mathbf{0,1}} \mathbf{I_{0i}} \\
+ \quad & \frac{A\sec(\theta)}{k_{e,mm}((\sec(\theta)+\sec(\theta_i))} \underline{\mathbf{P}}(\theta,\phi,\pi-\theta_\mathbf{i},\phi_\mathbf{i}) \underline{\mathbf{T}}_{\mathbf{0,1}} \mathbf{I_{0i}}
\end{aligned}$$

Where $\underline{\mathbf{P}}_{\mathbf{u,d}} = \underline{\mathbf{P}}(\theta,\phi,\pi-\theta',\phi')$ and $\underline{\mathbf{P}}_{\mathbf{u,d_i}} = \underline{\mathbf{P}}(\theta,\phi,\pi-\theta_\mathbf{i},\phi_\mathbf{i})$ depict the scattering from the downwards (d) to the upwards (u) direction (other indices respectively). The index i hereby indicates the original incidence angle. In region 0, the final specific intensity in backscattering direction direction is given by:

$$\begin{aligned}
\mathbf{I}_0 \quad (\theta=\theta_i,\phi=\pi+\phi_i) &= A\int d\Omega \frac{\sec(\theta')\sec(\theta_i)}{2k^2_{e,ii}(\sec(\theta')+\sec(\theta_i))} \underline{\mathbf{T}}_{\mathbf{1,0}} \underline{\mathbf{P}}_{\mathbf{u,u}} \underline{\mathbf{P}}_{\mathbf{u,d_i}} \underline{\mathbf{T}}_{\mathbf{0,1}} \mathbf{I_{0i}} \\
+ \quad & A\int d\Omega \frac{\sec(\theta_i)\sec(\theta')}{k^2_{e,ii}(\sec(\theta_i)-\sec(\theta'))} \left(\frac{1}{(\sec(\theta_i)+\sec(\theta'))} - \frac{1}{2\sec(\theta_i)} \right) \underline{\mathbf{T}}_{1,0} \underline{\mathbf{P}}_{\mathbf{u,d}} \underline{\mathbf{P}}_{\mathbf{d,d_i}} \underline{\mathbf{T}}_{\mathbf{0,1}} \mathbf{I_{0i}} \\
+ \quad & A\frac{1}{k_{e,ii}} \underline{\mathbf{T}}_{1,0} \underline{\mathbf{P}}_{\mathbf{u_i,d_i}} \underline{\mathbf{T}}_{\mathbf{0,1}} \mathbf{I_{0i}}.
\end{aligned}$$

The different backscattering coefficients can now be directly computed:

$$
\begin{aligned}
\frac{\sigma_{vv}(\theta=\theta_i,\phi=\pi-\phi_i)}{4\pi A\cos(\theta_{oi})} &= \int d\Omega \frac{\sec(\theta')\sec(\theta_i)}{2k_{e,22}^2(\sec(\theta')+\sec(\theta_i))} t_{v1,0}t_{v0,1} \\
&\quad (P_{11,ui,u}P_{11,u,di}+P_{12,ui,u}P_{21,u,di}+P_{13,ui,u}P_{31,u,di}+P_{14,ui,u}P_{41,u,di}) \\
&+ \int d\Omega' \frac{\sec(\theta_i)\sec(\theta')}{k_{e,ii}^2(\sec(\theta_i)-\sec(\theta'))}\left(\frac{1}{(\sec(\theta_i)+\sec(\theta'))}-\frac{1}{2\sec(\theta_i)}\right) t_{v1,0}t_{v0,1} \\
&\quad (P_{11,ui,d}P_{11,d,di}+P_{12,ui,d}P_{21,d,di}+P_{13,ui,d}P_{31,d,di}+P_{14,ui,d}P_{41,d,di}) \\
&+ \frac{1}{k_{e,11}} t_{v1,0}t_{v0,1}P_{11,ui,di} \\
\frac{\sigma_{vh}(\theta=\theta_i,\phi=\pi-\phi_i)}{4\pi A\cos(\theta_{oi})} &= \int d\Omega' \frac{\sec(\theta')\sec(\theta_i)}{2k_{e,22}^2(\sec(\theta')+\sec(\theta_i))} t_{h1,0}t_{h0,1} \\
&\quad (P_{21,ui,u}P_{11,u,di}+P_{22,ui,u}P_{21,u,di}+P_{23,ui,u}P_{31,u,di}+P_{24,ui,u}P_{41,u,di}) \\
&+ \int d\Omega' \frac{\sec(\theta_i)\sec(\theta')}{k_{e,ii}^2(\sec(\theta_i)-\sec(\theta'))}\left(\frac{1}{(\sec(\theta_i)+\sec(\theta'))}-\frac{1}{2\sec(\theta_i)}\right) t_{h1,0}t_{v0,1} \\
&\quad (P_{21,ui,d}P_{11,d,di}+P_{22,ui,d}P_{21,d,di}+P_{23,ui,d}P_{31,d,di}+P_{24,ui,d}P_{41,d,di}) \\
&+ \frac{1}{k_{e,11}} t_{h1,0}t_{v0,1}P_{21,ui,di} \\
\frac{\sigma_{hh}(\theta=\theta_i,\phi=\pi-\phi_i)}{4\pi A\cos(\theta_{oi})} &= \int d\Omega' \frac{\sec(\theta')\sec(\theta_i)}{2k_{e,22}^2(\sec(\theta')+\sec(\theta_i))} t_{h1,0}t_{h0,1} \\
&\quad (P_{21,ui,u}P_{12,u,di}+P_{22,ui,u}P_{22,u,di}+P_{23,ui,u}P_{32,u,di}+P_{24,ui,u}P_{42,u,di}) \\
&+ \int d\Omega' \frac{\sec(\theta_i)\sec(\theta')}{k_{e,ii}^2(\sec(\theta_i)-\sec(\theta'))}\left(\frac{1}{(\sec(\theta_i)+\sec(\theta'))}-\frac{1}{2\sec(\theta_i)}\right) t_{h1,0}t_{h0,1} \\
&\quad (P_{21,ui,d}P_{12,d,di}+P_{22,ui,d}P_{22,d,di}+P_{23,ui,d}P_{32,d,di}+P_{24,ui,d}P_{42,d,di}) \\
&+ \frac{1}{k_{e,22}} t_{h1,0}t_{h0,1}P_{22,ui,di} \\
\frac{\sigma_{hv}(\theta=\theta_i,\phi=\pi-\phi_i)}{4\pi A\cos(\theta_{oi})} &= \int d\Omega' \frac{\sec(\theta')\sec(\theta_i)}{2k_{e,22}^2(\sec(\theta')+\sec(\theta_i))} t_{v1,0}t_{h0,1} \\
&\quad (P_{11,ui,u}P_{12,u,di}+P_{12,ui,u}P_{22,u,di}+P_{13,ui,u}P_{32,u,di}+P_{14,ui,u}P_{42,u,di}) \\
&+ \int d\Omega' \frac{\sec(\theta_i)\sec(\theta')}{k_{e,ii}^2(\sec(\theta_i)-\sec(\theta'))}\left(\frac{1}{(\sec(\theta_i)+\sec(\theta'))}-\frac{1}{2\sec(\theta_i)}\right) t_{v1,0}t_{h0,1} \\
&\quad (P_{11,ui,d}P_{12,d,di}+P_{12,ui,d}P_{22,d,di}+P_{13,ui,d}P_{32,d,di}+P_{14,ui,d}P_{42,d,di}) \\
&+ \frac{1}{k_{e,22}} t_{v1,0}t_{h0,1}P_{12,ui,di}
\end{aligned}
$$

All integrals have a (converging) singularity at $\theta = \pi/2$, this can be treated with standard numerical approaches.

C. Characterization of glaciological conditions at Halvfarryggen ice dome, Dronning Maud Land, Antarctica

Own contribution: Data acquisition and processing of low-frequency GPR and GPS from the 2010 survey; Synthesis of the local elevation model; Localization of ice divides; Derivation of accumulation from the 2007 GPR data (data processing done by D. Steinhage); Horizontal and vertical characterization of the isochrone arch around the triple junction; Literature review; Writing of publication; Creation of Figures 1–6 and 8. Figure 7 in cooperation with C. Martín, who is in charge of the ice-flow model.
Current status: Submitted to Journal of Geophysical Research-Solid Earth

Characterization of glaciological conditions at Halvfarryggen ice dome, Dronning Maud Land, Antarctica

R. Drews[1], D. Steinhage[1], C. Martín[2], and O.Eisen[1]

Abstract. This study infers glaciological parameters for Halvfarryggen, an ice dome in coastal Dronning Maud Land, Antarctica, by using remote sensing techniques in combination with on-site radar and GPS measurements. The dome appears as a promising drill site for the International Partnerships in Ice Core Sciences 2k and 40k arrays. Airborne and ground-based radar surveys image bedrock topography and internal layering in the vicinity of the dome, which is located near a triple junction where three ice divides merge. The surface topography is determined by a combination of different remote-sensing techniques resulting in an elevation model with a grid spacing of 100 m x 100 m and a standard deviation along ground control points of 11 m. The internal layering as seen via radar bends upwards beneath the divides, indicating the operation of the Raymond effect. The upward-bending increases in amplitude with larger depths down to the lower third of the ice column, where the isochrone arch develops into a double bump in some radargrams. We visualize the three dimensional characteristics in internal layering in a 15–20 km radius around the dome. Accumulation estimates from internal layers near the surface vary from 400–1670 kg/(m^{2}a) with an asymmetry caused by preferred wind directions and changing surface slope. We use the derived datasets as input for a two dimensional full Stokes, anisotropic ice-flow model to predict the age–depth relationship and compare the modelled isochrones with the radar layer architecture. In the vicinity of the dome we estimate 13 ka old ice at 90% of the total ice thickness.

1. Introduction

Ice cores provide valuable input for both, climate and ice-sheet models. Impurities, stable isotopes and enclosed gases give insight to atmospheric conditions in the past, and measurements on physical properties like crystal orientation fabric (COF) contribute to the parameterization of the flow law of ice. Drill locations at domes or divides often simplify the interpretation of ice-core records as horiztonal ice flux is small, the catchment area is well defined and flow disturbances are minimized [*Waddington et al.*, 2001]. However, near-divide flow imposes high demands to the modelling of ice dynamics. Commonly used approximations, like the shallow ice approximation or plug-flow, do not apply in the divide area because all the components of the stress tensor are significant. This is problematic, as a correct modelling for example of the age–depth relationship is a crucial criterion for choosing a drill site. Our motivation to investigate Halvfarryggen, an ice dome in coastal Dronning Maud Land (Figure 1), emerges out of these seemingly contrasting priorities. On the one hand, the dome of Halvfarryggen appears as a candidate for the International Partnerships in Ice Core Sciences (IPICS) 2k and 40k arrays [*Brook et al.*, 2006]. This program aims to increase the spatial and temporal coverage with a series of ice cores to intermediate depths. The focus is on the beginning of anthropogenic impacts in the more recent history as well as, amongst others, on the transition from the last glacial maximum to the current Holocene. Contrasting the search for the oldest ice, potential drill sites within that array should have high accumulation rates to increase the vertical resolution so that annual and seasonal cycles can be resolved. On the other hand, the internal stratigraphy beneath ice divides often shows a distinct upwarping of layers which is not related to the bedrock topography. This complicates the age–depth relationship and necessitates a detailed characterization of the glaciological setting as boundary conditions for sophisticated modelling studies. The disadvantage of a complex internal stratigraphy may then be turned into an advantage, as additional conclusions with respect to the temporal stability of the dome can be drawn prior to drilling. Apart from pre-site surveys, the investigation of basic glaciological principles in divide-flow regimes is interesting in itself. The setting can be used as a spatially confined case study to constrain an anisotropic flow law further, using the typical upward-bending of layers as a reference.

We present the results of recent radar and GPS surveys in the Halvfarryggen area and combine those with additional remote sensing techniques and an ice-flow model. The glaciological setting is described in terms of surface topography, internal layering, and spatial variation in accumulation. We describe the upwarping of layers with the term isochrone arch which inherently assumes that the internal layers as seen via radar are isochrones. Other publications use the term Raymond bump. The term apex describes the maxima of the isochrone arch. To distinguish between airborne and ground-based radar profiles we use the abbreviations RES (radio-echo sounding) and GPR (ground-penetrating radar), respectively. Depth intervals relative to the total ice thickness are described from top to bottom, with the origin being at the surface. The terms 'shallow' and 'deep' refer to near the surface and near the bedrock, respectively.

The upwarping of internal layers beneath divides has been predicted by *Raymond* [1983] as a consequence of the nonlinearity in Glen's flow law in which ice behaves stiffer at lower deviatoric stresses. Therefore, the downward motion of internal layers at certain depths beneath the divide is slower compared to the downward motion away from the divide. The upwarping typically ceases at a distance of a few

[1]Alfred Wegener Institute for Polar and Marine Research, Postfach 12 01 61, 27515 Bremerhaven,Germany

[2]British Antarctic Survey, Natural Environment Research Council, Cambridge, UK

0148-0227/11/$9.00

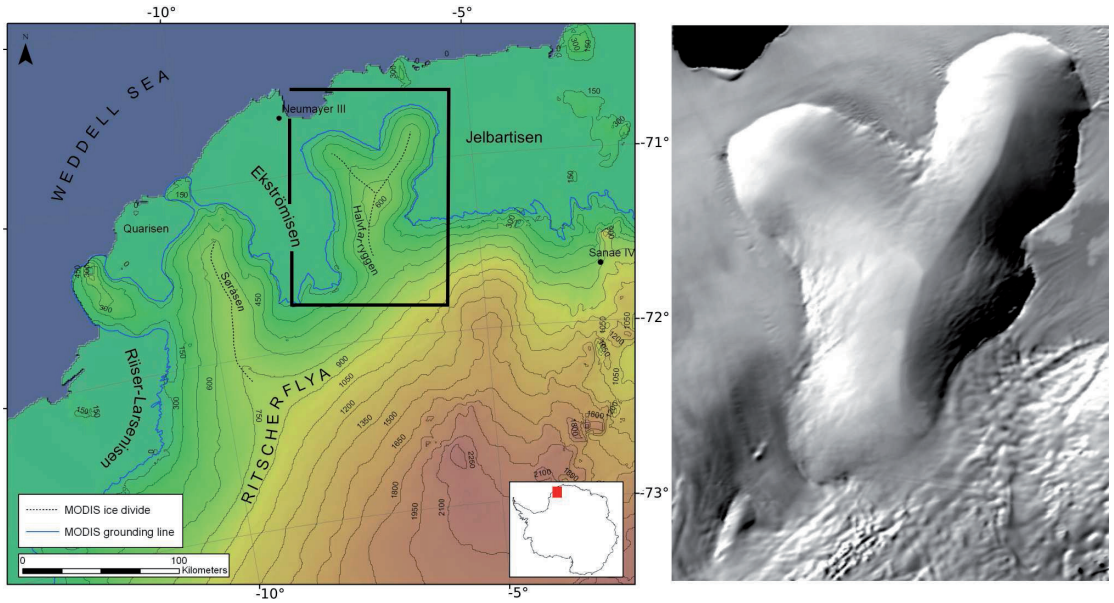

Figure 1. Left: Overview of the survey area (adapted from *Neckel* [2011]). The black box marks Halvfarryggen which is zoomed in on the right. The inset delineates the location (red box) within Antarctica. **Right:** Image of Halvfarryggen taken from MODIS [*Scambos et al.*, 2002]. The Y-shaped ice divides appear clearly and are partly accompanied by double-ridge features.

ice thicknesses away from the divide position. It has been observed in many radargrams across ice divides in Antarctica for example at Berkner Island [*Steinhage and Blindow*, 1996; *Sandhäger*, 1996], Siple Dome [*Nereson and Raymond*, 1996], Fletcher Promotory [*Vaughan et al.*, 1999], and Roosevelt Island [*Conway et al.*, 1999].

Since the geometry of the isochrone arch contains a wealth of information about the divide evolution and physical properties, a number of dedicated modelling studies focused on near-divide flow [*Schøtt-Hvidberg*, 1996; *Hindmarsh*, 1996; *Nereson et al.*, 1998a, b; *Nereson et al.*, 2000; *Nereson and Raymond*, 2001; *Nereson and Waddington*, 2002; *Pettit and Waddington*, 2003; *Pettit et al.*, 2003; *Jacobson and Waddington*, 2005; *Martín et al.*, 2009a]. However, the correct reproduction of the amplitude versus depth distribution of the isochrone arch remains a challenge. Similarly, the downwards-warping of the isochrone arch at larger depths, which is visible in some radargrams and also referred to as a double-bump, remained mysterious and could not be replicated with an isotropic rheology. An anisotropic rheology due to aligned COF has been considered by *Pettit et al.* [2007] and *Martín et al.* [2009b], both showing that anisotropic COF generally increases the arch amplitude. *Martín et al.* [2009b] use an initially random fabric, which develops with ongoing ice dynamics. This model reproduces the downwards bending, and also interprets other features like the flanking synclines of the isochrone arch, or the subtle surface concavities observed in some satellite images next to the divides [*Goodwin and Vaughan*, 1995]. It is hypothesized, that theses features are a consequence of anisotropic ice flow and appear at fully developed, steady-state ice divides which are frozen to the bed and have been stable over multiples of their characteristic time scales (i.e. ice thickness divided by accumulation in ice or water equivalent).

A fully three dimensional model with an anisotropic rheology is applied in the Dome Fuji area, Antarctica, by *Seddik et al.* [2011]. In two publications [*Gillet-Chaulet and Hindmarsh*, 2011; *Hindmarsh et al.*, 2011] the flow at ice-divide triple junctions is specifically investigated in terms of the internal layering and the age–depth relationship beneath the divides. *Hindmarsh et al.* [2011] presents the results of radar surveys around triple junctions of Antarctic ice ridges (Fletcher Promotory and Berkner Island) which are in a comparable setting to the Halvfarryggen ice ridge. The internal layering is visualized three-dimensionally and compared to modelling results given by *Gillet-Chaulet and Hindmarsh* [2011]. They predict that the amplitude in upwarping should be strongest beneath the dome and decline rapidly beneath the individual arms with increasing surface slope. The observations partly match the modelled results, but particularly the increase in upwards-bending with increasing proximity to the dome could not be confirmed.

1.1. Site description

The area was first surveyed on the ground during the Norwegian-British-Swedish Antarctic Expedition from 1949 to 1952 [*Glæver and Schytt*, 1963]. On Halvfarryggen, a "Half-Way-Depot" was established which eventually led to the unique name of the ice ridge ("ryggen"). The Y-shaped ridge faces the northern Weddel Sea and extends the grounded ice seawards, separating the Ekströmisen and Jelbartisen ice shelves to the West and East, respectively. The German overwintering station Neumayer III is located on the Ekströmisen ice shelf with an air-line distance of about 80 km to the dome of Halvfarryggen. The access route can be traveled within one day. Since 1987/88 Halvfarryggen accommodates on its western arm a stake array and a remote seismographic station which was upgraded in 1997 with several seismometers forming a seismic array. The stake field has been abandoned by now. High accumulation rates as well as the proximity to the Weddel Sea at intermediate elevation favour Halvfarryggen as a future drill site. For example direct measurements retrieved since 1983 at the nearby air-chemistry observatory of Neumayer III can be compared to shallow ice-core samples which improves the understanding of both, the deposition history, as well as the transport processes of aerosols to higher elevated areas like the Antarctic plateau. At intermediate depths, the high accumulation rates result in an increased vertical resolution which may be able to capture seasonal signals. Deep ice potentially covers the transition to the last glacial, but up to now age–depth estimates are uncertain at best. Within this study a new age–depth estimate will be established, based on an ice-flow model.

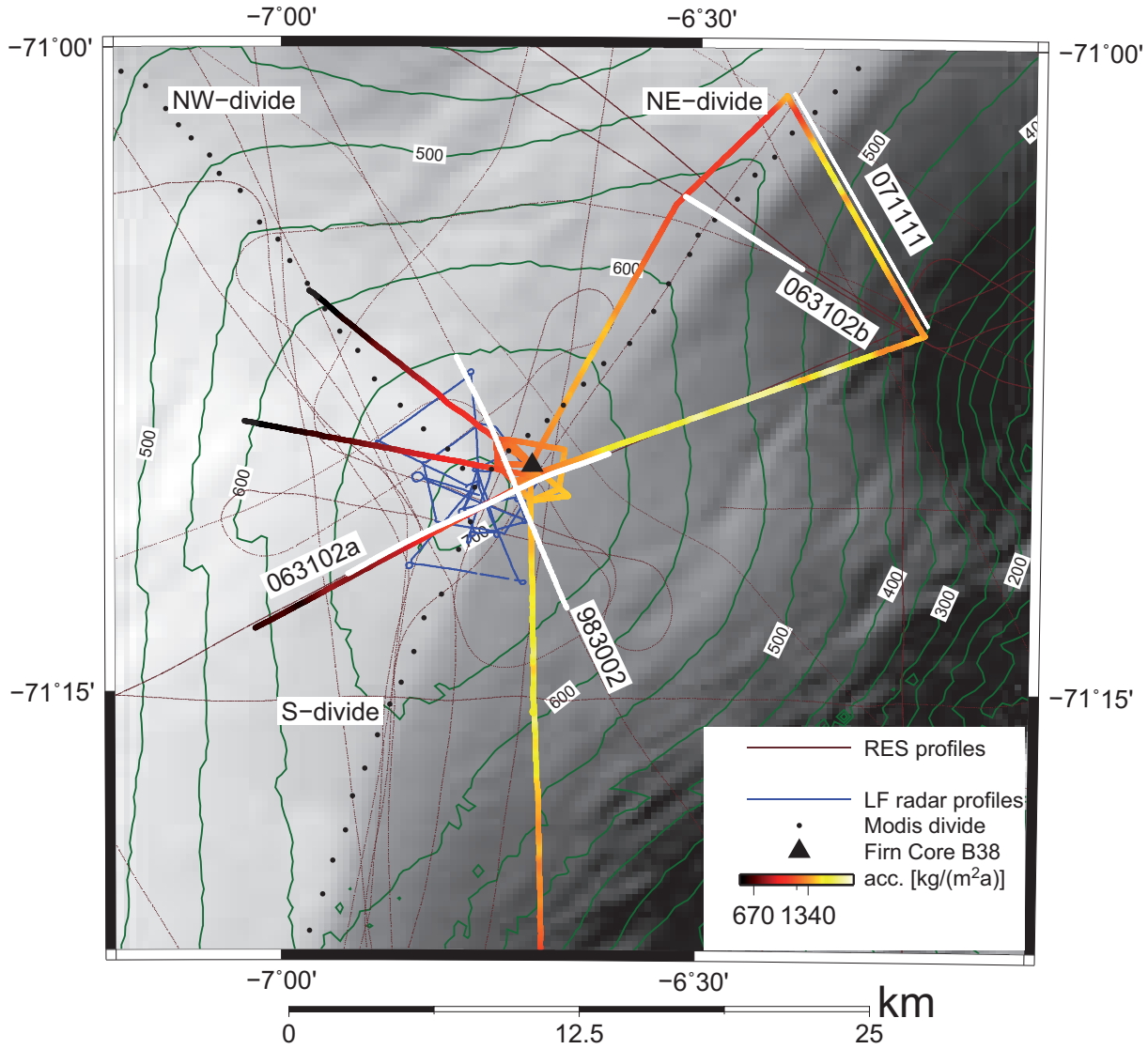

Figure 2. Overview of the airborne RES profiles (burgundy lines) and ground-based GPR (low-frequency GPR blue lines, higher frequency GPR color coded). The location of the firn core B38 is marked with a black triangle. Contour lines are based on merged elevation models explained in the text. The background image is clipped from MODIS data [*Scambos et al.*, 2002]. Sections of profiles shown in other Figures are marked with white lines.

2. Methods and Data

We investigate the internal layering by means of GPR and RES profiles. Primary outcomes are the spatial variation in accumulation, the bedrock topography, and the three-dimensional structure of the isochrone arch around the triple junction. Existing elevation models for Halvfarryggen are combined in order to get one good elevation model describing the surrounding of the dome. On-site GPS measurements together with air- and spaceborne laser altimetry data deliver ground control points for the evaluation of the individual and final elevation model. The position of ice divides is derived from satellite imagery. The next sections comprise a discussion of the radar profiles, followed by the derivation of surface topography, divide location, and accumulation rates.

2.1. Ground-based Radar

All of the radar systems emit an electromagnetic pulse in the downward direction and record the signal's reflections caused by dielectric non-uniformities within the travel path. Changes of dielectric properties in ice are primarily caused by variations in density, electrical conductivity, and COF. Internal changes in density and conductivity are linked to depositional events on the former surface and as such have isochronous character. Lateral coherent changes in the dielectric properties appear as internal reflection horizons (IRH) in the radargrams, which display amplitude vs. two-way traveltime (TWT)—or corresponding depth—of the individually recorded traces side by side.

A field campaign in 2007 mapped the upper 100 m with respect to accumulation (Figure 2). A follow-up campaign in 2010 used a low-frequency radar to image the geometry of the isochrone arch in the vicinity of the triple junction. The data from the field campaign in 2007 presented here have been acquired with a commercial shielded 100 MHz, bistatic GPR from Malå Geoscience. Shots were triggered approximately every meter in constant offset mode. Simultaneous measurements with a Trimble GPS receiver geolocate the profiles. The raw data is high pass filtered (lower cutoff frequency 5 MHz), bandpass filtered (lower/upper cutoff frequency 65 MHz/150MHz), and amplified with an automatic gain control window of 75 ns. More details of the acquisition

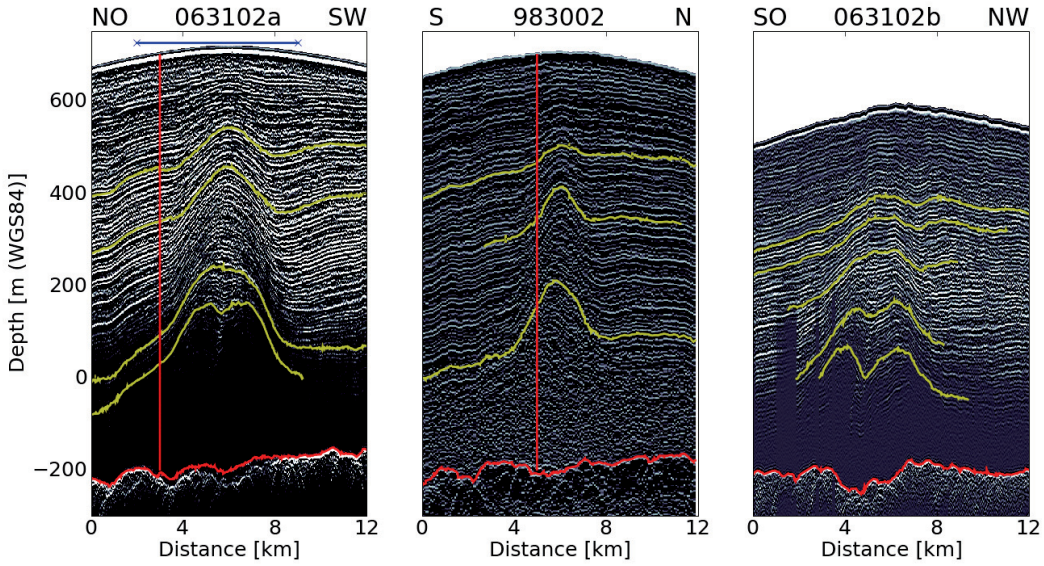

Figure 3. Radargrams of airborne RES profiles (marked with white lines in Figure 2), with picked horizons (yellow lines). The red vertical lines indicate the cross-over points of profiles 063102a and 983002. The picked red line marks the bedrock, the horizontal blue line at the top of profile 063102a indicates the overlap with a near-parallel ground-based radar profile in Figure 6. Isochrone arches are clearly visible in all three radargrams. Double bumps appear in the profiles 063102a and 0631202b at a depth of approx. 510 m and 370 m below the surface, respectively.

system, post-processing, and layer tracking are described by *Eisen et al.* [2004]. The profiles are arranged in a star-like pattern with six 13–20 km long legs, centered approximately 1 km to the North-East of the dome position (see Figure 2).

The survey in 2010 used a low-frequency radar with resistivity loaded dipoles [*Funk et al.*, 1994] and a transmitter as suggested by *Narod and Clarke* [1994]. The antenna length can be adapted for nominal frequencies of 3.75, 15, or 30 MHz. A Tektronix THS 730 A storage oscilloscope records the data and transfers it to a field laptop. The radar has been towed with a skidoo at a velocity of approximately 10 km/h. A Trimble GPS was mounted on the skidoo. Shots were taken at a constant time interval and interpolated via the GPS to 20 m postings during the post-processing. This corresponds to a horizontal stacking of about 2 shots per trace. The 15 MHz profiles are arranged pentagon-like, centered at the triple junction as picked from the MODIS Mosaic [*Haran et al.*, 2005]. The 30 MHz profiles are star-like and centered on the apex of the isochrone arch seen in the RES profile 063102a (see Figure 2 and Figure 3). Signal processing included static correction, bandpass filtering and background removal where necessary. The appliance of the background removal and the exact values of the cutoff frequencies varied between the individual profiles aiming to maximize contrast of internal layering in the upper 100–300 m.

2.2. Airborne Radar

Airborne RES profiles have been collected in the area of interest over a number of Antarctic field seasons within the years 1997–2011. The airborne radar system emits a pulse at a center frequency 150 MHz with an alternating pulse duration of 60 ns and 600 ns, resulting in a theoretical vertical resolution of 5 m and 50 m, respectively. In this toggle mode, the short pulse aims at imaging the internal structure of ice sheets, whereas the long pulse is designed for the sounding ice thickness. A radar altimeter records variations in flight altitude. Other key components and the technical specifications of the system have been described by *Nixdorf et al.* [1999] and *Steinhage et al.* [2001]. Standard signal processing of the airborne data encompasses ten or two fold stacking, differentiation, a hanning tapered low pass filtering (tapering window between 100 MHz and 150 MHz) and automatic gain control with a 100 ns time window. See *Steinhage et al.* [1999] for more details on the individual processing steps and the software used. Topographic corrections are done with local elevation models (see section Surface topography) after variations of flight altitude are compensated by means of the radar altimeter. Two fold stacked data has a horizontal shot spacing of ∼20 m, depending on the flight speed. The horizontal accuracy for the geolocation of the shots via the airplane's internal navigation system depends on the spatial baseline to available reference station, but it is usually considered to be accurate within $\pm 5 \pm 100$ m [*Nixdorf et al.*, 1999].The travel-time to depth conversion is done assuming a constant speed of light in ice of 169 m/μs [*Bogorodsky et al.*, 1985]. To correct for lower propagation velocity in the top firn layer, a constant offset of 13 m has been subtracted based on density profiles from firn cores in Dronning Maud Land.

2.3. Surface topography

Antarctic-wide elevation models are often based on spaceborne altimetry data [e.g. *Bamber et al.*, 2009], which perform well in areas with low surface slope, but deteriorate at the steeper margins of the Antarctic ice sheet [*Griggs and Bamber*, 2009]. In our area of interest the surface slope is relatively large and Antarctic-wide elevation models deviate up to hundreds of meters [*Wesche et al.*, 2009]. We therefore use three local elevation models: CW [*Wesche et al.*, 2009], RD [*Drews et al.*, 2009], and BB [*Bindschadler et al.*, 2011] to describe the topography near the summit of Halvfarryggen. The CW model interpolates between airborne radar altimetry data, complemented with spaceborne laser altimetry (ICESat), and ground-based GPS surveys. In particular the CW model incorporates the ground-based GPS

data from 2007. It is gridded to 1 km x 1 km. The RD model has been derived via differential SAR interferometry. It has the benefit of a higher horizontal resolution (50 m x 50 m grid), at the cost of partly unknown atmospheric contributions and a strong dependency on the coherence of the processed image pairs. The BB model is based on photoclinometry with data from the Enhanced Thematic Mapper Plus (ETM+) instrument on board the Landsat-7 satellite. It is gridded to 30 m x 30 m. The primary pitfall of this method is albedo variation caused by other factors than changing surface slope.

In order to get one single elevation model the individual models are sampled to a common 100 m x 100 m grid and compared with independent ground-truth data. For RD and BB the GPS data from the surveys in 2007 and 2010 are being used. In both GPS surveys a local reference station has been positioned in the center of the survey area to enable a differential post-processing with baselines smaller than 30 km. Details for the differential processing of the GPS data can be found in *Wesche et al.* [2009]. The estimated vertical accuracy from cross-over points within the individual surveys is in the sub-meter range. The 2010 GPS elevations have a 1.3±0.2 m offset compared to the 2007 GPS elevations. This may be caused by a real change in surface elevation or by and imprecise static solution for the local reference station which dependents on longer baselines to fixed reference stations. Additionally, profiles from an airborne laserscanner which are not incorporated in the CW model are being used. The vertical accuracy of the laserscanner data is discussed by *Helm et al.* [2007] and lies within the sub-meter range.

The ground control points from the GPS surveys and the airborne laserscanner enable the identification of weak areas in the individual elevation models. For example around the dome, the BB and CW model perform well, whereas the RD model deviates from the laserscanner and GPS data significantly (>40 m). However, in the larger vicinity (> 10 km) of the dome, the performance of the RD model improves. Based on the initial comparison with the control points, the individual models were masked in weak areas and then merged to a single elevation model. To minimize crossing edges, a 2-D cosine tapering function was applied at the boundaries and the RD model was additionally fitted to the BB model near the dome with a first-order polynomial function.

Eventually the grounded part of the merged elevation model is compared to all available ground control points, including ICESat data (GLA 12, Release 24, *Zwally et al.* [2003]). The comparison yields a mean and standard deviation of -0.4±11 m. In transitional areas of the different elevation models crossing edges inbetween 5–25 m are visible, at the north-western edge of Halvfarryggen they increase up to 50 m. However, in the vicinity of the dome no larger steps occur and the comparison with ground-truth data is within 10 m.

2.4. Divide location

Ice divides become evident in satellite imagery due to the dependency of backscattering on the surface slope. The divide location can be determined by following the transition between shaded and illuminated areas. In elevation models, ice divides run perpendicular to the contour lines and may be determined by finding maxima in profiles running perpendicular to the divides. In that case, vertical errors in the elevation model transfer into a horizontal misplacement of the divide location. This may be in the order of kilometers, since the slope near the divides is only around 0.002 (see red lines in Figure 4).

For determining the divide location from satellite images, the contrast of the scenes is enhanced, so that the transition between shaded and illuminated areas becomes more obvious. The derived line appears coherent in itself, but is inflicted with a systematic offset, compared to the ones based on other scenes. This offset depends on the illumination angle. To estimate the error, we picked the divides from different scenes with partly opposing look angles (MODIS(1) clipped from the MODIS Mosaic [*Haran et al.*, 2005], MODIS(2) from the MODIS image archive [*Scambos et al.*, 2002], and a clipped image from the Radarsat Mosaic [*Jetzek and RAMP-Product-Team*, 2002]). The results were compared with the 'true' divide locations derived from GPS transects (note that the GPS transects are not always perfectly perpendicular to the assumed divide position) . An example is shown for the two MODIS images in Figure 4. The Radarsat image does not have enough contrast in that area for a successful evaluation.

In spite of the uncertainty induced by differences in the look angle, picking the divides from satellite imagery seems superior compared to using the elevation model. As a result, points based on the MODIS(1) image were selected as they were closest to the GPS derived divide locations. The other solutions served as error estimates, which is ±750 m in the horizontal. In general the divides appear less clear when approaching the triple junction, and picking of the divides becomes more subjective.

2.5. Accumulation

In order to derive estimates for the spatial variation of accumulation we follow a standard procedure of accumulation mapping for example described by *Eisen et al.* [2008]. The relative distance of two continuous internal layers is converted into total accumulation by using density and age–depth data from the 85 m deep firn core B38 in the center of the profiles (see Figure 2). Details for the firn-core analysis are given by *Fernandoy et al.* [2010]. The age–depth relationship is known from the firn core via layer counting. The relation between two-way traveltime and depth is established using the empirical formula given by *Kovacs et al.* [1995]. It converts density to relative permittivity, which in turn determines the velocity profile in firn.

Error estimates for this approach are composed of errors in determining the depth of the reflectors, the cumulative mass above the reflectors, and their respective age. *Fernandoy et al.* [2010] estimates the dating uncertainty for the B38 core to be around ±1 year. The errors for the assigned depth and cumulative mass depend mainly on the density profile. For the B38 core this has been measured via the

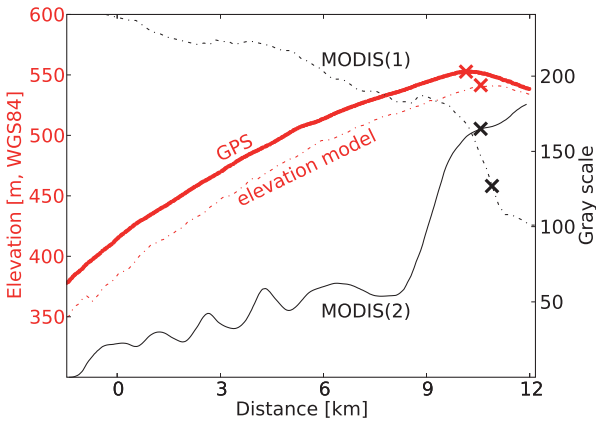

Figure 4. Different picks (x) for the ice-divide location, based on the elevation model and different MODIS scenes. The red continuous line marks the GPS transect (which is only near-perpendicular to the divide). See location for this profile (071111) in Figure 2.

absorption of γ-rays [*Wilhelms*, 2000] with a relative error of less than 1%. The spatial variation in density remains unknown but based on Sorge's law [*Bader*, 1954] we assume that on short time and spatial scales neither the age–depth profiles nor the density–depth profiles change considerably. Other studies summarized by *Eisen et al.* [2008] give error estimates within 5% for this approach, mostly caused by uncertainties in dating.

For the derivation of accumulation we chose two horizons which could be continued over the longest distance in the radar data. At the core site B38, these have a depth of 51.6 m and 63.0 m with a corresponding age of 27 years and 34 years before (January) 2007 AD, respectively. An excerpt of tracked horizons within the radar profile is shown in Figure 6. Accumulation estimates were calculated from the surface to the first layer, top to the second layer and between the first and second layer, each of them averaging different time periods. The results mostly differ by a constant offset. For the B38 firn core, *Fernandoy et al.* [2010] give an average accumulation of 1257 kg/(m^{2}a) with a standard deviation of 347 kg/(m^{2}a) averaged over a time period of 47 years. They observe a minimal positive trend towards higher accumulation rates in recent years. Across the isochrone arch, the relative distance between the two layers is also deformed by ice dynamics (see also Figure 6) and not solely influenced by a changing accumulation.

2.6. Modelling internal stratigraphy and the age–depth relationship

In order to estimate the dome's stratigraphy and age distribution, we use a transient thermo-mechanical full Stokes model that considers anisotropic rheology. The model is similar to those described in *Martín et al.* [2009a] and Gudmundsson and Martin (2011) **(Submitted paper that will be published prior to this study)**. We give a brief description of the model here and we refer the reader to those papers for details. The two-dimensional ice-flow submodel assumes plain strain across the ridge, a frozen ice–bedrock interface, and an outflow boundary condition with zeroth-order anisotropic shallow ice approximation that conserves the total ice mass. The temperature submodel assumes a uniform geothermal heatflux at the base, no horizontal temperature gradient at the margins and a uniform surface temperature. For the COF evolution, we presume that recrystallization processes do not occur and that the ice fabric is induced by deformation.

The primary model input is the topography of surface and bedrock and a non-uniform accumulation rate as described in the previous sections. The averaged surface temperature (-17.9°C) is taken from the AWS11 weather station near the summit (C. Tijm-Reijmer, pers. communication 2011) and since no measurements for the geothermal heatflux exist we assume 50 mW/m^2 which is often used as a modelling standard. The domain is chosen along the profile 063102a (Figure 3) which intersects the southern divide close to the dome and exhibits double-bumps in the lower third of the ice column. The accumulation rate along this profile is based on the underlying, quasi-parallel GPR line (Figure 2) and was smoothed with a linear regression.

The model outcomes are displayed in Figure 7 and compared to the internal stratigraphy as seen in the corresponding RES line 063102a.

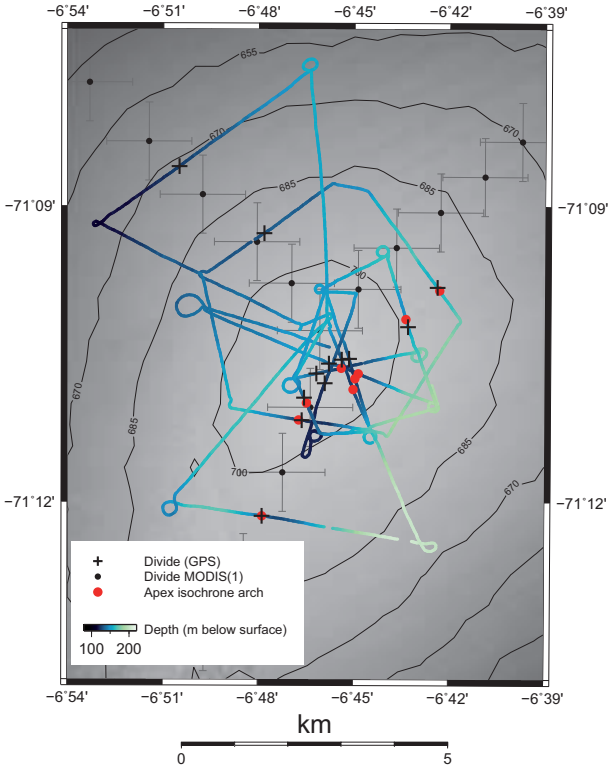

Figure 5. The spatial characteristics of the isochrone arch near the triple junction as seen in the low-frequency GPR profiles. The color code depicts the change in depth of an exemplary internal reflection horizon. The apices (red dots) are visible on the southern and north-eastern branch of the ice divides. The maxima in surface elevation of the GPS transects are marked with black crosses.

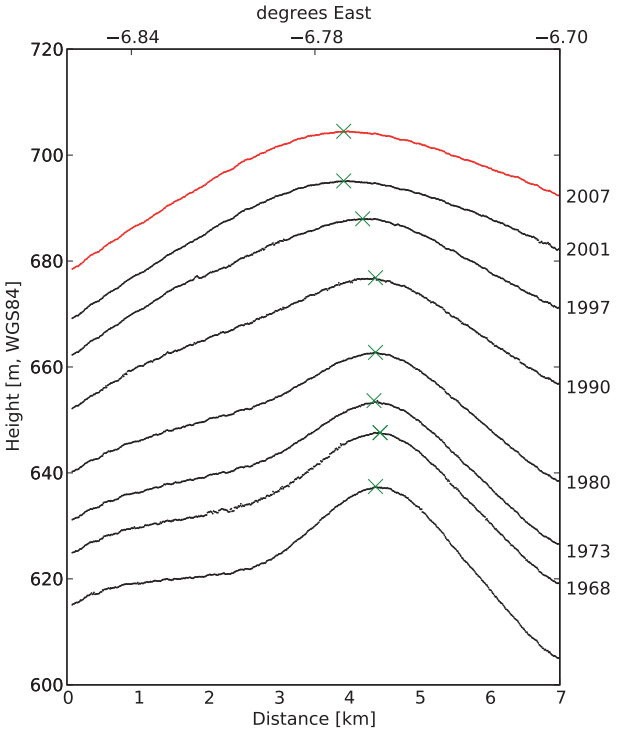

Figure 6. Internal reflection horizons (black lines) picked from the 100 MHz data parallel to the RES line 063102a (Figure 2). The isochrone arch develops in a depth of about 30–60 m below the surface (red). The apex (marked with crosses) has an offset with respect to the maximum surface topography of approximately 500 m to the East.

3. Results

3.1. Wind and topography induced accumulation pattern

The accumulation pattern derived from the 100 MHz data is depicted along the GPR profiles in Figure 2 by the color coded GPR lines. The western flank of Halvfarryggen has lower accumulation rates compared to the eastern side. The ice divides mark the boundary between the two regimes.

A map interpolated from point measurements [*Rotschky et al.*, 2007] confirms this general trend. However, for that study only one data point, located on the north-western side of Halvfarryggen, was available, which results in significantly lower absolute accumulation estimates than observed here. The analysis of the B38 and one higher elevated firn core [*Fernandoy et al.*, 2010] revealed higher accumulation rates at Halvfarryggen with a decreasing trend towards the North, and we confirm the gradient from East to West which was already speculated on by *Fernandoy et al.* [2010].

The automatic weather station AWS11 (run by the Institute for Marine and Atmospheric research in Utrecht) is located near the drill location of the firn core B38 (see Figure 2) and records data continuously since its deployment in 2007. The preferred wind direction originates from 110° (geographic) North, i. e. East-South-East, (C. Tijm-Reijmer, pers. communication 2011), indicating a strong influence of westerly low pressure systems. Therefore, it seems reasonable to assume that the recent accumulation pattern is dominated by orographic snowfall, which continuously deposits more snow on the eastern flank compared to the western flank, resulting in differences of up to 50%.

3.2. Divide characteristics

The highest points in the GPS profiles and the divide position as picked from MODIS data are shown in Figure 5. While the southern and north-western arm agree well in both datasets, the north-eastern divide based on MODIS appears shifted about 1.5 km further north compared to the peaks in the GPS profiles. The dome derived from the GPS data appears 1 km south-east of the MODIS based triple junction. We can only speculate on the origin of these differences, but the ice divides appear less clear in the MODIS imagery as they approach the triple junction. It is therefore likely, that the corresponding picks are misplaced, despite the apparent correspondence with the underlying elevation model.

Double-ridge features, as mentioned in the introduction, appear in the satellite imagery as faint lines, parallel to the divides. *Goodwin and Vaughan* [1995] analyzed examples from Landsat imagery of Fletcher Promotory and concluded, that these double-ridges are caused by subtle concavities in the surface topography which they measured with GPS profiles running perpendicular to the ice divide. In the case of Halvfarryggen, parallel lines to the divide are visible in full resolution satellite images, but their existence and specific location is subjective and by no means unambiguous.

In MODIS(1), a line of about 12 km south of the triple junction is visible on the eastern side of the divide. In the Radarsat Mosaic, both sides of the southern divide in this area are accompanied by dark lines, and also the north-western divide has a parallel line on its western side of roughly 13 km north of the triple junction. In MODIS(2) both sides of the north-eastern divide are accompanied by parallel lines, starting some 14 km north of the triple junction. All double-ridges disappear in the vicinity of the triple junction where also the divide itself is less clear in all images. In that area, the merged elevation models, as well as the GPS data which were acquired together with the radar profiles (Figure 2 and 3) do not show any concavities in the surface elevation (see for example the profile in Figure 4 crossing the north-western divide, or the profile in Figure 6 crossing the southern divide).

3.3. Horizontal extent of the isochrone arch

The GPR data map the area in the closer vicinity of the dome, and RES profiles image the larger surrounding. In the low-frequency data it becomes evident, that the maximum amplitude of the arch is approximately 1 km south-east of the (satellite-inferred) triple junction, which is close but not directly at the dome position as determined from the GPS data. An offset of 500 m to the East seems systematic and is also observed in the 100 MHz data (Figure 6). The isochrone arch extends beneath the southern branch and migrates to larger depths at the two northern branches. In particular it is not visible in the low-frequency data across the north-western part. Based on the results from the low-frequency survey, additional RES profiles were acquired in the season 2010/11.

Although it is generally difficult to trace individual layers across the isochrone arches, it was possible to connect the various RES profiles with the complementary dataset from 2011. In order to do so, we first chose prominent layers in profiles without an isochrone arch and crossed the divides either at points where no arch was evident, or where the layers across the arch could be distinguished. The more difficult sections with strong upward-bending beneath the divides were tackled once the horizons on both sides were fixed. A spatially interpolated horizon with an average depth of 260 m below the surface is displayed in Figure 8. It becomes evident that the isochrone arch beneath the southern divide slowly declines in amplitude and seems continuous up to 20 km from the triple junction. Below the north-eastern arm, the amplitude first declines with increasing distance from the triple junction, however, together with a decreasing surface slope the amplitude increases again. Below the north-western divide the isochrone arch is only faintly visible and decreases quickly with increasing distance from the triple junction.

3.4. Geometry of the isochrone arch along the vertical

In a 100 MHz profile that runs near-parallel to the RES line 063120a, the initial development of the isochrone arch can be observed (see Figure 6). The upwarping of layers starts at a depth of around 30–60 m below the surface. As mentioned above, the apex shifts to the East by about 500 m in this interval and remains stable below. The general shape of the isochrone arches at larger depths varies between the different RES lines. In most intersections the apices of the individual layers appear slightly tilted in the opposing direction of the bedrock slope (e.g. profiles 063102a and 063102b in Figure 3). It becomes increasingly difficult at larger depths to connect the different RES profiles and we cannot extent the downward-warping of the isochrone arch three dimensionally. However, the 'double-bump' feature is visible in multiple RES lines crossing the southern and the north-eastern divide. Flanking synclines can be observed in some profiles on the western side of the ice divide between $\sim$ 25–75 percent of the total ice-thickness. The internal layers on the eastern-side decline more rapidly and generally do not show a prominent flanking syncline.

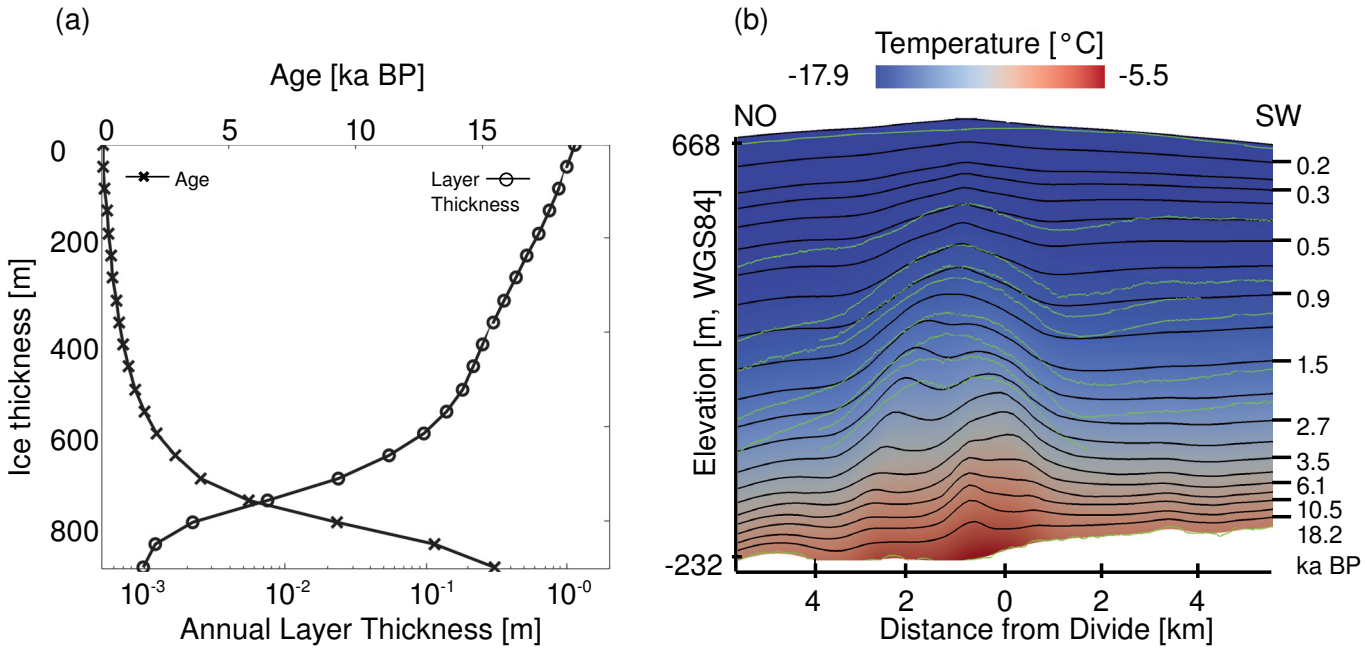

Figure 7. Model output along the RES line 063102a close to the dome (see Figure 3 for location), **(a)** shows the calculated age–depth relationship and the expected annual layer thicknesses at the divide position, **(b)** displays the modelled isochrones (black lines) in comparison to the measured RES layers (green lines). The temperature field is displayed in the background and predicts -5.5°C at the ice–bed interface.

3.5. Model outcomes

Ice-flow modelling along the RES line 063102a (Figure 7(a)) predicts about 13 ka (BP) old ice at 90% of the ice thickness beneath the divide. The corresponding annual layer thickness is approximately 1 mm. At larger depths the projected age exceeds 18 ka and indicates the existence of glacial ice. In 30–70% of the ice thickness the ice age ranges between 0.4–2.8 ka with a corresponding layer thickness of 0.4–0.06 m. The temperature at the ice–bedrock interface is estimated to be -6 °C . The model outcomes for quasi steady-state are displayed in Figure 7(b). The modelled surface topography places the ice flux divide position about 750 m to the East of the highest point in the elevation model. The topographic divide does not coincide with the flux divide due to the asymmetry in accumulation. The observed elevation differences are within the uncertainty of the satellite-based elevations. The modelled isochrones match the RES layers at the apices of the isochrone arches, but deviate with increasing distance from the divide. Particularly the strong descent in internal layering at the eastern flank is not reproduced. The slight tilt in the horizontal position of the apices towards the West is replicated and appears as a consequence of the bedrock slope.

4. Interpretation and Discussion

Radar studies and firn core analysis identify the summit region generally as a high accumulation site, with a large spatial variability due to a preferred wind direction from the South-East and the symmetrical alignment of Halvfarryggen towards the North. The variability in accumulation is associated with a variability in age–depth relationships, calling for a correct positioning of shallow drill locations which always compromise vertical layer resolution with the achievable age. The relatively shallow layering (>30 m depth) close to the divides and the dome is already affected by both, accumulation and ice dynamics (i. e. the Raymond effect). Therefore, a changing relative distance of internal layers cannot solely be interpreted as a spatial change in accumulation.

The merging of available elevation models results in a higher resolved map in the vicinity of the dome.

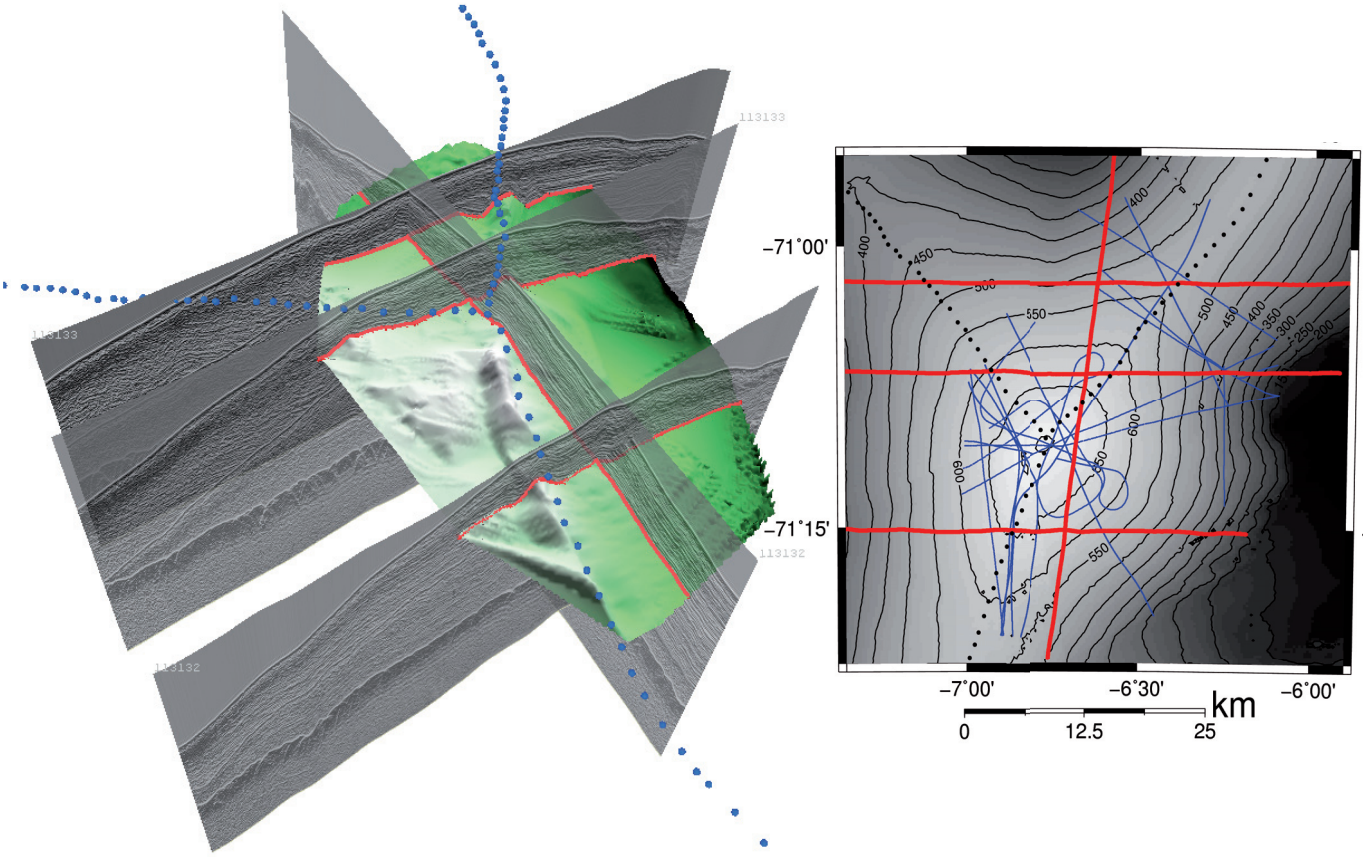

Figure 8. Left: Three dimensional representation of some RES profile near summit. The green surface is the interpolated surface of a picked horizon with an average depth of 260 m below the surface. The blue dots mark the location of the ice divides. **Right:** RES profiles (blue and red) that were used for the interpolation. The red lines mark the RES profiles shown on the left. In the background is the merged elevation model with 50 m contour lines.

However, although Halvfarryggen seems steep from the viewpoint of satellite altimeters, the elevation gradient at the dome and its surrounding is subtle in terms of deriving the ice divides, even with the help of ground-based GPS measurements. The offset between the highest point in surface topography and the apex of the isochrone arch near the dome is nevertheless visible in both, GPS and elevation model heights. Further away from the triple junction ($\sim$ 3 km) the offset ceases. We don't have conclusive evidence for what causes the observed offset. Potentially the southern divide migrated recently (within the last 10–20 years), or the offset is related to the different rheologies of firn and ice.

It seems likely, that the changing amplitude beneath the north-eastern divide and the weakly pronounced isochrone arch beneath the north-western divide are linked to the respective changes in surface topography and the corresponding along-ridge flow velocities. The modelled ice flow generally reproduces the internal architecture beneath the dome and relates the small horizontal tilt in apex positions to a sloped bedrock topography, and the appearance of double-bumps to an ice-dynamical induced anisotropic COF. Based on the model, the divide position has likely been stable over the last 10 ka. The mismatch of the two-dimensionally modelled isochrones and RES layers is probably due to three-dimensional effects and also changes in past accumulation patterns cannot be excluded. The underlying RES profile 063102a is not perpendicular to the ice divide, and the divide itself is inclined. Therefore, the RES layering is to a certain extent imprinted by along-ridge flow and mass is being redistributed across the divide plane. The mismatch when modelling the line 063102b increases, probably due to the same reasons. Nevertheless, near the apices the model replicates the internal stratigraphy well. According to the model results, the upward bending of layers in conjunction with the high accumulation rates favours potential ice core studies targeting the time-frame of 500–2000 a. At larger depths, the transition into the last glacial may also be resolved. Therefore, the site is promising particularly for the goals of the IPICS 2k array, providing large annual layer thicknesses. At a larger depths, the

potential presence of ice from the last termination make it also suitable for the IPICS 40k array objectives.

From an ice-dynamical point of view the two-dimensional approach gives good insight in terms of what to expect for the age–depth relationship and the anisotropy in COF. The derived datasets are also suited as boundary conditions for a three dimensional modelling study (as done in *Gillet-Chaulet and Hindmarsh* [2011]) which may help to constrain the anisotropic rheology of ice further and improve the understanding of the complex internal stratigraphy around triple junctions.

5. Summary

In this study we derived an elevation model and located the ice divides via a combination of different remote sensing techniques with ground control points. The internal layering was investigated by means of airborne RES and ground-based GPR surveys. Analysis of the top layers reveals a strong spatial variation in accumulation which appears to be driven by a preferred wind direction and changing surface slope. Starting 30–60 m below the surface the layers beneath the dome start to bend upwards due to the Raymond effect. At the dome, we observe a small offset of the apices compared to the highest point in the surface topography. Isochrone arches without offset are also observed beneath the other divides. The characteristics of the isochrone arches around the triple junction is not symmetric which is primarily attributed to the large gradient in accumulation and changing along-ridge flow. Based on the ice-flow model, the vertical alignment of the isochrone arches beneath the dome points to a long-term stability of the dome position, with an anisotropic COF giving rise to the formation of double bumps below the divides and most likely also beneath the dome. Seismic surveys in the same area observe internal reflection horizons, which hint towards a layered strata of changing COF (pers. communication C. Hofstede, 2011). High accumulation rates and the upward bending of internal layers favour Halvfarryggen as drill site for studies which require a high vertical resolution in the time frame of 500–2000 a BP. At larger depths ice from the transition into the last glacial period is to be expected.

Acknowledgments. Preparation of this work was supported by the Emmy Noether-programme of the Deutsche Forschungsgemeinschaft Grant EI 672/5 to O. Eisen and a scholarship of the Evangelisches Studienwerk e.V. Villigst to R. Drews. We thank V. Helm for the airborne laser scanner data, and C. Tijm-Reijmer and M.R. van den Broeke (both at the Institute for Marine and Atmospheric research Utrecht, Netherlands) for providing the data from the automatic weather station AWS11. We thank M. Funk at the Laboratory of Hydraulics, Hydrology and Glaciology, ETH, Zürich, Switzerland for providing details of the low-frequency radar antenna design. Initial ideas for comparison of data and models at Halvfarryggen are based on discussions with R. Hindmarsh and C. Martín during a stay at the British Antarctic Survey, funded by the SCAR fellowship scheme 2006-7 and a Emmy Noether-scholarship of the Deutsche Forschungsgemeinschaft Grant EI 672/1 to O. Eisen.

References

Bader, H., Sorge's Law of densification of snow on high polar glaciers, *Journal of Glaciology*, *2*, 319–323, 1954.

Bamber, J. L., J. L. Gomez-Dans, and J. A. Griggs, A new 1 km digital elevation model of the antarctic derived from combined satellite radar and laser data part 1: Data and methods, *The Cryosphere*, *3*, 101–111, 2009.

Bindschadler, R., et al., Getting around antarctica: new high-resolution mappings of the grounded and freely-floating boundaries of the antarctic ice sheet created for the international polar year, *The Cryosphere Discussions*, *5*, 183–227, 2011.

Bogorodsky, V., C. Bentley, and P. Gudmandsen, *Radioglaciology*, D. Reidel Publishing Co., 1985.

Brook, E., E. W. Wolff, D. Dahl-Jensen, H. Fischer, and E. Steig, The future of ice coring: International Partnerships in Ice Core Sciences (IPICS), *PAGES News*, *14*, 6–10, 2006.

Conway, H., B. L. Hall, G. H. Denton, A. M. Gades, and E. D. Waddington, Past and Future Grounding-Line Retreat of the West Antarctic Ice Sheet, *Science*, *286*, 280–283, 1999.

Drews, R., W. Rack, C. Wesche, and V. Helm, A Spatially Adjusted Elevation Model in Dronning Maud Land, Antarctica, Based on Differential SAR Interferometry, *IEEE Transactions on Geoscience and Remote Sensing*, *47*, 2501–2509, 2009.

Eisen, O., U. Nixdorf, F. Wilhelms, and H. Miller, Age estimates of isochronous reflection horizons by combining ice core, survey, and synthetic radar data, *Journal of Geophysical Research - Solid Earth*, *109*, 2004.

Eisen, O., et al., Ground-based measurements of spatial and temporal variability of snow accumulation in East Antarctica, *Reviews of Geophysics*, *46*, RG2001, 2008.

Fernandoy, F., H. Meyer, H. Oerter, F. Wilhelms, W. Graf, and J. Schwander, Temporal and spatial variation of stable-isotope ratios and accumulation rates in the hinterland of neumayer station, east antarctica, *Journal of Glaciology*, *56*, 673–687(15), 2010.

Funk, M., G. H. Gudmundsson, and F. Hermann, Geometry of the glacier bed of the Unteraarglacier, Bernese Alps, Switzerland., *Zeitschrift f. Gletscherkunde und Glazialgeologie*, *30*, 187–194, 1994.

Gillet-Chaulet, F., and R. C. A. Hindmarsh, Flow at ice-divide triple junctions i: three-dimensional full-stokes modelling, *Journal of Geophysical Research*, *116*, F02,023, 2011.

Glæver, V., and V. Schytt, *General Report of the Expedition, Norwegian-British-Swedish Antarctic Expedition, Scientific Results*, vol. 6, Norsk Polarinstitutt, 1963.

Goodwin, A. H., and D. G. Vaughan, A topographic origin for double-ridge features in visible imagery of ice divides in Antarctica, *Journal of Glaciology*, *41*, 483–489, 1995.

Griggs, J. A., and J. L. Bamber, A new 1 km digital elevation model of antarctica derived from combined radar and laser data part 2: Validation and error estimates, *The Cryosphere*, *3*, 113–123, 2009.

Haran, T., J. Bohlander, T. Scambos, and M. c. Fahnestock, MODIS mosaic of Antarctica (MOA) image map., *Boulder, CO, USA: National Snow and Ice Data Center. Digital media.*, 2005.

Helm, V., W. Rack, R. Cullen, P. Nienow, D. Mair, V. Parry, and D. J. Wingham, Winter accumulation in the percolation zone of Greenland measured by airborne radar altimeter, *Geophysical Research Letters*, *34*, L06,501, 2007.

Hindmarsh, R. C. A., Stochastic perturbation of divide position, *Annals of Glaciology*, *23*, 105–115, 1996.

Hindmarsh, R. C. A., E. C. King, R. Mulvaney, H. F. J. Corr, G. Hiess, and F. Gillet-Chaulet, Flow at ice-divide triple junctions ii: three-dimensional views of isochrone architecture from ice-penetrating radar surveys, *Journal of Geophysical Research*, *161*, F02,024, 2011.

Jacobson, H. P., and E. D. Waddington, Recumbent folding of divide arches in response to unsteady ice-divide migration, *Journal of Glaciology*, *51*, 201–209, 2005.

Jetzek, V., and RAMP-Product-Team, RAMP AMM-1 SAR Image Mosaic of Antarctica, *Fairbanks, AK: Alaska Satellite Facility, in association with the National Snow and Ice Data Center, Boulder, CO. Digital media*, 2002.

Kovacs, A., A. J. Gow, and R. M. Morey, The in-situ dielectric constant of polar firn revisited, *Cold Regions Science and Technology*, *23*, 245 – 256, 1995.

Martín, C., G. H. Gudmundsson, H. D. Pritchard, and O. Gagliardini, On the effects of divide migration, alongridge flow, and basal sliding on isochrones near an ice divide , *Journal of Geophysical Research*, *114*, 2009a.

Martín, C., G. H. Gudmundsson, H. D. Pritchard, and O. Gagliardini, On the effects of anisotropic rheology on ice flow, internal structure, and the age-depth relationship at ice divides, *Journal of Geophysical Resarch*, *114*, F04,001, 2009b.

Narod, B. B., and G. K. C. Clarke, Miniature high-power impulse transmitter for radio-echo sounding, *Journal of Glaciology*, *40*, 190–194, 1994.

Neckel, N., Surface velocities in the hinterland of the Neumayer III station (Antarctica) derived from SAR-Interferometry, Master's thesis, Universität Heidelberg, Fachbereich Geographie, 2011.

Nereson, N., and C. Raymond, The elevation history of ice streams and the spatial accumulation pattern along the Siple Coast of West Antarctica inferred from ground-based radar data from three inter-ice-stream ridges, *Journal of Glaciology*, *47*, 303–313(11), 2001.

Nereson, N., C. Raymond, R. Jacobel, and E. Waddington, The accumulation pattern across siple dome, west antarctica, inferred from radar-detected internal layers, *Journal of Glaciology*, *46*, 75–87(13), 2000.

Nereson, N. A., and C. F. Raymond, Recent migration of siple Dome ice divide determined from 1994 radio-echo sounding measurements, *Antarctic Journal U.S.A (Review)*, *27*, 207–214, 1996.

Nereson, N. A., and E. D. Waddington, Isochrones and isotherms beneath migrating ice divides, *Journal of Glaciology*, *48*, 95–108(14), 2002.

Nereson, N. A., R. C. A. Hindmarsh, and C. F. Raymond, Sensitivity of the divide position at Siple Dome, West Antarctica, to boundary forcing, *Annals of Glaciology*, *27*, 207–214, 1998a.

Nereson, N. A., C. F. Raymond, E. D. Waddington, and R. W. Jacobel, Migration of the Siple Dome ice divide, West Antarctica, *Journal of Glaciology*, *44*, 643–652, 1998b.

Nixdorf, U., D. Steinhage, U. Meyer, L. Hempel, M. Jenett, P. Wachs, and H. Miller, The newly developed airborne radio-echo sounding system of the AWI as a glaciological tool, *Annals of Glaciology*, *29*, 231–238(8), 1999.

Pettit, E. C., and E. D. Waddington, Ice flow at low deviatoric stress, *Journal of Glaciology*, *49*, 359–369(11), 2003.

Pettit, E. C., H. P. Jacobson, and E. D. Waddington, Effects of basal sliding on isochrones and flow near an ice divide, *Annals of Glaciology*, *37*, 370–376, 2003.

Pettit, E. C., T. Thorsteinsson, H. P. Jacobsen, and E. D. Waddington, The role of crystal fabric in flow near an ice divide, *Journal of Glaciology*, *53*, 277–288(12), 2007.

Raymond, C. F., Deformation in the vicinity of ice divides, *Journal of Glaciology*, *29*, 357–373, 1983.

Rotschky, G., P. Holmlund, E. Isaksson, R. Mulvaney, H. Oerter, M. Van den Broeke, and W. J., A new surface accumulation map for western Dronning Maus Land, Antarctica, from interpolation of point measurments., *Journal of Glaciology*, *53*, 385–398, 2007.

Sandhäger, H., Review of the münster airborne radio-echo sounding data set; marine ice beneath filchner-schelfeis; bottom reflectivity and internal structures of berkner island, *FRISP Report*, *9*, 111–114, 1996.

Scambos, R., J. Bohlander, and B. Raup, Images of Antarctic ice shelves, updated 2011, *Boulder, CO, USA: National Snow and Ice Data Center. Digital media.*, 2002.

Schøtt-Hvidberg, C., Steady-state thermomechanical modelling of ice flow near the centre of large ice sheets with the finite-element technique, *Annals of Glaciology*, *23*, 116–123, 1996.

Seddik, H., R. Greve, T. Zwinger, and L. Placidi, A full stokes ice flow model for the vicinity of dome fuji, antarctica, with induced anisotropy and fabric evolution, *The Cryosphere*, *5*, 495–508, 2011.

Steinhage, D., and N. Blindow, First results of short pulse radio echo sounding on the top of berkner island, *FRISP Report*, *9*, 123–126, 1996.

Steinhage, D., U. Nixdorf, U. Meyer, and H. Miller, New maps of the ice thickness and subglacial topography in dronning maud land, antarctica, determined by means of airborne radio-echo sounding, *Annals of Glaciology*, *29*, 267–272(6), 1999.

Steinhage, D., U. Nixdorf, U. Meyer, and H. Miller, Subglacial topography and internal structure of central and western dronning maud land, antarctica, determined from airborne radio echo sounding, *Journal of Applied Geophysics*, *47*, 183 – 189, 2001.

Vaughan, D. G., H. F. J. Corr, D. C. S. M., and E. D. Waddington, Distortion of isochronous layers in ice revealed by ground-penetrating radar, *Nature*, *398*, 323–326, 1999.

Waddington, E. D., J. F. Bolzan, and R. B. Alley, Potential for stratigraphic folding near ice-sheet centers, *Journal of Glaciology*, *47*, 639–648(10), 2001.

Wesche, C., S. Riedel, and D. Steinhage, Precise surface topography of the grounded ice ridges at the ekstrmisen, antarctica, based on several geophysical data sets, *ISPRS Journal of Photogrammetry and Remote Sensing*, *64*, 381 – 386, 2009.

Wilhelms, F., Measuring the Dielectric Properties of Polar Ice Cores, *Berichte zur Polarforschung*, *367*, 171, 2000.

Zwally, H. J., R. Schutz, C. Bentley, J. Bufton, T. Herring, J. Minster, J. Spinhirne, and R. Thomas, GLAS/IceSAT L2 Antarctic and Greenland Ice Sheet Altimetry Data V001, *Boulder, Colorado USA: National Snow and Ice Data Center. Digital media.*, 2003.

D. Getting around Antarctica: New high-resolution mappings of the grounded and freely floating boundaries of the Antarctic ice sheet created for the International Polar Year

Own contribution: Participation at the workshop for the International Polar Year project "Antarctic surface accumulation and ice discharge" (March 10–12 at NASA Goddard Space Flight Center, Greenbelt, USA; Principal Investigator R. Bindschadler); Provision of InSAR data and delineation of grounding zone for the Halvfarryggen area; Participation in writing the manuscript and creating of Figure 2.
Current status: published.

The Cryosphere, 5, 569–588, 2011
www.the-cryosphere.net/5/569/2011/
doi:10.5194/tc-5-569-2011

The Cryosphere

Getting around Antarctica: new high-resolution mappings of the grounded and freely-floating boundaries of the Antarctic ice sheet created for the International Polar Year

R. Bindschadler[1], H. Choi[2], A. Wichlacz[2], R. Bingham[3], J. Bohlander[4], K. Brunt[5], H. Corr[6], R. Drews[7], H. Fricker[8], M. Hall[9], R. Hindmarsh[6], J. Kohler[10], L. Padman[11], W. Rack[12], G. Rotschky[10], S. Urbini[13], P. Vornberger[2], and N. Young[14]

[1]Code 614.0, NASA Goddard Space Flight Center, Greenbelt, MD 20771, USA
[2]SAIC, NASA Goddard Space Flight Center, Greenbelt MD 20771, USA
[3]School of Geosciences, University of Aberdeen, Aberdeen, AB24 3FX, UK
[4]National Snow and Ice Data Center, University of Colorado, Boulder CO 80309-0449, USA
[5]Code 614.1, NASA Goddard Space Flight Center, Greenbelt MD 20771, USA
[6]British Antarctic Survey, High Cross, Madingley Road, Cambridge, CB3 0ET, UK
[7]Alfred Wegener Institut for Polar and Marine Research, Postfach 12 01 61, 27515 Bremerhaven, Germany
[8]Scripps Institute of Oceanography, University of California at San Diego, 9500 Giman Drive, La Jolla CA 92093, USA
[9]Climate Change Institute, University of Maine, Orono ME 04469, USA
[10]Norwegian Polar Institute, Polar Environmental Centre, 9296 Tromso, Norway
[11]Earth and Space Research (ESR), 3350 SW Cascade Ave., Corvallis, OR 97333-1536, USA
[12]Gateway Antarctica, University of Canterbury, Private Bag, Christchurch 8140, New Zealand
[13]Istituto Nazionale di Geofisica e Vulcanologia, Via di Vigna Murata, 605, 00143 Rome, Italy
[14]Australian Antarctic Division, University of Tasmania, Kingston, Tasmania 7050, Australia

Received: 28 December 2010 – Published in The Cryosphere Discuss.: 19 January 2011
Revised: 22 June 2011 – Accepted: 27 June 2011 – Published: 18 July 2011

Abstract. Two ice-dynamic transitions of the Antarctic ice sheet – the boundary of grounded ice features and the freely-floating boundary – are mapped at 15-m resolution by participants of the International Polar Year project ASAID using customized software combining Landsat-7 imagery and ICESat/GLAS laser altimetry. The grounded ice boundary is 53 610 km long; 74 % abuts to floating ice shelves or outlet glaciers, 19 % is adjacent to open or sea-ice covered ocean, and 7 % of the boundary ice terminates on land. The freely-floating boundary, called here the hydrostatic line, is the most landward position on ice shelves that expresses the full amplitude of oscillating ocean tides. It extends 27 521 km and is discontinuous. Positional (one-sigma) accuracies of the grounded ice boundary vary an order of magnitude ranging from ±52 m for the land and open-ocean terminating segments to ±502 m for the outlet glaciers. The hydrostatic line is less well positioned with errors over 2 km. Elevations along each line are selected from 6 candidate digital elevation models based on their agreement with ICESat elevation values and surface shape inferred from the Landsat imagery. Elevations along the hydrostatic line are converted to ice thicknesses by applying a firn-correction factor and a flotation criterion. BEDMAP-compiled data and other airborne data are compared to the ASAID elevations and ice thicknesses to arrive at quantitative (one-sigma) uncertainties of surface elevations of ±3.6, ±9.6, ±11.4, ±30 and ±100 m for five ASAID-assigned confidence levels. Over one-half of the surface elevations along the grounded ice boundary and over one-third of the hydrostatic line elevations are ranked in the highest two confidence categories. A comparison between ASAID-calculated ice shelf thicknesses and BEDMAP-compiled data indicate a thin-ice bias of 41.2 ± 71.3 m for the ASAID ice thicknesses. The relationship between the seaward offset of the hydrostatic line from the grounded ice boundary only weakly matches a

Correspondence to: R. Bindschadler
(robert.a.bindschadler@nasa.gov)

Published by Copernicus Publications on behalf of the European Geosciences Union.

prediction based on beam theory. The mapped products along with the customized software to generate them and a variety of intermediate products are available from the National Snow and Ice Data Center.

1 Introduction

One of the most basic features of the Antarctic ice sheet is its boundary. However, even utilizing the broad spatial coverage afforded by satellite data, comprehensively mapping the boundary of a region the size of Antarctica is an inherently challenging undertaking. The International Polar Year 2007–2009 (IPY) called for benchmark data sets and provided the motivation for the mapping reported here. The broader goals of that IPY project, called Antarctic Surface Accumulation and Ice Discharge (ASAID) are yet to be completed, but the ASAID intermediate products described here have extensive applicability beyond the specific project goals.

The boundary of the grounded ice sheet includes a variety of situations: glacier tongues, where the ice thickness gradually decreases to zero; ice cliffs, where ice breaks off and falls onto the ground or sea ice or into the ocean; and ice shelves, where ice flows into the ocean and remains attached to the grounded ice sheet until it calves, forming icebergs. The last case of flow from grounded ice into floating ice shelves has received considerable attention because it is the dominant situation in Antarctica and represents a significant dynamic shift in the stress state that has challenged ice-flow modelers (see Schoof, 2007 for a recent treatment of the transitional ice dynamics). This case also is complicated by the effects of oscillatory ocean tides that alter the grounded state of ice in the vicinity of the ice sheet boundary and can dramatically alter the speed of the discharging ice sheet (Anandakrishnan et al., 2003; Bindschadler et al., 2003; Wiens et al., 2008). These complexities are worth tackling because it is across this interface that the ocean influences the ice sheet (through the ice shelf) (e.g., Payne et al., 2004, 2007; Joughin et al., 2010) and changes of the interior grounded ice sheet are amplified as they propagate toward this boundary. It is also in this region that the changes in both ice thickness and ice velocity are largest (as expected by ice dynamics theory) (Shepherd et al., 2002; Thomas et al., 2004; Pritchard et al., 2009). The relatively low subglacial bed slopes in these areas (slopes of 10^{-3} to 10^{-5} are typical) amplify relatively small local changes in ice thickness to relatively large horizontal shifts in the boundary between grounded and floating ice, illustrating the value of repeatedly mapping this boundary as a sensitive indicator of change.

In the region where the seaward-flowing ice sheet loses contact with the bed, part of the ice sheet is ephemerally grounded by ocean tides and the connected ice shelf is prevented from fully floating by beam stresses transmitted from the grounded ice. Care is required to ensure that comparisons between seemingly equivalent data sets do not lead to false conclusions of change. We present new mappings of two important boundaries in this region of the ice sheet: the first is the seaward boundary of surface morphology associated with grounded ice and the second is the landward boundary of freely floating ice shelves. In addition to the positions of these two boundaries, surface elevations of the ice along these boundaries are also extracted from various digital elevation data sets along with a calculation of ice-equivalent ice-shelf thickness (including a correction for lower density firn in the upper layers of the ice shelf). Independent data compiled by BEDMAP (Lythe et al., 2001) are used to quantify the accuracy of the elevations and ice thicknesses assigned to our boundaries. Finally, the separation between the boundaries is examined with a beam flexure theory.

2 The grounding zone

Attempts to define the boundary of the grounded ice sheet and a floating ice shelf have led to the concept of a "grounding line". However, the term "grounding line" has been applied to available data sets employing different methodologies, some sensitive to different topographic or dynamic features of the region. The use of a single term to refer to different boundaries invites confusion within the science community. The differences in various "grounding lines", including a careful comparison among a number of "grounding lines", have been discussed most completely in Fricker et al. (2009).

Far offshore, a floating ice shelf will rise and fall an amount equal to the tidal variations of the ocean in which it floats. However, closer to shore, the stiffness of the ice and the fact that ice well inland is securely resting on the subglacial bed will limit the amount of vertical deflection experienced within the marginal region. The general situation is illustrated in Fig. 1: location F refers to the most seaward point not vertically displaced by tidal flexure even at the highest tide; G is the location where the ice loses contact with the bed (at low tide); I_b and I_m represent inflections of the surface slope where the slope changes most rapidly (the "slope break") and where the slope is zero (the "hinge line valley"), respectively; and H is the most landward location that experiences vertical motion equal to the magnitude of the tide. Oscillating ocean tides interacting with the floating fringe of the ice sheet will move the point of initial ungrounding landward and seaward as the tide rises and falls.

The boundary in the grounding zone presented in this paper is determined primarily by interpreting the seaward limit of the region of grounded ice features in optical imagey and secondarily from derived surface elevations. Thus, we refer to it as the "ASAID grounded ice boundary". It is most consistent with point I_b, the slope break, in Fig. 1. Interferometric analysis of multiple synthetic aperture radar images (InSAR) detects the band of flexure between locations F and H (Fricker et al., 2009); Rignot (1996) refers to the landward

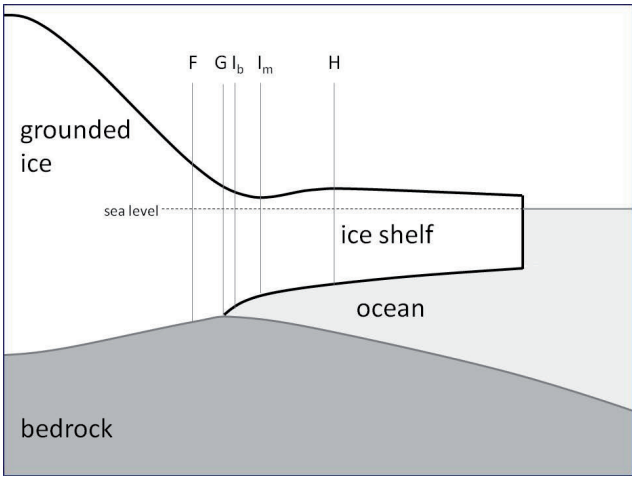

Fig. 1. Schematic of cross-section through the margin of the Antarctic ice sheet. F refers to the most seaward point not vertically displaced by tidal flexure; G is the point where the ice loses contact with the bed (at low tide); I_b and I_m represent inflection points of the surface slope; and H is the most landward point that experiences full tidal flexure (adapted from Fricker et al., 2009). The ASAID grounded ice boundary is most consistent with point I_b.

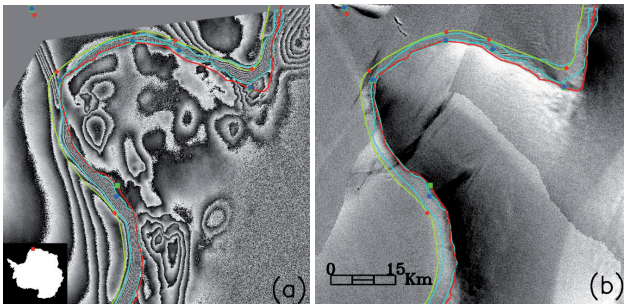

Fig. 2. Section of Antarctic coast (Halvfarryggen Ridge on the Princess Martha Coast with Ekström Ice Shelf on left) 71.6 km × 69.7 km comparing mappings of different features of the grounding zone with different methods. **(a)** Interferometric fringe pattern produced by InSAR methods and **(b)** an enhanced subset of the Landsat Image Mosaic of Antarctica. Cyan lines represent edges of the tidally flexed grounding zone between points F and H (see Fig. 1). Symbols are key points of the grounding zone identified from repeat-track GLAS elevation profiles (F, green square; I_b, blue circle; H, red diamond). Red and green lines are ASAID grounded ice boundary and hydrostatic lines, respectively.

limit of this flexure zone as the "hinge line". Repeat laser altimetry can often detect F and H from repeat-track analysis and I_b and I_m from single profiles (Yamanokuchi et al., 2005; Fricker and Padman, 2006).

Which boundary within the grounding zone is relevant will usually depend on the nature of the science question being posed. The grounded ice boundary we delineate has dynamic significance: the presence of a grounded ice surface morphology demonstrates that not only is the ice contacting the bed, but the ice "feels" the bed sufficiently to react to the stresses associated with this contact resulting in an ice sheet geometry that creates stresses within the ice to accommodate the stresses at the bed. This is distinctly different from identifying an area that becomes grounded briefly during lower tide levels and for which there is no discernable change in the geometry of the ice sheet even though the velocity may be modulated by the tidal oscillations (Anandakrishnan et al., 2003; Bindschadler et al., 2003; Wiens et al., 2008).

Figure 2 illustrates boundaries in the grounding zone from these different approaches for a portion of Antarctic margin near the Ekström Ice Shelf and Neumayer Station. There is broad agreement between the region of flexure zone, defined by the band of dense InSAR fringes, the I_b and H points, defined by the GLAS analysis, and the delineation of the grounded ice boundary, interpreted from the Landsat imagery (discussed in more detail later). However there are some differences, such as in the upper left of the scene where the flexure zone narrows while the hydrostatic line, guided only by the few GLAS points, remains farther offshore. In the inlet near the upper right corner of Fig. 2, the ASAID grounded ice boundary passes farther inland than the band of dense InSAR fringes, but agrees with the I_b point (blue circle) determined from GLAS data. There will always be some differences between boundaries within the grounding zone produced by these different methods, at times due to incorrect interpretation or data quality and availability, but also because different features are being detected. Our observations of the differences between the different boundaries in the grounding zone determined by these various methods, now including the ASAID grounded ice boundary and hydrostatic line, match those discussed and illustrated at greater length in Fricker et al. (2009).

Previous mappings of the "grounding line" based on satellite optical imagery have been produced and are available through data centers. Two of these familiar to many Antarctic researchers are the "grounding line" contained in the Antarctic Digital Database (ADD) (http://www.add.scar.org:8080/add/index.jsp), where the latest revisions were based on prints of Landsat imagery at 1:250 000 scale, and a "grounding line" mapped from the MODIS Mosaic of Antarctica (MOA) at 125-m resolution (Bohlander and Scambos, 2007). A third partial mapping is being released incrementally as coastal change maps (Ferrigno et al., 1996 and http://pubs.usgs.gov/imap/2600/). Each of these mapped boundaries corresponds to either the most rapid change in surface slope (e.g., I_b in Fig. 1) or an end of grounded ice (in the case of terminating ice cliffs or grounded glacier tongues). Because each uses a similar visual interpretative method to ASAID, they are comparable to each other and to the ASAID grounded ice boundary. Figure 3a illustrates differences between these various boundary products. It appears the data base used in the ADD boundary in this region contained

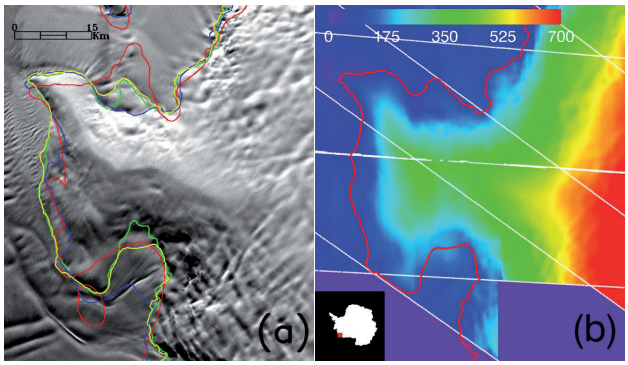

Fig. 3. Section of Antarctic coast (Scott Peninsula along Bakutis Coast) approximately 60 km × 69 km. **(a)** Enhanced Landsat image comparing various image-based mappings of the "grounding line" or grounded ice boundary: red, Antarctic Digital Database; blue, USGS Coastal Change map series; green, MODIS Mosaic of Antarctica; yellow, ASAID. **(b)** Color-coded surface elevations (in meters above mean sea level) derived from ASAID application of photoclinometry using image on left and GLAS elevation profiles. Thin white lines show the location of GLAS profiles interpolated by photoclinometry. ASAID grounded ice boundary from **(a)** is reproduced (now in red).

some significant geolocation errors and it is possible some aerial photography may have been included since some portions of this persistently cloudy coast were never adequately imaged with the early Landsat instruments. Reduced spatial or feature acuity might have also contributed to the discrepancies in the ADD boundary. The MOA line is more accurate than the ADD in defining the overall shape of the coastal feature, but at times deviates from the other interpretations when coastal features associated with lightly grounded ice and transitions to the floating ice shelf are encountered. There also are some differences between the USGS coastal change maps and ASAID that we attribute to the fact that the USGS procedure used paper prints of lower resolution Landsat images while ASAID could vary the enhancement of any image in a digital environment to optimize the visual appearance of any local region as different conditions of topography and illumination orientation were encountered along the coast.

3 Data

The primary data sets used to define and provide surface elevations of the grounded ice boundary and hydrostatic line are images from the Enhanced Thematic Mapper Plus (ETM+) instrument onboard the Landsat-7 satellite and surface elevation profiles measured by the Geoscience Laser Altimeter System (GLAS) onboard the Ice, Cloud, and Land Elevation Satellite (ICESat). The Landsat data were used in the construction of the Landsat Image Mosaic of Antarctica, another IPY project (Bindschadler et al., 2008). This image set consists of mostly cloud-free images. They also cluster within a relatively narrow time window (1999–2003). All images were accessed from the USGS EROS Data Center, usually by ftp-download after a visual review of possible candidate images that cover the appropriate region of the ice sheet perimeter. 196 images of this collection cover the entire grounded ice boundary to 82.5° S. Farther south, two ASTER images provide coverage that complete the Ronne Ice Shelf portion of the grounded ice boundary, and imagery from MOA is used to complete the southernmost section of the Ross Ice Shelf. For all but the MOA imagery, the panchromatic band image was visually interpreted at full 15-m resolution (panchromatic band) to identify the grounded ice boundary (cf., Fig. 3a).

GLAS/ICESat data of precise surface elevation information along satellite groundtracks is used in three different ways. The first two uses employ the set of F, I_b and H points available from the National Snow and Ice Data Center (Brunt et al., 2010a). The locations of most rapid slope change I_b, determined along single profiles are used to help confirm the identification of the grounded ice boundary based primarily on the imagery. The H locations, determined by a differencing technique employing repeat GLAS passes collected at different phases of the tide to reveal the tidal flexure of the ice shelf as described in Fricker et al. (2006), are used to determine the position of the hydrostatic line. The third use of the GLAS elevation profile data are in combination with the ETM+ images to produce surface elevation fields through application of photoclinometry (Wildey, 1975; Bindschadler and Vornberger, 1994).

4 Methods

To satisfy the IPY objectives of international collaboration and inspiring young researchers, the ASAID project invited partners across the world to participate. Customized software was created, along with appropriate documentation describing standardized procedures so that the eventual aggregate product is as uniform as possible. The Antarctic perimeter was divided into a number of segments with different ASAID participants accepting responsibility for mapping portions of the grounded ice boundary and producing photoclinometric elevation fields for that segment (the hydrostatic line and elevation selection were completed at the end of the project exclusively at NASA Goddard Space Flight Center). The software is designed so that the participant's results are written to files with standardized names, facilitating both review of the data at NASA Goddard, but also easing the combination of multiple participant results into a single aggregate. Ultimately, all data products were reviewed by the Principal Investigator (Bindschadler, 2010) and final responsibility for their content and quality rests there.

4.1 Grounded ice boundary

Our procedure starts with selecting a particular ETM+ image covering the desired section of the Antarctic perimeter and downloading it from USGS EROS Data Center website. The ASAID software uses the image metadata supplied with the image to determine the sun azimuth for the image and rotates the image to a sun-at-the-top orientation (required for the later photoclinometry procedures). The software then displays the rotated image on a computer monitor and superimposes the location of ICESat reference groundtracks on the image. Actual groundtracks usually lie within 100 m of the reference groundtracks. Next, to reduce computer memory requirements and file sizes, the user defines sub-images to work on that encompass sections of the expected grounded ice boundary and include ICESat tracks near the top and bottom edges of the sub-image (so a photoclinometric elevation field spanning most of the sub-image can be produced). Once the sub-images are defined, each is written to a separate file directory and the GLAS data for that region are parsed from the complete set of GLAS data (provided to each ASAID user) and also written to the same directory. The GLAS data used are the GLA06 product (Release 28 and 29) from observation periods 2A (4 October 2003 to 19 November 2003) through 3K (4 to 19 October 2008) (Zwally et al., 2003). Both releases include an ocean tide correction which was retained; however, the saturation correction (i_satElevCorr) was only applied to Release 28 data as advised by ICESat data product experts (J. Saba, personal communication, 2009). The processed files provide surface elevation values at ground points spaced roughly 172 m apart along the actual groundtracks.

At this point, the user visually reviews the individual GLAS profiles for each reference track (using customized ASAID software) and selects the profiles most suitable for photoclinometry. Only one profile for each reference track is permissible. Averaged profiles are not used because individual profiles are often separated by tens and sometimes hundreds of meters and the individual laser footprint locations are not aligned. The coastal region of Antarctica is often cloudy, producing large and/or multiple gaps in the profiles. Our application of photoclinometry requires a GLAS elevation both up-sun and down-sun as starting and ending points for the interpolated. In general, the "best" profiles selected are usually the most continuous profiles because they provide the most complete photoclinometrically derived elevations along the grounding ice boundary.

Photoclinometry is then applied within the sub-image to produce elevation values at all image points between GLAS profiles using interpolations based on the image pixel brightnesses (Wildey, 1975; Bindschadler and Vornberger, 1994). The technique has been extensively developed for ice sheets where the existence of a homogenous surface of nearly constant albedo satisfies an important assumption for successful application of the technique. Image pixel brightness is related to surface slope by

$$\mathrm{DN} = A\cos\theta + B \quad (1)$$

where DN is the pixel brightness (in sensor units of digital number); θ is the angle between the solar illumination and the surface normal; coefficient A is the product of the solar irradiance, the surface reflectivity and the factor converting radiance to sensor DN units; and B is a bias due the sensor zero-radiance offset and atmospheric scattering (Bindschadler and Vornberger, 1994). In most ice sheet situations, B is negligible and we also choose to make this assumption. Equation (1) is applied independently for each image segment lying between an up-sun GLAS profile and a down-sun GLAS profile. Interpolation distances are kept as short as possible to minimize interpolation errors. To ensure that the GLAS profiles are continuous at the pixel scale, each profile is linearly interpolated across the standard GLAS point spacing of about 170 m as well across data gaps as large as 450 m. Larger gaps remain unfilled which can lead to longer interpolation segments and can create gaps in the elevation field. For each image segment, Eq. (1) is applied after solving for that segment's unique value of the scaling coefficient, A, using values of the average slope and image average brightness along that segment. This method ensures that the GLAS elevations along profiles remain unchanged although it can produce slight discontinuities between adjacent image segments when the scaling parameter for adjacent image segments varies significantly. These cross-profile discontinuities are sometimes referred to as "curtains" and are more severe the longer the interpolation segments become. The 8-bit quantization of Landsat DN values also contributes randomly to discontinuities between tracks. Alternative implementations of Eq. (1) were considered, but the GLAS data were deemed to be the best-known elevation information, so these values remain fixed. No attempt was made to smooth the resulting discontinuities because, in general, the calculated elevation fields in constant albedo areas lacked artifacts such as these curtains. Figure 3b shows the photoclinometrically derived elevation field for the image in Fig. 3a as well as the pattern of selected GLAS profiles used as control for that elevation field. The angled boundaries of the elevation field in the lower portion of the figure result from the requirement that there be an up-sun and down-sun GLAS elevation point for every interpolation segment.

While photoclinometry is very successful over much of the ice sheet perimeter, conditions of albedo variation not related to surface slope are encountered in some regions that made portions of the photoclinometric results unusable. These conditions include open (dark) ocean, exposed rock and open crevasses. An alternate elevation field is created from the GLAS elevations by applying a Delaunay triangulation scheme. In this instance, only the GLAS data are used; the image data are ignored entirely. The quality of the result varies by location, dependent primarily on the density

of GLAS profiles, but also on the topographic variation of the region. Other, more sophisticated interpolation methods were examined, but they had the propensity for very large errors over sparsely sampled, undulated topography. Ultimately, our more conservative approach was deemed preferable because it provided an elevation value close to the GLAS values and is reliable in providing a value when no other elevation methods work.

At this stage, with the image providing a nadir view of the sub-image region and the derived elevation field providing a view of the three-dimensional shape of the area, the boundary of the grounded ice features is drawn. Both data sets are linked in separate displayed windows on the computer monitor so that cursor movements can be followed in both windows. To assist the user, the displayed range of either gray-scale (of the image) or color scale (of the elevation field) can be adjusted and the user can zoom the displays to view detail at the 15-m pixel level. Guiding the cursor, the user either draws a continuous line, or clicks discrete points that the computer connects with linear segments, displaying the new grounded ice boundary on the image. The MOA "grounding line" is also displayed and provides useful guidance in areas where the ETM+ radiometric resolution (even with adjustable contrast applied by the user) fails to resolve important subtleties of the surface. In other areas, the increased spatial resolution of ETM+ enables corrections to the MODIS "grounding line" (cf., Fig. 3a).

The primary visual guide to tracing the precise location of the grounded ice boundary over most of the ice sheet perimeter is the visual detection of a change in image brightness that corresponds to the localized slope break between a relatively steep slope on the grounded ice and a relatively shallow slope seaward. The smoother surface of either the floating ice shelf or the fast sea ice relative to the more undulated surface associated with grounded ice features emphasizes this boundary. Marine features, such as offshore icebergs, sea ice lead and floe structures, or open ocean assist in identifying non-grounded regions. However, even with these numerous clues, defining the boundary at the full 15-m resolution is often challenging because the spatial scale of the transition can be many pixels wide. In such regions, the ability to change the image enhancement and zoom to any scale greatly assists precise positioning of the grounded ice boundary. In some regions, the GLAS profiles are useful in precisely locating the point of maximum slope change and the software allows single profiles to be displayed with a linked cursor function that ties position along the profile to the image at the single pixel level.

Bare rock is very easily identified, but uncertainty regarding the possible presence of seasonal snow often requires judgments as to the inclusion or exclusion of individual patches of bare rock within the ice sheet boundary. These situations often have a fractal nature to them and some smoothing is applied by both the operator's initial drawing and by post-drawing software (described later) to be practical. Some false extension of the ice sheet is possible due to seasonal snow and future monitoring of the ice sheet boundary in regions prone to this effect should be evaluated carefully.

The most challenging sections of the grounded ice boundary to identify are where fast-moving glaciers discharge into ice shelves. In these cases, the glacier is readily identified by surface undulations and the ice shelf by the absence of similar undulations, but the precise position of the boundary between the two is frequently difficult to locate accurately where the undulations become less dense and less distinct gradually. In general, the grounded ice boundary is drawn immediately seaward of the most downstream undulations and other features that appear to be formed by ice flow over regions of basal resistance and upstream of ice shelf features such as ice rumples or isolated ice rises. In these regions, the 8-bit radiometric resolution of the Landsat imagery often is stretched to its limit and the better 12-bit radiometric resolution of the MODIS sensor enables detection of more subtle surface undulations. For this reason, in many outlet glacier cases, the MOA imagery is examined alongside the Landsat imagery and, when the MOA imagery shows additional grounded ice features, the ASAID grounded ice boundary follows the trace of the MOA "grounding line".

The typically shallow surface and bed slopes in this type of region are well documented and have led to the recognition of lightly grounded ice plains (Thomas et al., 1988; Alley et al., 1989; Corr et al., 2001). These areas also probably exhibit a wide grounding zone, so large differences between the grounded ice boundary, as we define the seaward limit of grounded ice features in the surface morphology, and the hinge line, as identified in InSAR or altimetry data, are to be expected. Nevertheless, the regions that contain visible surface expressions of grounded ice are regions where the ice feels the bed strongly enough that the shape of the ice adjusts to the basal stresses, whereas the absence of these features indicates the ice does not feel the bed enough to change its shape and, with it, its internal stresses. This makes the grounded ice boundary a metric of the internal ice dynamics and, thus, is an important feature to map and to monitor, even on large fast outlet glaciers, regardless of its relation to the hinge line.

The work described above was completed for each sub-image, each in its own file directory. Combining these individual segments into a single continuous grounded ice boundary around the main ice sheet involves many additional steps. Each sub-image's grounded ice boundary is visually reviewed and, if necessary, revised, amended or corrected. There were 319 individual boundary segments that were combined. Gaps and overlaps between segments are corrected with additional editing. The two largest gaps occur south of 82.5° S, beyond Landsat coverage. On the Ronne Ice Shelf, three ASTER images are used in an equivalent manner and on the Ross Ice Shelf the MOA image is used, also as a proxy for Landsat imagery. In these areas, ICESat coverage

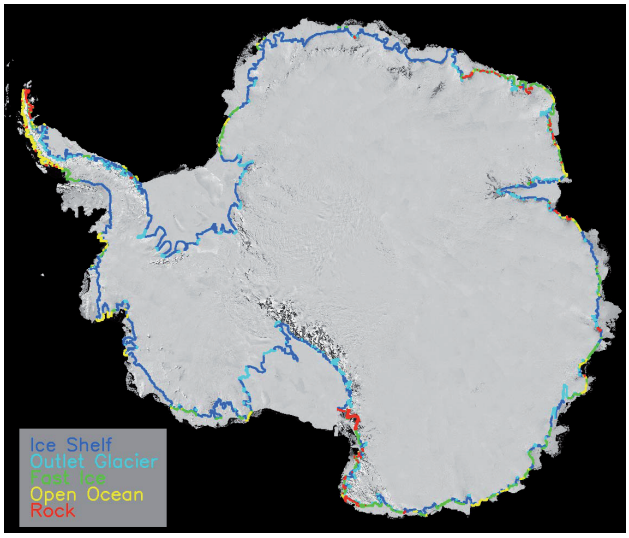

Fig. 4. The ASAID grounded ice boundary displayed on the Landsat Image Mosaic of Antarctica. Line color represents the type of transition for ice transiting the grounded ice boundary. The corresponding percent frequencies of occurrence are: Ice Shelf (dark blue, 61 %); Outlet Glacier (cyan, 13 %); Fast Ice (green, 10 %); Open Ocean (orange, 9 %); and Rock (red, 7 %).

is plentiful, and the photoclinometric elevation fields are high quality, providing an excellent information base from which the grounded ice boundary is drawn. Finally, to remove the unavoidable "jitters" and "stair-steps", inherent in either a hand-drawn or piecewise-linear line, the drawn lines are smoothed before joining segments. The smoothing approach used a forward-looking algorithm wherein the direction of the redrawn grounded ice boundary is guided by the direction of the next few drawn points rather than only the next point. The details of this approach are provided in separate documentation that will accompany the archived data files (discussed later).

Figure 4 shows the final grounded ice boundary produced by these procedures. It is 53 610 km long and contains 3 574 365 points at a 15-m resolution. The convoluted nature is less apparent at this scale, but for comparison's sake, the length of the 72° latitude line is 12 350 km. The colors in Fig. 4 indicate the nature of the ice transition at each point along the grounded ice boundary. Each boundary point was determined to be one of five categories: ice shelf; outlet glacier; fast (sea) ice; open ocean; and rock (or land). The number of points and percentage frequencies in each of these transition categories is given in Table 1. The common characteristics defining the outlet glacier class are: a spatially confined flow region, the presence of flow stripes oriented along the expected flow direction, and/or the presence of features on the ice shelf suggestive of a concentrated discharge from the grounded ice sheet. The extent of the outlet glacier was usually taken as the cross-flow "gate" and did not include any margin-parallel segment (that being assigned as an "ice shelf" transition). Differences between the categories of fast ice (which includes possible seasonal sea ice) and open ocean are ephemeral, depending on the specific date of the image used. On-land terminations, where the ice sheet thins to a vanishingly thin wedge adjacent to bare rock, are often highly convoluted and sometimes complicated by seasonal snow cover.

Table 1. Distribution of Antarctic Ice Sheet Grounded Ice Boundary Categories.

Transition Category	# of Points	
Ice Shelf	2 175 363	61 %
Outlet Glacier	478 883	13 %
Fast Ice	361 044	10 %
Open Ocean	325 876	9 %
Rock	233 182	7 %
Total	3 574 348	100 %

Nearly three-quarters (74 %) of the ice passing the grounded ice boundary transitions to an ice shelf (the combination of the ice shelf and outlet glacier categories). The fast ice and open ocean categories combine to a sub-total of 19 % of the grounded ice boundary, indicating that portion of the ice sheet that flows directly into the ocean and is not connected to an ice shelf fed by the grounded ice sheet. Finally, 7 % of the grounded ice boundary, the vast majority of which occurs in the Dry Valleys region near the northwest corner of the Ross Ice Shelf and the northeastern Antarctic Peninsula, terminates on land above sea level. This relatively high value is associated with the extreme serpentine nature of the grounded ice boundary in these valley incised mountains and includes a few, relatively small, outlet glaciers that terminate on land.

4.2 Hydrostatic line

The hydrostatic line is mapped using the same ASAID software as the grounded ice boundary mapping, but rather than following a brightness feature in satellite imagery, it is drawn such that it is tied to each H point supplied in the $F/I_b/H$ data set derived from repeat-track analysis of GLAS profiles (Brunt et al., 2010a). Between these points, the hydrostatic line is drawn to reflect the general shape of the grounded ice boundary. The smoother shape of the hydrostatic line is intentional, expressing the diffusion of beam supporting stresses onto the ice shelf as has been noticed in interferometric data analyses.

The hydrostatic line can only exist where there is floating ice mechanically connected to the grounded ice sheet, so it is discontinuous around the ice sheet. It occurs predominantly where the grounded ice transitions either to an ice

shelf or to an outlet glacier, but includes a few places where the grounded ice boundary wraps around a coastal nunatak and a continuous ice shelf exists on the seaward side of that nunatak. In some areas, there are no, or widely spaced H points, however, in general, the seaward offset of the hydrostatic line from the grounded ice boundary varies only slowly along the hydrostatic line, increasing our confidence that a reasonably accurate mapping of this feature is possible. An analysis of the seaward offset of the hydrostatic line from the grounded ice boundary appears later. Overall the hydrostatic line contains approximately 1.67×10^6 points for a total distance of 27 521 km, considerably shorter than the grounded ice boundary, reflecting its smoother, discontinuous nature.

While some segments of the ASAID hydrostatic line are poorly constrained by wide spacings between the H points, there are at least two reasons to attempt its definition. The first is associated with the ultimate goal of ASAID which is to quantify ice discharge. The H point is defined as the point on an ice shelf closest to land that responds fully to tidal oscillations (Fricker and Padman, 2006). Thus its freeboard is independent of the tidal amplitude and its thickness can be calculated from its surface elevation if the densities of the ice shelf and sea water are known. This enables a means to calculate ice thickness and, when combined with surface velocity (equal to column-averaged velocity on an ice shelf), the discharge can be calculated. This is a valuable set of conditions and even though such discharge calculations will not include basal melting landward of the hydrostatic line, when combined with discharge values at either the hinge line or the grounded ice boundary, they represent another discharge gate and will contribute to quantifying the basal melt between the more-landward gate and the hydrostatic line. A second, more general, reason to map the hydrostatic line is that, just as the grounded ice boundary represents a dynamic boundary separating ice that feels (and does not feel) the bed stresses sufficiently to affect the geometry of the ice, the hydrostatic line represents the boundary beyond which the beam stresses transmitted by the grounded ice sheet through the most-landward portion of the ice shelf are no longer felt. Thus, the hydrostatic line represents another type of dynamic boundary directly related to the transmission of stresses through the ice. As conditions within and around the ice shelf change, the position of the hydrostatic line will change, so mapping and monitoring the hydrostatic line holds the promise of identifying change at the sensitive margins of the Antarctic ice sheet and can be a check on changes inferred from changes in the position of other marginal boundaries (e.g., the hinge line or the grounded ice boundary).

4.3 Positional accuracy

Landsat-7 imagery has a general geo-registration precision of 50 m (one-sigma) (Lee et al., 2004). This precision was confirmed by the misfits experienced with the imagery when the Landsat Image Mosaic of Antarctica (LIMA) was produced (Bindschadler et al., 2008). Each image was orthorectified, using the RADARSAT Version-2 DEM as part of the LIMA image processing procedure, so this correction is included in the Landsat images used here. Later we establish that in the coastal areas the RADARSAT Version-2 DEM contains errors, as do other DEMs, and while these are generally a few tens of meters, they can exceed 100 m in places. Viewing angles in Landsat imagery are small (less than 10° at the image edge) limiting the impact of orthorectification errors on positional errors, and the elevations along the grounded ice boundary are only a few tens of meters. The end result is that orthorectification-induced positional errors are less than 15 % of the elevation error and can be neglected in most cases.

The error in the identification of the grounded ice boundary on an image varies with the nature of the boundary. When the transition type is either open ocean or rock, the boundary is able to be drawn to the nearest pixel. When a sea-ice transition occurs, the boundary is slightly less obvious, depending on the height difference between the surfaces of the grounded ice and the sea ice and the orientation of the sun relative to the direction of the transition boundary. In general, this boundary can be determined to two pixels (30 m). When the transition consists of slowly flowing grounded ice flowing into a floating ice shelf, the slope break is usually prominent and by zooming in sufficiently to resolve individual pixels, the boundary can be traced to the nearest 3 pixels (45 m). The grounded ice boundary is extremely serpentine. This character limits instances where a slope break is hard to see because it is both straight and oriented in the direction of the solar illumination. The least accurate delineation of the grounded ice boundary is across the mouths of outlet glaciers and ice streams. Here the accuracy varies enormously, based primarily on the spatial density and magnitude of the grounded ice features. As discussed above, the MODIS-based "grounding line" is often relied upon in these instances, but even in that lower resolution image space, the grounded ice features have diffuse edges so we assign a four MODIS pixel error (500 m) error to this boundary. The georegistration and delineation errors are the two major sources of positional error, so overall, our estimates of the positional errors (one-sigma) for the grounded ice boundary are the root-squared-sum of these two contributions: $\pm$52 m for the open ocean and rock boundaries; $\pm$58 m for the sea ice boundaries; $\pm$67 m for the ice shelf boundaries; and a much larger $\pm$502 m for the outlet glacier boundaries.

The positional accuracy of the hydrostatic line is much poorer. This line is pinned to the H points determined from the repeat ICESat pass analysis and interpolated in between. The positional uncertainty of individual H points from all factors included in their estimation method is stated as $\sim$2000 m (Brunt et al., 2010b). Interpolation of the hydrostatic line is only guided by the shape of the nearby grounded ice boundary and likely introduces a few additional

kilometers error. As such, we view the ASAID hydrostatic line as an initial estimate of the actual position that will be significantly revised once additional repeat pass altimetry or InSAR data of sufficient precision are collected and analyzed.

4.4 Elevations

In the coastal regions of Antarctica, the assumptions required for accurate photoclinometry are violated frequently enough and GLAS elevations are sparse enough that the assignment of elevations to points along either the grounded ice boundary or the hydrostatic line requires the consideration of additional digital elevation models (DEMs). There are a number to choose from, but each has weaknesses in particular regions or is incomplete, so no single elevation data set is sufficient by itself. Thus, our approach considers a number of elevation values in parallel and allows us to select the "best" elevation values based on their adherence to both nearby GLAS data and the shape of the local ice sheet surface inferred from the Landsat imagery and the GLAS data.

The elevation data sets considered include the photoclinometric and triangulation DEMs already discussed. In addition, a DEM based on a combination of radar and laser satellite altimetry (Bamber et al., 2009) and another based primarily on elevations in the Antarctic Digital Database (ADD) in coastal areas and ERS-1 radar altimetry in the ice sheet interior which was used by the RADARSAT project data (Liu et al., 2001) are included. The former, called here the "altimetry" DEM, specifies surface elevations on 1-km postings while the RADARSAT Version-2 DEM provides elevations on 400-m postings. Both are resampled to our 15 m grid using a bi-linear interpolation scheme. Finally, two stereo image-based photogrammetric DEMs are included: the G-DEM based on ASTER stereo imagery (http://www.ersdac.or.jp/GDEM/E/index.html) and, in a few available areas, local DEMs based on stereo SPOT imagery provided by the SPIRIT project (another IPY activity) (Korona et al., 2009). All elevation data sets are converted to a common mean sea level reference by using the EGM96 geoid referenced to the WGS-84 ellipsoid.

Additional customized software was developed to accommodate the needs of this elevation-selection task. The work returns to the sub-image level because the photoclinometric and triangulation DEMs exist only for each separate sub-image. For any sub-image, each DEM grid is interpolated to extract that DEM's elevation values along the trace of the grounded ice boundary. These boundary-following elevation profiles are superimposed on a single display plot (using distinct colors for each DEM) along with single elevation values corresponding to where GLAS elevation profiles cross the grounded ice boundary. Figure 5 shows an example of the computer screen produced by this software. In additional on-screen windows, the photoclinometric, altimetric, RADARSAT and ASTER DEMs are displayed as shaded relief images, rotated and illuminated to simulate the original Landsat sub-image. These shaded relief images are an excellent means to highlight subtle artifacts in each DEM, providing another test of each DEM's fidelity in matching the surface topography (cf., Fig. 5).

With this visual information, the operator is able to select a portion of the grounded ice boundary, define the best source of elevation data along that segment, and assign a quality (or confidence) rating to those elevations. GLAS data are regarded as "truth", so elevation values close to the GLAS data are weighted heavily in choosing the preferred elevation source, as well as in rating its quality, but a profile that matches the perceived shape of the surface along the grounded ice boundary is also important. The ability to define the preferred elevation in segments based on the relative, and shifting, strengths of the various elevation sources removes the dependence of the chosen elevations on a single elevation source and is both a critical software feature and an important characteristic of the ASAID products. Further, the ability to define the beginning and ending of each segment enables the preferred DEM source to switch at crossing points, thus avoiding a discontinuity in the profile of chosen elevations. Not all discontinuities are avoided, however, particularly in the case of small gaps in an otherwise preferred DEM. This was especially true for the SPIRIT DEMs that cover only limited areas and for the ASTER G-DEM that is hampered by the application of an inaccurate coastal mask that omits elevations in regions where it appears that excellent elevations might have been provided in the unmasked, but unfortunately unavailable, DEM. Where discontinuities occur, the quality rating is set to "Poor" (least confident rating) to acknowledge the fact that at least one chosen elevation is incorrect. An additional selectable elevation of "sea level" is available to identify the many instances of the grounded ice boundary occurring with a transition to the open ocean. No DEM correctly captures the elevation discontinuity at these locations. In these cases, the DEMs are ignored and an elevation of zero is specified. This occurs in 9 % of the grounded ice boundary points (cf., Fig. 4 and Table 1).

Figure 6a shows the preferred elevation source for each point along the ASAID grounded ice boundary; percentage amounts are also given and repeated in Table 2. The photogrammetric DEMs (from ASTER and SPOT) were chosen most frequently; nearly a third (33 %) of all elevations. The photogrammetric technique was particularly well adapted to the rugged topography along the coasts of the Antarctic Peninsula, the Dry Valleys and Victoria Land (the northern portion of the Transantarctic Mountains). The use of photogrammetric elevations probably would have been larger if more DEMs were produced by the SPIRIT project, the ASTER G-DEM data were not poorly masked, or the coverage of either extended south of 82° S. (Note: the unmasked G-DEM data no longer exist but a second version is scheduled for completion in 2011 with the masking issue yet undecided.) Photoclinometric elevations were selected 26 % of

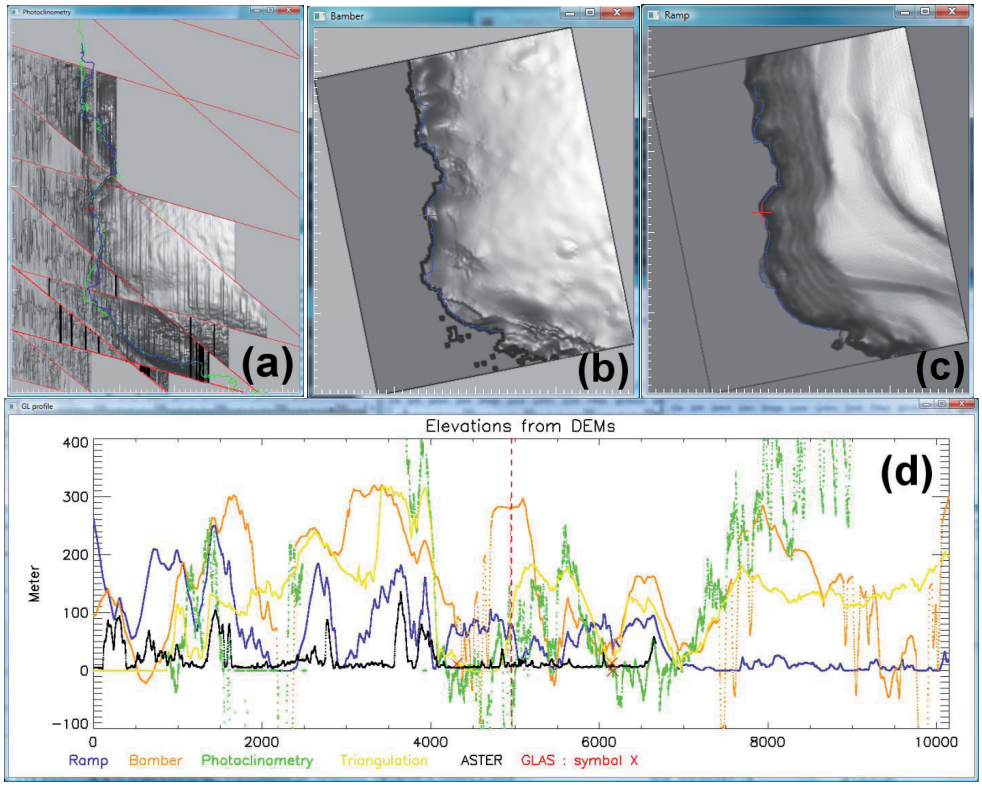

Fig. 5. Sample of screen display for elevation selection operation. **(a–c)** Shaded relief versions of photoclinometric, altimetric (aka. Bamber, 2009) and Radarsat DEMs, respectively, rotated and illuminated to match the original illumination of the Landsat sub-image. Blue line is the ASAID grounded ice boundary; green line is the MOA "grounding line". Red "+" symbols correspond to position of vertical dashed red line in lower panel. **(d)** Elevation profiles extracted from various DEMs indicated by lines of different color (legend below) with red X's being ICESat GLAS elevation values positioned where the ICESat profiles crosses the grounded ice boundary. Horizontal axis is in units of 15-m pixels. Vertical axis is elevation in meters above sea level.

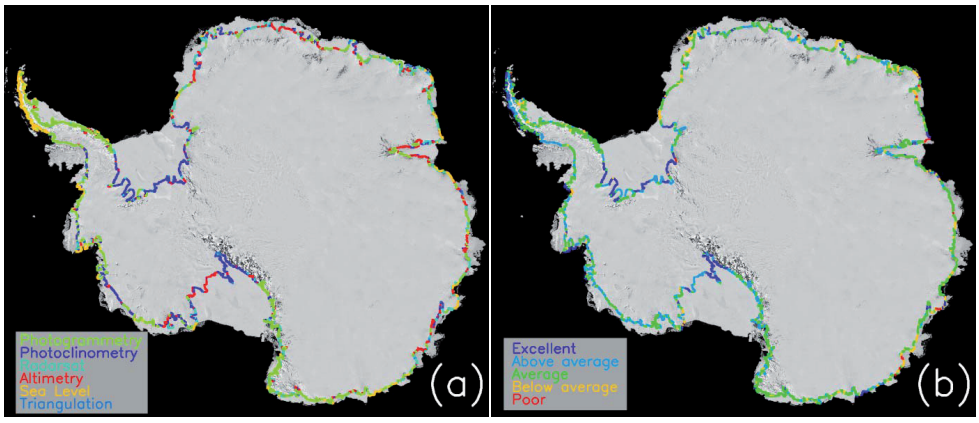

Fig. 6. The ASAID grounded ice boundary. **(a)** Colored lines represent the DEM source of selected elevation values. The corresponding percent frequencies of occurrence are: photogrammetry (green, 33 %); photoclinometry (dark blue, 26 %); Radarsat (cyan, 17 %); altimetry (red, 13 %); sea level (orange, 9 %); and triangulation (light blue, 2 %). **(b)** Colored lines represent the confidence in the selected elevations. The corresponding percent frequencies of occurrence are: Excellent (dark blue, 18 %); Above Average (cyan, 36 %); Average (green, 40 %); Below Average (orange, 5 %); and Poor (red, 0.5 %).

Table 2. Elevation Source for points along grounded ice boundary and hydrostatic line.

Source	Grounded Ice Boundary (%)	Hydrostatic Line (%)
Photogrammetry	33	4
Photoclinometry	26	37
RADARSAT	17	16
Altimetry	13	38
Sea Level	9	0.3
Triangulation	2	5

Table 3. Elevation Confidence for points along grounded ice boundary and hydrostatic line.

	Grounded Ice Boundary (%)	Hydrostatic Line (%)
Excellent	18	4
Above Average	36	32
Average	40	59
Below Average	5	4
Poor	0.5	0.1

the time, the next most used elevation source, with the largest region of use being along the grounded ice boundary of the Ronne/Filchner Ice Shelf. RADARSAT and the altimetric DEMs were used 17 % and 13 % of the time, respectively. The triangulation elevations, a worst-case alternative, only needed to be used 2 % of the time.

Table 3 summarizes the frequency of the selected elevations for each confidence class and Fig. 6b shows the spatial distribution. Quantitative accuracies are discussed in the next section. The "Excellent" ranking, reserved for those segments where the elevations matched the GLAS elevations very closely, occurs 18 % of the time and is largely confined to the southernmost boundaries of the Ross and Ronne/Filchner Ice Shelves. "Above Average" confidence (36 % occurrence) is assigned to segments along which there is close agreement with the GLAS elevations and the shape of the profile agrees with a visual interpretation of the imagery (i.e., the simulated image and the actual image were similar). This category also is located most frequently at ice shelf transitions, but is more widespread throughout West Antarctica. Segments ranked with an "Average" confidence in elevations (40 % occurrence) display more variations between DEMs but with a clear preference for the one DEM and are distributed along the entire boundary. "Below Average" confidence (5 % occurrence) usually corresponds to cases where the spread of DEMs is large with none standing out as the obvious choice. In these cases, the preference was usually assigned to the DEM profile that either most closely matches the GLAS elevations or that best expresses the shape of the elevation surface interpreted from the imagery. These are seen to occur in very isolated regions. In the cases of "Poor" confidence (0.5 % occurrence), there were no good elevations to choose from or there are elevation discontinuities along the boundary.

To ensure consistent application of this qualitative confidence assessment throughout the entire data set, the ratings were assigned by a single operator. The spatial pattern of confidence is not obviously correlated with the specific type of boundary – from rugged mountains to very smooth, nearly featureless terrain, to heavily crevassed regions – so its inclusion in the ASAID product provides an additional indication of elevation accuracy that cannot be gleaned from knowing either the type of transition or the source DEM.

The identical elevation-picking procedure is applied to the hydrostatic line. Figure 7 and Tables 2 and 3 present similar results for the hydrostatic line. The selections and statistics of the preferred elevation sources are distinctly different from those for the grounded ice boundary. In particular, photogrammetry is only selected 4 % of the time and is limited to the rougher coasts. This decrease in use is due to three factors: photogrammetry is most accurate in rugged terrain, where there are sharp features in the stereo imagery, but ice shelves tend to lack these features; there often is no hydrostatic line (i.e., no ice shelf) near some of these areas; and when there is a hydrostatic line, the frequently poor masking of the ASTER G-DEM eliminated potentially useful elevations in these regions. In its stead, at 38 % of the total, altimetry makes a much larger contribution to the chosen hydrostatic line elevations and is distributed across the coast. This is probably due to the smoothing effect of fitting an elevation surface to the altimetric data: a bias toward higher elevations will result at the grounded ice boundary where the slope change is most rapid, but this bias will be much reduced farther out on the ice shelf. Photoclinometry also increases its share of the selected elevations, to 37 %, because it works best in less rugged terrain and uncrevassed regions, but its distribution is still strongly confined to the same regions as for the grounded ice boundary. RADARSAT elevations are used about as frequently for the hydrostatic line (16 %) as for the grounded ice boundary (17 %) but with no particular spatial concentration. Sea level (zero elevation) is chosen less frequently (0.3 %) because the hydrostatic line is not included in open ocean regions.

The qualitative confidence ratings of the hydrostatic line are evaluated in a manner consistent with the grounded ice boundary elevation confidences and by the same operator. Overall, the confidences are lower, with only 4 % in the "Excellent" category; this time nearly exclusively in the southern Ross Ice Shelf and the confidence of much of the Ronne/Filchner Ice Shelf points decreasing to "Above

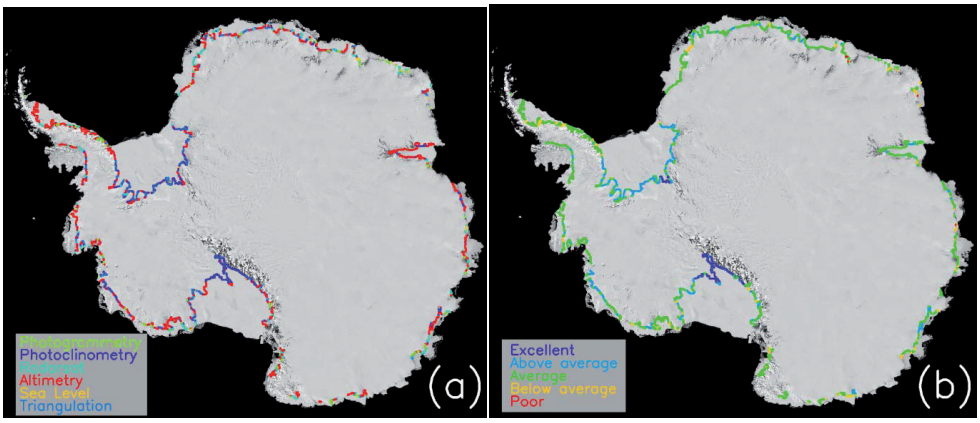

Fig. 7. The ASAID hydrostatic line. **(a)** Colored lines represent the DEM source of selected elevation values. The corresponding percent frequencies of occurrence are: photogrammetry (green, 4 %); photoclinometry (dark blue, 37 %); Radarsat (cyan, 16 %); altimetry (red, 38 %); sea level (orange, 0.3 %); and triangulation (light blue, 5 %). **(b)** Colored lines represent the confidence in the selected elevations. The corresponding percent frequencies of occurrence are: Excellent (dark blue, 4 %); Above Average (cyan, 32 %); Average (green, 59 %); Below Average (orange, 4 %); and Poor (red, 0.1 %).

Average". "Average" confidence is assigned to the majority (59 %) of hydrostatic line points, covering most of the coast. "Below Average" and "Poor" confidences are assigned to only 4 % and 0.1 % of points, respectively.

4.5 Elevation accuracy

Our elevation selection process includes many elevation sources and demonstrates that none are singularly preferred. To assess the accuracy of our chosen elevations, we compare them to two sets of field data. The first comes from an airborne mission conducted by the British Antarctic Survey (BAS) in the 2006–2007 austral summer, partly to support ASAID validation efforts. Surface elevations and ice thicknesses were measured over approximately 1500 flight kilometers along extensive reaches of the western boundary of the Ronne Ice Shelf from 200 km north of Evans Ice Stream to the north margin of Institute Ice Stream. Because the ASAID mapping of this region had not been completed at the time these data were collected, they do not directly coincide with either the ASAID grounded ice boundary or the hydrostatic line. However, because photoclinometry produces the preferred elevations in this region and this method produces an elevation field at 15-m spatial resolution, a direct comparison of ASAID elevations near the grounded ice boundary and hydrostatic line with BAS measurements at identical locations is possible. The confidence for all the ASAID elevations in this area is divided roughly equally between "Excellent" and "Above Average" (cf. Figs. 6b and 7b). 30 000 points spanning roughly 640 km are used covering the regions of Evans Ice Stream (and northward), across Carlson Inlet and around most of Fletcher Promontory. For each BAS measurement, its location is paired with the calculated elevation of the nearest pixel in the photoclinometry DEM and shown in Fig. 8. The linear fit through this distribution and forced to pass through (0, 0) has a slope of 0.997 and an R^2 of 0.986. The elevation differences (BAS minus ASAID) produced a Gaussian distribution with a mean difference of 0.24 ± 5.77 m. This region is experiencing a slight thickening of about 0.2 m yr^{-1} (Pritchard et al., 2009). No large elevation difference is expected because the 2006–2007 period of BAS data collection occurs roughly in the middle of the GLAS data time window (late 2003 to late 2008) and the GLAS data are used to control our photoclinometry elevations.

The second comparison of elevations draws upon the BEDMAP compilation of Antarctic field data (Lythe et al., 2001). Although BEDMAP's primary aim is to produce the best bed elevation map of Antarctica using all available measurements of ice thickness and surface elevation collected over the past 50 yr, some of the missions do include surface elevation data. The extended period represented by the data leave open the question of how much surface elevations may actually have changed from the time of collection to the epoch of our data sets. In addition, the elevation reference surfaces (i.e., geoid and ellipsoid) also have evolved and some of the documents supporting particular BEDMAP missions lack detail on this critical point. Despite these limitations, the BEDMAP data provide an independent and useful set of surface elevations to compare with the ASAID elevations.

The vast majority of the 127 missions compiled by BEDMAP cover interior regions of the ice sheet, but a few contain data that cross the ASAID grounded ice boundary, the hydrostatic line, or both. Crossings are defined as any ASAID point (of either line) that occurs within 30 m of a BEDMAP data point. Other distances were tried, but a shorter distance missed some crossings while a larger

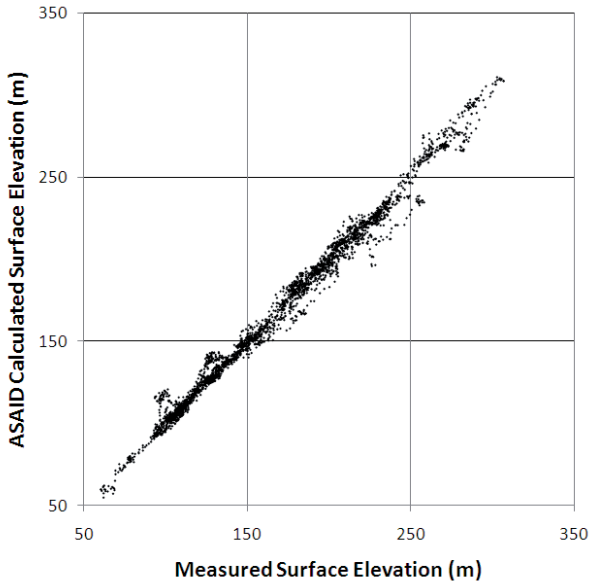

Fig. 8. Surface elevations measured by British Antarctic Survey near grounded ice boundary of Ronne Ice Shelf versus surface elevations at the same locations extracted from a photoclinometry DEM produced by ASAID.

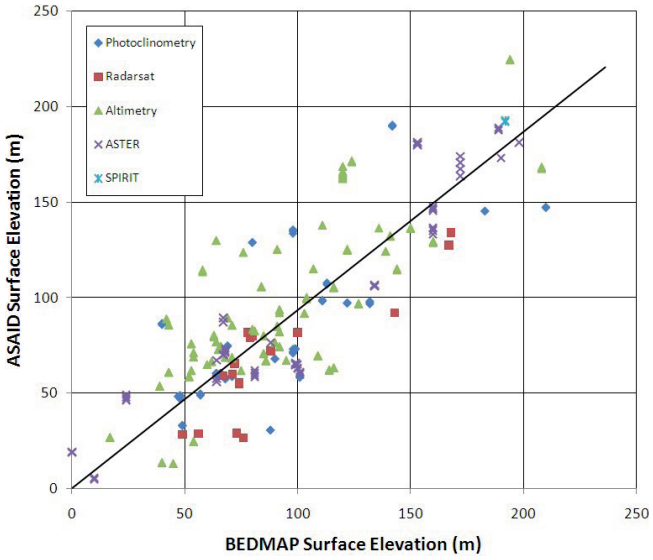

Fig. 9. Surface elevations at common locations along the ASAID grounded ice boundary extracted from BEDMAP missions versus preferred surface elevations selected from various DEMs by ASAID. Data symbols identify the source DEM used by ASAID. Sloped line is a linear fit through all points constrained to pass through (0, 0) (cf. Table 4).

distance includes too many ASAID points for a single crossing. 15 missions yield 954 crossing point pairs of the grounded ice boundary and 702 crossing point pairs of the hydrostatic line, clustered on the three largest ice shelves: the Ross, the Ronne/Filchner, and the Amery. Very few additional crossings result from the other missions and because the statistics would not be altered significantly even if they were included, we limit our comparisons presented here to the BEDMAP data in these three areas. These areas are not among the areas experiencing the greatest rates of thickness change (e.g., Pritchard et al., 2009) so the risk of temporal elevation changes compromising our results is reduced.

Because some BEDMAP data sets do not include surface elevations, the number of crossing point pairs for which elevations can be compared is less than the number of crossings. Figure 9 plots the BEDMAP surface elevations against the paired ASAID surface elevations (including an indication of the chosen DEM source) of the ASAID grounded ice boundary and Table 4 presents the statistics of both the grounded ice boundary and hydrostatic line comparisons. The data pairs in Fig. 9 are distributed roughly equally on either side of a line of slope 1. The statistical linear fits, forced to intersect the origin (0, 0), considered separately for the 417 pairs of the grounded ice boundary subset and the 262 pairs of the hydrostatic line subset are nearly identical in slope (0.93 and 0.95, respectively) and R^2 (0.64 and 0.66, respectively). There appears to be no strong bias in these comparisons that is related to the selected DEM source with the exception that the Radarsat DEM seems to be biased slightly lower than the BEDMAP elevations.

Table 4 also includes measures of the bias and standard deviations of the differences between paired ASAID and BEDMAP elevations. For the full set of elevation pairs of either the grounded ice boundary or hydrostatic line, the elevation bias is quite small (−4.7 and 1.5 m, respectively) and the standard deviations are also of similar magnitude (26.4 and 21.5 m, respectively). These values are worse than the comparison with the BAS data presented earlier and may reflect some of the limitations (i.e., variable accuracy of BEDMAP elevations, date of collection and reference surface uncertainty) of using the BEDMAP data for this accuracy assessment. Subdividing the BEDMAP-comparison data sets by confidence category (i.e, "Excellent" to "Below Average") produces bias values that range from −20.8 to 8.1 and standard deviations that range from 13.4 to 28.9. There does not appear to be any correspondence that associates a lower confidence in the elevation value selection with either a higher bias or a higher standard deviation, although some of the data sets are small, particularly for the "Below Average" category and no pairs were found for elevations with "Poor" confidence. The lack of a relation between confidence and accuracy is surprising given the often wide range of DEMs from which elevations were chosen. Because the next section (on ice thickness) also contains quantitative comparisons with BEDMAP data that infer a better accuracy for ASAID-selected surface elevations, the more complete discussion of elevation accuracy is deferred to the Summary.

Table 4. Comparison of BEDMAP and ASAID Surface Elevations. Slope and R^2 values refer to linear fits forced to pass through (0, 0) (cf., Fig. 9).

	Number of paired points	Slope of Linear Fit	R^2	Elevation Difference (m) (BEDMAP-ASAID)
Grounded Ice Boundary				
All Classes	417	0.93	0.64	-4.7 ± 26.4
Excellent only	58	0.75	0.81	-20.8 ± 19.7
Above Average only	92	0.95	0.57	-3.6 ± 28.9
Average only	261	0.94	0.66	-2.7 ± 24.9
Hydrostatic Line				
All Classes	262	0.95	0.66	1.5 ± 21.5
Excellent only	0			
Above Average only	89	0.91	0.67	5.4 ± 23.0
Average only	163	0.98	0.65	-1.0 ± 20.7
Below Average only	10			8.1 ± 13.4

4.6 Ice thickness

Surface elevations on floating ice are sometimes converted to ice thicknesses by invoking the hydrostatic equilibrium condition. While this conversion is sometimes applied immediately adjacent to the grounding ice sheet (e.g., Rignot et al., 2008), it is strictly only valid at the hydrostatic line, seaward of the hydrostatic line, and possibly at one or more locations between F and I_m (see Rignot et al., 2011, Fig. 1 for this final point). The conversion relationship can be written as

$$H_e = \frac{(Z_s - \Delta h)\rho_w}{\rho_w - \rho_i}; \quad \Delta h = h_f\left(1 - \frac{\rho_f}{\rho_i}\right) \tag{2}$$

where H_e, is the equivalent ice thickness; Z_s is the surface elevation above mean sea level, h_f and ρ_f are the depth and density of the firn, respectively; and ρ_i and ρ_w are the densities of pure ice and of seawater: 917 and 1026 kg m^{-3}, respectively. The term Δh is commonly referred to as the "firn-depth correction" and accounts for the air contained in the surface snow. A detailed meteorological model quantifying this air-in-firn effect has been published by van den Broeke et al. (2008). We were provided a file specifying the correction term on a 0.1 degree grid over the Antarctic continent that we bi-linearly interpolate to the location of each point along the grounded ice boundary and hydrostatic line. The distribution of this firn correction term around the perimeter of Antarctic was confirmed to be equivalent to Fig. 4 in van den Broeke et al. (2008).

In applying Eq. (2), there are a few instances where the firn-depth correction exceeds our surface elevation leading to negative equivalent ice thicknesses. This is clearly incorrect. Such occurrences are distributed widely around the continent and are often associated with where our hydrostatic line extends across short patches of fast ice between longer sections of floating ice shelf. The single largest concentration of very low elevations occurs between longitudes 40° E and 57° E. To avoid negative thicknesses, a variable coefficient is added to Eq. (2) modifying it to

$$H_e = \frac{(Z_s - f\,\Delta h)\rho_w}{\rho_w - \rho_i}; f = 1 - e^{-\frac{Z_s}{\Delta h}} \tag{3}$$

The coefficient, f, is only significant when the firn correction depth becomes a significant fraction of the surface elevation. f ranges from unity for large surface elevations to zero when the firn-depth correction is much larger than the surface elevation. Physically this coefficient can be interpreted as reducing the effect of included air in firn when the surface elevation is so low that much of that firn would be flooded by seawater and, presumably refrozen, thus increasing the density and reducing the air content.

Figure 10a shows the distribution of calculated hydrostatic line ice thicknesses around the continent along with a histogram of values. Very thick ice (sometimes over 2000 m) occurs where deep ice streams and glaciers feed the Ross, Ronne/Filchner and Amery ice shelves. The histogram of ice thicknesses (Fig. 10b) approximates a log-normal distribution with the most frequent ice thicknesses in the range 300–400 m. There are two other features to note. The first is the local minimum/local maximum couplet at 800–900 m thickness. We offer no explanation for this feature nor do we associate any significant characteristic of hydrostatic line ice thickness to it. The second feature is the high frequency of occurrence at very small ice thicknesses; 6 % of the equivalent ice thicknesses are less than one meter. This might be a real feature, reflecting the frequent occurrence of thin ice, but it also is caused, to some undetermined degree, by errors in measurement of thin coastal ice and the accuracy of geoid knowledge along the Antarctic coast.

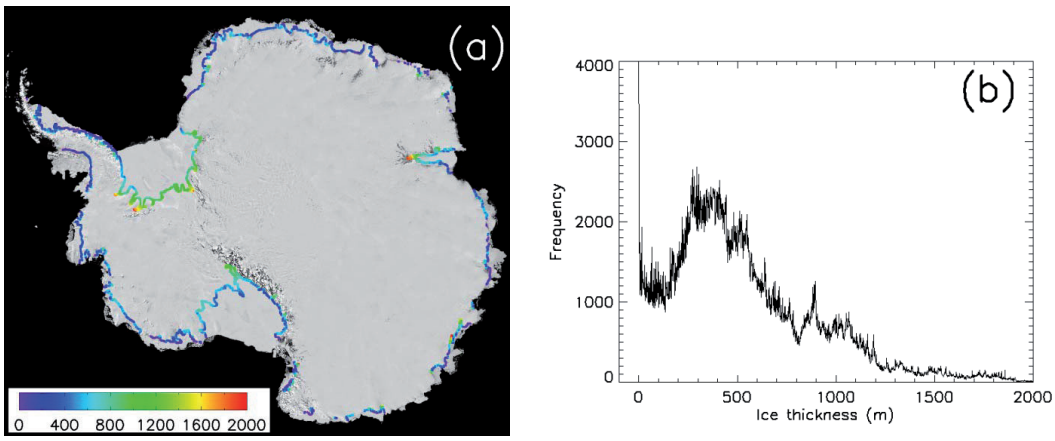

Fig. 10. Ice thickness calculated along the ASAID hydrostatic line **(a)** mapped on the Landsat Image Mosaic of Antarctica with color representing ice-equivalent thickness in meters (cf., Eq. 3 in text) and **(b)** presented as a histogram of values.

4.7 Ice thickness accuracy

Our quantitative assessment of ice thickness accuracy uses the same BEDMAP data set employed earlier to assess elevation accuracy. However, unlike those elevation comparisons, ice thickness comparisons are not encumbered by the uncertainty of using a consistent reference surface. There also are more data pairs to compare, because all BEDMAP data sets include ice thickness. The same criterion of pairing each BEDMAP point to any ASAID point within 30 m is applied and, repeating the results, there are 954 crossing point pairs of the grounded ice boundary and 702 crossing point pairs of the hydrostatic line, clustered on the three largest ice shelves: the Ross, the Ronne/Filchner, and the Amery.

To permit a valid comparison, the ASAID ice thicknesses are first converted from an ice-equivalent thickness to an expected actual ice thickness by accounting for the firn-depth correction included in Eqs. (2) and (3). This is simply done by calculating the expected actual ice-shelf thickness, H_a as

$$H_a = Z_s + H_e\left(\frac{\rho_i}{\rho_w}\right) \quad (4)$$

Figure 11 plots the measured BEDMAP ice-shelf thickness values against the calculated ASAID values of actual ice-shelf thickness (H_a from Eq. 4) for the crossing pairs along the hydrostatic line and Table 5 presents the statistical results. The agreement is considerably better than for the surface elevation comparison (cf. Fig. 9 and Table 4). The linear fit (again forced to intersect the origin (0, 0)) has a slope of 0.94 and an R^2 value of 0.92 with similar results when each of the three areas is considered separately: slopes ranging from 0.90 to 0.97 and R^2 ranging from 0.89 to 0.98 (cf., Table 5). The distributions of ice thickness differences indicate a consistent bias of ASAID calculated ice thickness lower than the BEDMAP-compiled ice thicknesses, although the magnitude of this bias, 41.2 m for all points, varies with the area considered and it is less than one-sigma from zero. It is difficult to identify the source of these differences: real thickness change between the collection times of the data sets, location errors, errors in the ASAID elevation and firn-depth correction errors could all be factors. The Ross Ice Shelf area exhibits the best agreement: 23.6 ± 44.2 m and is the data set collected with the least time difference between data sets.

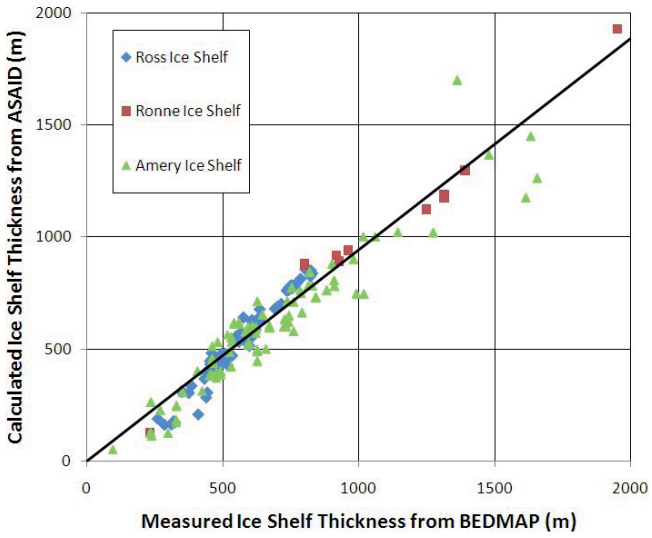

Fig. 11. Ice shelf thickness at common points along the ASAID hydrostatic line extracted from BEDMAP mission measurements versus actual ice thickness calculated from ASAID preferred surface elevations (as described in the text). Data symbols distinguish the three ice shelf regions. Sloped line is a linear fit through all points constrained to pass through (0, 0) (cf. Table 5).

Subdividing this distribution of thickness differences by confidence level reveals an increased standard error of ice thickness with decreased confidence level as well as a decrease in the fitted R^2 values as ASAID elevation confidence

Table 5. Comparison of BEDMAP and ASAID Actual Ice Thicknesses. Slope and R^2 values refer to linear fits forced to pass through (0, 0) (cf., Figs. 11 and 12). BEDMAP mission numbers refer to the specific source data sets.

	Number of paired points	BEDMAP Missions	Slope of Linear Fit	R^2	Ice thickness Difference (m) (BEDMAP-ASAID)
Grounded Ice Boundary					
All points	954		1.03	0.23	-57.3 ± 12.1
Ross Ice Shelf only	508	42, 53	0.99	0.86	9.1 ± 53.5
Ronne Ice Shelf only	25	34, 35, 37, 44, 74	0.95	0.91	86 ± 120.9
Amery Ice Shelf only	417	7–9 and 68–73	1.09	0.05	-139 ± 380
Hydrostatic Line					
All points	702		0.94	0.92	41.2 ± 71.3
Ross Ice Shelf only	231	42, 53	0.90	0.89	23.6 ± 44.2
Ronne Ice Shelf only	26	35, 36, 37, 38, 44	0.96	0.98	56.8 ± 62.9
Amery Ice Shelf only	445	5, 6, 9 and 69–74	0.97	0.92	73.5 ± 98.1
Excellent only	341		1.19	0.98	14.3 ± 29.6
Above Average only	162		0.91	0.93	68.7 ± 79.9
Average only	190		0.91	0.91	66.6 ± 94.7

decreases (cf., Table 5). These trends support our intention of providing users of these data sets a useful guide to indicate the variable accuracy of the elevations (and ice thicknesses derived from them). Applying Eqs. (2) and (4) to these ice thickness accuracies in Table 5, equivalent uncertainties in surface elevation can be extracted. The values are: ± 3.6, ± 9.6 and ± 11.4 for Excellent, Above Average and Average confidence levels, respectively. Without sufficient data pairs, the uncertainties for confidence levels 4 and 5 remain undetermined by this procedure, but we estimate them to be ± 30 and ± 100 m based on the conditions used to assign them (i.e, the spread among various DEMs and the occasional occurrence of discontinuities).

It has been stated repeatedly that hydrostatic equilibrium does not apply landward of the hydrostatic line. For this reason and to inhibit misuse of the grounded ice boundary data set, the ASAID data sets do not calculate an ice thickness from the preferred surface elevation along this boundary (although the firn-depth correction is provided for those who wish to take this risky step). However, to examine the magnitude of errors that would be made by assuming hydrostatic equilibrium at the grounded ice boundary, here we convert our ASAID surface elevations to hydrostatically equilibrated ice thicknesses at the grounded ice boundary points close to BEDMAP points and compare them to BEDMAP values. The procedure to convert the surface elevations to actual ice thicknesses is identical to the procedure described above for the hydrostatic line points. The point pairs are plotted in Fig. 12 and statistics summarized in Table 5 but, in this case, the points are subdivided by region. Grounded ice is expected to have surface elevations higher than if it were floating in hydrostatic equilibrium, so a bias of thicker-than-measured ice for the ASAID points is expected. Overall, this bias is apparent in Fig. 12, but when the comparisons are examined separately for the three ice shelves, the agreement on the Ross Ice Shelf is comparable to that for the hydrostatic line, the agreement on the Ronne Ice Shelf is somewhat equivocal and not well sampled, while it is the Amery Ice Shelf points that produce the expected too-thick ice bias. A possible explanation for the favorable agreement for the Ross

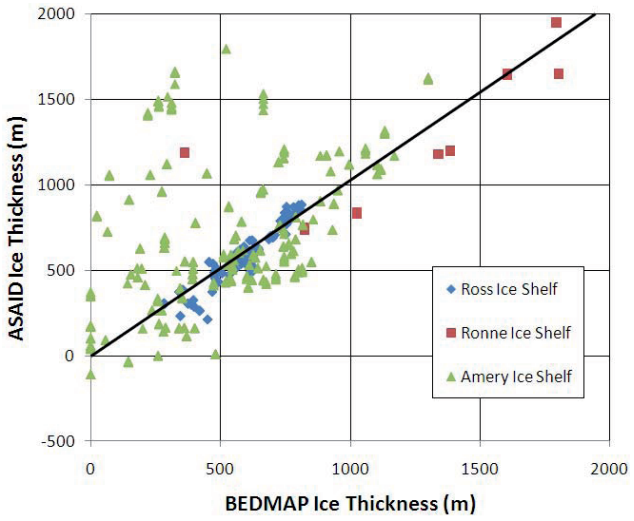

Fig. 12. Actual measured ice thickness at common points along the ASAID grounded ice boundary extracted from BEDMAP mission data versus actual ice thickness calculated from ASAID preferred surface elevations. Data symbols distinguish the three ice shelf regions. Sloped line is a linear fit through all points constrained to pass through (0, 0) (cf. Table 5).

Ice Shelf points is that the BEDMAP data were collected in an area of very fast moving, low slope ice streams that include a very extensive ice plain region of lightly grounded ice (Alley et al., 1989). It is in just such a region that the ice is already close to hydrostatic equilibrium even before the ice loses contact with the bed. The large differences found on the Amery Ice Shelf may represent a more typical situation of shorter or nonexistent ice plains where the transition to floating is more rapid; it is in those conditions that extreme caution is advised to avoid significant overestimates in grounding zone ice thickness.

4.8 Application to flexing beam theory

In drawing the hydrostatic line, it was noticed that the seaward offset of the GLAS-determined H points from the grounded ice boundary is relatively consistent locally, but varies gradually from region to region. This characteristic gives us confidence that interpolating the hydrostatic line between GLAS-determined H points is reasonable. Here we use our data set to more quantitatively examine this relationship.

From a purely mechanical point of view, the seaward offset of the hydrostatic line from the grounded ice boundary should depend on the stiffness of the ice, its weight and its thickness. A useful analysis of elastic beam deformation, presented in Vaughan (1995), expresses the beam deflection as

$$w(x) = A_0[1 - e^{-\beta x}(\cos\beta x + \sin\beta x)] \quad (5)$$

$$\beta^4 = 3\rho_w g \frac{1-\mu^2}{Eh^3} \quad (6)$$

where w is the vertical deflection from mean sea level, A_0 is the full tidal range, ρ_w is the density of seawater, g is gravitational acceleration, μ and E are Poisson's ratio and Young's modulus of ice, respectively, and h is the ice thickness. By examining multiple field data sets, Vaughan (1995) cites a best value of $\beta = 2.43 \pm 0.43 \times 10^{-4}\,\mathrm{m}^{-1}$. For our purposes, we require a relationship between ice thickness and the seaward offset of the hydrostatic line from the grounded ice boundary, x_H. For the Rutford Ice Stream examined in Vaughan (1995), x_H is approximately equal to 7000 m, thus $\beta x = 1.7 \pm 0.3$. By substituting this value into Eq. (5) to eliminate β, the following equation relates x_H to ice thickness, h,

$$x_H = 1.7\left[3\rho_w g \frac{(1-\mu^2)}{E}\right]^{\frac{1}{4}} h^{\frac{3}{4}} \quad (7)$$

Using standard values for ρ_w and g, and again referring to Vaughan (1995) for values of μ and E (0.3 and 0.88 ± 0.35 GPa, respectively) we arrive at the relationship,

$$x_H = (22.2 \pm 6.2)h^{\frac{3}{4}} \quad (8)$$

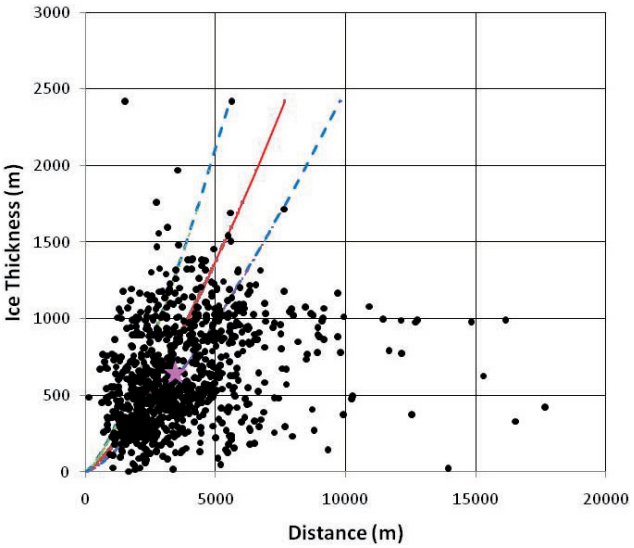

Fig. 13. Relationship of distance between ASAID grounded ice boundary and ASAID hydrostatic line to ice-equivalent thickness. Red line is theoretical relationship (Eq. 7) discussed in the text with blue dashed lines being one standard deviation from this theoretical relationship. Magenta star indicates the position occupied by the mean distance and mean ice thickness of all 930 points.

This relationship is slightly non-linear. The only spatially variables in the coefficient are E and μ, terms that vary with ice temperature, but their effects are diminished through the exponent that appears outside the square bracket of Eq. (7).

Figure 13 presents the distribution of ice thicknesses versus seaward offsets of the hydrostatic line from the grounded ice boundary for the ASAID data sets. The points plotted are selected as being those closest to the 930 GLAS-determined H points so the interpolation between H points does not affect these results. There is considerable scatter, but the first order relationship of increasing offset distance with ice thickness is borne out and the pattern generally matches the relationship suggested by Eq. (8). Both the varying temperature effect and the firn correction effect contribute to the scatter as does the two-kilometer positional uncertainty of the H points (Brunt et al., 2010b). The mean offset distance is 3.7 ± 2.2 km and the mean ice thickness is 632 ± 337 m. The locations of thickest ice occur on the Ronne Ice Shelf near Rutford Ice Stream and on the Ross Ice Shelf near Whillans and Mercer Ice Streams. The locations of largest offsets are scattered around the continent without significant clusters. These results agree reasonably well with the grounding zone width values (Ross: 3.2 ± 2.6 km and Ronne: 5.2 ± 2.7 km) by Brunt et al. (2010b) although it is important to note that their grounding zone width is the longer distance from point F to H, rather than our distance from I_b to H. At best, we can say that our data are consistent with Eq. (8), but it is not possible to use this empirical relationship as a means to define the hydrostatic line from only information on grounded ice boundary position and surface elevation.

5 Distribution and archiving

Ensuring the availability of our ASAID products in a useful form to the research community is an important objective of this IPY project. The files of the grounded ice boundary and hydrostatic line are generated in such a way to facilitate their use by researchers and have been delivered to the National Snow and Ice Data Center (NSIDC). The latitude/longitude coordinates of each point are given along with our preferred surface elevation and its confidence. Also included are the firn-depth correction, the full set of other surface elevations for each point and point coordinates linked to the specific sub-image used to generate that segment of each line. Finally, the grounded ice boundary file includes the nature of the grounded ice boundary transition (outlet glacier, ice shelf, rock, fast ice or open ocean) and, for the hydrostatic line file, the converted ice thickness (using Eq. (3) and the preferred elevation and interpolated firn correction) is included. Although the grounded ice boundary file does include a surface elevation and the interpolated firn-depth correction term, it does not include an ice thickness value calculated from these parameters because we do not wish to encourage use of an ice thickness value that may be seriously in error (cf. Fig. 12 and the earlier discussion of it).

In addition to the basic grounded ice boundary and hydrostatic line files, we have provided to NSIDC the generating files including the sub-images, line segments, GLAS elevation profiles and derived photoclinometric and triangulation DEMs. It is possible that these files may prove of value either to subsequent research into the data used to produce the higher-order products or to future projects that aim to repeat some or all of what this project accomplished.

Finally, the customized software tools written for ASAID also have been provided to NSIDC along with detailed documentation as a NASA Technical Memorandum (Bindschadler et al., 2011); however software support will not be supplied. The code is written exclusively in IDL so that anyone can run the various modules using a free-ware IDL engine.

6 Summary and lessons learned

The production of the grounding ice boundary and hydrostatic line at 15-m resolution completes what once seemed a daunting task. The definition of these Antarctic boundaries with the precision achieved by ASAID offers the research community a valuable new benchmark against which changes can be more conveniently and accurately monitored and quantified. These boundaries are dynamic both in the sense that they shift in time and in the sense that they represent boundaries across which the nature of the ice sheet's interaction with its environment changes. The ASAID grounded ice boundary represents a significant refinement in a series of "grounding lines" mapped with similar data sources, i.e., optical imagery or photography. In contrast, the ASAID hydrostatic line is new and represents the initiation of what will be progressively improved. By assessing the nature of the transition across the grounded ice boundary, the perimeter of the Antarctic is shown to consist of a floating fringe of ice over 74 % of its length. The main ice sheet terminates on land over only 7 % of the perimeter, the remaining 19 % being a boundary adjacent to either open ocean or sea ice in the ocean.

The inclusion of the surface elevation provides additional utility of these data sets. Our approach of selecting the best elevations highlighted significant inconsistencies within and between various DEMs in the coastal regions of Antarctica. No single DEM can be uniquely preferred. By using precise GLAS laser altimetric elevations, we cull from various DEM sources a higher value composite elevation set along both the grounded ice boundary and hydrostatic line and add our own confidence rating to inform users of the elevation quality on a point-by-point basis.

The assessments of our elevations' accuracy produces mixed results. Comparison with the BEDMAP-compiled surface elevations produces a consistent one-sigma standard error of surface elevation in the low-20 m (cf., Fig. 9 and Table 4), but the BEDMAP elevations contain various errors themselves, some of which are undocumented. Much smaller errors (0.24 ± 5.77 m, cf., Fig. 8) are indicated when elevations from the photoclinometry DEM spanning the ASAID grounded ice boundary are compared with a nearly contemporaneous and well-controlled data set. The confidences of these elevations are rated as Excellent and Above Average. Similar accuracies are inferred from the ice thickness comparison (cf., Fig. 11 and Table 5). Because these latter results are supported by the expected association of increased errors with decreased confidence in the selected ASAID elevations, we recommend their use. The recommended, one-sigma elevation uncertainties are: ± 3.6, ± 9.6 and ± 11.4 m for "Excellent", "Above Average" and "Average" confidence levels, respectively and ± 30 and ± 100 m for the "Below Average" and "Poor" confidence levels.

Computed values of firn densities around the coast enable the conversion of surface elevations to floating ice thicknesses (both ice-equivalent and actual). These compare favorably with measured ice thicknesses (cf., Table 5) despite some large temporal gaps and a bias that indicates ASAID ice thicknesses are too low by a few tens of meters, depending on location. This comparison also shows the closest correspondence between the confidence assigned to the ASAID-preferred elevations and the match between the calculated ice thickness and nearby measured ice thicknesses. Our comparison of measured ice thickness against the ice thickness calculated assuming hydrostatic equilibrium along our grounded ice boundary is mixed, with good agreement displayed for points along the Ross Ice Shelf edge and very poor agreement along the edge of the Amery Ice Shelf. We conclude from this that conversion of surface elevations to

ice thickness landward of the hydrostatic line should only be trusted if there is additional supporting data. The theoretical relationship between ice shelf thickness and the separation between the grounded ice boundary and the hydrostatic line is only weakly supported by our results. The major limitation is likely the positional uncertainty of the H points used to define the hydrostatic line, but these points did exhibit a broad spatial coherence less than the published two-kilometer uncertainty (Brunt et al., 2010b).

Undertaking this project was facilitated by the existence of the IPY and the primary objectives of this project were strongly influenced by the IPY objectives. This created benefits and disadvantages. The comprehensive nature of the product and the ability to divide the work among many participants were significant characteristics of ASAID, but the need to create customized software that could run on multiple platforms as well as the need to carefully review and, in many cases, revise submissions from multiple participants were burdensome. Eventually, the ownership of this product by a large international team is a significant characteristic that will help establish these products as standards in the glaciological community. In addition, the documentation of the methodology should facilitate future efforts at monitoring both the grounded ice boundary and hydrostatic line. The software and products now available are allowing for the creation of educational activities that promise to increase the impact of ASAID on future scientists.

Acknowledgements. A project of this magnitude and complexity could not have been accomplished without extensive contributions from many people, some of whom do not appear as authors on this paper. Funding support for the central work was provided through NASA grant 509496.02.08.01.81. Other domestic and international participants have been supported by other funding and we thank the British Antarctic Survey for adding flights specifically for ASAID to an already packed field schedule. Michiel van den Broeke was extremely gracious for providing his work on firn correction values. Two anonymous reviewers contributed persuasive criticisms of an earlier draft that led to the extensive use of BEDMAP-compiled data and greatly improved the quantitative assessment of the ASAID products' accuracies.

Edited by: I. M. Howat

References

Alley, R. B., Blankenship, D. D., Rooney, S. T., and Bentley, C. R.: Sedimentation beneath ice shelves – the view from ice stream B, Mar. Geol., 85, 101–120, 1989.

Anandakrishnan, S., Voigt, D. E., Alley, R. R., and King, M. A.: Ice stream D flow speed is strongly modulated by the tide beneath the Ross Ice Shelf, Geophys. Res. Lett., 30(7), 1361, doi:10.1029/2002GL016329, 2003.

Bamber, J. L., Gomez-Dans, J. L., and Griggs, J. A.: A new 1 km digital elevation model of the Antarctic derived from combined satellite radar and laser data – Part 1: Data and methods, The Cryosphere, 3, 101–111, doi:10.5194/tc-3-101-2009, 2009.

Bindschadler, R. A. and Vornberger, P. L.: Detailed elevation map of ice stream C using satellite imagery and airborne radar, Ann. Glaciol., 20, 327–335, 1994.

Bindschadler, R. A., Vornberger, P. L., King, M., and Padman, L.: Tidally-Driven Stick-Slip Motion in the Mouth of Whillans Ice Stream, Antarctica, Ann. Glaciol., 36, 263–272, 2003.

Bindschadler, R., Vornberger, P., Fleming, A., Fox, A., Mullins, J., Binnie, D., Paulsen, S. J., Granneman, B., and Gorodetzky, D.: The Landsat Image Mosaic of Antarctica, Remote Sens. Environ., 112(12), 4214–4226, doi:10.1016/j.rse.2008.07.006, 2008.

Bindschadler, R. A., Wichlacz, A., and Choi, H.: An Illustrated Guide to Using ASAID Software, NASA Technical Memorandum, TM-2011-215879, 21 pp., 2011.

Bohlander, J. and Scambos, T.: Antarctic coastlines and grounding line derived from MODIS Mosaic of Antarctica (MOA), Boulder, Colorado USA: National Snow and Ice Data Center, Digital media, 2007.

Brunt, K. M., Fricker, H. A., Padman, L., and O'Neel, S.: ICESat-Derived Grounding Zone for Antarctic Ice Shelves, Boulder, Colorado USA: National Snow and Ice Data Center, Digital media, 2010a.

Brunt, K. M., Fricker, H. A., Padman, L., Scambos, T. A., and O'Neel, S.: Mapping the grounding zone of the Ross Ice Shelf, Antarctica, Using ICESat laser altimetry, Ann. Glaciol., 51(55), 71–79, 2010b.

Corr, H. F. J., Doake, C. S. M., Jenkins, A., and Vaughan, D. G.: Investigations of an "ice plain" in the mouth of Pine Island Glacier, Antarctica, J. Glaciol., 47(156), 51–57, 2001.

Ferrigno, J. G., Mullins, J. L., Stapleton, J. A., Chavez, P. S., Velasco, M. G., Williams, R. S., Delinski, G. F., and Lear, D.: Satellite Image Map of Antarctica, U.S. Geological Survey, Miscellaneous Investigations Map Series, Map 1-2560, 1996.

Fricker, H. A. and Padman, L.: Ice shelf grounding zone structure from ICESat laser altimetry, Geophys. Res. Lett., 33, L15502, doi:10.1029/2006GL026907, 2006.

Fricker, H. A., Coleman, R., Padman, L., Scambos, T. A., Bohlander, J., and Brunt, K. M.: Mapping the grounding zone of the Amery Ice Shelf, East Antarctica using InSAR, MODIS and ICESat, Antarct. Sci., 21(5), 515–532, doi:10.1017/S095410200999023X, 2009.

Joughin, I., Smith, B. E., and Holland, D. M.: Sensitivity of 21st Century Sea Level to Ocean-Induced Thinning of Pine Island Glacier, Antarctica, Geophys. Res. Lett., 37, L20502, doi:10.1029/2010GL044819, 2010.

Korona J., Berthier, E., Bernard, M., Remy, F., and Thouvenot, E.: SPIRIT. SPOT 5 stereoscopic survey of Polar Ice: Reference Images and Topographies during the fourth International Polar Year (2007–2009), ISPRS J. Photogramm., 64, 204–212, 2009.

Lee, D. S., Storey, J. C., Choate, M. J., and Hayes, R. W.: Four Years of Landsat-7 On-Orbit Geometric Calibration and Performance, IEEE T. Geosci. Remote, 42(12), 2786–2795, doi:10.1109/TGRS.2004.836769, 2004.

Liu, H., Jezek, K., Li, B., and Zhao, Z.: Radarsat Antarctic Mapping Project digital elevation model version 2, Boulder, CO: National Snow and Ice Data Center, Digital media, 2001.

Lythe, M. B., Vaughan, D. G., and BEDMAP Consortium, BEDMAP: A new ice thickness and subglacial topographic model of Antarctica, J. Geophys. Res., 106(B6), 11335–11351, 2001.

Payne, A. J., Vieli, A., Shepherd, A. P., Wingham, D. J., and Rignot, E.: Recent dramatic thinning of largest West Antarctic ice stream triggered by oceans, Geophys. Res. Lett., 31(23), L23401, doi:10.1029/2004GL021284, 2004.

Payne, A. J., Holland, P. R., Shepherd, A. P., Rutt, I. C., Jenkins, A., and Joughin, I.: Numerical modeling of ocean-ice interactions under Pine Island Bay's ice shelf, J. Geophys. Res., 112, C10019, doi:10.1029/2006JC003733, 2007.

Pritchard, H. D., Arthern, R. J., Vaughan, D. G., and Edwards, L. A.: Extensive dynamic thinning on the margins of the Greenland and Antarctic ice sheets, Nature, 461, 971–975, doi:10.1038/nature08471, 2009.

Rignot, E.: Tidal motion, ice velocity and melt rate of Petermann Gletscher, Greenland, measured from radar interferometry, J. Glaciol., 42(142), 476–485, 1996.

Rignot, E., Bamber, J. L., van den Broeke, M. R., Davis, C., Yonghong, L., van deBerg, W. J., and van Meijgaard, E.: Recent Antarctic ice mass loss from radar interferometry and regional climate modeling, Nat. Geosci., 1, 106–110, doi:10.1038/ngeo102, 2008.

Rignot, E., Mouginot, J., and Scheuchl, B.: Antarctic grounding line mapping from differential satellite radar interferometry, Geophys. Res. Lett., 38, L10504, doi:10.1029/2011GL047109, 2011.

Schoof, C.: Ice sheet grounding line dynamics: Steady states, stability, and hysteresis, J. Geophys. Res., 112, F03S28, doi:10.1029/2006JF000664, 2007.

Shepherd, A., Wingham, D. J., and Mansley, J. A. D.: Inland thinning of the Amundsen Sea sector, Geophys. Res. Lett., 29(10), 1364, doi:10.1029/2001GL014183, 2002.

Thomas, R., Rignot, E., Casassa, G., Kanagaratnam, P., Acuna, C., Akins, T., Brecher, H., Frederick, E., Gogineni, P., Krabill, W., Manizade, S., Ramamoorthy, H., Rivera, A., Russell, R., Sonntag, J., Swift, R., Yungel, J., and Zwally, J.: Accelerated sea-level rise from West Antarctica, Science, 306(5694), 255–258, 2004.

Thomas, R. H., Stephenson, S. N., Bindschadler, R. A., Shabtaie, S., and Bentley, C. R.: Thinning and grounding line retreat on the Ross Ice Shelf, Ann. Glaciol., 11, 165–172, 1988.

van den Broeke, M. R., van de Berg, W. J., and van Meijgaard, E.: Firn depth correction along the Antarctic grounding line, Antarct. Sci., 20(5), 1–5, doi:10.1017/S095410200800148X, 2008.

Vaughan, D. G.: Tidal Flexure at Ice Sheet Margins, J. Geophys. Res., 100(B4), 6213–6224, 1995.

Wiens, D. A., Anandakrishnan, S., Winberry, J. P., and King, M. A.: Simultaneous teleseismic and geodetic observations of the stick-slip motion of an Antarctic ice stream, Nature, 453, 770–774, doi:10.1038/nature06990, 2008.

Wildey, R. L.: Generalized photoclinometry for Mariner 9, Icarus, 25, 613–626, 1975.

Yamanokuchi, T., Doi, K., and Shibuya, K.: Validation of grounding line of the East Antarctic Ice Sheet derived by ERS-1/2 interferometric SAR data, Polar Geoscience, 18, 1–14, 2005.

Zwally, H. J., Schutz, R., Bentley, C., Bufton, J., Herring, T., Minster, J., Spinhirne, J., and Thomas, R.: GLAS/ICESat L2 Antarctic and Greenland Ice Sheet Altimetry Data V001, Boulder, CO: National Snow and Ice Data Center, Digital media, 2003.

E. Basal melting at the Ekström Ice Shelf mapped by SAR interferometry using the mass continuity assumption

Own contribution: Initiation and supervision of the Diploma thesis Neckel (2011) which serves as the basis for this project; Participation in implementing the InSAR code, the InSAR analysis and in the application of the continuity equation; Description and interpretation of RES data (conversion to ice-thickness done by D. Steinhage); Support in writing the manuscript.

Current Status: Submitted Annals of Glaciology.

Basal melting at the Ekström Ice Shelf mapped by SAR interferometry using the mass continuity assumption

Niklas NECKEL,[1,*] Reinhard DREWS,[1] Wolfgang RACK,[2] Daniel STEINHAGE[1]

[1] *Alfred Wegener Institute for Polar and Marine Research, PO Box 120161, D-27515 Bremerhaven, Germany*
E-mail: Niklas.Neckel@awi.de
[2] *Gateway Antarctica, University of Canterbury, Private Bag 4800, Christchurch 8140, New Zealand*
[*] *now at: Institute of Physical Geography and GIS, University of Tübingen, Rümelinstr. 19-23, D-72070 Tübingen, Germany*

ABSTRACT. We characterize the basal mass balance of the Ekström Ice Shelf located in Dronning Maud Land, Antarctica, by means of interferometrically derived surface velocities and ice-thickness measurements from Radio Echo Sounding (RES). The surface velocities are based on data of the European Remote Sensing Satellites I and II (ERS-I/II) from 1994–1997. The ice-thickness grid consists of 136 RES profiles acquired between 1996–2006. Where possible, mass fluxes are calculated exactly along selected RES profiles reducing uncertainties from ice-thickness interpolation, elsewhere large scale mass fluxes are calculated using interpolated ice-thickness data. The mass flux into the Ekströmisen from the main grounded drainage basins is estimated to be 3.2 ± 0.5 Gt/a. The mass flux near the ice shelf front is 2.5±0.4 Gt/a. Assuming steady state and based on the equation of continuity, we interpret the residual mass flux as a combined effect of surface accumulation and sub-glacial melting/refreezing. Using accumulation rates from previous studies, we elucidate the limits to link the mass flux divergence in relatively small and irregular shaped polygons to processes beneath the ice shelf. The highest sub-glacial melt rates with about 1.1 m/a are found near the grounding zone of two main inflow glaciers, and around the German base Neumayer III (NM) near Atka Bay. Detection of unlikely refreezing in a confined area about 15 km west of NM is attributed to both the limitation of the method and a (possibly past) violation of the steady state assumption. In general, the method and input data allow mapping the spatial distribution of basal melting and the results are in good agreement with several previous studies.

INTRODUCTION

About three quarters of the Antarctic ice sheet's perimeter consists of floating ice (Bindschadler and others, 2011). Ice shelves and ice tongues link the grounded ice sheet to the Southern Ocean, and the associated melting and freezing at their base plays an important role in ice sheet mass balance and ocean processes (Hellmer, 2004; Payne and others, 2004; Jenkins and others, 2010). The coast–line of Dronning Maud Land between 27° W and 33° E, largely in the Atlantic sector of Antarctica, is almost entirely bordered by a number of comparatively small ice shelves. The Ekströmisen (or Ekström Ice Shelf), which is under investigation here, might be considered by its extent as a typical representative for ice shelves along this coast. It is confined by the ice ridges Søråsen in the West and Halvfarryggen in the East (Figure 1a) and covers an area of ~ 6800 km^2 (area measured between the grounding line as published by Bindschadler and others (2011) and the ice shelf front). The narrow continental shelf in this area permits a strong interaction of ice shelf water with the coastal current and associated heat transports into the ice shelf cavity (Nicolaus and Grosfeld, 2004). This characteristic geographic setting could make ice shelves in this location notably susceptible to rising ocean temperatures, either by ocean warming (Gille, 2008) or increased upwelling of warm circumpolar deep water (Holland and others, 2008). However, the relevance and magnitude of these effects for additional melting under specific ice shelves like the Ekströmisen is uncertain, as it also depends on ice shelf morphology (Little and others, 2009). So far, no unusual changes in ice shelf geometry along this coast have been observed, however, direct and indirect estimations of basal mass balance are scarce.

Because in-situ measurements of basal mass balance of ice shelves are not feasible, remote sensing methods need to play a central role to achieve this goal. The most accurate (indirect) measurement of basal melt to date is using a phase sensitive radar at the surface, which measures erosion of ice at the base at an accuracy of a fraction of the applied radar wavelength (Corr and others, 2002). Such measurements, carried out in a Lagrangian coordinate system flowing with the ice, have been achieved only at a few points so far as they require re-deployment of the radar antennae in exactly the same surface position after a prolonged period of time. It also requires measurements of strain rates at the same location to account for ice thickness change by deformation. A spatial distribution of basal mass balance in a fixed Eulerian coordinate system can be indirectly estimated for an ice shelf in equilibrium state using the mass continuity assumption (e.g. Joughin and Padman, 2003; Wen and others, 2010) a concept which

we also pursue in this work. This requires high quality datasets of ice velocity, ice thickness, and surface mass balance, as small uncertainties in the input data are more likely to dominate the residual mass flux.

At the Ekström Ice Shelf, in the immediate neighbourhood of the German permanent base Neumayer III (70.67° S, 8.27° W), we can make use of high quality input datasets. The ice shelf hosts the German over-wintering stations since 1980. Therefore this area is, unlike many other ice shelves, well surveyed. We make use of published data on surface mass balance and in-situ surface velocity measurements. The core of our analysis is based on ERS-I/II Synthetic Aperture Radar (SAR) interferometric data providing area-wide surface velocities, and ice thickness measurements from Radio Echo Sounding (RES) surveys. These data will also be used to investigate the limitations of the chosen method when applied to comparable small ice shelves.

We have organized the paper as follows: following the introduction, a review of related measurements over the past 30 years in our area of interest is presented in section two. In-situ measurements serve as ground control for the satellite analysis and support the assumption that the Ekströmisen is in a steady state. Section three describes the discretization and implementation of the continuity equation, as well as the derivation of the input datasets such as the surface velocity field and the ice thickness. In section four and five the results for the basal mass balance and the expected accuracy are presented and discussed.

PREVIOUS STUDIES

For the Ekströmisen area, Hinze (1990) published 52 in-situ velocity measurements from different campaigns between 1979–1987 using Navy Navigation Satellite System (NNSS) and Global Positioning System (GPS) measurements. He provided error estimates of < 15 m/a in magnitude and $\pm 2°$ in flow direction. Some of these measurements were excluded in this study, as they do not cover the area of investigation. In 1997, the tidal deformation of the ice shelf surface in the southern part of the Ekströmisen was investigated, and flow velocities were derived on grounded and floating ice by GPS measurements (Riedel and Vogel, 1998). Near the seismic observatory on the north-western flank of Halvfarryggen, an additional GPS velocity measurement from 2007 was provided by C. Wesche (pers. comm. Wesche, 2010). Assuming steady state conditions, the different datasets are considered suitable to serve as ground control points (GCPs) for the interferometric analysis (see Figure 1b for the respective location).

Accumulation estimates from snow-pits, firn cores and stake farms were interpolated to an accumulation map for the entire region of interest by Rotschky and others (2007). It is known by now that the map underestimates the accumulation for the Halvfarryggen area (Fernandoy and others, 2010). For the ice shelf, however, sufficient tie-points were available and the map is considered trustworthy for our purposes.

Ice thickness has been measured using RES since the 1980s (Thyssen and Grosfeld, 1988a). We used ice-thickness measurements from 1996–2006 (Figure 1), which will be discussed in more detail in the next section.

Maps of surface elevation, ice thickness and estimated subglacial topography of the Ekström Ice Shelf and its catchment area were published by Sandhäger and Blindow (2000). Based on these datasets and measured surface accumulation rates, they calculated an ice flux of ∼3.7 Gt/a from the drainage basin into the Ekström Ice Shelf. Müller and others (2000) estimated a seaward ice flux of 2.7 km^3/a (∼2.5 Gt/a) by combining RES measured ice thickness data and advance rates of the ice shelf front, derived from Landsat MSS and ERS satellite imagery. On the basis of both studies it is assumed that basal melting exceeds surface accumulation in the Ekströmisen region.

Using a three-dimensional ice shelf flow model, Sandhäger (2000) estimated an average basal melt rate of 0.53 m/a. Nicolaus and Grosfeld (2004) employed a three-dimensional ocean circulation model and obtained an average basal melt rate of 0.98 m/a for the Ekström Ice Shelf. For the grounding zone region they hypothesized modeled melt rates of up to 14 m/a.

In 1993, the Ekströmisen was perforated several times by means of hot-water drilling next to Neumayer base. In order to record the ablation rates at the ice shelf bottom, an ultrasonic echo-sounder was installed in one of these boreholes (Nixdorf and others, 1994; Lambrecht and others, 1995). The measured melt rate averages around 0.9 m/a at this location, which is marked as white dot in Figure 3. Based on the equation of continuity, Kipfstuhl (1991) calculated melt rates on selected points along an approximated flow-line (the points are marked as black dots in Figure 3). He used GPS derived surface velocities and interpolated ice-thickness data, compiled from airborne RES measurements. Accumulation rates were taken from measurements at Neumayer base. He estimated basal melt rates of ≥ 2 m/a in the proximity of the grounding line, 0.2 m/a in the central part of the ice shelf and 1.15 m/a near the ice shelf front (Table 3).

DATA AND METHODS

Assuming the Ekströmisen to be in steady state, basal melt rates can be estimated by using the equation of continuity,

$$\dot{a}_b = \nabla \cdot (H\mathbf{v}) - \dot{a}_s \quad (1)$$

with $\dot{a}_s$ and $\dot{a}_b$ as surface and basal accumulation rates (positive for mass gain), H as the ice thickness, and $\mathbf{v}$ for the ice velocity. A constant vertical velocity profile can be assumed for the floating ice shelf as basal friction is absent. The implementation of the spatial derivative varies between applications. In a numerical sense, it can simply be discretized on the respective grid cells of the input variables using different discretization schemes. In a budgeting sense, it can be calculated along the perimeter of arbitrarily closed shapes. Often polygons (regular or irregular shaped "boxes") are chosen which are somewhat aligned with the main flow direction. The difference of incoming and outgoing mass flux, is then given by the sum of surface and basal accumulation over the enclosed area. In case flux gates are chosen along a flow line, the precondition of closed shapes can be dropped. This is an attractive choice for the application of the continuity equation in field measurements (e.g. Jenkins and Doake, 1991; Kipfstuhl, 1991). Although the implementation in a numerical sense or in a budgeting sense average over

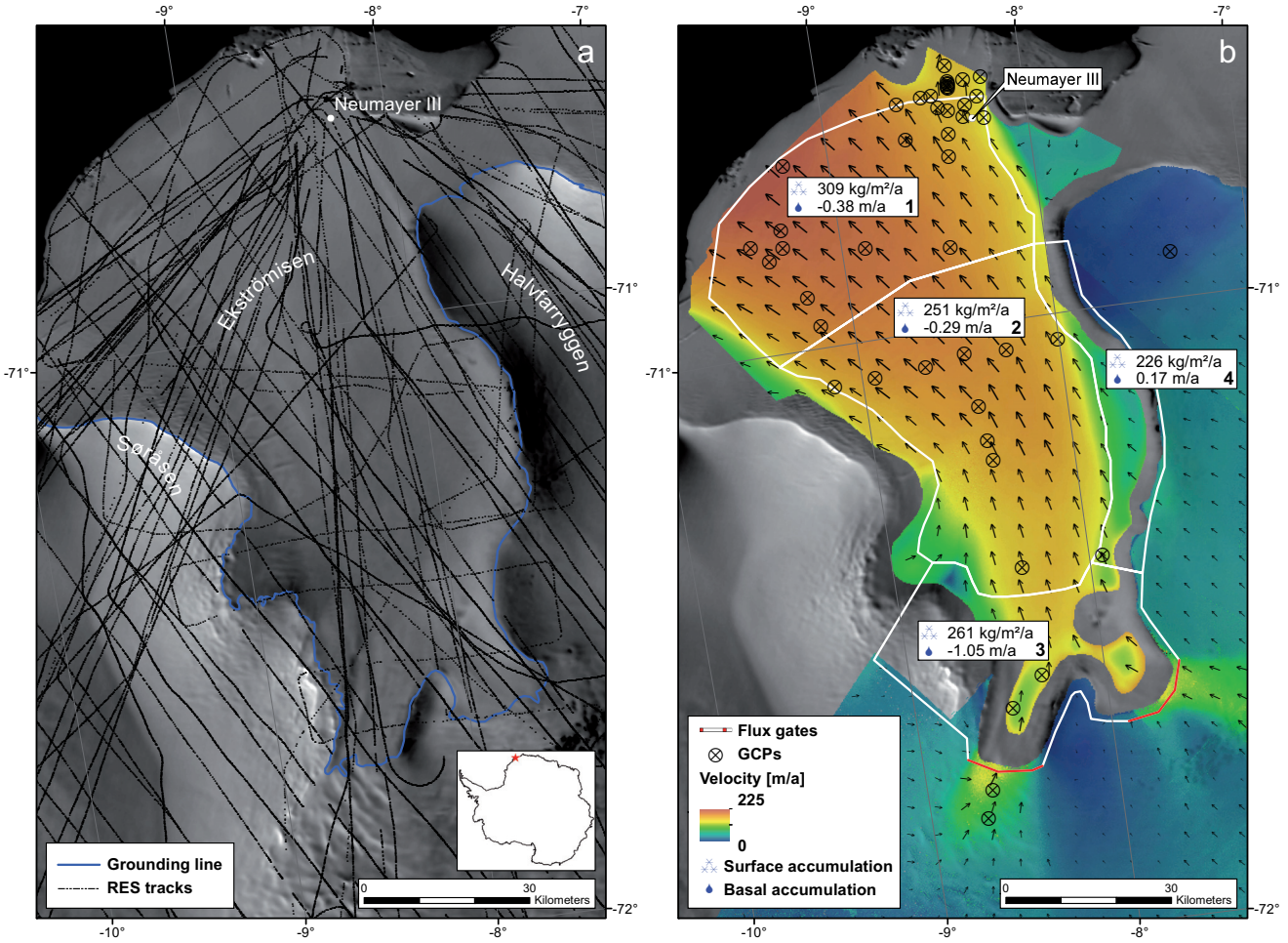

Fig. 1. (a) Region of interest with RES tracks and grounding line estimate as published by Bindschadler and others (2011). (b) InSAR derived velocity field, location of GCPs and estimated large scale surface and basal mass balance. Both maps are based on the MODIS Mosaic of Antarctica (Haran and others, 2006).

areas of different size, they do not differ in principal. Both methods blend into each other if the circumference of the polygons (i.e. the box size) is chosen to be in a similar order of magnitude as the pixel spacing in the respective discretization scheme. Since the requierd datasets are usually at first on different grids, it is tempting to subsample all data to the spatially highest resolved dataset (typically the interferometrically derived flow velocities), and then use the numerical derivation as it offers the highest spatial resolution. However, previous analysis using a similar approach (Seroussi and others, 2011) found that the gridding of the input data plays an important role, and especially sub-sampling of the ice-thickness grid can introduce severe artifacts. To avoid this problem, the spatial resolution of the incoming datasets is commonly reduced for example to the mean spacing of available RES lines. However, the question which spatial resolution can safely be achieved remains. This will be addressed after the next two sections describing the derivation of surface velocity and ice-thickness data.

Surface velocities

Surface velocities were derived from ERS-I/II repeat-pass SAR interferometry with the aid of the GAMMA SAR and interferometric processing software (e.g. Werner and others, 2000). In order to measure the full three-dimensional surface displacement, two 'topography-free' interferograms, one from a descending satellite pass and one from an ascending satellite pass were combined under the assumption of surface-parallel ice flow. This method, described for example by Joughin and others (1998), is by now routinely employed for measuring glacial movement. The topographic contributions on grounded ice were removed using a local DEM which was derived in a previous study by differential SAR interferometry (Drews and others, 2009). As this DEM excludes the floating ice shelf, elevation data from an altimetric DEM were used to remove the topographic induced phase difference in this region. For the grounded part of our area of interest, the local DEM from Wesche (2009) includes more data points for the interpolation as the Antarctic-wide DEM from Bamber and others (2009). However, for the floating ice shelf, we chose the DEM from Bamber and others (2009) over the DEM from Wesche (2009) as the resulting flow velocities showed a smaller standard deviation to the available velocity GCPs. The underlying SAR scenes for the derivation of surface velocities are listed in Table 1. Out of the available coherent image pairs, preference was given to the ones with a short spatial baseline to decrease the sensitivity towards topography. The spatial baseline was estimated from precision orbit ephemeris data provided by the Delft Institute for Earth-oriented Space Research. The relative un-

wrapped phase difference of the individual interferograms was turned into absolute values by offsetting the interferograms to a velocity GCP within the scene. For this step, the velocities of the respective GCPs were translated into a motion induced phase difference along the satellite's look vector using the orbital parameters of the corresponding interferograms. The relatively large baseline of track 493 was additionally refined with a least square fit based on several velocity GCPs. The baselines of the other satellite tracks were either too short for such a refinement or insufficient GCPs were available.

Table 1. Overview of ERS tracks, frames, date of data acquisition, perpendicular baseline ($B_\perp$) and satellite pass.

track	frame	date	$B_\perp$ [m]	pass
021	5085	02/05 Mar 1994	14	descend.
221	5121,5103	05/06 Mar 1996	233	descend.
493	5121,5103,5085	18/19 Feb 1996	214	descend.
002	5697	15/16 Jan 1996	50	ascend.
031	5661,5679,5697	06/09 Mar 1994	48	ascend.
045	5661,5679,5697	13/14 Mar 1997	193	ascend.
460	5715	22/23 Mar 1996	23	ascend.

Tidal movement between data acquisition is reflected in an interferogram by a high phase gradient in the grounding zone where the horizontal ice flow is overlayed by differential vertical displacement. On the one hand, this makes SAR interferometry a powerful tool for grounding zone detection (e.g. Sykes and others, 2009; Rignot and others, 2011) on the other hand, no horizontal displacement can be safely derived in this region. Therefore, we excluded the *InSAR* grounding zone from the analysis. Assuming that the remainder of the ice shelf is lowered and lifted uniformly, the vertical displacement for the freely floating parts cancels by offsetting of the unwrapped phase to a GCP.

The individual flow fields were mosaicked and sampled to a 100 m × 100 m grid (Figure 1b). In overlapping areas, the difference of individually processed flow fields is a first estimate for the overall accuracy. On the grounded part, overlapping edges differ between 1–35 m/a. For the floating parts, the difference between the northern frames (combination from track 021 and 460) and the southern frames (combination from track 493 and 002) is a constant offset of ∼ -22 m/a. We attribute this offset to the northern flow-field, as a similar offset is evident in a comparison to the (northern) GCPs, while no systematic offset is observed for the southern track combination. Neglecting the origin of this difference (e.g. atmospheric contribution, imprecise baseline estimates, tidal movement), we offset the northern flow-field and feather remaining differences with a distance weighted blend routine. For estimating the error we compare the velocity map to all available GCPs (Figure 2) excluding the ones used for offsetting the interferograms. The GCPs which were used for the baseline refinement of track 493 were included as the baseline refinement is not a direct fit to the GCPs but an adjustment of the baseline model. Mean and standard deviation compared to the velocity GCPs are 4 ± 18 m/a in magnitude and $12 \pm 8°$ in flow direction. As shown in Figure 2, the deviation in magnitude is not correlated to the location.

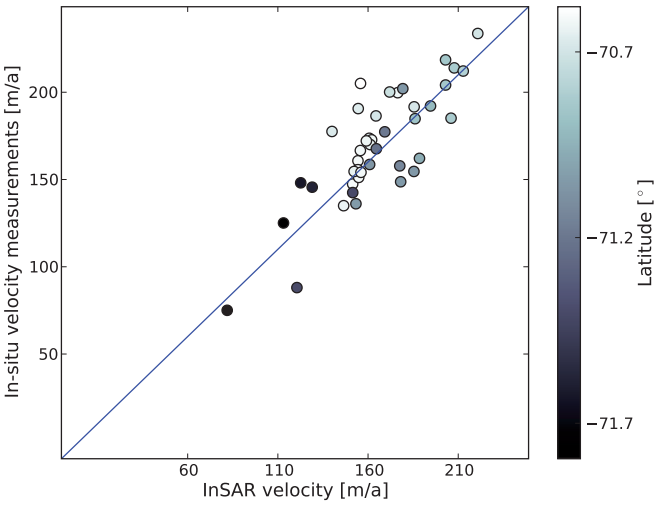

Fig. 2. Deviation between InSAR derived surface velocities and in-situ measured surface velocities. The error in magnitude is 4 ± 18 m/a. Latitude value of GCPs is gray-scaled.

Ice thickness

The airborne ice-thickness data have been acquired over the years 1996–2006 in various campaigns. Characteristics of the pulsed RES system are described in Nixdorf and others (1997) and Steinhage and others (2001). The center frequency of the emitted bursts is 150 MHz and the pulse length can be toggled between 60 ns and 600 ns. The short pulse is suited for applications which require a higher vertical resolution (and less penetration depth), whereas the long pulse aims to increase the penetration depth (while decreasing the vertical resolution). The dataset presented here are based on both modes since some RES profiles are only available with the long pulse. However, considering the ice-thicknesses encountered, the short pulse is the more appropriate choice for sounding the ice shelf. Data processing varies slightly between the profiles acquired in the various seasons. Standard processing encompasses tenfold stacking, differentiation, bandpass filtering, and an automatic gain control (Steinhage and others, 1999). The horizontal shot spacing of the stacked data depends on the flight speed, but generally varies between 20–30 m. The travel-time to depth conversion uses a constant propagation velocity of 168 m/μs in ice and includes a firn correction of 8 m to account for a higher radar velocity in firn. We use these values based on a column-averaged ice density of 878 kg/m^3 which is estimated after modeling studies from Ligtenberg and others (2011). The firn correction is similar to the firn correction of 8.8 m derived from common-midpoint measurements by Blindow (1994) on the Filchner Ronne Ice Shelf. Profiles crossing large crevasses at the surface (especially in the north-western part of the Ekströmisen) show a characteristic upward-bending of the bottom reflection. This originates from less consolidated snow and ice filling the crevasses which results in an increased signal propagation. This is not accounted for with the constant firn correction. These features were removed manually, and gaps were closed with an inverse distance weighting interpolation scheme.

In terms of deriving the ice thickness, the bottom reflection from ice shelves is ambiguous as it not necessarily originates from the ice–ocean interface, but rather repre-

sents the boundary of meteoric and (refrozen) marine ice. Previous studies (Thyssen, 1988; Jenkins and Doake, 1991; Blindow, 1994) investigated the marine–meteoric boundary and concluded that this internal reflection appears strongly. Depending on the thickness of the marine ice layer, the ice–ocean interface is potentially masked due to increased signal attenuation in the marine bottom layer. The total ice thickness is often inferred via an hydrostatic inversion scheme, which combines the freeboard height with a density–depth profile (e.g. Fricker and others, 2001; Lambrecht and others, 2007; Wen and others, 2010). Contrary to the larger Antarctic ice shelves, the comparatively small Ekströmisen does not show any signs of accreted ice and we argue that the RES lines considered here indeed image the ice–ocean interface and thus reflect the total ice thickness. The argument is four-fold: (1) Modeling studies (Nicolaus and Grosfeld, 2004) of the ocean circulation beneath the Ekströmisen predict the highest melt rates near the grounding line, but no accretion anywhere on the ice shelf, (2) the bottom reflection in the RES lines appears specular, laterally smoothed and shows no sign of a second reflector at larger depths. This is the case for the long and short pulse. We would expect some kind of penetration at least for the long-pulse datasets, if marine ice was present, (3) Thyssen and Grosfeld (1988a) compared the RES inferred ice thickness over the Ekströmisen, to the ones inferred from a hydrostatic equilibrium. He found no positive anomalies and therefore concluded that no accreted ice is present. Similarly, in an enhanced dataset of RES lines Sandhäger and Blindow (2000) also interpreted the bottom reflection from the Ekströmisen as the ice–ocean interface, (4) Griggs and Bamber (2011) compiled a new Antarctic-wide ice-thickness map of ice shelves based on elevations from satellite altimetry and a modeled density–depth profile. A comparison with our interpolated RES ice thickness map shows a mean deviation of 15 ± 16 m. There is a bias towards the northern part of the Ekströmisen where the RES inferred ice thickness is systematically below the ice thickness derived from the flotation criterion. This potentially indicates the presence of marine ice, however, the difference is especially large near Neumayer base where direct measurements from Lambrecht and others (1995) showed basal melting. The difference is also not large enough to exclude errors in surface elevation or the density profile which deteriorate the hydrostatic inversion. Therefore, based on previous studies and our own analysis we conclude that the RES ice-thickness map actually represents the total ice-thickness and is not flawed by an undetected marine ice layer.

Quantification of sub-glacial melting

In order to get a large scale estimate of basal melting beneath the Ekströmisen we calculated the residual mass flux F along the perimeter of the polygons shown in Figure 1b using interpolated ice-thickness data on a 5 km x 5 km grid. F is calculated as the cumulative sum of the mass flux f_i across the individual pixels i

$$F = \sum_{i=2}^{i=N-1} f_i = \sum_{i=2}^{i=N-1} \mathbf{v}_i \cdot \cos(\phi_i') \cdot H_i \cdot d_i \qquad (2)$$

where N is the number of pixels in the flux gate and ϕ_i' is the normal angle to the flux gate at position i which is calculated to be perpendicular to the line connecting position $i+1$ and $i-1$. The pixel spacing is indicated by d_i. For the conversion between m/a and kg/a we used a column-averaged ice density of 878 kg/m^3 based on modeling studies from Ligtenberg and others (2011). As the flux gates on the grounded ice are in close vicinity to the grounding line, basal sliding is assumed in this region. Therefore, $\mathbf{v}_i$ is estimated to equal the surface velocity for all flux gates.

Following the budgeting approach, the difference between incoming and outgoing fluxes F of each polygon is determined by $\dot{a}_s + \dot{a}_b$. Whether F represents incoming or outgoing flux is defined by the algebraic sign of $\cos(\phi_i')$, therefore $\dot{a}_b$ can simply be calculated by

$$\dot{a}_b = \frac{F}{A} - \dot{a}_s \qquad (3)$$

where F is calculated along the perimeter of a polygon enclosing the area A.

To evaluate the spatial distribution of basal melting on a finer scale, we averaged the RES data (mean shot spacing $\sim$30 m) along the profiles to the same grid cell spacing as the surface velocities (grid spacing 100 m). The intersecting RES lines form polygons (black lines in Figure 3) which we used to estimate $\dot{a}_b$ in the same way as demonstrated above. The resulting melt rates of each polygon were interpolated across the ice shelf using an inverse distance weighted interpolation scheme. Choosing the polygons along the RES flight tracks circumnavigates the interpolation of the RES data and thus excludes interpolation artifacts.

RESULTS

Table 2 lists the estimated incoming and outgoing fluxes for the four polygons shown in Figure 1b and the resulting melt rates. As no surface velocities are available in the *InSAR* grounding zone, uncertainties are larger for polygons 3 and 4. The positive value for polygon 4 is smaller than the error boundary and also small basal melting is possible. However, a value close to zero is likely. The interpolated melt rates for the polygons along the RES flight tracks are shown in Figure 3 and error estimates are discussed in the following section.

Table 2. Estimated ice flux, mean surface accumulation ($\dot{a}_s$), size and estimated basal accumulation ($\dot{a}_b$) for the polygons shown in Figure 1b.

id	in-flux	out-flux	$\dot{a}_s$	size	$\dot{a}_b$
1	2.71 Gt/a	2.67 Gt/a	0.53 Gt/a	1718 km^2	-0.38 m/a
2	2.59 Gt/a	2.58 Gt/a	0.52 Gt/a	2089 km^2	-0.29 m/a
3	2.54* Gt/a	1.68 Gt/a	0.34 Gt/a	1302 km^2	-1.05 m/a
4	0.65 Gt/a	0.85 Gt/a	0.12 Gt/a	524 km^2	0.17 m/a

*including an ice flux of 1.11 Gt/a and 0.94 Gt/a across the western and eastern red colored flux gates in Figure 1b.

We compared our results to previous estimates from Kipfstuhl (1991) and Lambrecht and others (1995). The different values are listed in Table 3. The ultra-sonic measurements from Lambrecht and others (1995) near Neumayer base are considered to be the only direct ground

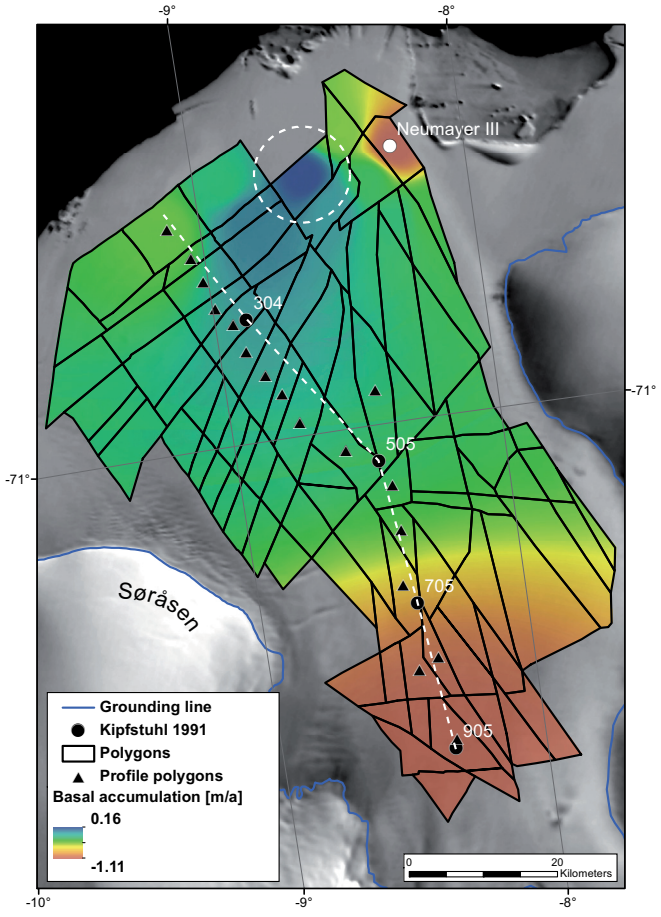

Fig. 3. Model output for closed boxes along the flown RES tracks. In the background is the MODIS Mosaic of Antarctica (Haran and others, 2006), grounding line estimate as published by Bindschadler and others (2011).

truth to validate our approach. The basal melt rates derived by Kipfstuhl (1991) are based on an interpolated ice-thickness map and the assumption that the two available velocity measurements for each point were aligned along a flow-line. In his approach, errors can arise from neglecting transverse strain, interpolated RES lines and assuming that the surface accumulation at the individual sites equals the accumulation rate measured at Neumayer base.

Table 3. Deviation between modeled and basal melt rates from previous studies (Kipfstuhl, 1991; Lambrecht and others, 1995). Location of references can be found in Figure 3.

name	304	505	705	905	NM*
previous studies [m/a]	0.44	0.40	0.20	1.20	0.93
this study [m/a]	0.40	0.38	0.13	1.13	1.11
difference [m/a]	-0.04	-0.02	-0.07	-0.07	0.18

*ultrasonic echo-sounder measurements at Neumayer base, white dot in Figure 3.

DISCUSSION

The usage of the continuity equation to infer basal melt rates is based on the reliable determination of spatial changes in accumulation and mass flux. In terms of accumulation, precise absolute values are required, in terms of velocity and ice thickness it is more important to capture the relative changes accurately. It is in the nature of the spatial derivative, that during the differencing small relative errors of incoming and outgoing mass flux add up to a larger error for the residual mass flux. This problem can be treated in two ways, either by minimizing the errors in the input data, or by averaging the data to a larger cell size. In this study, the latter is achieved by choosing larger polygons which in turn is associated to the loss of spatial resolution. In order to minimize uncertainties in the input data, polygons were chosen along the RES lines which avoids artificially introduced interpolation errors in the ice-thickness data. Similar to Seroussi and others (2011) we noticed that this problem is not negligible, because the resulting maps of basal melt rates significantly depended on the applied interpolation scheme and grid spacing. Independent of the specific implementation for the spatial derivative, errors in flow velocities, ice thickness and accumulation must be considered separately.

The interferometrically derived surface velocities may be flawed by a variety of reasons, among these an erroneous elevation model, uncertainties in baseline estimates, atmospheric path delays and tide induced phase ramps. We have relatively good ground truth data to evaluate the overall accuracy of the flow field. It seems unlikely that atmospheric effects induce errors on a spatial scale which is smaller than the average spacing of the velocity GCPs shown in Figure 1b. However, systematic errors depending on the processing history remain and may not be reduced by averaging the flow velocities along the perimeter of the polygons. Based on the GCPs we estimate a mean error and standard deviation of 4 ± 18 m/a in magnitude for the satellite derived velocities.

Similar arguments apply for the RES data. In this study, ice-thickness data from different RES campaigns are used. Errors are potentially introduced by using different RES systems which require different processing schemes leading to offsets between the flight lines. Additionally, the manual and subjective removal of effects induced by crevasses increases the uncertainties. This is especially the case for the western part of the ice-shelf where crevasses are also evident in ERS satellite imagery (Müller and others, 2000). As the ice-thickness data are only interpolated along the RES flight lines, erroneous offsets from the different RES systems would remain. We evaluated the ice-thickness dataset by means of a cross-over analysis of the different flight lines. This results in a mean and standard deviation of 0.6 m $\pm$18 m.

The overall error in residual mass flux F can roughly be estimated by the individual errors of the input datasets. If the data is not averaged beforehand the absolute errors may add up during the summation of incoming and outgoing fluxes leading to an accumulated error for the residual mass flux which is usually much larger than F. Therefore, spatial averaging of the input datasets is necessary.

Averaging reduces the noise in the input data, but does not diminish systematic errors. In our approach, the degree of averaging is basically given by the size of the polygons. In the following back-of-the-envelope calculation, we estimate the random errors in velocity and ice thickness with the previously derived standard deviations of 18 m/a and 18 m, respectively. We have no direct evidence for the

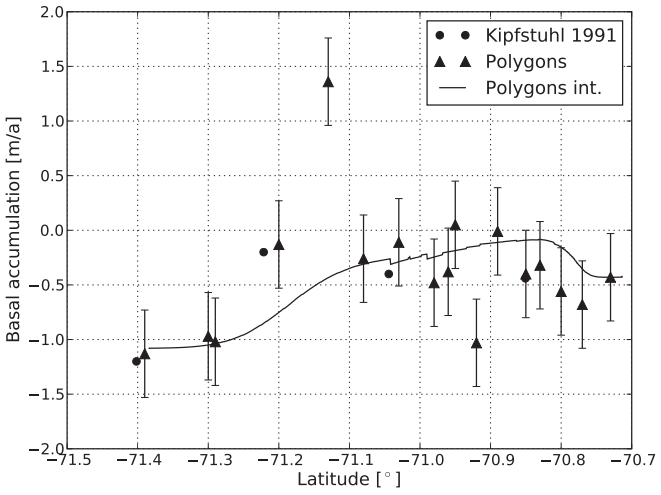

Fig. 4. Comparison between estimated basal accumulation of each polygon and interpolated values. The profile follows the estimates made by Kipfstuhl (1991). Error bars indicate the standard deviation between the data points and the interpolated field.

magnitude of systematic errors and estimate 5 m/a and 10 m in ice-thickness to account for offsets introduced by the various systems. In a best case scenario for averaging, the random errors become smaller proportional to the square root of the number of averaged data points. In our case, a typical polygon is formed by four intersecting RES lines with a total perimeter of 30 km containing 300 data points of ice-thickness and velocity. If we consider the four sides separately, the summation along the individual lines reduces the random component by a factor of 7, leaving a random error of only a few percent for the average value of the flux field $\mathbf{v}H$. Systematic errors may or may not be present between the four sides of the polygons. In the unfavorable case that all four sides are inflicted with the systematic errors estimated above, the error in differencing the individual sides of the polygons may be 12%, for the average changes in $\mathbf{v}H$ for a typical polygon in the center of the ice shelf. In terms of basal melting errors in accumulation increase the error.

In Figure 4 our estimate of basal melting is plotted along latitude in direct comparison with the estimates made by Kipfstuhl (1991) (see dashed white line in Figure 3 for profile location). Next to the estimated melt rates for each polygon along this profile (Polygon), we show the interpolated basal melt rate (Polygon int.). The local outlier at $\sim$-71.15° latitude can be related to a small discontinuity in the mosaicked velocity field. Figure 4 shows, that the interpolated basal melt strongly smooths the variability in melt rates between neighboring boxes. The standard deviation between the data points and the interpolated field is 0.4 m/a. This variability of the (detrended) polygons gives an upper estimate of errors for the basal melt rates, assuming that melting should be more or less homogeneous between neighboring polygons. However, the difference of our estimates to previous studies is less than that (see Table 3).

The dashed white circle in Figure 3 marks an area with basal accumulation of about 0.16 m/a which suggests the accretion of ice. The crossing-over analysis of the RES profiles shows no irregularities in this region and no outliers are found in the velocity field. Unlike for the rest of the ice shelf, the flow regime in this area is compressive. This is also the case in the modeled flow velocities of Sandhäger (2000) who identifies the Neumayer ice rumple at the shelf ice front as the primary reason for the compression. Although we cannot exclude the presence of marine ice, it seems more likely that the apparent accretion of ice is actually related to the changing flow regime which potentially violates the steady-state assumption in this area. However, there is no conclusive evidence.

CONCLUSION

In this paper we estimated the magnitude and local variation in basal melt rate beneath the Ekström Ice Shelf based on the assumption of mass continuity. Interferometrically derived surface velocities, RES ice-thickness measurements and interpolated surface accumulation data served as main input datasets. By differentiating between systematic and random errors, we provide an estimation for the expected accuracy of our method in dependence of the chosen polygon size. It lies in the nature of our approach, that uncertainties in basal melt rates strongly increase with decreasing areas under consideration. Especially for small ice shelves like the Ekströmisen strong spatial averaging of the input data is not possible, which puts high demands on the quality and accuracy of the input data. Relatively small inaccuracies in the input data are amplified by the spatial derivative in the continuity equation. In order to overcome additional uncertainties caused by the interpolation of ice-thickness data we calculated the mass flux exactly along narrowly spaced RES lines. Accretion of basal ice is not believed to be present at the Ekströmisen and its occurrence in the final basal mass balance map is related to inaccuracies in the datasets or a violation in the steady state assumption. However, our estimates are in good overall agreement with previous studies and may serve as a baseline for further research monitoring temporal changes in basal melt.

ACKNOWLEDGEMENTS

We thank D. Jansen for providing literature which is hard to get otherwise, S. Ligtenberg, M. Helsen and M. van den Broeke for information of depth and density of the firn layer, J. Griggs and J. Bamber for the ice-shelf thickness from satellite radar altimetry. Preparation of this work was supported with the scholarship of the Evangelisches Studienwerk e.V. Villigst to R. Drews. We appreciate helpful discussions with Olaf Eisen. ERS satellite data were made available through ESA Project *AO*3.108.

REFERENCES

Bamber, J. L., J. L. Gomez-Dans and J. A. Griggs, 2009. A new 1km digital elevation model of the Antarctic derived from combined satellite radar and laser data Part 1: Data and methods, *The Cryosphere*, **3**, 101–111.

Bindschadler, R., H. Choi, A. Wichlacz, R. Bingham, J. Bohlander, K. Brunt, H. Corr, R. Drews, H. Fricker, M. Hall, R. Hindmarsh, J. Kohler, L. Padman, W. Rack, G. Rotschky, S. Urbini, P. Vornberger and N. Young, 2011. Getting around Antarctica: new high-resolution mappings of the grounded and freely-floating boundaries of the

Antarctic ice sheet created for the International Polar Year, *The Cryosphere*, **5**, 569–588.

Blindow, N., 1994. The central part of the Filchner-Ronne Ice Shelf, Antarctica: internal structures revealed by 40 MHz monopulse RES, *Annals of Glaciology*, **20**, 365–371.

Corr, H. F. J., A. Jenkins, K. W. Nicholls and C. S. M. Doake, 2002. Precise measurement of changes in ice-shelf thickness by phase-sensitive radar to determine basal melt rates, *Geophysical Research Letters*, **29**, 1232.

Drews, R., W. Rack, C. Wesche and V. Helm, 2009. A spatially adjusted elevation model in Dronning Maud Land, Antarctica, based on differential SAR Interferometry, *IEEE Transactions on Geoscience and Remote Sensing*, **47**, 2501–2509.

Fernandoy, F., H. Meyer, H. Oerter, F. Wilhelms, W. Graf and J. Schwander, 2010. Temporal and spatial variation of stable-isotope ratios and accumulation rates in the hinterland of Neumayer station, East Antarctica, *Journal of Glaciology*, **56**, 673–686.

Fricker, H. A., S. Popov, I. Allison and N. Young, 2001. Distribution of marine ice beneath the Amery Ice Shelf, *Geophysical Research Letters*, **28**, 2241–2244.

Gille, S. T., 2008. Decadal-Scale Temperature Trends in the Southern Hemisphere Ocean, *Journal of climate*, **21**, 4749–4765.

Griggs, J. A. and J. L. Bamber, 2011. Antarctic ice-shelf thickness from satellite radar altimetry, *Journal of Glaciology*, **57**, 485–498.

Haran, T., J. Bohlander, T. Scambos, T. Painter and M. Fahnestock, 2006. MODIS mosaic of Antarctica (MOA) image map.

Hellmer, H. H., 2004. Impact of Antarctic ice shelf melting on sea ice and deep ocean properties, *Geophysical research letters*, **31**, L10307.

Hinze, H., 1990. Zum Einsatz von Satelliten-Positionierungsverfahren für glaziologische Aufgaben in der Antarktis, *Wissenschaftliche Arbeiten der Fachrichtung Vermessungswesen der Universität Hannover*, **163**, 179.

Holland, P. R., A. Jenkins and D. M. Holland, 2008. The Response of Ice Shelf Basal Melting to Variations in Ocean Temperature, *Journal of Climate*, **21**, 2558–2572.

Jenkins, A. and C. S. M. Doake, 1991. Ice-Ocean Interaction on Ronne Ice Shelf, Antarctica, *Journal of Geophysical Research*, **96**, 791–813.

Jenkins, A., P. Dutrieux, S. S. Jacobs, S. D. McPhail, J. R. Perrett, A. T. Webb and D. White, 2010. Observations beneath Pine Island Glacier in West Antarctica and implications for its retreat, *Nature*, **3**, 468–472.

Joughin, I., R. Kwok and M. Fahnestock, 1998. Interferometric estimation of three-dimensional ice-flow using ascending and descending passes, *IEEE Transactions on Geoscience and Remote Sensing*, **36**, 25–37.

Joughin, I. and L. Padman, 2003. Melting and freezing beneath Filchner-Ronne Ice Shelf, Antarctica, *Geophysical Research Letters*, **30**, 1477.

Kipfstuhl, J., 1991. Zur Entstehung von Unterwassereis und das Wachstum und die Energiebilanz des Meereises in der Atka Bucht, Antarktis, *Berichte Polarforschung*, **85**, 88.

Lambrecht, A., U. Nixdorf and Zurn W., 1995. Ablation rates under the Ekström Ice Shelf deduced from different methods, *FRISP Report*, **9**, 50–56.

Lambrecht, A., H. Sandhäger, D. G. Vaughan and C. Mayer, 2007. New ice thickness maps of Filchner-Ronne Ice Shelf, Antarctica, with specific focus on grounding lines and marine ice, *Antarctic Science*, **19**, 521–532.

Ligtenberg, S. R. M., M. M. Helsen and M. R. van den Broeke, 2011. An improved semi-empirical model for the densification of Antarctic firn, *The Cryosphere Discuss.*, **5**, 1921–1948.

Little, C. M., A. Gnanadesikan and M. Oppenheimer, 2009. How ice shelf morphology controls basal melting, *Journal of Geophysical research*, **114**, C12007.

Müller, U., H. Sandhäger, J. Sievers and N. Blindow, 2000. Glacio-Kinematic Analysis of ERS-1/2 SAR Data of the Antarctic lce Shelf Ekströmisen and the Adjoining Inland lce Sheet, *Berichte Polarforschung*, **67**, 15–26.

Nicolaus, M. and K. Grosfeld, 2004. lce - Ocean Interactions underneath the Antarctic lce Shelf Ekströmisen, *Polarforschung*, **72**, 17–29.

Nixdorf, U., A. Lambrecht and D. Steinhage, 1997. Geophysical - glaciological studies in the grounding zone area of the Ekström Ice Shelf (EIS), *FRISP Report*, **11**, 51–54.

Nixdorf, U., H. Oerter and H. Miller, 1994. First access to the ocean beneath Ekströmisen, Antarctica, by means of hot-water drilling, *Annals of Glaciology*, **20**, 110–114.

Payne, A. J., A. Vieli, A. P. Shepherd, D. J. Wingham and Rignot E., 2004. Recent dramatic thinning of largest West Antarctic ice stream triggered by oceans, *Geophysical research letters*, **31**, L23401.

Riedel, B. and D. Vogel, 1998. Geodätische Messungen an der Grounding Line des Ekström-Schelfeises, *Berichte Polarforschung*, **267**, 125–131.

Rignot, E., J. Mouginot and B. Scheuchl, 2011. Antarctic grounding line mapping from differential satellite radar interferometry, *Geophysical Research Letters*, **38**, L10504.

Rotschky, G., P. Holmlund, E. Isaksson, R. Mulvaney, H. Oerter, M. R. Van Den Broeke and J. Winther, 2007. A new surface accumulation map for western Dronning Maud Land, Antarctica, from interpolation of point measurements, *Journal of Glaciology*, **53**, 385–398.

Sandhäger, H., 2000. Quantifizierung eisdynamischer und massenhaushaltsrelevanter Basisgrössen eines antarktischen Inlandeis-Schelfeis-Systems unter Einsatz eines numerischen Fliessmodells, (PhD thesis), University of Münster.

Sandhäger, H. and N. Blindow, 2000. Surface elevation, ice thickness, and subglacial-bedrock topography of Ekström Ice Shelf (Antarctica) and its catchment area, *Annals of Glaciology*, **30**, 61–68.

Seroussi, H., M. Morlighem, E. Rignot, E. Larour, D. Aubry, H. Ben Dhia and S. S. Kristensen, 2011. Ice flux divergence anomalies on 79north Glacier, Greenland, *Geophysical Research Letters*, **38**, L09501.

Steinhage, D., U. Nixdorf, U. Meyer and H. Miller, 1999. New maps of the ice thickness and subglacial topography in Dronning Maud Land, Antarctica, determined by means of airborne radio-echo sounding, *Annals of Glaciology*, **29**, 267–272.

Steinhage, D., U. Nixdorf, U. Meyer and H. Miller, 2001. Subglacial topography and internal structure of central and western Dronning Maud Land, Antarctica, determined from airborne radio echo sounding, *Journal of Applied Geophysics*, **47**, 183–189.

Sykes, Helena J., Tavi Murray and Adrian Luckmann, 2009. The location of the grounding zone of Evans Ice Stream, Antarctica, investigated using SAR interferometry and modelling, *Annals of Glaciology*, **50**, 35–40.

Thyssen, F., 1988. Special aspects of the central part of Filchner-Ronne Ice Shelf, Antarctica, *Annals of Glaciology*, **11**, 173–179.

Thyssen, F. and K. Grosfeld, 1988a. Ekström Ice Shelf, Antarctica, *Annals of Glaciology*, **11**, 180–181.

Wen, J., Y. Wang, W. Wang, K. C. Jezek, H. Liu and I. Allison, 2010. Basal melting and freezing under the Amery Ice Shelf, East Antarctica, *Journal of Glaciology*, **56**, 81–90.

Werner, C., U. Wegmüller, T. Strozzi and A. Wiesmann, 2000. GAMMA SAR and Interferometric Processing Software, ERS - ENVISAT Symposium, Gothenburg, Sweden.

Wesche, C., 2009. Evaluation and application of GPS and altimetry data over central Dronning Maud Land, Antarctica: anual elevation change, a digital elevation model and surface flow velocity, (PhD thesis), University of Bremen.

Acknowledgements

Olaf Eisen was the overall supervisor and the working brain behind this thesis. With patience, humor, and an extremely motivating style, he introduced me into the ice-penetrating radar world and while doing so, taught me lots about writing and organizing myself (....yes, it was worse before I started). Olaf filled me with self-confidence when I encountered what I thought to be a dead-end road (well, it wasn't), and eased my concerns with showing me lots of other options (which I never needed). Thank you Olaf. The LIMPICS team has a somewhat distributed style all over Germany, but it nevertheless felt like a family during the impressive field campaigns (2xColle Gnifetti and 1xAntartica). Thanks to Pascal Bohleber, Anja Diez, Achim Heilig, and Coen Hofstede, it is a pleasure to work with all of you. In Antarctica, Christoph Meyer and Astrid Lambrecht showed me which buttons to press for the low-frequency radar, and Daniela Jansen as well as Niklas Neckel teamed with me in collecting the data. Thanks also to Ralf Witt and Andreas Frenzel for the technical support. Niklas Neckel not only provided the cover picture, but also contributed with results based on his well done diploma thesis.

The "Evangelisches Studienwerk Villigst e. V." provided financial support for the entire time and also financed extra travel expenses for the research stay in Christchurch, New Zealand, as well as for the participation at the conference "24. Internationale Polartagung der Deutschen Gesellschaft für Polarforschung" in Obergurgl, Austria. Apart from the finances, Villigst is a great place to be and I benefited from several interdisciplinary meetings. Actually, without Villigst I would never have found my way to AWI.

The Glaciology Section at the AWI, led by H. Miller, is a joyful group of scientists from whom I learned a lot and many of them appear as coauthors in the published-papers-to-be. Thank you for the provision of a great working environment and infrastructure, I will miss being there. It was always worth going to AWI, if not for work than for sitting next to Veit Helm and Anna Wegner. Daniel Steinhage helped a lot, especially with the large pool of RES data which he provided. Frank Wilhelms' office is an excellent address for mathematical discussions, and the experience of Hans Oerter greatly improved the Halvfarryggen manuscript. Veit Helm is the supplier of the highest precision and best processed laser scanner data ever. He also taught me the GPS processing. Christine Wesche supplied me several times with good surface elevations. Sepp Kipfstuhl, Johannes Freitag and Ilka Weikusat are on the other end of the (unfinished) link between radar and the micro-structure of ice. All of them engaged me in funny and fruitful discussions covering all spatial scales of ice sheets.

The Gateway Antarctica - Center for Antarctic Studies and Research at the Canterbury University in Christchurch, New Zealand, hosted me during a five months research stay, which focused on the derivation of interferometric flow velocities and the analysis of anisotropic backscatter in SAR satellites scenes. Bryan Storey and the entire Gateway Antarctica team provided a terrific working environment. Wolfgang Rack diligently supervised the search for errors in the flow fields and guided the processing and analysis of (polarimetric) PalSAR scenes. Wolfgang—once again—thank you very much.

Michael Bässler shared is his experience in InSAR analysis and I hope one day we will meet in person. Sebastian Ruhnau, Peter Köhler, Anna Wegner and Adriana Drews mastered the daunting task to proofread through the raw-data of the text surrounding the manuscripts. A big thank you to all of you.